

SEASONAL WIND VARIATIONS IN THE MID-
LATITUDE NEUTRAL THERMOSPHERE

by

BARBARA ANN EMERY

B.S., University of Illinois in Urbana
1972

S.M., Massachusetts Institute of Technology
1975

SUBMITTED IN PARTIAL FULFILLMENT
OF THE REQUIREMENTS FOR THE
DEGREE OF

DOCTOR OF SCIENCE

at the

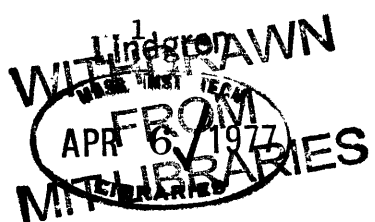
MASSACHUSETTS INSTITUTE OF TECHNOLOGY

MAY, 1977

Signature of Author... Department of Meteorology, February 21, 1977

Certified by..... Thesis Supervisor

Accepted by..... Chairman, Departmental Committee on Graduate Students



SEASONAL WIND VARIATIONS IN THE MID-LATITUDE
NEUTRAL THERMOSPHERE

by

Barbara Ann Emery

Submitted to the Department of Meteorology
on February 21, 1977 in partial fulfillment
of the requirements for the degree of
Doctor of Science

ABSTRACT

Incoherent scatter radar measurements of ionospheric properties above Millstone Hill, Mass. (42.6°N , 71.5°W) were the basic data source for this study of the neutral quiet-time thermospheric circulation. Two years (1970-1971) of data (36 days) were analyzed beginning at sunspot maximum. The radiation absorbed by the thermosphere was about 30% less in the second year although the magnetic activity remained about the same. Neutral number densities were taken from the MSIS (mass spectrometer/incoherent scatter) global atmospheric model of Hedin *et al* (1977) and used as a supplement to the ionospheric data to derive neutral exospheric temperatures and the horizontal neutral wind parallel to the magnetic field line.

The exospheric temperatures were derived through the solution of the ion heat balance equation. Diurnal average temperatures were about 1025°K during the winter and about 1140°K and 990°K for the first and second summers. The day-night difference in the temperatures was about 250°K in the winter and 375°K in the summer.

Estimates of the neutral wind parallel to the magnetic field line were derived from measured vertical ion drift velocities and diffusion velocities deduced from gradients in the ionospheric data. Electric field effects were ignored and ion-neutral collision frequencies were taken from Banks (1966b).

A two-dimensional model was devised to solve the neutral equations of motion where the ion-drag was specified by the ionospheric data, the zonal pressure gradients were determined by the diurnal variation of the exospheric temperature, and the estimates of the magnetic meridional wind were used as constraints on the size of the (geographic) meridional wind. The meridional pressure gradient was a free parameter, found through the constraint on the meridional winds.

The exospheric temperature was expressed as a truncated Fourier-Taylor series as a function of time and latitude. Using this form to specify the pressure and its gradients at another latitude, a third dimension could be added to the model so that the vertical velocity could be solved from the continuity equation.

There was an approximate balance between the pressure gradient and the ion drag, with the winds blowing from high to low pressures. Wind magnitudes were of the order of 100 m/sec and 300 m/sec for the meridional and zonal winds, respectively. Diurnal averages showed a seasonal variation of south-westward winds in the summer and north-eastward winds in the winter. Average daily vertical winds, which were not considered reliable because of the assumptions made about latitudinal gradients, were downwards for most of the year. The annual average wind at 300 km was 22 m/sec to the south and 3 m/sec to the west. Annual variations were ± 52 and ± 42 m/sec for the meridional and zonal winds respectively.

The question about the diffusive transport of the lighter constituents from the summer to the winter poles by transequatorial flows was examined. The annual meridional wind variations at Millstone Hill were 3 or 4 times larger than was necessary to crudely reproduce the winter oxygen bulge assuming only a solar heat source (Mayr and Volland, 1972). However, there has not been a theoretical study of diffusion that includes the high latitude heat source in addition to the solar heat source. The Millstone Hill results which can be explained in terms of a high latitude heat source are the mean annual equatorwards wind and the large seasonal variation in the mean daily winds.

MSIS model pressure gradients were used with Millstone Hill ionospheric data to derive winds. The results were similar to those of the Millstone Hill model except the intensity of the circulation was decreased from 1970 to 1971 instead of increased. It was suggested that the increased circulation of the Millstone Hill model was a result of the increasing importance of the high latitude heat source in relation to the solar heat source at the beginning of the descent in the sunspot cycle.

Name and Title of Thesis Supervisors:

John V. Evans
Reginald E. Newell

Senior Lecturer
Professor

ACKNOWLEDGEMENTS

I am deeply indebted to Dr. John V. Evans for the use of the facilities at the Millstone Hill incoherent scatter radar in Westford, Mass., and for his constant advice and support during the period of this work. Dr. Reginald E. Newell has provided encouragement and advice throughout my tenure at M.I.T., especially in these past few months.

Assistance in examining the stability criteria for the inclusion of the non-linear terms has come from Drs. Eugenia Kalnay-Rivas and Dale Haidvogel. Dr. Edward N. Lorenz provided some insight into the uncertainty analysis and Dr. Ronald G. Prinn has given general advice.

The two persons at Millstone Hill whom I would especially like to thank are Dr. John M. Holt and Mrs. Alice Freeman. The former provided many of the preliminary computer programs which were used and was a general fund of advice about the data. Alice offered me a place to stay in her home near Millstone Hill and thus eliminated much of the tedium and fatigue associated with many frequent trips to the radar site.

I would like to thank Dr. Joseph E. Salah for his interest and support in this project, and Drs. Lynn A. Carpenter and Volker W. J. H. Kirchhoff for their electric field data. The Goddard Institute for Space Studies in New York provided most of the computer time for the final data analysis.

My parents deserve a special acknowledgement for initially encouraging me to enter the sciences. I also acknowledge the influence of Dr. Sidney A. Bowhill of the Aeronomy Laboratory at the University of Illinois, who first introduced me to the study of the ionosphere. Dr. Raymond G. Roble was my scientific advisor in the summer of 1973 when I was in the Advanced Study Program at the National Center for Atmospheric Research in Boulder, Colorado. This particular project was born there, and Ray has continued to lend me his support and interest.

Finally, thanks are due to Miss Isabelle Kole who spent two weeks preparing all of the drawings, and to Mrs. Penny Gosdigian who stayed up late several nights typing this manuscript.

Financial support for this work came from a three-year National Science Foundation graduate fellowship and from a research assistantship under a National Science Foundation grant (NSFG-76-22279ATM).

TABLE OF CONTENTS

	Page
Title Page	1
Abstract.....	2
Acknowledgments.....	4
Table of Contents.....	5
List of Figures.....	9
List of Tables.....	17
1. INTRODUCTION.....	18
1.1 The Neutral Atmosphere.....	18
1.2 The Ionized Atmosphere.....	26
1.3 Historical Background.....	35
1.4 Extent and Purpose of Thesis.....	39
2. THE INCOHERENT SCATTER RADAR.....	42
2.1 General Theory.....	42
2.2 The "One-Pulse" Experiments at Millstone Hill.....	45
3. THE INPUT DATA.....	50
3.1 Exospheric Temperature.....	51
3.1.1 Form of the Neutral Temperature.....	51
3.1.2 Heat Balance Equation	51
3.2 Plasma Diffusion Velocity	56
3.2.1 Ion-Neutral Collision Frequencies.....	58
3.2.3 Comparison with Previous Results.....	59
3.3 Neutral Wind Component.....	61

3.4	Electric Fields.....	68
3.5	Ion Composition	71
3.6	Seasonal Variations of O/N ₂	75
4.	THE EQUATIONS FOR THE NEUTRAL THERMOSPHERE	79
4.1	Horizontal Equations of Motion	79
4.2	Continuity Equation	86
5.	DATA ANALYSIS	89
5.1	The Millstone Hill Model	89
5.2	Neutral Temperature and Density	93
5.3	Exospheric Temperature Structure	96
5.4	Derivation of the Meridional Pressure Gradient Term	97
5.5	Final Velocity Calculations	103
5.5.1	Assumptions about Latitudinal Variations	104
5.5.2	Averages	105
6.	REPRESENTATIVE RESULTS	107
6.1	Representative Summer Day	107
6.1.1	The Equations of Motion	113
6.1.2	The Continuity Equation	119
6.1.3	Comparison with Other Models	128
6.2	Representative Winter Results	141
6.2.1	Comparison with Other Models	150

7.	UNCERTAINTIES AND CONSEQUENCES OF VARIOUS ASSUMPTIONS.....	160
7.1	Experimental Uncertainties.....	160
7.2	Uncertainties Concerning Assumptions about Electric Fields.....	162
7.2.1	General Discussion	162
7.2.2	Specific Example	164
7.3	Uncertainties Introduced by the Form of the Neutral Atmospheric Model	168
7.3.1	General Discussion	168
7.3.2	Corrections Made to Average Velocities	174
7.4	Uncertainties Concerning Assumptions about Latitudinal Gradients	176
7.4.1	Summary and Conclusions	178
7.5	Uncertainties Introduced by the Neglect of the Non-Linear Terms	180
7.5.1	Other Non-Linear Studies.....	182
7.6	Effects of the Uncertainty in the Ion-Neutral Collision Frequency	184
7.7	Total Uncertainties in the Velocities	186
7.7.1	Daily Uncertainties	187
7.7.2	Diurnal Average Uncertainties	188
7.7.3	Uncertainties in Seasonal Differences.....	189
7.7.4	Uncertainties in the MSIS Model Velocities.....	190
8.	RESULTS.....	191
8.1	Solar and Geomagnetic Conditions Encountered	191
8.2	Exospheric Temperature	198
8.3	Zonal Velocities	202
8.4	Meridional Velocities	207

8.5	Summary of Results for the Horizontal Velocities.....	217
8.6	Vertical Velocities.....	218
8.7	Magnitudes of the Neglected Non-Linear Terms.....	220
8.8	Comparison with Previous Work.....	221
8.9	Comparison with Other Observations.....	223
9.	DISCUSSION AND CONCLUSIONS.....	227
9.1	A Self-Consistent Model of the Effects of Non-Diffusive Equilibrium.....	228
9.2	Theoretical Models Based on Heating Rates.....	232
9.2.1	Solstice Model Results Including a High Latitude Heat Source	234
9.3	Discussion of the Present Results.....	240
9.4	Average Zonal Velocities.....	246
9.5	Summary and Conclusions.....	248
9.6	Suggestions for Future Work.....	252
	References.....	255
	Appendix A: Correction of B Mode Temperature.....	262
	Appendix B: Estimating the Effect of Neglecting a Bottom Boundary Meridional Gradient in Atomic Oxygen.....	274
	Appendix C: Detailed Examination of the Various Latitudinal Gradients.....	287
	Appendix D: Non-Linear Terms: Stability Criteria and Role as Outside Forcing Functions.....	307
	Curriculum Vitae.....	315

LIST OF FIGURES

Figure No.		Page
1.1	Vertical distribution of temperature in the homosphere and heterosphere. (Adapted from Fig. 1.2 of Banks and Kockarts, 1973)	19
1.2	Daytime ionospheric and atmospheric composition at solar minimum based on mass spectrometer measurements (from Figure 14 of Johnson, 1969).	23
1.3	Altitude regions of dominance of neutral constituents as a function of thermopause temperature. (From Fig. 6 of Kockarts and Nicolet, 1963).	25
1.4	An idealized electron density distribution in the ionosphere for sunspot maximum in mid-latitudes. (From Fig. 2.14 of Evans and Hagfors, 1968).	27
1.5	Typical sunspot maximum electron density and temperature profiles at Millstone Hill.	32
2.1	Example of incoherent scatter spectrum measured by UHF zenith radar at Millstone Hill. (Adapted from Fig. 2.2 of Salah, 1972).	48
3.1	The exospheric temperature on March 23-24, 1970 at Millstone Hill.	55
3.2	The diffusion velocity calculated at 300 km for Millstone Hill on March 23-24, 1970.	60
3.3	Schematic of the components of the ion drift in the plane of the magnetic meridian (B field should point downward).	62
3.4	The vertical ion drift at 300 km measured at Millstone Hill on March 23-24, 1970.	65
3.5	The horizontal component of the neutral wind in the magnetic meridian plane calculated at 300 km for Millstone Hill on March 23-24, 1970.	67
3.6	Ion drifts induced throughout the day by the Kirchhoff and Carpenter (1975) electric field model for Millstone Hill. The figure is reproduced from their paper.	70

Figure No.

3.7	Percent of atomic oxygen ion concentrations used in the present study and ratios of $\text{NO}^+ / (\text{NO}^+ + \text{O}_2^+)$. (From Fig. 3.1 of Emery, 1975).	74
3.8	Selected values of the ratio O/N_2 and their harmonic analysis retaining mean, annual, and semiannual terms.	77
5.1a	Flow diagram of data processing for present Millstone Hill model	90
5.1b	Flow diagram of data processing for the MSIS model case.	91
6.1	Smoothed electron densities in intervals of \log_{10} measured above Millstone Hill on June 23-24, 1970.	108
6.2	Spline fit to the exospheric temperature above Millstone Hill for June 23-24, 1970. Also included is its representation in 3 harmonics and the exospheric temperatures deduced by the Jacchia 1971, OGO-6, and MSIS models. R and S are sunrise and sunset at 250 km.	109
6.3	Neutral temperatures above Millstone Hill on June 23-24, 1970.	111
6.4	Zonal exospheric temperature gradient above Millstone Hill on June 23-24, 1970. Also plotted are gradients from the Jacchia 1971, OGO-6, and MSIS models.	112
6.5	Derived meridional exospheric temperature gradient above Millstone Hill on June 23-24, 1970. Also plotted are gradients from the Jacchia 1971, OGO-6, and MSIS models.	114
6.6	Experimentally derived V_{th} at 300 km for June 23-24, 1970 and the fit achieved by the Millstone Hill case using 3 harmonics in the meridional exospheric temperature gradients.	115
6.7a	Variations and averages of the terms in the zonal momentum equation 4.5 at 300 km plus estimates of the non-linear terms for the Millstone Hill model of June 23-24, 1970. See text for explanation of abbreviations. All terms which were omitted were less than $\pm 0.6 \text{ cm/sec}^2$.	117

Figure No.

6.7b	Same as Figure 6.7a except this is for the meridional momentum equation.	118
6.8	Horizontal velocities at 300 km calculated with the Millstone Hill model on June 23-24, 1970. Positive velocities are towards the east (u), north (v) and magnetic north ($V_{Hn}(\text{calc})$).	120
6.9a	Zonal velocity computed with the Millstone Hill model on June 23-24, 1970. Positive velocities are toward the east.	121
6.9b	Meridional velocity computed using the Millstone Hill model on June 23-24, 1970. Negative values are towards the south.	122
6.10	Vertical velocity at 500 km on June 23-24, 1970 and its components. Pressure gradients were derived from the Millstone Hill model. See text for explanation of abbreviations.	124
6.11	Vertical velocity computed from the Millstone Hill model on June 23-24, 1970.	126
6.12a	Same as Figure 6.7a except the pressure gradients come from the MSIS model.	131
6.12b	Same as Figure 6.7b except the pressure gradients come from the MSIS model.	132
6.12c	Horizontal velocities calculated at 300 km for June 23-24, 1970 using the MSIS model pressure gradients	134
6.12d	Same as Figure 6.10 only pressure gradients are from the MSIS model.	135
6.13a	Same as Figure 6.7a except the pressure gradients from the OGO-6 model.	137
6.13b	Same as Figure 6.7b except the pressure gradients came from the OGO-6 model.	138
6.13c	Horizontal velocities at 300 km on June 23-24, 1970 calculated using the OGO-6 model pressure gradients.	139
6.13d	Same as Figure 6.10 only the pressure gradients were from the OGO-6 model.	140

Figure No.

6.14	Smoothed electron densities in intervals of \log_{10} measured over Millstone Hill on January 20-21, 1971	142
6.15a	Same as Figure 6.2 only for January 20-21, 1971.	143
6.15b	Same as Figure 6.4 only for January 20-21, 1971.	144
6.16	Same as Figure 6.5 only for January 20-21, 1971	146
6.17	Same as Figure 6.6 only for January 20-21, 1971.	147
6.18a	Same as Figure 6.7a except this is for January 20-21, 1971.	148
6.18b	Same as Figure 6.7b except this is for January 20-21, 1971.	149
6.19a	Horizontal velocities at 300 km calculated with the Millstone Hill model on January 20-21, 1971.	151
6.19b	Same as Figure 6.10 only for January 20-21, 1971.	152
6.20a	Same as Figure 6.7a only for January 20-21, 1971 using pressure gradients from the MSIS model.	154
6.20b	Same as Figure 6.7b only for January 20-21, 1971 using pressure gradients from the MSIS model.	155
6.21a	Horizontal velocities at 300 km calculated with MSIS model pressure gradients for January 20-21, 1971	156
6.21b	Experimentally derived V_{Hn} at 300 km for January 20-21, 1971 and the values found through the use of the MSIS model pressure gradients.	157
6.21c	Same as Figure 6.10 only for January 20-21, 1971 using pressure gradients from the MSIS model.	158
7.1	Plot of geographic and geomagnetic coordinates illuminating the effect of Coriolis forces and the constraint of fitting to $\Delta V_{Hn}(E)$ upon the first order guess that the change in u and v due to electric fields is equal to u_{ie} and v_{iE} .	165
7.2	Plot of electric field-induced ion drifts(—) from the Kirchhoff-Carpenter average model (1975) and plot of the difference between the zonal and meridional velocities with and without the field model (---) at 300 km for December 8-9, 1969 above Millstone Hill.	167

Figure
No.

7.3	An illustration of the consequences of using an "effective" meridional exospheric temperature gradient.	173
7.4	Plot of the corrections $\Delta \bar{v}$ at 300 km to the average meridional velocities \bar{v} calculated according to the procedures in Appendix B and designed to correct for the absence of the meridional gradient in atomic oxygen at 120 km in the present analysis.	175
8.1	Average daily 10.7 cm solar flux values computed 24 hour previous to each of the days analyzed.	192
8.2a	Average exospheric temperatures above Millstone Hill.	199
8.2b	Comparison of the diurnal average exospheric temperatures above St. Santin (44.6°N) and Millstone Hill (42.6°N). The values from St. Santin and from the previous analysis at Millstone Hill were taken from Fig. 3 of Salah <i>et al</i> (1976).	201
8.3a	Average zonal velocities at 300 km calculated above Millstone Hill and a harmonic analysis of all but 3 of the data points.	204
8.3b	Average zonal velocities at 300 km computed using the MSIS atmospheric model. Also plotted is the harmonic analysis of all but 3 points in the data set.	206
8.4a	Average meridional velocities at 300 km above Millstone Hill and a harmonic analysis of all but 3 of the 39 days plotted.	208
8.4b	Average meridional velocities at 300 km computed using the MSIS atmospheric model. Also plotted is a harmonic analysis of 36 of the 39 days present.	209
8.5a	Electron maximum concentrations at 1200 LT above Millstone Hill.	211
8.5b	Electron maximum concentrations at 1200 LT as a function of average meridional velocities at 300 km above Millstone Hill.	212
8.6a	Plot of the average horizontal wind in the plane of the magnetic meridian, \bar{V}_{HN} , calculated at 300 km above Millstone Hill and assuming no electric fields are present.	214

Figure Nos.

8.6b	Plot of the average diffusion velocities parallel to the magnetic field, $\bar{V}_{D//}$, and of the average vertical ion drifts, \bar{V}_{iz} , above Millstone Hill.	215
8.7	Average vertical velocities, \bar{w} , and average $\overline{WDVY} = 1/\rho \int_z^\infty \rho \partial v / \partial y dz$ calculated using the MSIS atmospheric model and the ionospheric data above Millstone Hill. The electron density is assumed to decrease polewards by 4% in 1 degree of latitude except for points marked with a cross, where it is assumed to be latitudinally constant.	219
9.1	The calculated global mean gas heating rate for solar heating and for the assumed Joule heating due to ionospheric heating. (Taken from Dickinson <u>et al</u> , 1975).	233
9.2	The calculated contours of the perturbation diurnal and zonal mean temperature and winds due to forcing by solar heating alone: (a) meridional winds (ms^{-1}), (b) zonal winds (ms^{-1}), (c) temperature ($^{\circ}\text{K}$) and (d) vertical velocity (cms^{-1}). (Taken from Dickinson <u>et al</u> , 1977).	235
9.3	Same as Fig. 9.2, with the addition of the OGO-6 inferred momentum source and a symmetrical high latitude heat source.	236
9.4	Same as Fig. 9.3, with the high latitude heating in the summer hemisphere two and one half times greater than the winter hemisphere.	238
9.5	The calculated contours of mass flow stream function (gs^{-1}) for (a) solar heating alone, (b) solar heating plus the OGO-6 inferred momentum source, (c) solar heating plus the OGO-6 inferred momentum source plus the symmetrical high latitude heating source, and (d) solar heating plus the OGO-6 momentum source and the asymmetrical high latitude heat source (taken from Dickinson <u>et al</u> , 1977).	239
9.6	Plot of the difference between the average daily meridional velocity and the harmonic analysis of the entire data set versus magnetic activity. Negative values are a stronger equatorwards flow than average.	242
A.1	Deviation between single short and long pulse ion temperature (from Fig. A.2 of Salah, 1972).	263

Figure No.

A.2	T_e/T_i derived from short and long single pulses (from Fig. A.1 of Salah, 1972).	264
A.3	Averaged B mode ion temperature data and the quartic fit.	268
A.4	Averaged data of the ratio of T_e/T_i in the B mode data and the quartic fit.	269
B.1a	Deviations of the average zonal velocity at 300 km as a function of r for December 8-9, 1969.	277
B.1b	Deviations of the average meridional velocity at 300 km as a function of r for December 8-9, 1969.	278
B.1c	Deviations of the average vertical velocity at 300 km as a function of r, for December 8-9, 1969 above Millstone Hill.	279
B.1d	Deviations of the average meridional exospheric temperature gradient as a function of r for December 8-9, 1969.	280
B.1e	Deviations of the average meridional pressure gradient force as a function of r for December 8-9, 1969 over Millstone Hill.	281
B.2	Plot of $\Delta \bar{u}$ for a $\Delta T_e/\Delta \phi$ of $100^\circ\text{K}/\text{rad}$ as a function of the absolute value of the average meridional velocity at 300 km for $r=0$.	285
C.1	Plot of Δu and Δv at 300 km in 0.2° of latitude deduced from changing the latitude by 1° at Millstone Hill on June 23-24, 1970.	289
C.2a	Plot of the contributors to the difference in zonal velocity Δu between 42.6°N at 300 km for the present analysis of June 23-24, 1970. The x's are the values of Δu derived using constant electron densities (see Figure C.3a)	293
C.2b	Plot of the contributors to the difference in meridional velocity Δv between 42.6°N and 42.8°N at 300 km for the present analysis of June 23-24, 1970. The x's are the values of Δv derived using constant electron densities (see Figure C.3b).	294

Figure No.

- C.3a Plot of the contributors to the difference in zonal velocity Δu between 42.6° N and 42.8° N at 300 km assuming constant electron densities for the present analysis of June 23-24, 1970. 296
- C.3b Plot of the contributors to the difference in meridional velocity Δv between 42.6° N and 42.8° N at 300 km assuming constant electron densities for the present analysis of June 23-24, 1970. 297
- C.4a Plot of the contributors to the difference in zonal velocity Δu between 42.6° N and 42.8° N at 300 km for the MSIS model on June 23-24, 1970. The x's are the values of Δu derived using constant electron densities. 300
- C.4b Plot of the contributors to the difference in meridional velocity Δv between 42.6° N and 42.8° N at 300 km for the MSIS model on June 23-24, 1970. The x's are the values of Δv derived using constant electron densities. 301
- C.5 Plot of Δv at 300 km in 0.2° of latitude for mid-latitudes deduced from Figures 8 and 9 of Blum and Harris (1975). 305

LIST OF TABLES

Table No.

2.1	Characteristics of the data modes of the Millstone Hill UHF single-pulse experiment.	46
4.1	Magnitudes of terms in the equations of motion 4.4 for September 7-8, 1971 at various altitudes. Units are in cm/sec ² .	84
8.1	List of days analyzed, their geomagnetic and solar conditions, and average values derived from the Millstone Hill (M.H.) and MSIS models.	194
8.2	Comparison of the average input parameters and results at 300 km for different analyses using Millstone Hill data.	222
8.3	Seasonal meridional wind variations at thermospheric heights above Millstone Hill (42.6° N, 71.5°W) and St. Santin (44.6°N, 2.3°E).	224
9.1	Annual variations (\pm or $\bar{\pm}$) above Millstone Hill (42.6°N) taken from the present work and other studies.	230
9.2	Some characteristic parameters of the summers of 1970 and 1971.	244
A.1	Variations in the true heights for various delay times in the B and C modes	266
A.2	Quartic coefficients for the fits to T_i and T_e/T_i C mode used in Eq. A.2.	271
A.3	Deviations of corrections to T_i and T_e/T_i of the B mode from average values	272
B.1	Table of the effects of having a non-zero bottom boundary meridional gradient in atomic oxygen.	276

1. INTRODUCTION

1.1 The Neutral Atmosphere

The variation of temperature with height gives rise to the nomenclature used to designate various different regions in the atmosphere. The vertical distribution of temperature through the different atmospheric layers is pictured in Figure 1.1. The troposphere is the lowest level, beginning at the earth's surface, which acts as a heat source resulting from the absorption of the visible sunlight. The temperature decreases in this region up to approximately 12 km, where it reverses and begins to increase. The height of this reversal is termed the tropopause and the overlying region is the stratosphere.

The increasing temperature in the stratosphere is brought about by the presence of a heat source centered around the stratopause at 50 km. This heat source is the absorption of ultraviolet (UV) solar radiation by ozone (O_3) which is formed by 3-body collisions and destroyed by recombination with oxygen atoms or by photodissociation. Above the stratopause, the temperature decreases again in the mesosphere up to the mesopause, which is located around 80 km. The general circulation pattern of the stratosphere and mesosphere is one of eastward winds around a low pressure region during the winter and westward winds around a high pressure region in the summer. The wind flow around the pressure centers results from a balance between the pressure gradient force directed from low to high pressures and the Coriolis force which is introduced by the rotation of the earth and causes the winds to turn to the right in the northern hemisphere.

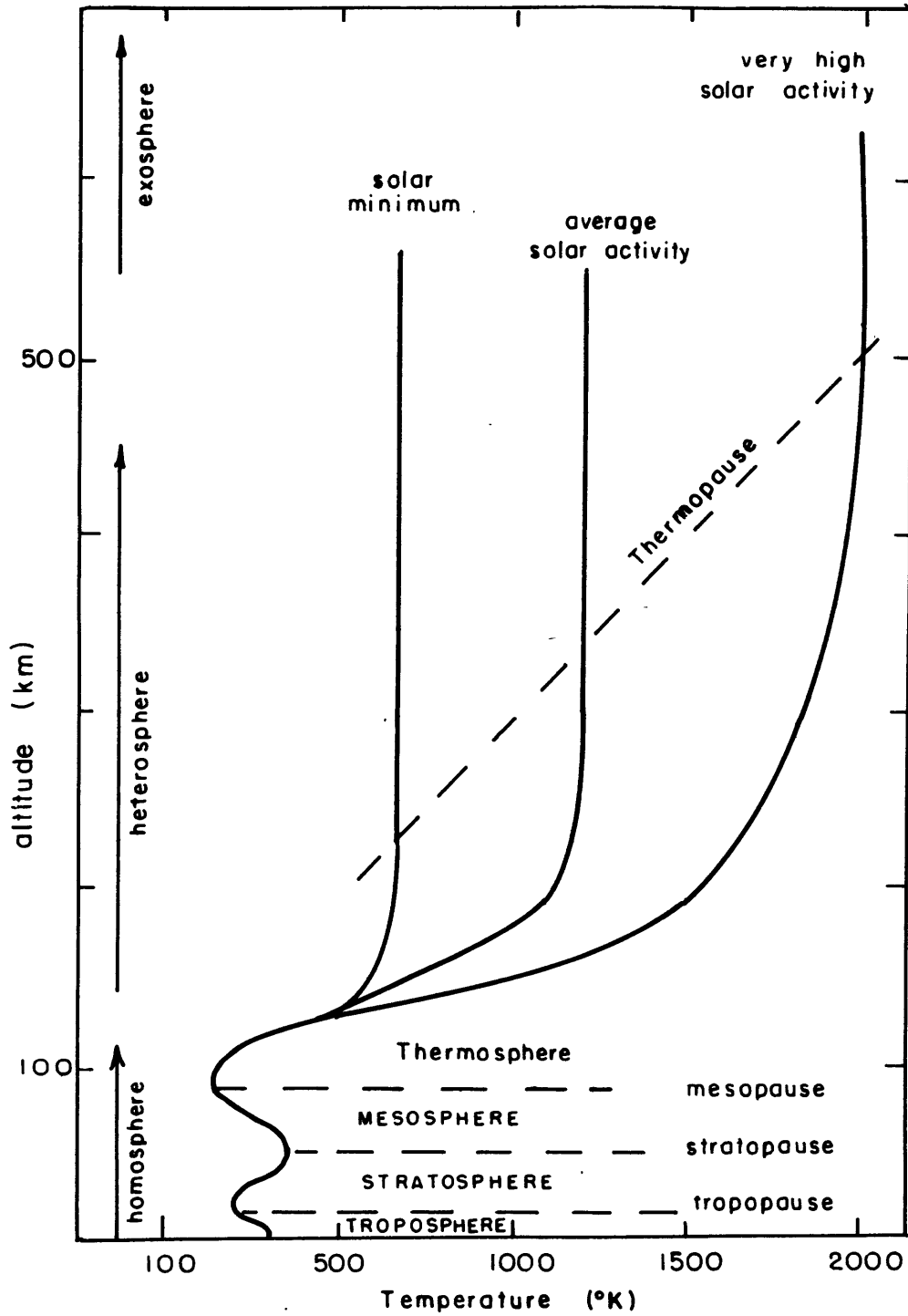


Fig.1.1: Vertical distribution of temperature in the homosphere and heterosphere. (Adapted from Fig. 1.2 of Banks and Kockarts, 1973).

There is a dramatic increase in the temperature above the mesopause in the region called the thermosphere. The large temperature gradient is a result of the absorption of extreme ultraviolet (EUV) radiation and the lack of any effective means of thermal emission. The temperature does not increase indefinitely because the heating falls off as the density decreases, and the thermal conductivity, which is independent of pressure, becomes large enough to transport downwards all the heat deposited above the thermopause with only a very small further temperature increase.

This limiting temperature is called the exospheric temperature and its magnitude is greatly dependent on the existing solar conditions. The EUV solar flux, unlike the black body radiation received at the earth's surface, is quite variable, fluctuating with solar flare activity and varying month-to-month and year-to-year with the solar rotation and sunspot cycle variations, respectively. Different solar conditions can produce exospheric temperatures that are over 1000°K apart as is shown in Figure 1.1. In addition to these solar variations, the seasonal variation of the daily mean exospheric temperature is about $\pm 100^{\circ}\text{K}$ at mid-latitudes (Salah et al., 1976) and the diurnal variation is between 200 and 400°K .

The turbopause located around 110 km, marks the height at which molecular diffusion becomes capable of dissipating eddies. Below this level, the atmosphere is well mixed and is termed the homosphere. The dominant heat transfer processes are radiation below 60 km and eddy transport between 60 and 110 km. The dominant process

is molecular conduction above the turbopause in the heterosphere, where the neutral atmospheric constituents separate out according to their molecular weights.

Most of the atmosphere is considered to be in diffusive equilibrium above some heights, z_0 , which means the various constituents are distributed according to the perfect gas law

$$p = n k T \quad (1.1)$$

and the law of hydrostatic equilibrium

$$\frac{dp}{dz} = - \rho g = - nmg \quad (1.2)$$

Here p is pressure, n is number density, T is temperature, k is Boltzmann's constant, z is height above the surface, ρ is density, g is the acceleration due to gravity, and m is the mean mass. The vertical velocity w_i of a minor constituent can be written as (Banks and Kockarts, 1973),

$$w_i = - D_i \left[\frac{1}{n_i} \frac{dn_i}{dz} + \frac{1}{H_i} + (1 + \alpha_T) \frac{1}{T} \frac{dT}{dz} \right] \quad (1.3)$$

where α_T is the thermal diffusion factor, $H_i = kT/m_i g$ the scale height of the i^{th} constituent, m_i is the mass of the i^{th} constituent, and D_i is an average diffusion coefficient.

Diffusive equilibrium ($w_i = 0$) leads to

$$n_i(z) = n_i(z_0) \left(\frac{T(z_0)}{T(z)} \right)^{1 + \alpha_T} \exp \left(- \int_{z_0}^z dz/H_i \right) \quad (1.4)$$

which is similar to the case of perfect mixing where α_T disappears

and H is the average scale height. It can be seen from equation 1.4 that the concentration of the heavier constituents with larger molecular weight (and smaller scale height) will decrease more rapidly with height than the concentration of the lighter constituents.

Molecular nitrogen, N_2 , is the most abundant neutral constituent in the lower thermosphere followed by molecular oxygen, O_2 , and atomic oxygen, O . The atomic oxygen is formed by the dissociation of molecular oxygen by solar ultraviolet radiation in the Schumann-Runge continuum above 80 km ($\lambda \leq 1750 \text{ \AA}$). The peak production occurs between 90 and 95 km. Atomic oxygen is lost through 3-body processes and through combination with ozone. Its sink is thus lower than its source, and atomic oxygen diffuses downward until it is lost.

Figure 1.2 illustrates the vertical distribution of neutral number densities in the region between 100 and 1000 km for mid-latitude, average daytime conditions during sunspot minimum. Molecular nitrogen is the dominant species up to about 200 km above which atomic oxygen becomes predominant. There is another transition region around 600 km where helium, He , becomes the major species. Still higher atomic hydrogen, H , becomes the dominant constituent. Occasionally, the region where helium is a major species is absent and the transition goes directly from atomic oxygen to atomic hydrogen. Helium originates from the radioactive decay of thorium and uranium while atomic hydrogen results from the photodissociation of water (H_2O) and methane (CH_4). The transition heights from one

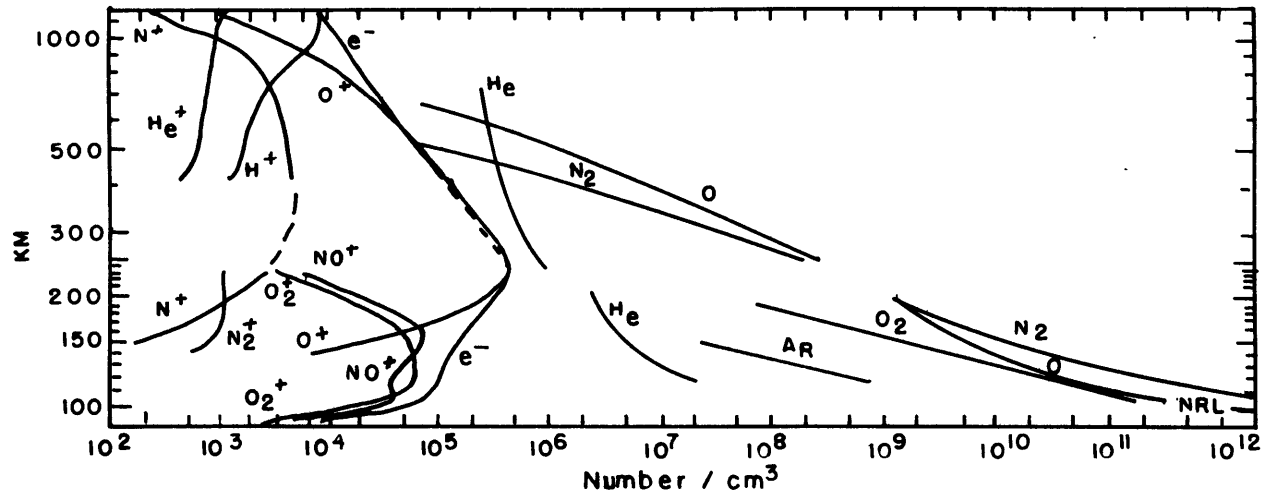


Fig. 1.2: Daytime ionospheric and atmospheric composition at solar minimum based on mass spectrometer measurements. (From Fig. 14 of Johnson, 1969).

dominant species to another increase with increasing exospheric temperature. Figure 1.3 plots these transition heights as a function of thermopause temperature.

Below the exosphere (see Figure 1.1), where collisions are sufficiently frequent to maintain a Boltzmann energy distribution, the atmosphere can be described in terms of fluid equations. Particles in the exosphere travel in ballistic orbits and are unlikely to make any further collisions. The lighter atoms, helium and hydrogen, are able to escape from the exosphere if their velocities exceed the escape velocity (11.4 km/sec). (The root mean square velocity for atomic hydrogen at 2000^oK is 7.06 km/sec).

Molecular nitrogen is generally considered to be in diffusive equilibrium because it is a major constituent at the lower levels and is not chemically active. The lighter species such as atomic oxygen, helium, and atomic hydrogen are generally not in diffusive equilibrium in regions where they are minor constituents because they are preferentially transported by the horizontal wind system [Mayr and Volland (1972, 1973)].

The circulation pattern in the thermosphere is generally the result of a balance between the pressure gradient forces set up by the diurnal and seasonal movements of the sun, and the frictional drag exerted on the neutral particles by the ionized particles. Therefore, the winds generally blow from regions of high pressure to regions of low pressure rather than circling around them as is the case in the lower atmosphere.

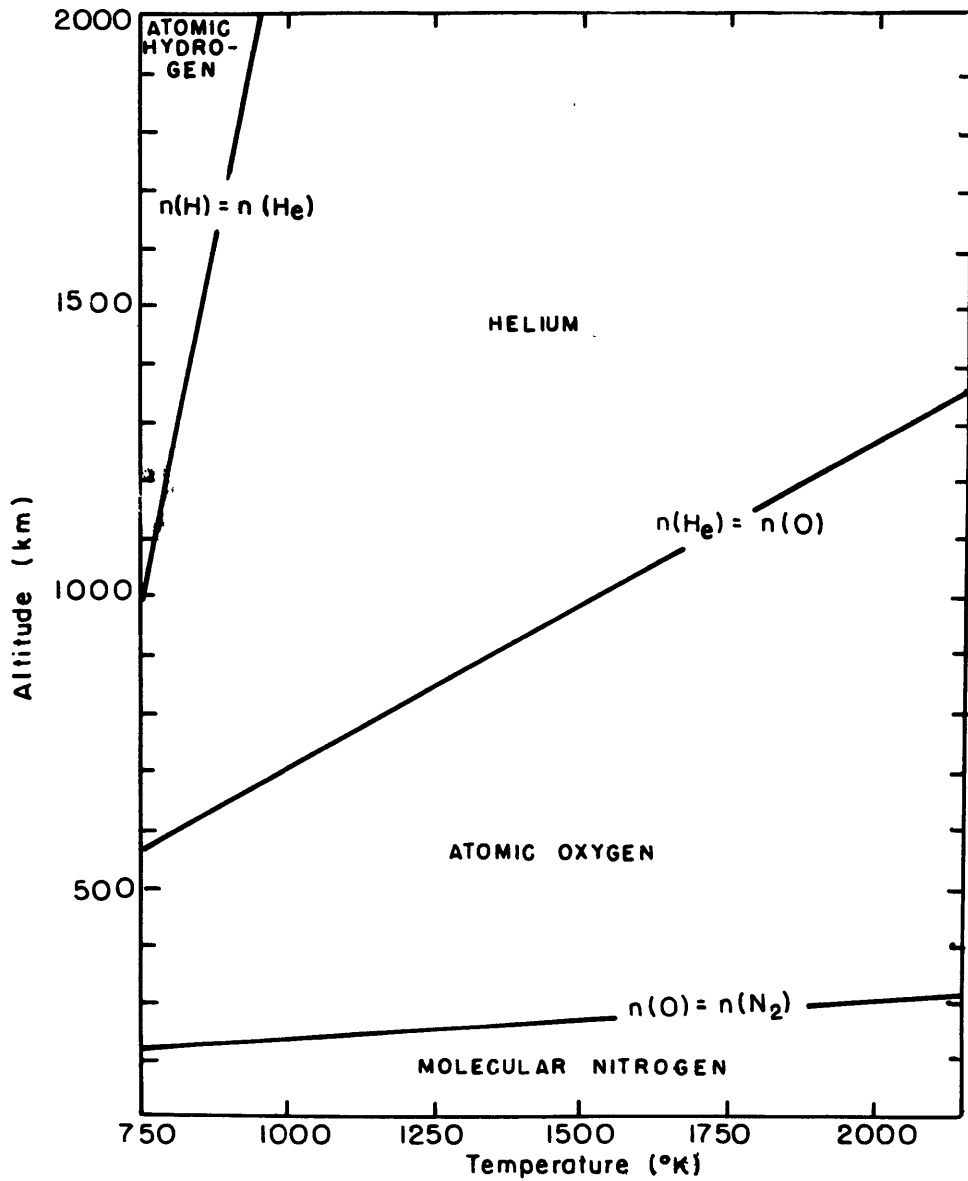


Fig. 1.3: Altitude regions of dominance of neutral constituents as a function of thermopause temperature. (From Fig. 6 of Kockarts and Nicolet, 1963).

Only solar radiation has been cited as a heat source for the upper atmosphere. This is the major source but others exist such as wave dissipation, particle precipitation, and Joule heating by electric currents.

1.2 The Ionized Atmosphere

Solar UV and EUV photons which are sufficiently energetic are able to ionize the neutral atmospheric constituents by removing an electron. The ionosphere is usually defined as that part of the upper atmosphere in which there are sufficient numbers of free electrons to affect the propagation of radio waves. So defined, it extends from about 65 km to several earth radii. However, it is usual to refer to the ionized region above about 1000 km as the magnetosphere. Figure 1.4 shows the electron density distribution (number/cm³) with height at sunspot maximum for day and night conditions.

The electron density is usually referred to in terms of the layers D, E, and F (F1 and F2), which mark inflections in the electron density profile (see Figure 1.4). The electron density peaks at about 10^6 electrons/cm³ around 300 km in the F or F2 layer.

The precise shape of the electron profile is determined by production, loss, and transport. The basic theory of photoionization was developed by Chapman and has been described in many text books. (See, for example, Rishbeth and Garriott, 1969). Ionization is produced by a wide spectrum of solar x-ray and extreme ultraviolet radiation, the x-rays being particularly important in the formation

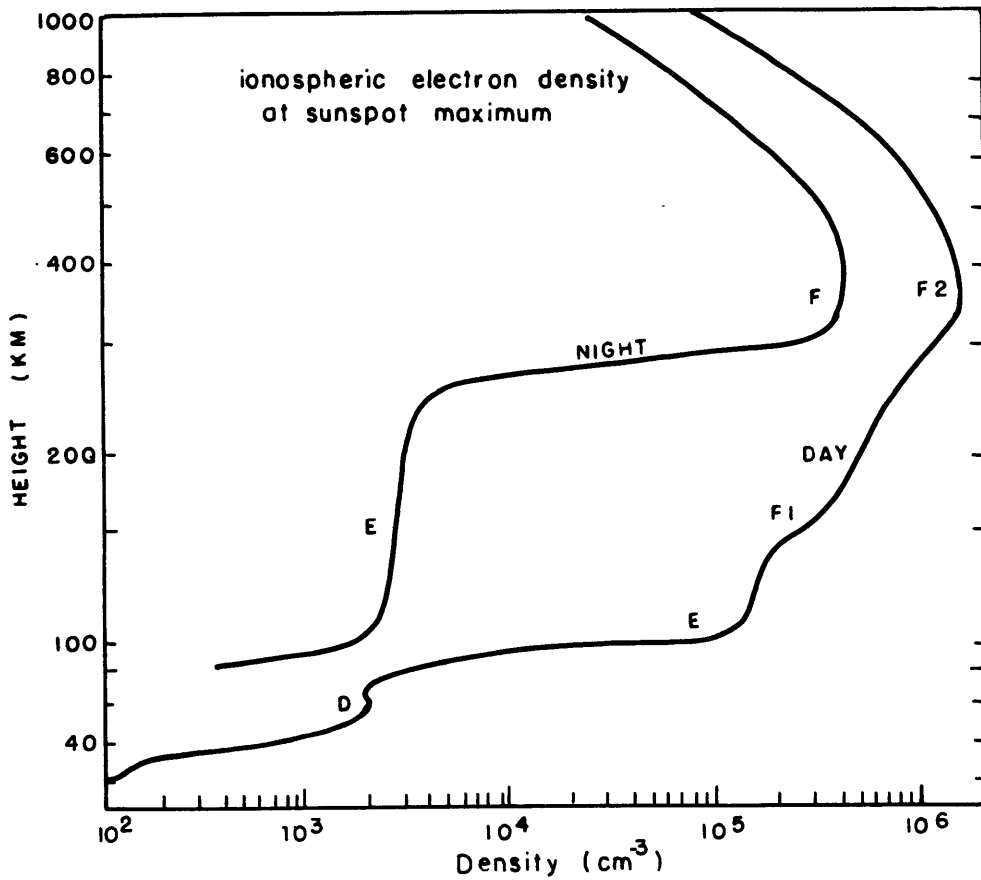


Fig. 1.4: An idealized electron density distribution in the ionosphere for sunspot maximum in mid-latitudes. (From Fig. 2.14 of Evans and Hagfors, 1968).

of the E and D regions. Ionization is also produced by energetic charged particles which enter the atmosphere most easily at high magnetic latitudes. The depth to which these particles penetrate the atmosphere depends on their energy. Cosmic rays are the most energetic of these particles, producing ionization below about 70 km, and forming the lower part of the D region (sometimes called the C region).

The mechanism for the loss of ionization are discussed by Rishbeth and Garriott (1969). The principle loss process in the E and F regions is ion-atom interchange (rate coefficient γ)



followed by dissociative recombination (rate coefficient α)



where the asterisks indicate that the atoms may be left in excited states. Figure 1.2 shows the vertical ion distribution for daytime conditions at sunspot minimum. The principal ions below 150 km are molecular oxygen and nitric oxide, O_2^+ and NO^+ . Atomic oxygen, O^+ , predominates in the F region and is succeeded by hydrogen ions, H^+ , around 1000 km. There are very few negative ions in the E and F regions because they are destroyed by photodetachment



Ignoring transport processes, the continuity equations for the concentration of electrons, N , atomic ions, N_A , and

molecular ions, N_{M^+} can be written approximately as

$$\begin{aligned} dN/dt &= q - \alpha N N_{M^+} \\ dN_{A^+}/dt &= q - \gamma n(M) N_{A^+} \\ dN_{M^+}/dt &= \gamma n(M) N_{A^+} - \alpha N N_{M^+} \end{aligned} \quad (1.8)$$

where q is the production rate of ionization, α and γ are the rate coefficients, and $n(M)$ is the number density of the molecular gas involved in the ion-atom interchange reaction. Charge conservation requires that

$$N = N_{A^+} + N_{M^+} \quad (1.9)$$

Assuming equilibrium conditions ($d/dt = 0$), the ratio of atomic and molecular concentrations can be written as

$$N_{A^+}/N_{M^+} = \alpha N / \gamma n(M) \quad (1.10)$$

Eliminating the ion concentrations results in a quadratic equation for N :

$$\alpha \gamma n(M) N^2 - \alpha q N - \gamma n(M) q = 0 \quad (1.11)$$

which can be written as

$$\frac{1}{q} = \frac{1}{\gamma n(M) N} + \frac{1}{\alpha N^2} \quad (1.12)$$

The two important limiting cases are the square-law loss

$$q = \alpha N^2 \quad (1.13)$$

if $\gamma n(M) \gg \alpha N$, so that $N_{M^+} \gg N_{A^+}$, and the linear loss

$$q = \gamma n(M)N \quad (1.14)$$

if $\gamma n(M) \ll \alpha N$, so that $N_{M^+} \ll N_{A^+}$.

This analysis shows that the electron density is less if the proportion of molecular ions is greater with respect to the amount of atomic ions.

The peak production in the F region occurs near 150 km, but the peak density is much higher around 250 km. This is largely the result of a rapid upward decrease in the loss coefficient. The loss rate is governed by the abundance of O_2 and N_2 , which control the charge transfer processes that precede dissociative recombination. The electron density does not increase indefinitely upward because diffusion causes the plasma to diffuse downwards along the magnetic field lines under the influence of gravity.

The photoionization process creates energetic photoelectrons which cascade downward toward thermal energies. Fast electrons lose energy through the excitation of N_2 and O_2 electronic states until the energy falls to about 7eV. Between 2eV and 7eV, the main energy loss occurs in the vibrational excitation of N_2 . Below 2eV, the thermalization process proceeds through elastic Coulomb collisions and collisions with various scattering particles. The rate of energetic electron energy loss for elastic collisions is approximately (Banks, 1966a)

$$\frac{dE_{ee}}{dt} \approx - \frac{2m_e m}{(m_e + m)^2} \nu_e E \quad (1.15)$$

where E is the electron energy, m_e is the electron mass, m is the mass of the scattering particles, and ν_e is the electron collision frequency. Due to the mass factor, fast electrons will tend to lose their energy more rapidly to ambient electrons through elastic collisions than to ions or neutral particles. The result is that the temperature of the electrons, T_e , is elevated over that of the ions, T_i , or neutrals, T_n .

Figure 1.5 shows electron and ion temperature profiles along with the electron density profile measured during the day at high sunspot number over the mid-latitude incoherent scatter radar station at Millstone Hill, Massachusetts. Thermal equilibrium ($T_e = T_i = T_n$) exists below about 150 km. Above this height, the electron temperature is greater than the ion and neutral temperatures, which remain approximately the same up to 300 or 400 km. Above this altitude, the thermal coupling between electrons and ions begins to outweigh that between ions and neutrals and this then raises the ion temperature to a value intermediate between the electron and neutral temperatures. The electron (and thus ion) temperatures continue to increase with altitude as the result of heating from photoelectrons that escaped upward from the region where they were produced. The mean free path of a 10 eV photoelectron traveling upwards above 300 km is greater than the scale height of the atmosphere. Accordingly, a

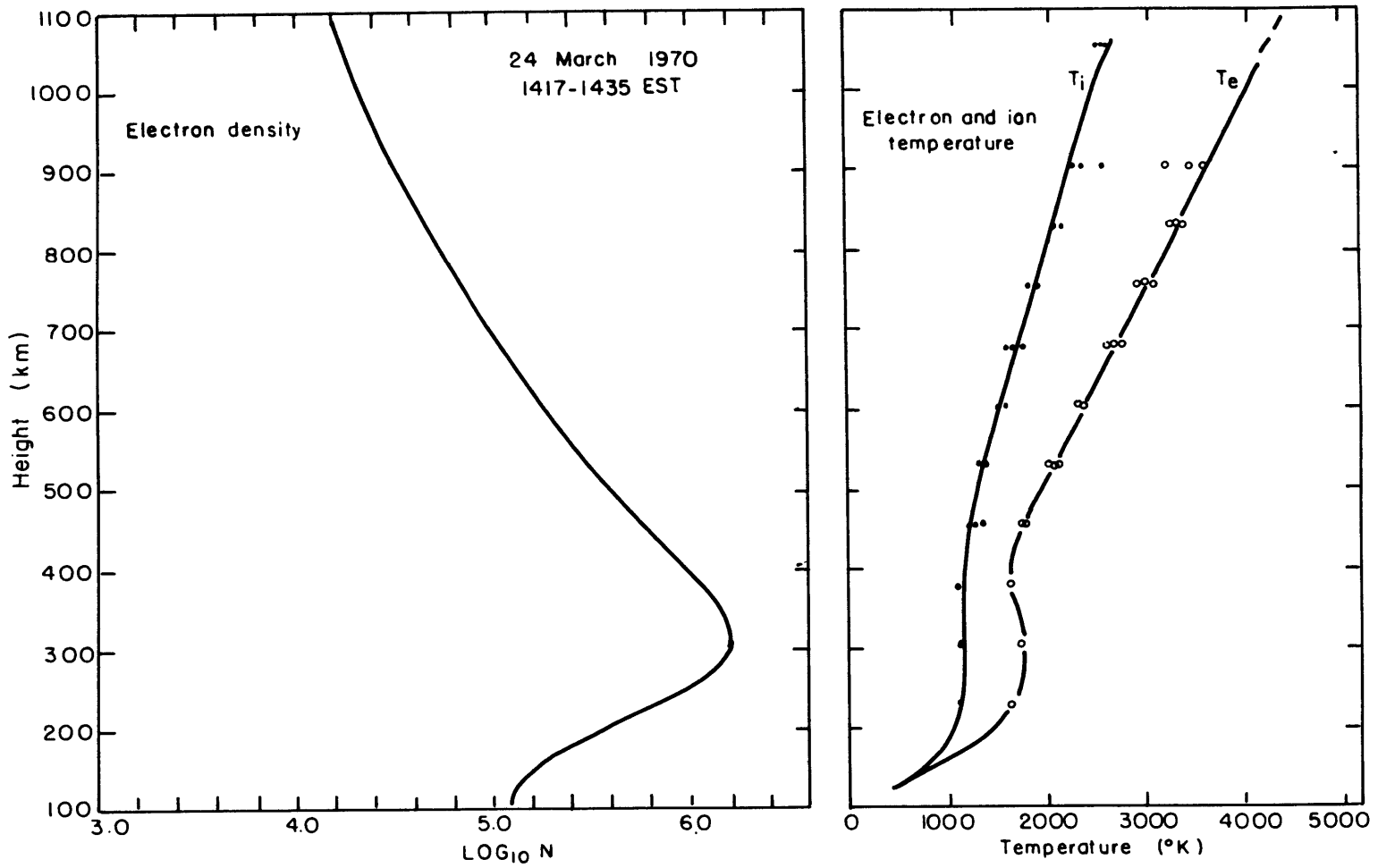


Fig. 1.5: Typical sunspot maximum electron density and temperature profiles at Millstone Hill.

number of photoelectrons escape upward to deposit their energy higher up in the ionosphere or in the magnetosphere. The magnetosphere gains energy from these photoelectrons and this heat is then conducted downward via the ambient electrons.

A minimum in the electron temperature is sometimes observed around 400 km as the result of rapid energy exchange between electrons and ions (which depends on the square of the electron density). During sunspot minimum, this feature disappears as a result of the decreasing electron density, and thermal conductivity then dominates the behavior above 300 km. A review of the processes that govern the temperatures of the ions and electrons is given by Banks (1969).

As a consequence of being charged, the electrons and ions have some constraints imposed on their movements by the presence of the magnetic field which determines ω , the gyrofrequency. The electron and ion gyrofrequencies can be written as

$$\omega_{e(i)} = e B / m_{e(i)} \quad (1.16)$$

where e is the electronic charge, B is the magnetic field strength, and $m_{e(i)}$ is the electron (ion) mass. At low altitudes collisions become important and can be described by a collision frequency. The collision frequency ν_{ab} does not represent the real frequency of collisions between particles a and b , but is a coefficient defining the rate of transfer of momentum from particles a to particles b . The collision frequency ν_{ab} is directly proportional to the number density of the species b . The important collision frequencies in

the F region are ν_{en} , ν_{in} , ν_{ei} and ν_{ni} , where e represents electrons, i ions and n neutrals.

Charged particles spiral along the magnetic field line at the gyrofrequency and this restricts their ability to move in the direction of the neutral wind in response to collisions with neutrals, whenever $\omega_e > \nu_e$ or $\omega_i > \nu_{in}$. In the presence of an electric field, charged particles will drift in the direction $\vec{E} \times \vec{B}$, where E and B stand for the electric and magnetic fields. In the lower ionosphere the precise direction in which the charged particles move depends upon the ratio of the collision frequencies to the gyrofrequencies, ν_{in}/ω_i and ν_{en}/ω_e . This ratio is approximately unity around 80 km for electrons and 140 km for ions. Below these heights, and in the absence of electric fields, the neutral winds can blow the charged particles across the magnetic field lines. Above, the charged particles are constrained to gyrate around the magnetic field lines. Between 80 and 140 km, ions can move with the neutral winds but electrons cannot. This can lead to the separation of charge and the establishment of polarization electric fields which map themselves up along magnetic field lines to higher altitudes. In a similar fashion, electric fields originating in the magnetosphere can map themselves down to lower altitudes along field lines.

The ionized component of the atmosphere is very small in the F region (see Figure 1.2) but its presence has a profound effect on the circulation pattern of the neutrals. Part of this effect is the frictional drag exerted on the neutrals by the charged particles

constrained to spiral along the magnetic field lines. Another effect is in the production of secondary heat sources, mostly at high latitudes, such as the heat due to particle precipitation and the Joule heating of ionospheric currents.

In return, the neutral wind can move the charged particles up and down magnetic field lines in the region where the gyro-frequencies are much larger than the collision frequencies and can create polarization fields in the E region where the electrons are confined to the field lines and the ions are not. The neutrals also exert a drag force on the charged particles.

The presence of the ionosphere makes it possible to study the thermosphere from ground-based stations which employ electromagnetic radiation as a measuring tool. One of these measurement techniques is called incoherent scatter radar and is the major data source for the present work. This technique measures charged particle densities, temperatures, and drift velocities between approximately 100 and 1000 km (Evans, 1969). Since the neutrals and the ions affect each other through collisions, this information on the charge species can yield information on the neutrals as well.

1.3 Historical Background

The incoherent scatter radar technique is probably the most useful ground-based source of information on the thermosphere, but other measurement methods are in use as well. Ionosonde measurements were among the earliest means of studying the ionosphere.

They can be used to determine the electron number density as a function of height up to the electron peak (e.g. Rishbeth and Garriott, 1969). Ionosondes placed on satellites such as the Allouette I and II (Warren, 1963), can be used to derive the top-side electron density. Rockets carrying mass spectrometers are able to determine densities for the various ion species (e.g. Holmes et al., 1965). The frictional drag on satellites (Jacchia, 1965) gives an estimate for the total neutral density, and mass spectrometers carried on satellites can measure the various neutral densities (e.g. Hedin et al., 1974). There are also Fabry-Perot spectrometer measurements of the Doppler broadening and shift of the 6300 Å atomic oxygen emission line, that give neutral temperatures and winds, respectively, at F region heights (Hernandez and Roble, 1976). Finally, electric field measurements can be derived from whistler data (Carpenter and Seely, 1976) as well as from incoherent scatter radar ion drift measurements (Kirchhoff and Carpenter, 1975).

The major early work on the thermosphere was concentrated on the ionosphere and its ability to reflect radio waves. This characteristic makes it useful for earth-based communication systems. Studying the neutrals became important in order to explain some of the anomalous features of the ionosphere. In 1961, Rishbeth and Setty showed that the mid-latitude winter maximum in peak electron density (the seasonal anomaly) could be explained by a change in the neutral composition ratio of O/N₂. This ratio increases in the winter months with the diffusive transport of atomic oxygen from

the summer to the winter pole. An increase in this ratio leads to an increase in the ratio of atomic to molecular ions, and hence leads to a lower loss rate. Diurnal anomalies such as the maintenance of the electron layer at night and a midday minimum, can be explained by the presence of neutral winds as was demonstrated by Rishbeth (1967) and Kohl and King (1967). The winds at night flow over the poles and towards the equator, blowing the plasma up the magnetic field line into regions of lower loss rates. The reverse is true during the day when the winds generally flow towards the poles.

Among the first models of the neutral thermosphere was the one-dimensional heat conduction model of Harris and Priester (1962). This model predicted a late afternoon peak in temperature and density. This was in disagreement with the observations of peak densities around 1400 LT (local time) derived from satellite drag data. Jacchia (1965) created a model of global densities and temperatures based on the satellite drag data. Pressure gradients can be deduced from such a model, and these were used along with the temperature and the densities in the semi-empirical models of Geisler (1967) and Kohl and King (1967) to derive horizontal neutral winds from the horizontal equations of motion. Given these winds, the continuity equation can be solved for the vertical velocity. It was shown by Dickinson and Geisler (1968) that the adiabatic heating and cooling associated with the downward motions at night and upward motions

during the day tended to shift the hour of maximum density somewhat earlier than expected from the heat conduction model.

Early incoherent scatter radar results on the diurnal temperature variation showed that the temperature maximizes in the late afternoon, and later analyses of much larger data samples (e.g. Salah, 1974) showed that this was a function of season. These incoherent scatter results were thus in better agreement with the one dimensional conduction models and raised questions concerning the interpretation of the satellite drag data. In part the discrepancy may have been caused by excessive smoothing of the satellite drag data, but the principal cause appears to be that the densities of the various neutral species maximize at different local times as shown by mass spectrometer data obtained with the OGO-6 satellite (Hedin et al (1974), Mayr et al (1974)). The OGO-6 neutral mass spectrometer operated between June 1969 and May 1971 during sunspot maximum and covered the altitude range 400-600 km. The data showed that the lightest species (He) peaks in the morning, while O peaks near 1500 hours and N₂ peaks still later in the day near 1600 hours. The phase of the temperature variation generally matches the phase of the N₂ density because that species is most likely to be in diffusive equilibrium when dynamical processes are considered. By contrast the satellite drag is chiefly determined by the O density and hence maximizes earlier.

The OGO-6 data also demonstrated seasonal differences in the various neutral species with winter maxima for the lighter

constituents. Such diurnal and seasonal differences in composition imply a lack of diffusive equilibrium and a transport of the minor atmospheric constituents by winds. Mayr and Volland (1973) have created a self-consistent two-component diffusion model to study the diurnal variations in composition. Their results show that in the lower thermosphere where oxygen and helium are minor constituents, the diffusion process tends to increase the amplitudes of these constituents and to advance the times of their diurnal maxima by several hours with respect to the gas temperature and the major species. Mayr and Volland (1972) also studied the seasonal variations with a three-dimensional self-consistent model driven by solar heating. This model exhibited enhanced concentrations of atomic oxygen in the winter hemisphere.

1.4 Extent and Purpose of Thesis

There are three major objectives of the present work. The first is to secure a large sample of estimates of the mean thermospheric circulation above the incoherent scatter radar station at Millstone Hill (42.6°N , 71.5°W). These results will then be used to: (1) Determine if the seasonal variation in atomic-oxygen can be explained as a consequence of seasonal variations in the thermospheric winds; and (2) shed more light on the question of the relative importance to the mid-latitude circulation of the EUV solar heat source and high latitude (auroral) heat source associated with particle precipitation and Joule heating.

A two-year period from December 1969 to December 1971 is examined. The first year is one of high sunspot number and the second one of decreasing sunspot number. It will be necessary to use a model of neutral densities in order to derive information on the neutral temperature and winds from ionospheric data. The model that will be used is the latest of its kind, the MSIS (Mass-Spectrometer/Incoherent-Scatter) model that combines incoherent scatter radar data for the neutral temperature and mass spectrometer data on neutral abundances from several satellites over a sunspot cycle (Hedin et al, 1977). The incoherent scatter measurements to be analyzed provide the diurnal variation of the neutral (exospheric) temperature and the meridional neutral wind. These data are combined in a semi-empirical model which solves the horizontal equations of motion and the continuity equation. The resulting circulation is compared with present theories. Particular emphasis is placed on the derived seasonal variation of the average meridional velocity as a means of transporting lighter constituents from the summer to the winter pole, and as an indicator of high latitude heating in auroral regions.

Chapter 2 describes in some detail the ionospheric results available from the incoherent scatter facility at Millstone Hill. Chapter 3 describes further information that can be derived from these ionospheric measurements when used in conjunction with other sources of data. The equations for the neutral atmosphere are presented in Chapter 4, and the method used for solving them in

Chapter 5. Chapter 6 presents illustrative results for the deduced diurnal circulation and compares them with other work. Chapter 7 outlines all the uncertainties entailed in the reduction. These include errors in the measurements and in their interpretation, and approximations made in order to obtain solutions. The seasonal variations of the temperature and circulation are presented in Chapter 8. The results obtained here are also compared with previous attempts that have been made to estimate global mean winds. The results are discussed in Chapter 9 in relation to current theories for the circulation of the neutral atmosphere. Chapter 9 concludes with a summary and suggestions for future work.

2. THE INCOHERENT SCATTER RADAR

2.1 General Theory

The theory and practice of the incoherent (or Thomson) scatter radar technique has been reviewed by Evans (1969). What follows is a brief description of some of the theory as it relates to the operation of the radar at Millstone Hill.

J. J. Thomson, the discoverer of the electron, showed that electrons are capable of scattering electromagnetic radiation. The radar cross-section of an electron σ_e can be written as

$$\sigma_e = 4 \pi (r_e \sin \psi)^2 \quad (2.1)$$

where r_e is the classical electron radius and ψ is the angle between the direction of the incident electric field and the direction to the observer. In the case of backscattering, $\psi = \pi/2$ and σ becomes $4 \pi r_e^2$. Due to their random thermal motion, the electrons would be expected to scatter radar signals with all possible phases for the reflected signals--hence the name "incoherent scatter."

The first practical experiments proposed (Gordon, 1958), predicted that the spectrum of the returned signal would be Gaussian in shape with a half-width of $0.71 \Delta f_e$, where Δf_e is the Doppler shift of an electron approaching the radar at the mean thermal speed, i.e.

$$\Delta f_e = 1/\lambda (8 k T_e / m_e)^{1/2} \quad (2.2)$$

where k is Boltzmann's constant, T_e and m_e are the electron temperature and mass, and λ is the exploring wavelength. ($\lambda = 68$ cm for Millstone Hill).

The first experimental test of these ideas (Bowles, 1958) revealed that the observed echoes resembled the expected Thomson scattered signals in most respects except that the half-width was considerably less than $0.71 \Delta f_e$. Later theoretical work (Fejer, 1960), showed that the presence of ions influences the scattering characteristics when the exploring wavelength is very much larger than the Debye length. Defined for electrons, the Debye length or shielding distance D_e is

$$D_e = (\epsilon_0 k T_e / 4 \pi N e^2)^{1/2} \quad \text{meters} \quad (2.3)$$

where ϵ_0 is the permittivity of free space, N is the electron density, and e is the electronic charge. The Debye length is somewhat less than 1 cm in the E and F regions of the ionosphere below about 400 km. Above this height, the Debye length increases, reaching a value of about 4 cm at 1000 km.

For wavelengths much larger than the Debye length, the scattering is no longer from individual electrons, but results from density fluctuations brought about by ion-acoustic waves and electron-induced waves in the plasma. The "electronic" component of the spectrum appears as a single "plasma resonance line" at a Doppler shift approximately equal to the plasma frequency

$$f_N = 1/2\pi (N e^2 / m_e \epsilon_o)^{1/2} \quad \text{Hz} \quad (2.4)$$

The "ionic" component of the spectrum is Doppler broadened approximately by the amount Δf

$$\Delta f = \Delta f_i (T_e / T_i)^{1/2} \quad \text{Hz} \quad (2.5)$$

where

$$\Delta f_i = 1/\lambda (8 k T_i / m_i)^{1/2} \quad \text{Hz} \quad (2.6)$$

is the Doppler shift of an ion with mass m_i and temperature T_i . The Doppler shift Δf can thus be looked upon as being produced by an imaginary particle with the mass of an ion and the temperature of an electron. The spectrum is also double humped (see Figure 2.1), the relative height of the hump increasing with larger ratios of T_e / T_i . The effect on the spectrum of decreasing the Debye length is equivalent to decreasing the ratio of T_e / T_i (Moorcroft, 1963). Therefore, these two effects must be kept separate.

In addition to being Doppler broadened, the spectrum is also Doppler shifted away from the radar frequency by an amount Δf_d which is proportional to the mean drift of the ions \vec{V}_i , i.e.

$$\Delta f_d = - 2 \vec{V}_i \cdot \hat{ob} / \lambda \quad \text{Hz} \quad (2.7)$$

where \hat{ob} is a unit vector directed from the observer to the scattering volume.

The scattered power P_s returned to the receiver terminals from some height h is related to the electron density N as

$$P_s = \text{const. } N \sigma / h^2 \quad (2.8)$$

The constant depends on characteristics of the radar and σ is the electron scattering cross-section which can be written as

$$\sigma = \frac{\sigma_e}{(1 + \alpha^2)(1 + T_e/T_i + \alpha^2)} \quad (2.9)$$

where $\alpha = 4 \cdot \pi D_e / \lambda$.

2.2 The "One-Pulse" Experiments at Millstone Hill

The "one-pulse" experiments at Millstone Hill entail operating the incoherent scatter radar over a sequence of three data gathering modes. The first, the A mode, employs a 0.1 msec pulse length yielding a height resolution of 15 km. It covers an altitude range of between 150 and 900 km and is used to recover profiles of electron density N . The second and third modes, B and C, employ pulse lengths of 0.5 and 1.0 msec, respectively, yielding height resolutions of 75 and 150 km, and are used to explore the altitude intervals of 225-675 km and 450-1125 km. These modes are used to recover electron and ion temperature T_e and T_i , and the vertical ion drift velocity V_{iz} . During "normal" operations, each mode (A, B or C) is run for 8 min, thus yielding a time resolution between complete cycles of about 30 minutes. During a "drift" operation, the sequence ABCC was employed to

enhance the number of independent measurement of high altitude ion drift velocities. For these operations the A and B modes were run for 4 minutes each and the C modes for 8 minutes each, still yielding a time resolution between cycles of about 30 minutes. Table 2.1 summarizes the characteristics of these different modes.

Table 2.1

Characteristics of the Data Modes of the Millstone Hill UHF Single-Pulse Experiment

	MODE		
	<u>A</u>	<u>B</u>	<u>C</u>
Pulse length (msec)	.1	.5	1.0
Height resolution (km)	15	75	150
Sample spacing (km)	7.5	75	75
Altitude coverage (km)	150-900	225-675	450-1125
Delay times of spectrum (msec)	---	1.5-4.5	3.0-7.5
Output	N	T_e, T_i, V_{iz}	T_e, T_i, V_{iz}

In the A mode, only the backscattered power P_s is measured as a function of height (see equations 2.8,9). To avoid trying to maintain constant the radar sensitivity, usually just the shape of the electron density profile is recovered. A nearby ionosonde then supplies the value for the peak density N_{\max} from the critical frequency of the "ordinary" wave in the F2 region (f_oF_2). f_oF_2 is the plasma frequency for the electron density N_{\max} (see eq. 2.4). For a frequency in Hz, the maximum electron density can be written as

$$N_{\max} = 1.24 * 10^{-2} (f_o F2)^2 \text{ electrons/m}^3 \quad (2.10)$$

Since σ is a function of the temperature ratio T_e/T_i , measurements made using the A mode cannot unambiguously determine the electron density.

In the other two modes (B and C), the returns are applied to a spectrum analyzer to measure the backscattered power as a function of frequency. Figure 2.1 shows a typical echo spectrum. The major characteristics of this spectrum are the values of the half-power width L, the ratio H of the power in the wings to the power in the center frequency, and the Doppler shift D of the entire spectrum from the radar frequency. (D is exaggerated in the figure).

Referring back to the theory,

$$L = 0.71 \Delta f \quad (2.11)$$

and hence depends on T_e . H varies with T_e/T_i and so is a measure of this parameter. The Doppler shift D can be written as

$$D = \Delta f_d = - 2 V_{iz} / \lambda \quad \text{Hz} \quad (2.12)$$

where V_{iz} is in m/sec and $\lambda = .68$ m. Since V_{iz} is at most a few tens of meters per second, Δf_d is usually less than 100 Hz. The overall width of the spectrum is usually more than 10 kHz so extremely precise spectrum measurements are needed to measure V_{iz} accurately.

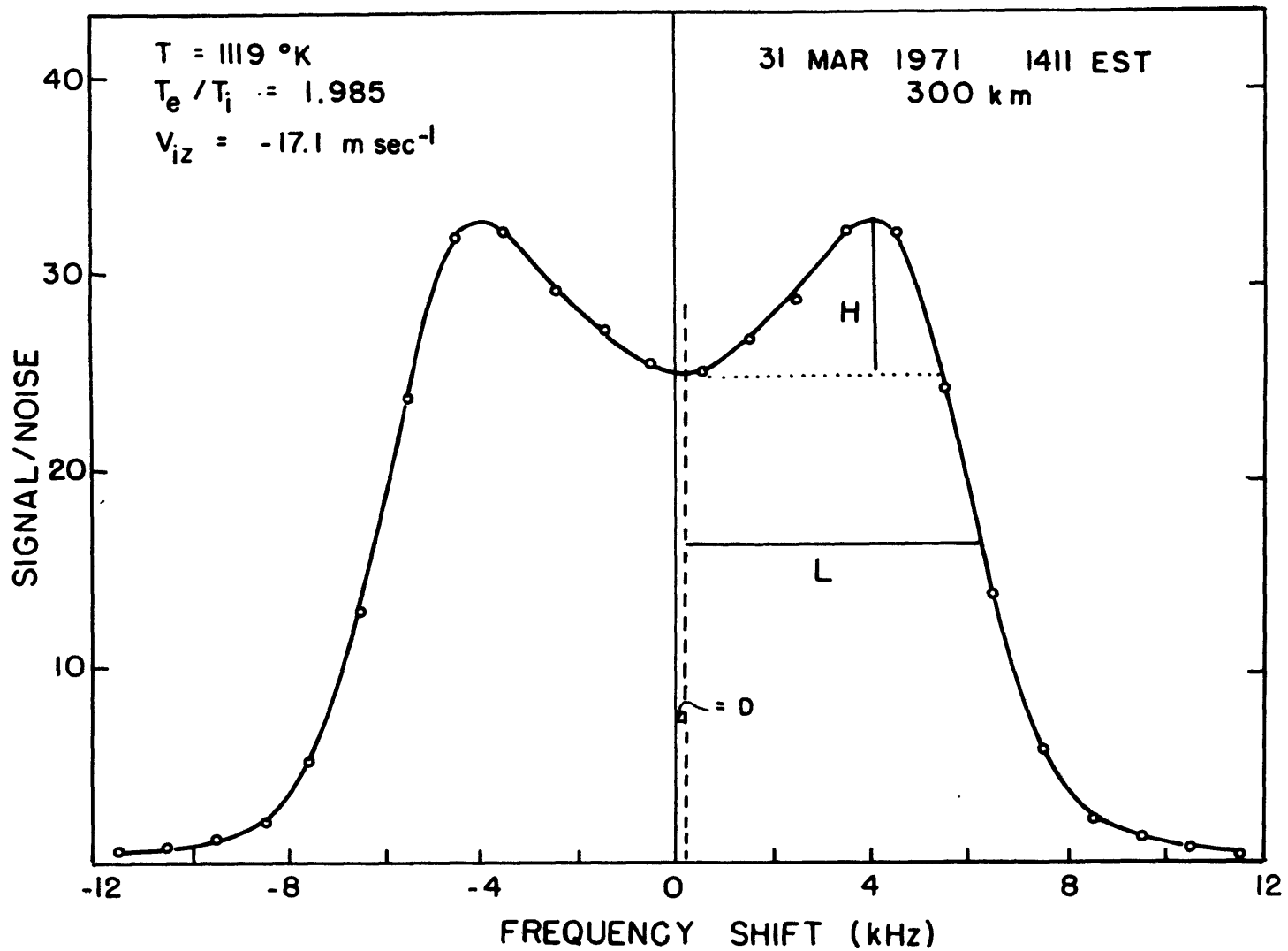


Fig. 2.1: Example of incoherent scatter spectrum measured by UHF zenith radar at Millstone Hill. (Adapted from Fig. 2.2 of Salah, 1972).

An unsatisfactory feature of the temperature results gathered between 1969 and 1975 is that at night there is a systematic difference between the values for T_i derived from the B and C modes, the B mode ion temperature being as much as 200°K smaller. After careful analysis of the probable sources of error, it was concluded that the discrepancy was largely the result of a mismatch between the frequency response of the filters and spectrum of the transmitted pulse. This mismatch is observed to be greater for the shorter B mode pulse. A scheme was devised to overcome this problem and is described in Appendix A.

The ionospheric data which are recovered from the A, B, and C modes (N , T_e , T_i , V_{iz}) can then each be smoothed with respect to time and height by a computer program INSCON designed by J. M. Holt (Evans and Holt, 1976). The smoothing is accomplished by fitting the data to a least-mean-squares two-dimensional polynomial. The number of terms in the polynomial depends upon the number of experimental times and heights which are covered. An effort is made to eliminate bad points prior to the fitting process. Given the INSCON fit, the polynomial representation of the data can be recovered for any time and altitude within the range of the data. If INSCON has determined that the quality of the fit was questionable, the recovered fit value is negative. INSCON fits to the ionospheric data were used in the present study.

3. THE INPUT DATA

As described in Chapter 2, the Millstone Hill incoherent scatter radar can directly provide values of the electron density N , the electron and ion temperatures T_e and T_i , and the ion drift in the vertical direction V_{iz} . As explained in this chapter, this ionospheric data can be used in conjunction with a neutral density model to find other variables such as the exospheric temperature T_∞ , the diffusion velocity $V_{D//}$, the electric field induced perpendicular drift V_\perp , the neutral wind parallel to the magnetic field $V_{n//}$, the ion composition ratio $O^+/(NO^+ + O_2^+)$, and the seasonal variation of O/N_2 (Salah and Evans (1973), Salah and Holt (1974), Kirchhoff and Carpenter (1975), Evans and Cox (1970), Cox and Evans (1970)). The best available model of the neutral density in the thermosphere presently available is the 1977 MSIS model of Hedin et al which is based on mass spectrometer number density data and incoherent scatter temperature data. The data base for this model includes the OGO-6 satellite mass spectrometer data taken during high sunspot number and the more recent AEROS-A and AE-C satellite data taken during low sunspot number (AEROS-A operated during the first half of 1973 between 200 and 500 km. AE-C operated during 1974 from 140 to 600 km). As a result of the larger data base, it is believed the sunspot cycle variations are better described than in previous models.

3.1 Exospheric Temperature

3.1.1 Form of the Neutral Temperature

Above about 120 km, the neutral temperature T_n increases exponentially to a limiting value around 450 km. This temperature is called the exospheric temperature, T_∞ . When analyzing the incoherent scatter data the height increase in neutral atmospheric temperature is modeled after Bates (1959) in the form

$$T_n(z) = T_\infty - (T_\infty - T_{120}) \exp(-s(z-120)) \quad (3.1)$$

where z is the height in km, $T_n(z)$ is the neutral temperature in $^{\circ}\text{K}$ at height z , T_{120} is the neutral temperature at 120 km, and s is the shape parameter.

3.1.2 Heat Balance Equation

An estimate of neutral temperature T_n can be found from the radar measurements through the ion heat balance equation. Above about 200 km, the temperatures of the electrons T_e , ions T_i , and neutrals T_n are different since low energy photoelectrons preferentially lose their energy to electrons (see Section 1.2). Some of this energy is then transferred to the ions through elastic (Coulomb) collisions between the ions and ambient electrons. In turn, some of this is passed on to the neutrals through ion-neutral collisions. The ion thermal energy balance requires that the heat transferred from the electrons to the ions equal the heat transferred from the ions to the neutrals, (since heat transport is not important).

This is written as (Salah and Evans, 1973)

$$4.82 \times 10^7 N n(O^+) \frac{T_e - T_i}{T_e^{3/2}} = (6.6 n(N_2) + 5.8 n(O_2)) \quad (3.2)$$

$$+ 0.21 n(O) (T_i + T_n)^{1/2} n(O^+) (T_i - T_n)$$

where $n(N_2)$ is the number density of N_2 , etc.

This equation assumes that the major ion is O^+ . It further assumes that the major neutral species are O, N_2 , and O_2 . These assumptions are valid roughly between 250 and 600 km. At 300 km for high sunspot number, $n(N_2)/n(O) \approx 0.20 - 0.3$ and $n(O_2)/n(O) \approx 0.008 - 0.016$. These ratios decrease with altitude. Evidently, by adopting values for $n(N_2)$, $n(O)$ and $n(O_2)$ Eq. 3.2 can be solved for T_n since T_e , T_i and N are known. The values adopted for the neutral densities can be obtained from a neutral model.

Three or four altitudes were chosen at which to attempt to solve Eq. 3.2. These were at the nominal heights of 300, 375, 450, and 525 km. The lowest height 300 km was not used consistently, although it could have been. (Equivalent height corrections (Appendix A) were part of the ensuing calculation.) The values of T_n derived at the four altitudes were then employed to determine T_∞ in Eq. 3.1, where T_{120} was chosen to be 355°K and s to be 0.020 km^{-1} . Changing T_{120} by $\pm 100^\circ\text{K}$ has been found to introduce less than $\pm 1\%$ error in T_∞ , and varying s between 0.015 and 0.030 km^{-1}

introduces less than $\pm 2\%$ error in T_{∞} (Salah and Evans, 1973). Given a single value of T_n at an altitude well above 120 km, one can estimate a value for T_{∞} . The accuracy is improved if several values of T_n are obtained at different altitudes. The exospheric temperature T_{∞} tends to be fixed by the mean of the ion temperatures, while the density of the major neutral ion species, here atomic oxygen, primarily determines the altitude variation of the fitted ion temperatures.

An alternative method of solving 3.2 is to seek a simultaneous solution for T_{∞} (Eq. 3.1) and the abundance of atomic oxygen (whose distribution is controlled by T_n in 3.1) at some reference altitude. Changing T_{∞} (or equivalently, T_n), results in shifting the fitted ion temperatures in a uniform manner. At a particular altitude, a decrease in T_{∞} can mimic the effects of a decrease in $n(0)$ and vice versa. However, an iterative solution for these two unknowns, T_{∞} and $n(0)$ at some reference height, usually results in a better fit to the ion temperature data at three different heights.

An attempt was made to solve for T_{∞} and $n(0)$ at 400 km for 5 days of data. The derived daytime atomic oxygen densities looked sensible and compared well with neutral model densities. However, the derived nighttime atomic oxygen densities looked unreasonably high for 4 days out of the 5, giving one little confidence in the results of the remaining day. This failure to deduce atomic oxygen densities at night arises because the temperature difference ($T_i - T_n$) falls to a very small value at night and this is an inherent difficulty with the technique (Bauer et al, 1970). It was therefore decided to solve only for the exospheric temperature in the fitting procedure, and to take the neutral densities for 0,

N_2 , and O_2 from the MSIS model. Since, during the day, $(T_i - T_n) \leq 125^\circ\text{K}$ at 375 km and T_∞ is of the order of 1000°K , a 20% error in the value of $n(0)$ adopted will result in about a 25°K or 2.5% error in T_∞ . The ionospheric data for N , T_e , and T_i used in solving for T_n (Eq. 3.2) were taken from the polynomial fit of INSCON described in Chapter 2.

Ignoring systematic errors in atomic oxygen number densities, the total uncertainty in the exospheric temperature is estimated to be $\pm 50^\circ\text{K}$ or 5% from one observation to another (Salah and Evans, 1973). The INSCON program smooths the results in time as well as height, and reduces this uncertainty to about $\pm 25^\circ\text{K}$. Figure 3.1 shows the exospheric temperature deduced for March 23-24, 1970 for two cases. In the first case (Salah and Evans, 1973), the old B mode temperature corrections were employed (see Appendix A), only smoothing in height was performed, and neutral densities were taken from the Jacchia 1971 atmospheric model. The second case shows results from the present analysis which used INSCON smoothing, the new B mode corrections, and the MSIS model. The average exospheric temperature is 1024°K for the first case and 1077°K for the second, with a day-night variation of about 350°K . The peak temperature occurs at 1500 LT (local time), and the minimum around 0100 LT. Most of the differences in exospheric temperature between the two cases are a result of the different B mode temperature corrections. The exospheric temperatures are one of the more important inputs of the present study since they determine the east-west pressure gradient forces.

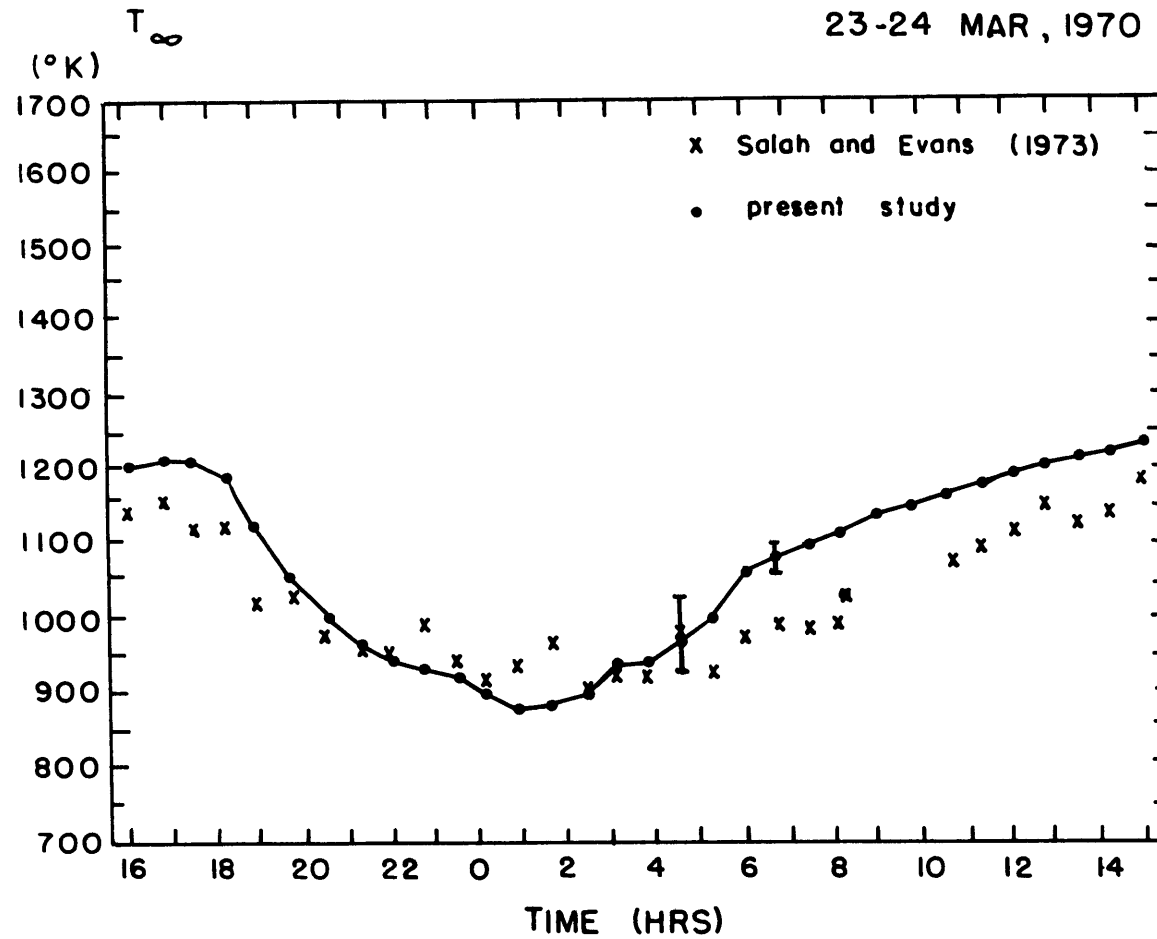


Fig. 3.1: The exospheric temperature on March 23-24, 1970 at Millstone Hill.

3.2 Plasma Diffusion Velocity

In the region above about 180 km, the electron and ion gyrofrequencies $\omega_{e(i)} = eB/m_{e(i)}$, are much larger than collision frequencies $\nu_{e(i)n}$. Here e =electronic charge, B =magnetic field strength, and $m_{e(i)}$ =electron (ion) mass. In the absence of electric fields, particles are compelled to gyrate about the magnetic field lines. With this assumption, a plasma diffusion velocity $V_{D//}$ (m/sec) can be defined. This is the velocity of the plasma (ions and electrons both) in response to gravity and gradients in density and temperature. It can be derived from the equations of motion for the electron and ion gases where viscosity and the non-linear acceleration terms are neglected and the ion and electron velocities are assumed to be the same (i.e. there are no electrical fields and no net electrical current). If the plasma were in diffusive equilibrium, $V_{D//}$ would be zero. The diffusion velocity is defined positive upwards along field lines and can be written as (Schunk and Walker, 1970)

$$V_{D//} = -D_a \sin I \left[\frac{1}{N} \frac{\partial N}{\partial z} + \frac{1}{T_e + T_i} \frac{\partial (T_e + T_i)}{\partial z} + \frac{.38}{T_i + T_n} \frac{\partial (T_i + T_n)}{\partial z} + \frac{m_i g}{k(T_i + T_e)} \right] \quad (3.3)$$

where D_a is the ambipolar diffusion coefficient (Stubbe, 1968)

$$D_a = \frac{k(T_e + T_i)}{\nu_{in} \mu_{in}} = \frac{k(T_e + T_i)}{(\nu_{O^+O} \mu_{O^+O} + \nu_{O^+N_2} \mu_{O^+N_2} + \nu_{O^+O_2} \mu_{O^+O_2})} \quad (3.4)$$

and I = magnetic dip angle (72° for Millstone Hill), z = altitude, g = gravity, k = Boltzmann's constant, $\mu_{in} = m_i m_n / (m_i + m_n)$ reduced particle mass, m_n = neutral particle mass, and ν_{in} ($\propto n(\text{neutral})$) = ion-neutral collision frequency. The values used for the ion-neutral collision frequencies were taken from Banks (1966b).

To compute $V_{D//}$ from the incoherent scatter radar data, it was assumed that the only ion is O^+ , and from charge conservation $n(O^+) = N$. Values for N , T_e , T_i , and their height derivatives were found through the polynomial fit of INSCON. T_n and its height derivative are found from T_∞ and the Bates (1959) profile described by Eq. 3.1. Values for $n(O)$, $n(N_2)$, and $n(O_2)$ were taken from the MSIS model. (It should be noted that accurate values for $n(O)$ are much more important in the determination of $V_{D//}$ than they are in the determination of T_∞ . Since $V_{D//} \propto 1/n(O)$, a 20% error in $n(O)$ would create a 20% error in $V_{D//}$ compared to a 2.5% error in T_∞ .)

Equation 3.3 is useful between about 250 km and 400 km. Below 250 km, there are no measurements of temperature and above 400 km, the magnification of errors caused by the exponential decrease with height of $n(O)$ becomes important. Also, hydrostatic balance is more nearly attained, leaving the determination of the diffusion velocity dependent on the poorly estimated temperature derivatives with height. Neglecting any systematic errors in $n(O)$ or in the ion-neutral collision frequencies, the errors in $V_{D//}$ are estimated to be about 1-3 m/sec around the electron density peak at 300 km (Salah and Holt, 1974).

3.2.1 Ion-Neutral Collision Frequencies

An important systematic source of error in the determination of $V_{D//}$ is the value taken for the ion-neutral collision frequency ν_{in} .

Experimental data on ion-neutral collision frequencies is scarce and is estimated to be only accurate to $\pm 25\%$ at temperatures of ionospheric interest (Mason, 1970), even assuming the mechanism involved in the collision process is understood. For the case of ions in their parent gases at ionospheric temperatures, this mechanism is resonant charge-exchange. For ions in unlike gases, the mechanism depends on the short-range force between ions and neutrals which can be repulsive, or attractive. In the region between about 250 and 600 km, practically the only ion present is O^+ , while the dominant neutral species is O . In the lower part of this region, N_2 and O_2 can be important. The mechanism between $O^+ - O$ is charge-exchange, and that between $O^+ - O_2$ involves attractive forces. It is not clear whether the force between $O^+ - N_2$ is attractive, as is normally assumed, or repulsive. If it were repulsive, $\nu_{O^+N_2}$ would be reduced to nearly half the value it would have with an attractive force in the temperature range of interest. Banks (1966b) has used the experimental values and theory to estimate the collision frequencies.

In a later study, Stubbe (1968) assumed that the long range attractive forces added to the charge-exchange mechanism, increasing ν_{O^+O} by about 25%. Since $V_{D//} \propto 1/\nu_{O^+O}$, a 25% increase

in the $O^+ - O$ collision-frequency proposed by Stubbe results in a reduction of $V_{D//}$ of approximately the same percentage. Most of the present study was carried out using Banks' values for the collision frequencies, although one case using the proposed Stubbe collision frequencies was included to explore the effects of a 25% change in the value of the collision frequency.

3.2.2 Comparison with Previous Results

Figure 3.2 shows the diffusion velocity calculated using Eq. 3.3 at 300 km for March 23-24, 1970. The "Banks" case uses collision frequencies taken from Banks (1966b) and the "Stubbe" case uses collision frequencies taken from Stubbe (1968). The x 's are taken from the Salah and Holt (1974) paper, in which the Dalgarno (1964) value for the $O^+ - O$ collision frequency which is similar to that given by Banks was used. In this paper it was also assumed that only atomic oxygen was present at 300 km, and the Jacchia (1971) neutral atmosphere model was utilized to obtain values of $n(O)$.

The diffusion velocity is downward during the entire period, although it approaches zero velocity around 0800 LT. On other days, there can be a small upward velocity about this time. The strongest downward velocities are around midnight at about 37 m/sec for the "Banks" case, and about 55 m/sec for the Salah and Holt (1974) analysis. This 30% difference can partially be explained by the inclusion in the "Banks" case of N_2 and O_2 collisions with O^+ , which decreases $V_{D//}$ by about 7 m/sec at this time.

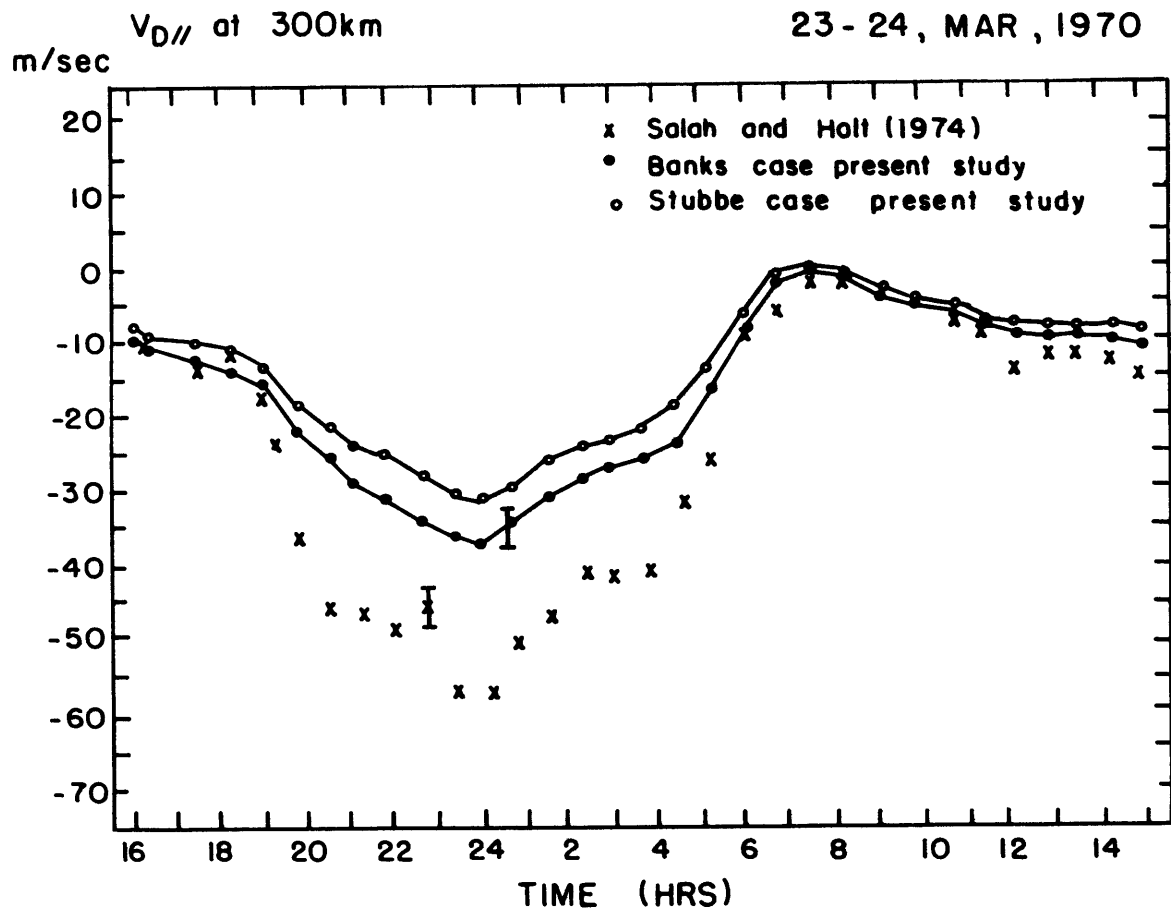


Fig. 3.2: The diffusion velocity calculated at 300 km for Millstone Hill on March 23-24, 1970.

Other contributors to the difference include the use of different neutral atmosphere models (which determine the atomic oxygen abundances) and the manner in which the data were smoothed. At 300 km, the MSIS model atomic oxygen densities were about the same as the Jacchia (1971) model densities used, so this will not have an effect. Instead it appears that the largest difference stems from using INSCON smoothed values for the "Banks" case. Specifically, the electron density gradient is usually found to be smaller using INSCON smoothed electron densities. This accounts for most of the decrease in the diffusion velocities in the present analysis as compared to the Salah and Holt (1974) analysis. There is also some effect due to the differences in correcting the lower altitude ion and electron temperatures, but this is a smaller effect. The difference between the "Banks" case and the "Stubbe" case is found to be about a 7 m/sec or 14% decrease in velocity for the latter case around midnight.

3.3 Neutral Wind Component

The ion drift velocity \vec{V}_i can be attributed to three separate components (Salah and Holt, 1974)

$$\vec{V}_i = \vec{V}_{D//} + \vec{V}_{n//} + \vec{V}_\perp \quad (3.5)$$

One component is the diffusion velocity $\vec{V}_{D//}$ discussed above, a second is the motion attributable to neutral winds $\vec{V}_{n//}$, and the third to electric fields \vec{V}_\perp . Figure 3.3 shows a diagram of the

components of \vec{V}_i in the plane of the magnetic meridian. The components due to diffusion and neutral winds are parallel to the magnetic field line since ion gyrofrequencies are much larger than ion-neutral collision frequencies above about 180 km. The ion drift due to electric fields is perpendicular to both electric and magnetic fields and can be written as

$$\vec{V}_\perp = \vec{E} \times \vec{B}/B^2 = \vec{v}_{ewE} + \vec{v}_{nsE} \quad (3.6)$$

where \vec{v}_{ewE} and \vec{v}_{nsE} are in magnetic coordinates. \vec{v}_{nsE} points D degrees to the east of geographic north and $(90^\circ - I)$ degrees above the horizontal. D is the magnetic declination angle and I the inclination angle. ($D = -14^\circ$ and $I = 72^\circ$ for Millstone Hill). \vec{E} and \vec{B} are the electric and magnetic field strengths.

The neutral wind component $\vec{V}_{n//}$ defined positive upwards along the field line can be written as (Salah and Holt, 1974)

$$\begin{aligned} V_{n//} &= -\vec{V}_n \cdot \vec{B}/B = -u \sin D \cos I - v \cos D \cos I \\ &\quad + w \sin I \cong - (u \sin D + v \cos D) \cos I \quad (3.7) \\ &= -V_{Hn} \cos I \end{aligned}$$

where u, v, and w are the neutral zonal, meridional and vertical velocities defined to be positive eastwards, northwards, and upwards. $V_{Hn} (= \sin D + v \cos D \sim v$ for Millstone Hill) is the horizontal part of the neutral wind component parallel to the magnetic field line. This component of the neutral wind attempts to drive ions in a direction parallel to the magnetic field with

velocity $V_{Hn} \cos I$. This motion is resisted by vertical diffusion $V_{D//}$. The vertical velocity V_{iz} observed for the ions is therefore

$$V_{iz} = -V_{Hn} \cos I \sin I + w \sin^2 I + V_{D//} \sin I + v_{nsE} \cos I \quad (3.8)$$

This equation is not quite correct because the antenna does not point straight up, but rather points 2° to the south of vertical. Correcting for this 2° slant and defining V_{iz} as the ion drift in this direction, the equation for V_{Hn} ignoring the vertical velocity w becomes

$$V_{Hn} \approx \frac{V_{D//}}{\cos I} + \left[-V_{iz} + v_{nsE} (\cos I \cos 2^\circ - \sin I \cos D \sin 2^\circ) + v_{ewE} \sin D \sin 2^\circ \right] / \cos I (\sin I \cos 2^\circ + \cos I \cos D \sin 2^\circ) \quad (3.9)$$

V_{iz} will henceforth be called the vertical ion drift with the understanding that it is really the component of the ion drift 2° to the south of vertical.

The measured vertical plasma drifts at 300 km for March 23-24, 1970 are shown in Figure 3.4. Both the Salah and Holt (1974) results as well as the present INSCON smoothed results are shown. The drift is downward at all times and varies around a value of about 17 m/sec. The errors in the experimental measurements at this altitude are estimated to be ± 5 to ± 10 m/sec. The time and height smoothing in the INSCON values reduces this statistical uncertainty by about a factor of two. Ignoring electric fields and neglecting any systematic errors in $V_{D//}$, the experimental error in V_{Hn} may be shown to depend mainly on the error in V_{iz} . This varies with time

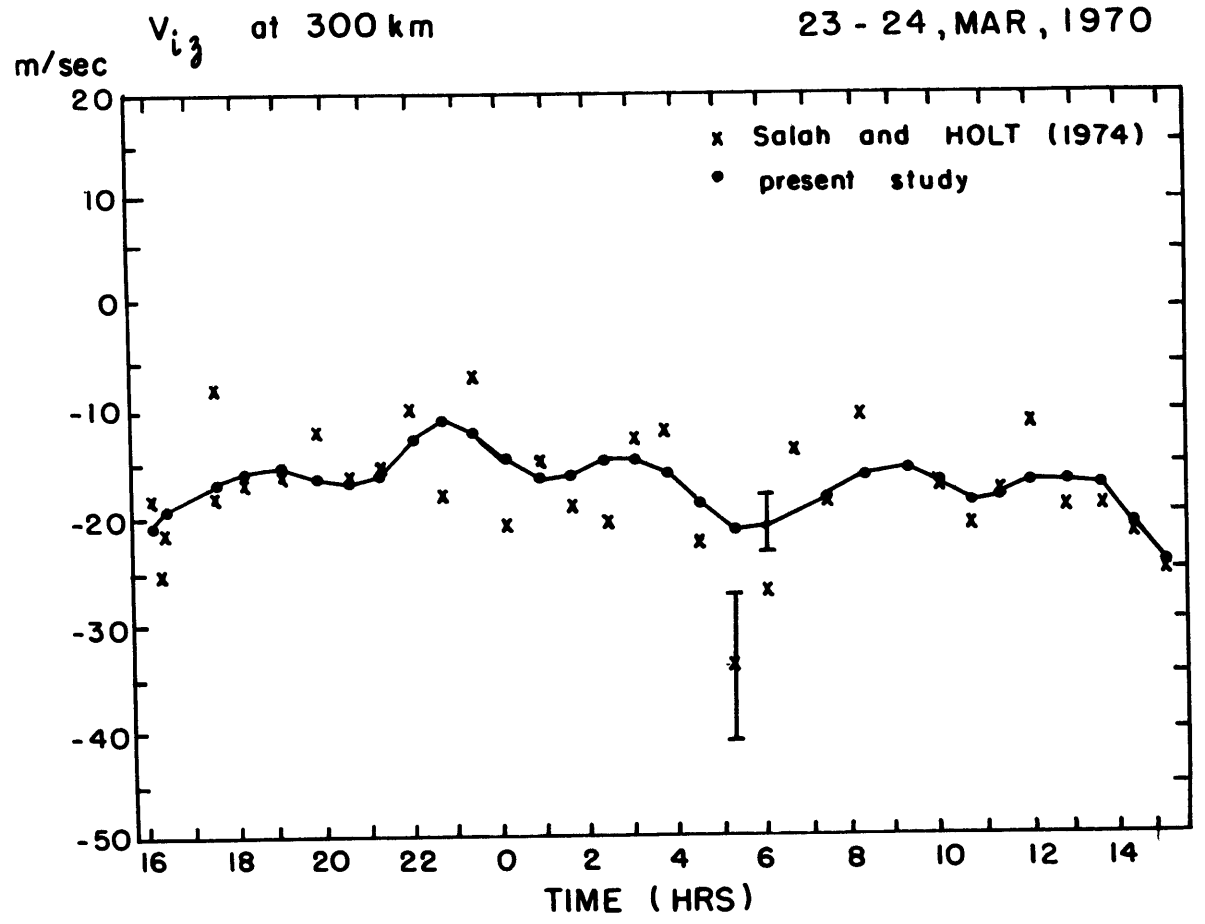
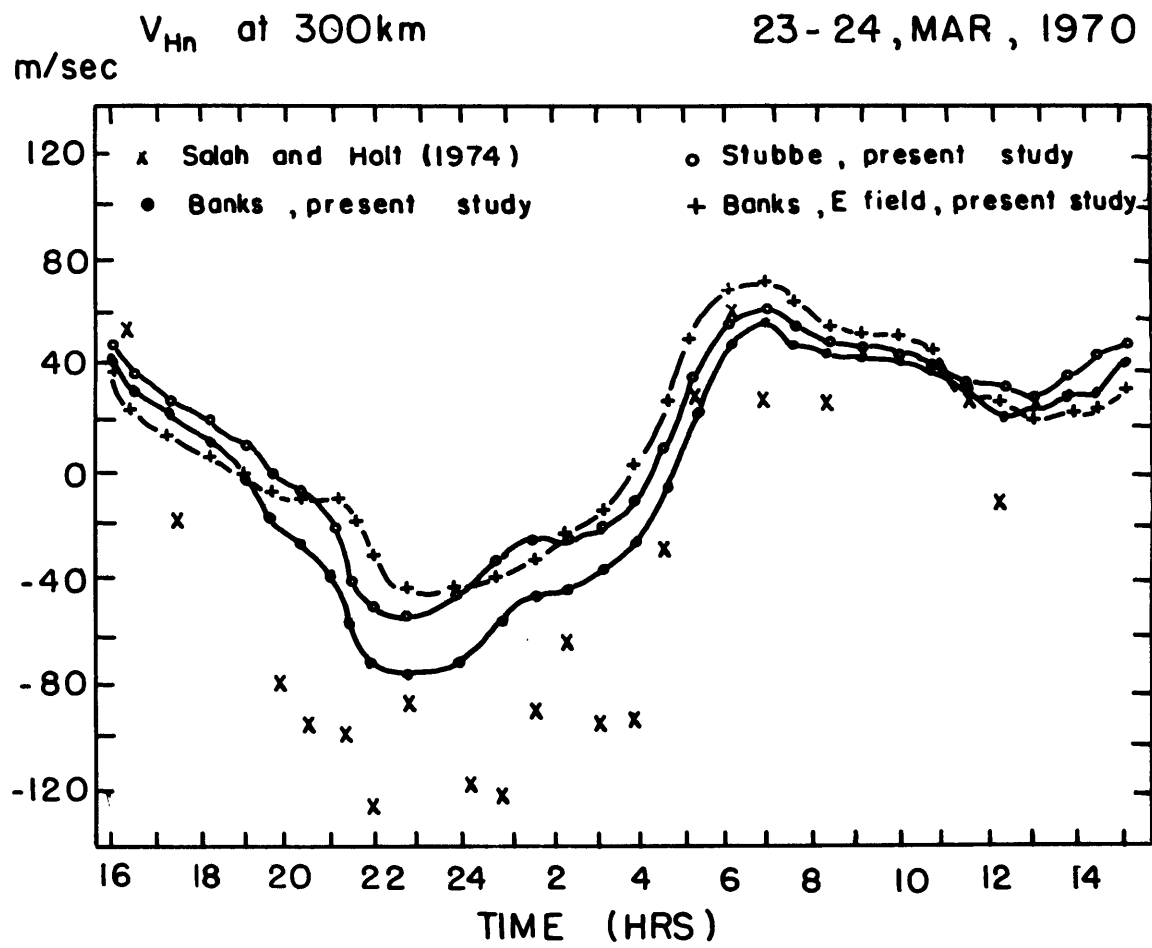


Fig. 3.4: The vertical ion drift at 300 km measured at Millstone Hill on March 23-24, 1970.

of day as a consequence of changes in the signal-to-noise ratio of the echoes. Because of the factor $\cos I \sin I$, it is estimated to be about ± 30 m/sec at 300 km at night. This is reduced by the time smoothing provided by the INSCON program to about ± 15 m/sec.

Figure 3.5 shows the deduced horizontal neutral wind component V_{Hn} for March 23-24, 1970 at 300 km. The previous analysis by Salah and Holt (1974), the "Banks" case, and the "Stubbe" case are plotted with electric fields set to zero in Eq. 3.9. In addition, the "Banks" case is plotted with the electric field model described in the next section. The neutral winds are equatorwards at night and polewards during the day. The maximum "poleward" velocities are just before midnight at about 120 m/sec for the Salah and Holt (1974) analysis, 75 m/sec for the "Banks" case, 50 m/sec for the "Stubbe" case, and about 45 m/sec for the "Banks" case with an electric field model. The differences are a direct consequence of the differences in diffusion velocities magnified by the factor $1/\cos(I)$ (see Eq. 3.9). As can be seen, the presence of electric fields can make a significant difference, and so the fields should be known if a precise measurement of the neutral wind along the field line is desired. These estimates for the "meridional" wind are the basic input that determines the variation of the north-south pressure gradient above Millstone Hill.



67

Fig. 3.5: The horizontal component of the neutral wind in the magnetic meridian plane calculated at 300 km for Millstone Hill on March 23-24, 1970.

3.4 Electric Fields

Electric fields can be deduced from plasma drifts measured in two directions perpendicular to the magnetic field. Such measurements were made at Millstone Hill using a steerable radar and have been reported by Evans (1972), Carpenter and Kirchhoff (1974), Kirchhoff and Carpenter (1975), and Kirchhoff and Carpenter (1976). Similar measurement of V_{\perp} have been reported for the magnetic equator facility at Jicamarca by Woodman (1970, 1972), at Arecibo (18°N) by Behnke and Harper (1973), Behnke and Hagfors (1974), at St. Santin (44.6°N) by Blanc et al (1976), and at Malvern (52°N) by Taylor (1974). Richmond (1976) has combined this incoherent scatter data with data derived by tracking whistler ducts in the plasmasphere (Carpenter and Seely, 1976) into a global electric field model for geomagnetically quiet days.

The Millstone Hill observations were obtained with a fully steerable (25 meter diameter) reflector used with a radar operating at $\lambda = 23$ cm wavelength described by Evans (1969). This L-band radar is smaller and less sensitive than the large (65 m diameter) fixed vertically directed, parabolic reflector antenna operating with a wavelength of 68 cm which was described in Chapter 2. However, the steerable character of the L-band radar gives it certain advantages over the larger radar system. By tilting the antenna, it is possible to observe the horizontal component of the plasma drift, and by combining measurements made in three separate directions, the drifts parallel and perpendicular to the magnetic field may be

resolved. However, the smaller size of the collecting antenna means that the signal-to-noise ratio is decreased, and it has proved difficult to make useful measurements at night when the signal-to-noise ratio is reduced by the decrease in the ambient electron density.

The measurements made at Millstone Hill for 14 relatively quiet days were combined by Kirchhoff and Carpenter (1975) into an average model. The electric field-induced plasma drifts V_{\perp} predicted by this model are shown in Figure 3.6, which was taken from their paper. Expressed in terms of frequency harmonics, the experimental data, can be represented by

$$\begin{aligned} v_{nsE}(\text{average model}) = & 11.3 + 18.2 \cos(15t - 24.6) \\ & + 6.4 \cos(30t + 69.3) + 6.1 \cos(45t + 108.3) \\ & + 6.6 \cos(60t + 96.8) + 2.7 \cos(75t + 108.8) \quad \text{m/sec} \end{aligned} \tag{3.10}$$

$$\begin{aligned} -v_{ewE}(\text{average model}) = & 11.3 + 29 \cos(15t + 38.4) \\ & + 16.1 \cos(30t + 108.3) + 13 \cos(45t + 49.3) \\ & + 2.3 \cos(60t + 0) + 3.5 \cos(75t - 35) \quad \text{m/sec} \end{aligned}$$

where t is local time in hours.

During the day, the electric fields are thought to be of dynamo origin and produce drifts of ~ 20 m/sec toward the north in the morning and toward the south in the afternoon. This pattern seems reliably established. At night, the fields are probably of

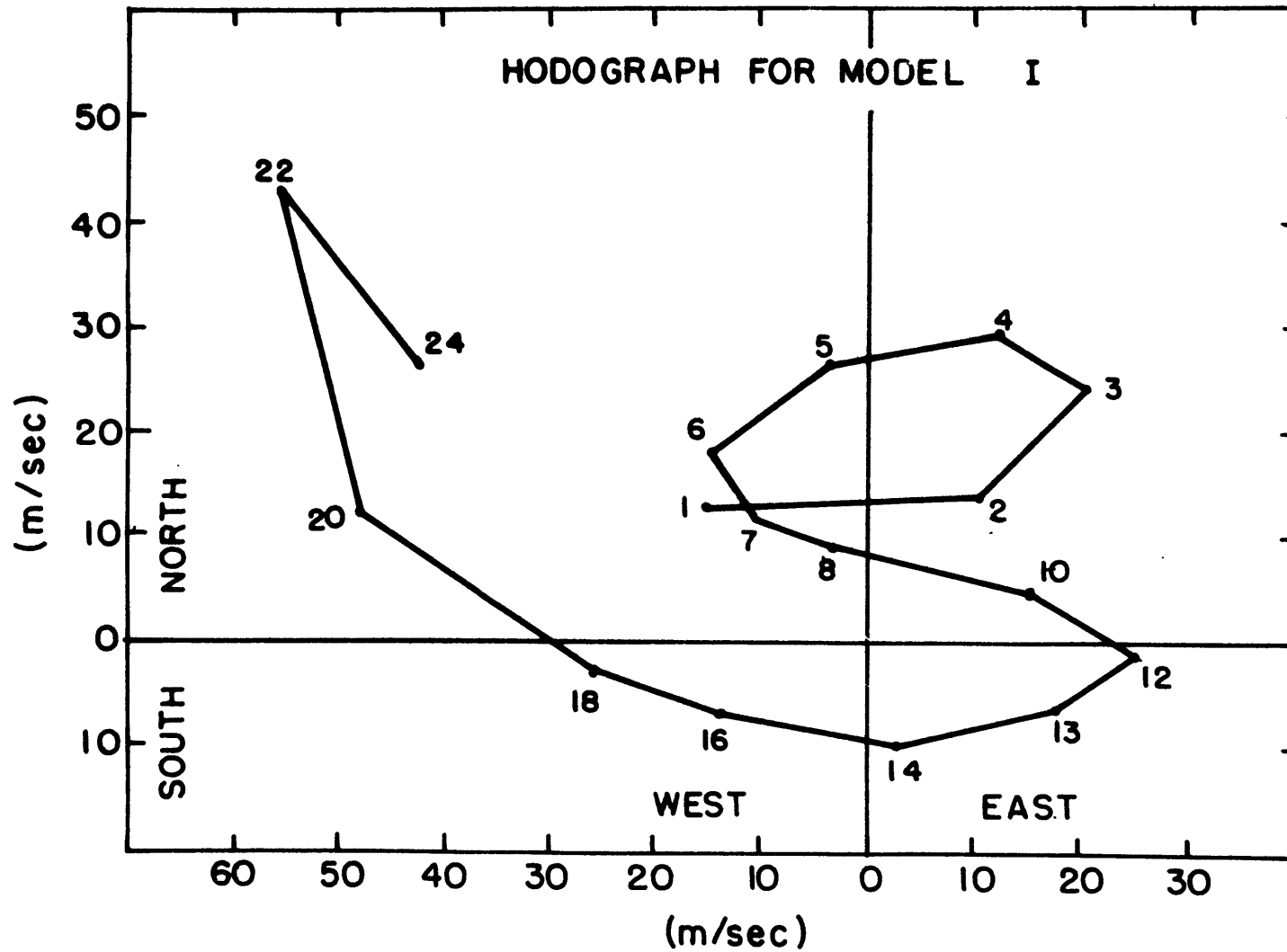


Fig. 3.6: Ion drifts induced throughout the day by the Kirchhoff and Carpenter (1975) electric field model for Millstone Hill. The figure is reproduced from their paper.

magnetospheric origin and are larger, causing northward drifts of up to 50 or 60 m/sec. Unfortunately, these nighttime values are very uncertain because of the reasons stated above. In addition, large fluctuations in the drifts seem to occur possibly reflecting changes associated with auroral substorms (Richmond and Matsushita, 1975). Consequently, nighttime measurements are few in number and subject to considerable scatter.

The electric field model of Eq. 3.10 was used to derive the results for the "Banks" electric field case shown in Figure 3.5. The effect of its inclusion was to decrease V_{Hn} by 20 to 50 m/sec at night. During the day, the effect was small. The field model described above has been used in some parts of the present analysis, but more commonly, V_{\perp} was assumed to be zero. Since the majority of the days analyzed did not include cross-field drift measurements, and we remain uncertain about the nighttime electric fields and their possible local time, seasonal, and substorm dependence, this appeared to be the best procedure.

3.5 Ion Composition

The particular combination of ions and neutrals determines the form of the ion-neutral collision frequency and thus part of the ion drag. In addition, the amount of O^+ in relation to other ions in the region below 200 or 150 km is an indicator of the amount of neutral atomic oxygen at the bottom boundary of 120 km in relation to the other constituents. The bottom boundary value of atomic

oxygen coupled with the value of the exospheric temperature, largely determine the number density at ionospheric heights where atomic oxygen is the major species.

The major ions in the lower thermosphere are O_2^+ and NO^+ , with a transition to O^+ occurring between about 170 and 225 km, depending on the time of day (e.g. Holmes et al, 1965) and on the season (e.g. Evans and Cox, 1970). Protons (H^+) then become the dominant ions above about 900 km at night, and 2000 km during the day for mid-latitudes (e.g. Brinton et al, 1969b)(see Figure 1.2). Direct sampling of the ion composition has been largely accomplished with rocket- and satellite-borne ion mass spectrometers. Most rocket launches were able to sample the ionosphere between about 100 and 250 km (e.g. Taylor and Brinton, 1961), though a few rockets have been able to gather data up to nearly 650 km (e.g. Brinton et al, 1969a). The range of the satellite observations are usually between about 280 and 2700 km.

In addition to these direct measurement, incoherent scatter radar measurements have been used to estimate the ratio of O^+ to the sum of NO^+ and O_2^+ (mean mass of 31) in the lower thermosphere. These results depend upon certain assumptions regarding the altitude variation of electron or ion temperatures (e.g. Evans and Cox, 1970).

The results of such studies showed a seasonal variation in the daytime ratio of $O^+/(NO^+ + O_2^+)$ with a greater molecular

ion abundance at altitudes around 200 km in the summer months. The explanation advanced for this was that there is a seasonal variation of the neutral composition ratio of O/N₂ with larger concentrations of N₂ in the summer (Evans, 1967, Cox and Evans, 1970). The presence of additional N₂ molecules increases the rate of loss of O⁺ ions to NO⁺ ions via the charge exchange reaction



Such a seasonal variation in the O/N₂ ratio has since been confirmed by mass spectrometer measurements on satellites (e.g. Hedin et al., 1974).

The average composition ratio curves vs altitude adopted in this study are plotted in Figure 3.7. These are based on a combination of the ion composition results for Millstone Hill (Evans and Cox, 1970), and various rocket measurements at the same approximate latitude which have been reported in the literature (e.g. Holmes et al., 1965, Brinton, et al., 1969a, 1969a, Taylor and Brinton, 1961). Separate day and night curves were obtained for summer and winter. In using the curves, a transition between the day and night variations was made over a period of 100 minutes centered around sunrise and sunset at 250 km altitude. For simplicity, the ratio of NO⁺/(NO⁺+O₂⁺) was assumed to be constant. This constant was chosen to be valid above about 200 km. Since this study is mainly concerned with results above 250 km, the inclusion of these molecular ions probably has only a small influence on the results.

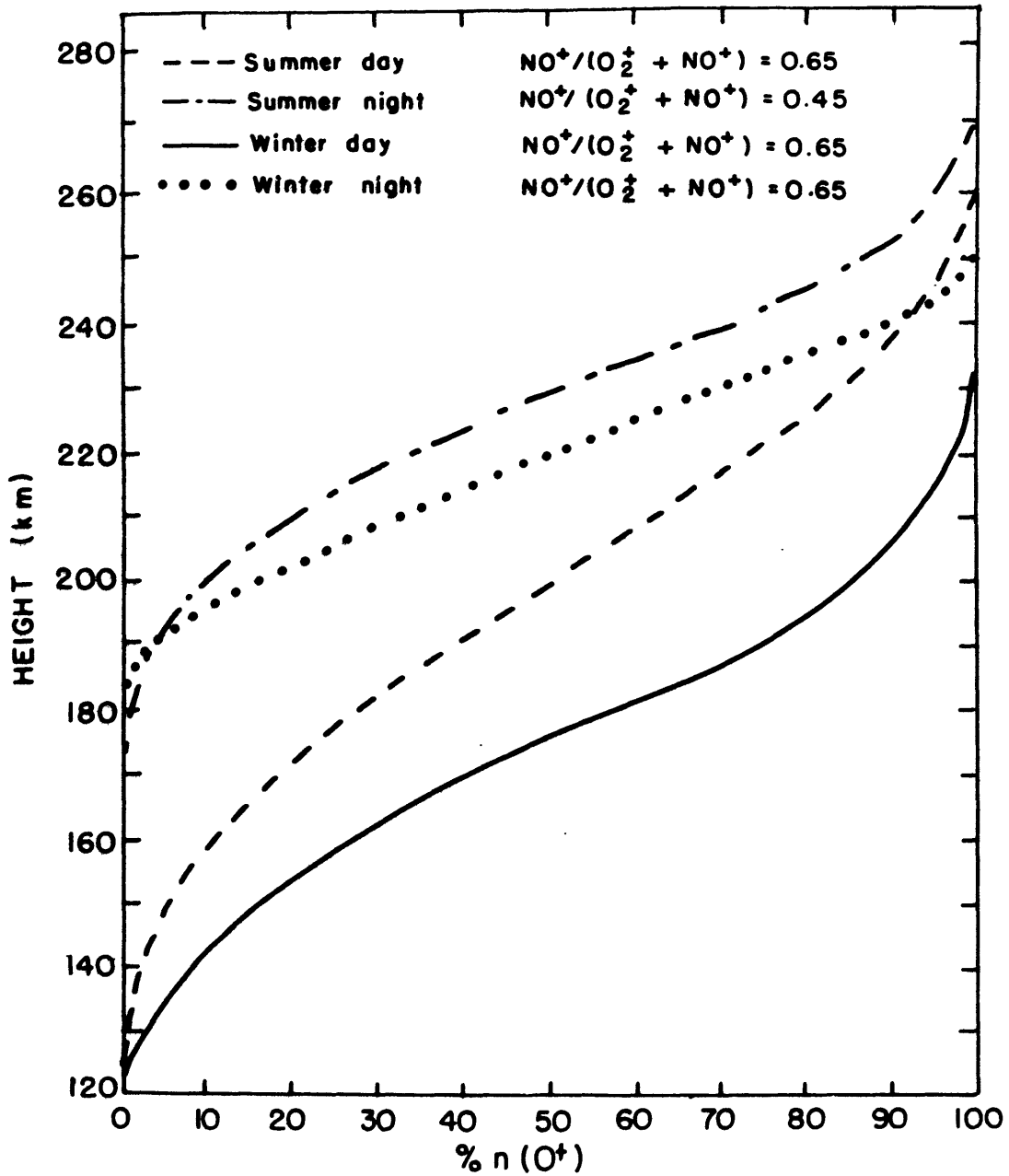


Fig. 3.7: Percent of atomic oxygen ion concentrations used in the present study and the ratios of $\text{NO}^+ / (\text{NO}^+ + \text{O}_2^+)$. (From Fig. 3.1 of Emery, 1975).

3.6 Seasonal Variations of O/N_2

One of the main objectives of this work is to determine the seasonal variations in the mean daily winds. In order to get more accurate results, any seasonal variations in the neutral density which cannot be attributed to seasonal temperature variations, need to be modeled. This is particularly true for atomic oxygen since this is the major constituent at the thermospheric heights of interest in this study. Large seasonal variations of O/N_2 are an indicator of variations in the constituents which are not tied to the temperature variations.

Seasonal variation in the composition ratio of O/N_2 was suggested by Rishbeth and Setty (1961) as the explanation for the observed winter maximum in electron density. Since then, the variation has been measured by incoherent scatter observation (Cox and Evans, 1970) and rocket- and satellite-borne mass spectrometers (e.g. Hedin et al., 1974), as described above. The manner in which this ratio can be deduced from incoherent scatter radar data has been described by Cox and Evans (1970).

For the purposes of the present study, it was decided to model the O/N_2 variation using their incoherent scatter results rather than appeal to the MSIS model. In this way it should be possible to derive seasonal variations in the winds that can be compared with those computed from the pressure gradients contained in the MSIS model.

A harmonic analysis was performed on the seasonal variation of O/N_2 deduced from the incoherent scatter results and the values for the mean, annual, and semiannual terms were retained. In order to derive absolute magnitudes, the corresponding MSIS model composition ratio of O/N_2 at 198 km at noon was formed for each of the 8 days analyzed by Cox and Evans (1970), and a harmonic fit to these ratios was obtained. The amplitudes of the Millstone Hill harmonic terms were then multiplied by the factor

$$\frac{(n(O)/n(N_2))_{198 \text{ km, MSIS}}}{(n(O)/n(N_2))_{198 \text{ km, M.H.}}}$$

The multiplicative factor is 1.635, and the resulting harmonic analysis of the Millstone Hill data can be written as

$$\begin{aligned} (n(O)/n(N_2))_{198 \text{ km, noon, M.H.}} &= 1.3861 + .9057 \cos((\text{day}-343.7)*2\pi/365) \\ &+ .1758 \cos((\text{day}-119.7)*4\pi/365) \end{aligned} \quad (3.12)$$

Figure 3.8 shows the values of O/N_2 at 198 km at noon derived from the MSIS model and from the Cox and Evans (1970) analysis multiplied by 1.635, along with their corresponding harmonic analyses containing only mean, annual, and semiannual terms. The Millstone Hill results show a maximum of about 2.37 in November and a minimum of about .44 at the end of June. The MSIS model shows a maximum of 1.91 around January 1, and a minimum of .79 at the end of June. The days upon which these results were based were in 1968 and 1969, high sunspot number years. The required boundary values for O at 120 km in the present analysis were then derived from a downward extrapolation of

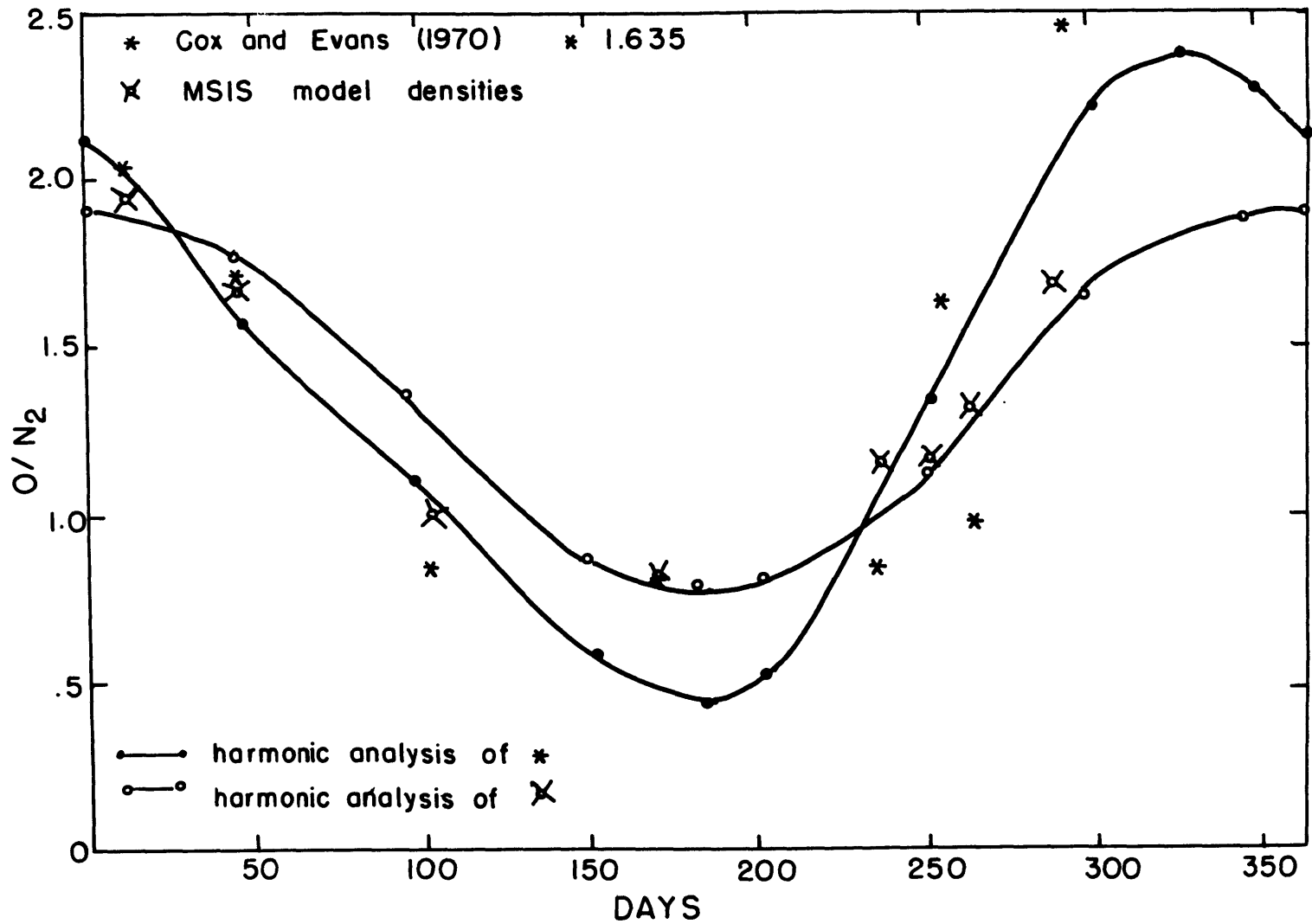


Fig. 3.8: Selected values of the ratio O/N_2 and their harmonic analysis retaining mean, annual, and semiannual terms.

Eq. 3.12, assuming the N_2 density at 120 km remained constant throughout the year. Neither the temperature nor any of the number densities varied diurnally at 120 km.

4. THE EQUATIONS FOR THE NEUTRAL THERMOSPHERE

4.1 Horizontal Equations of Motion

The horizontal equations of motions in spherical coordinates can be written as

$$\frac{\partial u}{\partial t} + u \frac{\partial u}{\partial x} + v \frac{\partial u}{\partial y} + w \frac{\partial u}{\partial z} - \frac{uv \tan \varphi}{r} = - \frac{1}{\rho} \frac{\partial p}{\partial x} + f v - 2 \Omega w \cos \varphi + F_x \quad (4.1)$$

$$\frac{\partial v}{\partial t} + u \frac{\partial v}{\partial x} + v \frac{\partial v}{\partial y} + w \frac{\partial v}{\partial z} + \frac{u^2 \tan \varphi}{r} + \frac{uw}{r} = - \frac{1}{\rho} \frac{\partial p}{\partial y} - fu + F_y$$

where x , y , and z are directed east, north, and up; u , v , and w are the eastward, northward, and vertical neutral velocities; ρ and p are the neutral density and pressure; $f = 2 \Omega \sin \varphi$ the Coriolis parameter ($\Omega = \text{Earth's rotation rate}$, $\varphi = \text{latitude}$); r is the distance from the center of the Earth; and F_x and F_y are frictional forces in the x and y directions. The left hand sides of the equations contain the inertial and the curvature terms. The inertial force is composed of the acceleration term $\partial \vec{v} / \partial t$ and non-linear terms of the form $\vec{v} \cdot \nabla \vec{v}$. The curvature terms are all proportional to $1/r$, and are introduced because the eastward and northward unit vectors change direction on the surface of a sphere. The right hand sides of the equations are composed of the pressure gradient, Coriolis, and frictional terms. The Coriolis force is introduced

because of the rotation of the Earth, and causes wind vectors to turn clockwise in the northern hemisphere.

The important frictional forces in the thermosphere are molecular viscosity and ion drag, which for an incompressible gas can be written as

$$\begin{aligned}
 F_x &= \frac{1}{\rho} \left[\mu \left(\frac{\partial^2 u}{\partial x^2} + \frac{\partial^2 u}{\partial y^2} + \frac{\partial^2 u}{\partial z^2} \right) + 2 \frac{\partial \mu}{\partial x} \frac{\partial u}{\partial x} \right. \\
 &\quad \left. + \frac{\partial \mu}{\partial y} \left(\frac{\partial u}{\partial y} + \frac{\partial v}{\partial x} \right) + \frac{\partial \mu}{\partial z} \left(\frac{\partial u}{\partial z} + \frac{\partial w}{\partial x} \right) \right] + \lambda(u_{ion} - u) \\
 F_y &= \frac{1}{\rho} \left[\mu \left(\frac{\partial^2 v}{\partial x^2} + \frac{\partial^2 v}{\partial y^2} + \frac{\partial^2 v}{\partial z^2} \right) + \frac{\partial \mu}{\partial x} \left(\frac{\partial v}{\partial x} + \frac{\partial u}{\partial y} \right) \right. \\
 &\quad \left. + 2 \frac{\partial \mu}{\partial y} \frac{\partial v}{\partial y} + \frac{\partial \mu}{\partial z} \left(\frac{\partial v}{\partial z} + \frac{\partial w}{\partial y} \right) \right] + \lambda(v_{ion} - v) \quad (4.2)
 \end{aligned}$$

where $\mu = AT \cdot 69$ is the coefficient of molecular viscosity for a gas consisting of N_2 , O_2 , and O (Banks and Kockarts, 1973); $A = \sum_n n_n A_n / \sum_n n_n$ where n_n is the neutral number density and A_n is the molecular viscosity constant appropriate for each species n ; T is the neutral temperature; $\lambda = n_i \mu_{in} \nu_{in} / \rho$ is the ion drag parameters; n_i , μ_{in} , and ν_{in} are the ion number density, the ion-neutral reduced particle mass, and the ion-neutral collision frequencies, taken here from Banks (1966b); and u_{ion} and v_{ion} are the eastward and northward ion velocities which can be written as (Salah and Holt, 1974)

$$\begin{aligned}
u_{ion} &= (u \sin D + v \cos D) \sin D \cos^2 I \\
&\quad - V_{D//} \sin D \cos I + u_{iE} \\
v_{ion} &= (u \sin D + v \cos D) \cos D \cos^2 I \\
&\quad - V_{D//} \cos D \cos I + v_{iE}
\end{aligned}
\tag{4.3}$$

where D is the declination angle of the magnetic field at Millstone Hill ($D = -14^\circ$), I is the inclination angle of the magnetic field ($I = 72^\circ$), $V_{D//}$ is the diffusion velocity parallel to the magnetic field, and u_{iE} and v_{iE} are the components of $\vec{E} \times \vec{B}/B^2$ in the eastward and northward directions. \vec{E} and \vec{B} are the electric and magnetic field strengths.

At mid-latitudes the pressure variation in the thermosphere is dominated by in-situ solar heating, giving rise to a diurnal circulation pattern. Because of this control, the temporal and the zonal length scales are assumed to be directly proportional to one another in the fashion $dx = dt \, 2\pi r \cos \phi / 24$ hours. This direct linkage of the x and t scales can give rise to stability problems in the solution when the east-west non-linear term is included in the equations of motion and the zonal velocity is sufficiently large. This problem is discussed in Chapter 7 and in Appendix D.

The momentum balance in the daytime thermosphere at 300 km (i.e., near the F region electron density peak) is between

the neutral pressure gradient and the ion drag forces. At night when the ion drag term is reduced in proportion to the electron density, terms of secondary importance such as the Coriolis, viscous, inertial, and curvature terms combine with the ion drag term to balance the pressure gradient. In general, the curvature and Coriolis terms are more important in the meridional momentum equation because the zonal velocity is usually two or three times larger than the meridional velocity. Above the electron density peak, the primary balance eventually becomes one between the viscous and pressure gradient forces, each of which contains the term $1/\rho$ and hence grows in height as the density decreases.

The major viscous force is provided by the $\frac{\mu}{\rho} \frac{\partial^2 \vec{v}}{\partial z^2}$ term, which dominates over the other viscous terms in the altitude region from 120 to about 500 km. In the part of this region below 300 km, the temperature increases exponentially, and the winds vary from being semi-diurnal (tidal) winds with magnitudes of about 50 m/sec at 115 km (Salah et al, 1975) to diurnal winds with magnitudes of the order of 100 m/sec for the meridional wind and 300 m/sec for the zonal wind at 300 km. Over this interval, the viscous term $1/\rho \partial\mu/\partial z \partial\vec{v}/\partial z$ can be of significance. At its maximum value, it represents about 10% of the pressure gradient at 200 km, and about 3% at 300 km. Its presence is therefore not critical, but since it is simple to compute, it was included in the equations. At higher altitudes, the horizontal viscous terms

$\mu/\rho (\partial^2 \vec{v}/\partial x^2 + \partial^2 \vec{v}/\partial y^2)$ grow faster than the vertical viscous term $\mu/\rho \partial^2 \vec{v}/\partial z^2$, and are of the same order of magnitude between about 500 and 600 km.

Neglecting the second order viscous terms and all the terms involving w , which is of the order of a few meters per second in the thermosphere, the equations in 4.1 reduce to

$$\begin{aligned} \frac{\partial u}{\partial t} + u \frac{\partial u}{\partial x} + v \frac{\partial u}{\partial y} - \frac{u v \tan \phi}{r} &= -\frac{1}{\rho} \frac{\partial p}{\partial x} + f v \\ &+ \frac{\mu}{\rho} \left(\frac{\partial^2 u}{\partial x^2} + \frac{\partial^2 u}{\partial y^2} + \frac{\partial^2 u}{\partial z^2} \right) + \frac{1}{\rho} \frac{\partial \mu}{\partial z} \frac{\partial u}{\partial z} + \lambda(u_{ion} - u) \end{aligned} \tag{4.4}$$

$$\begin{aligned} \frac{\partial v}{\partial t} + u \frac{\partial v}{\partial x} + v \frac{\partial v}{\partial y} + \frac{u^2 \tan \phi}{r} &= -\frac{1}{\rho} \frac{\partial p}{\partial y} - f u \\ &+ \frac{1}{\rho} \left[\mu \left(\frac{\partial^2 v}{\partial x^2} + \frac{\partial^2 v}{\partial y^2} + \frac{\partial^2 v}{\partial z^2} \right) + \frac{\partial \mu}{\partial z} \frac{\partial v}{\partial z} \right] + \lambda(v_{ion} - v) \end{aligned}$$

Table 4.1 lists the range of magnitudes of these terms found for September 7-8, 1971 at various altitudes.

In practice, the two horizontal viscous terms and the two non-linear terms are removed when solving the equations of motion in finite difference form in the altitude region from 120 to 600 km. The resulting momentum equations are written as

Table 4.1: Magnitudes of terms in the equations of motion 4.4 for September 7-8, 1971 at various altitudes. Units are in cm/sec².

Zonal Equation:

Term	200 km	300 km	400 km	500 km	600 km
$\frac{\partial u}{\partial t}$	-2.3 to 4.3	-3.2 to 5.8	-3.7 to 6.3	-3.9 to 6.4	-3.9 to 6.4
$-u \frac{\partial u}{\partial x}$	-2.1 to 1.7	-4.2 to 2.8	-5.0 to 3.5	-5.2 to 3.6	-5.2 to 3.6
$-v \frac{\partial u}{\partial y}$	-2.0 to .1	-4.4 to .4	-5.5 to .7	-5.7 to .7	-5.7 to .7
$\frac{uv \tan \phi}{r}$	-.3 to .8	-.1 to 2.1	-.2 to 2.5	-.2 to 2.6	-.2 to 2.6
$-\frac{1}{\rho} \frac{\partial p}{\partial x}$	-3.2 to 3.7	-8.3 to 9.4	-12.8 to 14.5	-16.9 to 19.2	-20.8 to 23.6
$f v$	-1.4 to .2	-2.9 to .9	-3.4 to 1.2	-3.5 to 1.2	-3.5 to 1.2
$\frac{\mu}{\rho} \frac{\partial^2 u}{\partial z^2}$	-1.6 to 1.0	-1.0 to 2.6	-7.3 to 7.4	-15.4 to 11.7	-21.8 to 16.7
$\frac{\mu}{\rho} \frac{\partial^2 u}{\partial x^2}$	-.0 to .0	-.0 to .0	-.2 to .1	-1.9 to .7	-13.3 to 3.4
$\frac{\mu}{\rho} \frac{\partial^2 u}{\partial y^2}$	-.0 to .0	-.0 to .0	-.1 to .1	-1.5 to 4.2	-17.0 to 8.5
$\frac{1}{\rho} \frac{\partial \mu}{\partial z} \frac{\partial u}{\partial z}$	-.2 to .1	-.1 to .1	-.0 to .0	-.0 to .0	-.0 to .0
$\lambda(u_{ion} - u)$	-1.0 to 2.0	-8.6 to 3.5	-7.0 to 2.0	-3.9 to 1.4	-2.3 to .9

Table 4.1 continued

Meridional Equation:

Term	200 km	300 km	400 km	500 km	600 km
$-\frac{\partial v}{\partial t}$	-1.7 to 1.3	-3.3 to 1.9	-3.8 to 2.1	-4.0 to 2.1	-4.0 to 2.1
$-u \frac{\partial v}{\partial x}$	-.5 to 1.2	-2.8 to 1.7	-3.6 to 2.0	-3.8 to 2.1	-3.8 to 2.1
$-v \frac{\partial v}{\partial y}$	-.6 to 1.2	-.2 to 1.3	-.1 to 1.3	-.1 to 1.3	-.1 to 1.3
$-\frac{u^2 \tan \phi}{r}$	-1.9 to -.0	-3.9 to -.0	-4.5 to -.0	-4.6 to -.0	-4.5 to -.0
$-\frac{1}{\rho} \frac{\partial p}{\partial y}$	-2.3 to 3.5	-5.8 to 9.0	-8.9 to 14.0	-11.8 to 18.5	-14.4 to 22.8
$-fu$	-3.2 to 3.5	-3.8 to 4.7	-4.1 to 4.9	-4.2 to 5.0	-4.2 to 5.0
$\frac{\mu}{\rho} \frac{\partial^2 v}{\partial z^2}$	-.1 to .4	-2.6 to 2.5	-6.9 to 5.6	-11.8 to 8.5	-16.7 to 11.1
$\frac{\mu}{\rho} \frac{\partial^2 v}{\partial x^2}$	-.0 to .0	-.0 to .0	-.1 to .2	-.7 to 1.2	-5.1 to 5.6
$\frac{\mu}{\rho} \frac{\partial^2 v}{\partial y^2}$	-.0 to .0	-.0 to .0	-.2 to .3	-1.3 to 1.7	-6.5 to 19.3
$\frac{1}{\rho} \frac{\partial \mu}{\partial z} \frac{\partial v}{\partial z}$	-.1 to .1	-.1 to .1	-.1 to .0	-.0 to .0	-.0 to .0
$\lambda(v_{ion} - v)$	-.6 to .7	-1.3 to 2.2	-.8 to 1.5	-.6 to 1.0	-.4 to .7

$$\begin{aligned}
0 &= -\frac{\partial u}{\partial t} + \frac{u v \tan \varphi}{r} - \frac{1}{\rho} \frac{\partial p}{\partial x} + f v \\
&\quad + \frac{1}{\rho} \left(\mu \frac{\partial^2 u}{\partial z^2} + \frac{\partial \mu}{\partial z} \frac{\partial u}{\partial z} \right) + \lambda (u_{\text{ion}} - u) \\
0 &= \frac{\partial v}{\partial t} - \frac{u^2 \tan \varphi}{r} - \frac{1}{\rho} \frac{\partial p}{\partial y} - f u \\
&\quad + \frac{1}{\rho} \left(\mu \frac{\partial^2 v}{\partial z^2} + \frac{\partial \mu}{\partial z} \frac{\partial v}{\partial z} \right) + \lambda (v_{\text{ion}} - v)
\end{aligned} \tag{4.5}$$

The neglected viscous terms are probably unimportant, but the non-linear terms are not. The two zonal derivatives were removed because of stability problems, and the two meridional gradients because they are approximations based on assumptions discussed in Section 5.5.1. The consequences of these approximations are discussed in Chapter 7. Chapter 7 also discusses the results of an attempt to include the non-linear terms in an approximate fashion.

4.2 Continuity Equation

The vertical velocity is derived from a continuity equation for the neutral air expanded in spherical coordinates in a manner similar to that of Amayenc et al (1975). The equation can be written as

$$\begin{aligned}
0 &= \frac{\partial \rho}{\partial t} + \nabla \cdot (\rho \vec{v}) = \frac{\partial \rho}{\partial t} + \frac{1}{r^2} \frac{\partial}{\partial r} (r^2 \rho w) \\
&\quad + \frac{1}{r \sin \theta} \frac{\partial (\rho (-v) \sin \theta)}{\partial \theta} + \frac{1}{r \sin \theta} \frac{\partial (\rho u)}{\partial \lambda}
\end{aligned}$$

$$\begin{aligned}
&= \frac{\partial \rho}{\partial t} + \frac{\partial(\rho w)}{\partial z} + \frac{2\rho w}{r} + \frac{\partial(\rho v)}{\partial y} - \frac{\rho v \tan \varphi}{r} \\
&\quad + \frac{\partial(\rho u)}{\partial x}
\end{aligned}
\tag{4.6}$$

where r is the distance from the center of the earth, θ is the co-latitude, and λ is the longitude. The term $2\rho w/r$ is neglected since w is small compared to $v \tan \varphi$.

To find the vertical velocity at some height z , this equation is integrated over z from z to infinity (where ρ goes to zero).

$$w(z) = \frac{1}{\rho(z)} \int_z^\infty \left[\frac{\partial \rho}{\partial t} + \left(\frac{\partial(\rho u)}{\partial x} + \frac{\partial(\rho v)}{\partial y} \right) - \frac{\rho v \tan \varphi}{r} \right] dz
\tag{4.7}$$

The first term can be approximated using the hydrostatic equation and neglecting the variation of gravity with height as

$$\begin{aligned}
\frac{1}{\rho(z)} \int_z^\infty \frac{\partial \rho}{\partial t} dz &\approx \frac{1}{\rho(z)} \left(\frac{-1}{g} \right) \int_z^\infty \frac{\partial}{\partial z} \frac{\partial p}{\partial t} dz \\
&= \frac{1}{\rho(z)g} \frac{\partial p(z)}{\partial t}
\end{aligned}
\tag{4.8}$$

The vertical velocity is then seen to be composed of two major parts: that due to the rise and fall of the pressure surfaces throughout the day, and a second part due to the divergence of the horizontal wind.

The last term, which is a result of the convergence of the meridians, is smaller than the others, but can be significant in the mean since the average meridional wind is usually non-zero.

One of the terms in the Eq. 4.7 refers to the north-south gradient of the meridional wind. The computation of this term requires solving the momentum equations at another latitude. Certain assumptions must be made about the latitudinal gradients of the ionospheric data (particularly the electron density) and of the meridional pressure gradient. These assumptions will be discussed in section 5.5.1 and a general error analysis of the continuity equation will be performed in Chapter 7. The continuity equation was used to solve for w as opposed to the thermodynamic (or energy equation because auroral heating is known to be important, but is very difficult to estimate (Straus et al, 1975)). In addition, there are questions about the size of the EUV heat source (Roble and Dickinson, 1973). The energy balance will not be discussed further in this work. The next chapter will discuss the method used to solve the momentum and continuity equations.

5. DATA ANALYSIS

Figures 5.1a and b are flow charts of the two data analysis processes followed to find the neutral velocities above Millstone Hill. In the first of these, Millstone Hill data was used to the fullest extent possible to define all the parameters and in the second, only the ionospheric data gathered at Millstone Hill was used. The remainder of the inputs for the second case were taken from the MSIS neutral atmospheric model. What follows is a description of the processes shown schematically in the flow charts to derive the wind velocity over Millstone Hill.

5.1 The Millstone Hill Model

A two-dimensional model of the neutral thermosphere was created to solve the horizontal equations of motion (Eq. 4.5) above Millstone Hill using as input the data described in Chapters 2 and 3. The model describes the atmosphere between 120 and 600 km, and interchanges time and longitude in derivative calculations, i.e., it assumes that the earth rotates under a fixed pattern of pressure variation. As will be made clear later, there are 3 unknowns in the 2 horizontal momentum equations of 4.5. These are the horizontal velocities u and v , and the meridional pressure gradient $\partial p / \partial y$. The east-west pressure variation $\partial p / \partial x$ is assumed to be given by the variation with time of the observed exospheric temperature $\partial T_{\infty} / \partial t$. The radar data also provides values of the horizontal neutral wind

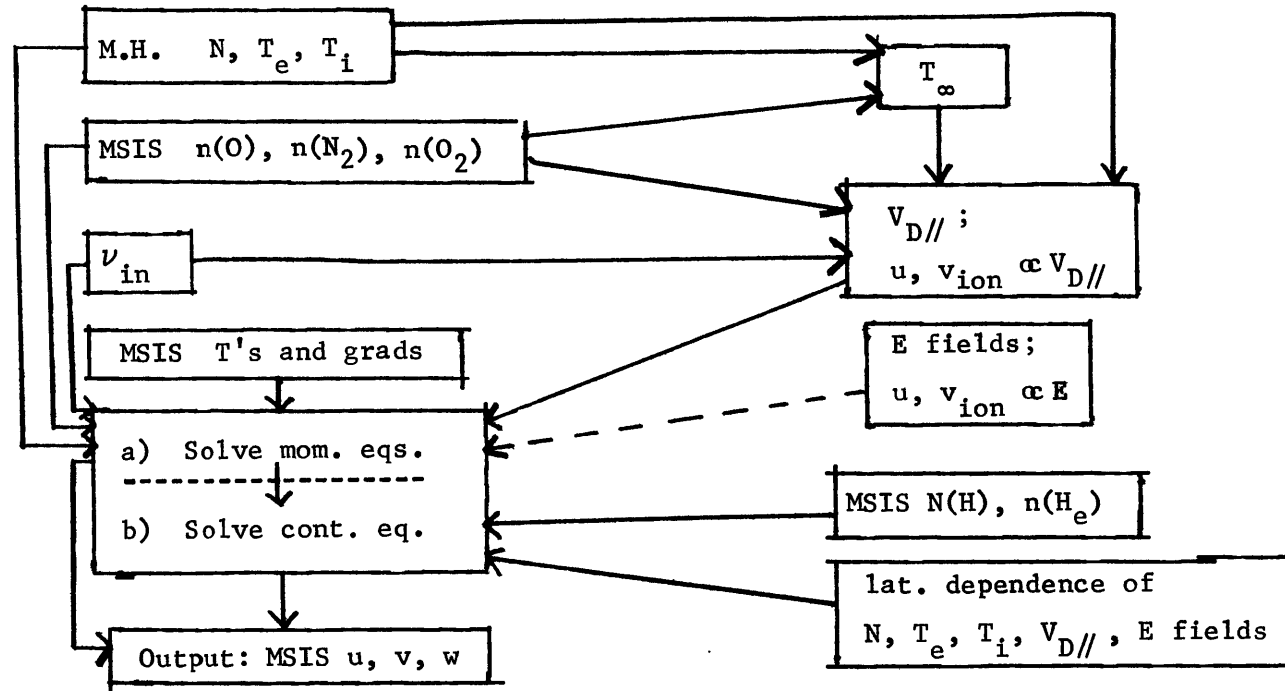


Figure 5.1b: Flow diagram of data processing for the MSIS model case.

wind parallel to the magnetic field V_{Hn} (given by Eq. 3.8) so that a third equation

$$v = (V_{Hn} - u \sin D) / \cos D \quad (\text{at } 300 \text{ km}) \quad (5.1)$$

can be added to the set giving 3 equations and 3 unknowns. This set is solved simultaneously for u , v , and the north-south pressure gradient (or more accurately, the north-south exospheric temperature gradient). The meridional exospheric temperature gradient is then harmonically analyzed.

Using the harmonic analysis, the horizontal momentum equations are solved again for two latitudes: 42.6° N (Millstone Hill latitude) and 42.8° N, which is about 23.2 km to the north of Millstone Hill. Calculations at the higher latitude are made first and require assumptions to be made about the latitudinal dependence of ionospheric data and the pressure gradients. These assumptions will be discussed in more detail in Section 5.5.1. Values of the meridional velocity v at this higher latitude are stored and are used with the meridional wind calculated at the Millstone Hill latitude to compute $\partial v / \partial y$, for use in the continuity equation. When calculating w , it is also necessary to extend the top boundary to infinity, or more practically, to 1500 km. In this situation, the atmospheric composition calculations have to be extended to include helium He and atomic hydrogen H in order to calculate w . The values for these lighter constituents and their gradients at the bottom boundary of 120 km are taken from the OGO-6 model. Since, however, these results

are required only for the purpose of solving the continuity equation and determining the vertical velocity they do not influence the estimates derived for the horizontal winds.

5.2 Neutral Temperature and Density

The neutral temperature and number densities are written in the Bates (1959) - Walker (1965) analytical forms

$$\begin{aligned} T(z) &= T_{\infty} - (T_{\infty} - T_{120}) \exp \left[-s(z-120) \right] \\ &\cong T_{\infty} - (T_{\infty} - T_{120}) \exp(-\sigma \xi) \end{aligned} \quad (5.2)$$

$$n_j(z) = n_{j120} \left[T_{120}/T(z) \right]^{1+\alpha_j+\gamma_j} \exp(-\sigma \gamma_j \xi) \quad (5.3)$$

while the pressure is given in terms of the gas law

$$p = kT \sum_{j=1}^{3 \text{ or } 5} n_j = \rho RT/\bar{M} \quad (5.4)$$

Here p is pressure, k is Boltzmann's constant, T is the neutral temperature, T_{120} the temperature at 120 km (355°K), s the shape factor (0.020 km⁻¹), $\sigma = s + 1/(R_E + 120)$, R_E the Earth radius, $\xi = (z-120)(R_E + 120)/(R_E + z)$ the geopotential height, ρ the density of the neutral gas, n_j the number density in cm⁻³ of species j , n_{j120} the number density at 120 km (assumed constant for N₂ and O₂), $\gamma_j = M_j g_{120}/\sigma RT_{\infty}$, M_j the molecular weight of species j , \bar{M} the average molecular weight of the neutral gas, R = universal gas

constant, and α_j the thermal diffusion factor. The thermal diffusion factors of O, N₂, and O₂ for a mixture consisting chiefly of O were assumed to be zero. The thermal diffusion factors for He and H were taken to be -0.4. The form for the neutral density Eq. 5.3 can be derived from the form for the neutral temperature Eq. 5.2, the gas law Eq. 5.4, and the hydrostatic approximation

$$d p/d z = - \rho g \quad (5.5)$$

(See, for example, the derivation in Stein and Walker (1965)). Including thermal diffusion effectively adds the term α_j in Eq. 5.3 (Walker, 1965).

Equations 5.2 and 5.3 assume that the temperature and density vary in phase. This is not actually true. Above about 200 km, the maximum in the density of the neutral particles, (chiefly atomic oxygen), has been found to precede the maximum in temperature by about 0.7 hours (Reber et al, 1973). Mayr and Volland (1973) suggest that this phase difference is a result of diffusion effects. For the sake of simplicity, any phase difference is ignored in the present model.

With the temperature, number density, and pressure written in the forms of equations 5.2, 5.3, and 5.4 their horizontal derivatives can be expressed as

$$\begin{aligned}
d T_{\text{horiz}} = & \left[1 - \exp(-\sigma \xi) \right] d T_{\infty \text{horiz}} + \exp(-\sigma \xi) d T_{120 \text{horiz}} \\
& + \xi (T_{\infty} - T_{120}) \exp(-\sigma \xi) d \sigma_{\text{horiz}}
\end{aligned} \tag{5.6}$$

$$\begin{aligned}
d n_{j \text{horiz}} = & n_j \left\{ -\gamma_j \xi d \sigma_{\text{horiz}} + \left[\ln(T_{120}/T) - \sigma \xi \right] d \gamma_j \text{horiz} \right. \\
& + (1 + \gamma_j + \alpha_j) (d T_{120 \text{horiz}}/T_{120} - d T_{\text{horiz}}/T) \\
& \left. + d n_{j 120 \text{horiz}}/n_{j 120} \right\}
\end{aligned} \tag{5.7}$$

$$d p_{\text{horiz}} = k \left(\sum_{j=1}^{3 \text{ or } 5} n_j \right) d T_{\text{horiz}} + k T \sum_{j=1}^{3 \text{ or } 5} d n_{j \text{horiz}} \tag{5.8}$$

where

$$d \gamma_j \text{horiz} = -\gamma_j (d T_{\infty \text{horiz}}/T_{\infty} + d \sigma_{\text{horiz}}/\sigma) \tag{5.9}$$

Since σ , T_{120} , and $n_{j 120}$ for N_2 and O_2 (and H when calculating w) are assumed to be constant, the unknown gradients reduce to $d T_{\infty \text{horiz}}$ and $d n(O)_{\text{horiz}}$. The east-west variation of the exospheric temperature is proportional to the diurnal variation of the input T_{∞} data described in Section 3.1, and the east-west variation of $n(O)_{120}$ is assumed to be zero. The north-south variation of $n(O)_{120}$ and T_{∞} cannot be separated, so an "effective" meridional exospheric temperature gradient is calculated as will be described in Section 5.4, and the north-south density gradient for atomic oxygen at 120 is set

to zero. This "effective" meridional exospheric temperature gradient is equal to the sum of the effects of the north-south variations of T_{∞} and $n(0)_{120}$ at 200 km. The consequences of using this one gradient in place of two will be discussed in Chapter 7. Variations of He at the bottom boundary are taken from the OGO-6 model for the vertical velocity calculation.

5.3 Exospheric Temperature Structure

It is assumed that the latitudinal and longitudinal variations in the exospheric temperature can be represented by a truncated Fourier-Taylor series of the form (Roble et al, 1974)

$$\begin{aligned}
 T_{\infty}(\varphi, t) &= \sum_{n=0}^{n \text{ harm}} \left[(a_n + \partial a_n / \partial \varphi (\varphi - \varphi_{\text{MH}})) \cos \frac{n\pi}{12} t \right. \\
 &\quad \left. + (b_n + \partial b_n / \partial \varphi (\varphi - \varphi_{\text{MH}})) \sin \frac{n\pi}{12} t \right] \quad (5.10) \\
 &= \sum_{n=0}^{n \text{ harm}} \left[c_n \cos \frac{n\pi}{12} (t - t_n) + (\varphi - \varphi_{\text{MH}}) d_n \cos \frac{n\pi}{12} (t - s_n) \right]
 \end{aligned}$$

where $n \text{ harm}$ is the number of harmonics searched for (usually 3), φ_{MH} is the latitude of Millstone Hill (42.6°N), t is the time in hours, c_n and t_n are the amplitude and phase of the harmonics describing the diurnal or east-west variation of T_{∞} , and d_n and s_n are the amplitude and phase of the harmonics describing the variation of the north-south derivative of T_{∞} . The zero harmonic refers to the average temperature or meridional temperature gradient

of the day under study, and the first, second, third, etc. harmonics refer to the diurnal, semi-diurnal, terdiurnal, etc. terms. The east-west coefficients c_n and t_n are found from a harmonic analysis of the observed T_∞ input data. The north-south coefficients d_n and s_n are found from a harmonic analysis of the north-south "effective" exospheric temperature gradient derived during the solution to the horizontal momentum equations and described in the following section.

5.4 Derivation of the Meridional Pressure Gradient Term

The finite difference form of the zonal momentum equation (4.5) can be written as

$$\begin{aligned}
0 = & \frac{-u_i^{n+1} + u_i^n}{\Delta t} + \frac{v_j^{n+\frac{1}{2}} \tan \phi}{r} \left(\lambda_1 u_j^{n+1} + \lambda_2 u_j^{n+1} \right) - \left(\frac{1}{\rho} \frac{\partial p}{\partial x} \right)^{n+\frac{1}{2}} \\
& + f v_j^{n+\frac{1}{2}} + \left(\frac{\mu}{\rho} \right)^{n+\frac{1}{2}} \frac{1}{(\Delta z)^2} \left[\lambda_1 \left(u_{j+1}^{n+1} + u_{j-1}^{n+1} - 2u_j^{n+1} \right) \right. \\
& \left. + \lambda_2 \left(u_{j+1}^n + u_{j-1}^n - 2u_j^n \right) \right] + \left(\frac{1}{\rho} \frac{\partial \mu}{\partial z} \right)_j^{n+\frac{1}{2}} \frac{1}{\Delta z} \left[\lambda_1 \left(u_{j+1}^{n+1} - u_{j-1}^{n+1} \right) \right. \\
& \left. + \lambda_2 \left(u_{j+1}^n - u_{j-1}^n \right) \right] + \lambda_j^{n+\frac{1}{2}} \left[- \left(v_{D//} \right)_j^{n+\frac{1}{2}} \sin D \cos I + (u_{iE})_j^{n+\frac{1}{2}} \right. \\
& \left. + v_j^{n+\frac{1}{2}} \cos D \sin D \cos^2 I + (\sin^2 D \cos^2 I - 1) * \right. \\
& \left. \left(\lambda_1 u_j^{n+1} + \lambda_2 u_j^n \right) \right] \tag{5.11}
\end{aligned}$$

where Δt is the time step (20 min ordinarily or 5 min around sunrise) Δz is the height step (10 km), λ_1 and λ_2 are positive constants whose sum is one, and n and j refer to the particular time and height step. $v(\text{est})_j^{n+1/2}$ is a linear extrapolation of v_j^n and v_j^{n-1} , i.e.

$$v(\text{est})_j^{n+1/2} = v_j^n + 1/2 (v_j^n - v_j^{n-1}) \quad (5.12)$$

Equation 5.11 can be condensed to the form

$$(\vec{I}/\Delta t - \lambda_1 \vec{C}) \vec{v}^{n+1} = (\vec{I}/\Delta t + \lambda_2 \vec{C}) \vec{v}^n + \vec{F} \quad (5.13)$$

where \vec{I} is the identity matrix; \vec{v}^n is the horizontal velocity vector u at time step number n , \vec{C} is a tridiagonal matrix whose sub-diagonal, diagonal, and super-diagonal terms multiply velocities \vec{v}^n and \vec{v}^{n+1} at the height steps of $j-1$, j , and $j+1$ respectively; and \vec{F} is a vector containing everything else.

The finite difference form for the meridional momentum equation is similar to equation 5.11 and can be condensed to the form of equation 5.13 with \vec{V}^n standing for the meridional velocity and \vec{C} and \vec{F} changed.

The boundary conditions imposed are zero velocity at 120 km and constant velocity (or zero height gradient) at 600 km. The conditions at the bottom boundary are not critically important since the exponential increase of temperature above this boundary serves to insulate the higher altitudes from the conditions at the

boundary (Rishbeth, 1972b). The top boundary condition of constant velocity is necessary to stop the growth of the viscous term in the equations of motion 4.5 and seems physically reasonable. The velocities are initially set to be zero, and then integrated over a 24 hour period. The results obtained are then adopted as initial conditions and averages are computed over a second 24 hour period. Since calculations are made over a total of 48 hours, there must be continuity between the first and second 24 hour period. For geomagnetically quiet days this can be enforced by assuming that the diurnal variation of the sun dominates and that all quantities are the same at the beginning and end of a 24 hour period. This assumption may require the blending of the experimental data together at the endpoints of a 24 hour observing period. This is usually done over a period of one hour. For days where the observations last less than 24 hours, extrapolations are made beyond the limits of the data, and these extrapolations are blended over a one hour period.

This procedure would not be proper for geomagnetically disturbed days when the heat input at the auroral zones is considerable. Geomagnetic disturbances have time scales of the order of hours, and can introduce considerable differences in the electron density and exospheric temperature observed at times separated by 24 hours. Here a possible solution would be to force the results at the end of the first 24 hour period to be the same as observed at the beginning of the period. Then, over the second 24 hour period, allow the results to match the data as it is, extrapolating at the ends

if necessary to complete a full 24 hours. At least two more terms would then have to be added to describe the exospheric temperature (Eq. 5.10). These would define the linear dependence of the temperature on time and its north-south derivative. More terms may be added to represent the non-cyclic behavior in a more complicated manner. No such procedure was adopted here because the present study confined itself to geomagnetically quiet days. For quiet days, the differences at the beginning and end of a 24-hour observation period were usually less than 50°K in exospheric temperature and were less than 30% for electron densities.

Each horizontal equation of motion is solved separately using the Crank-Nicholson iteration scheme where $\lambda_1 = \lambda_2 = \frac{1}{2}$. This method is considered to be more stable than the explicit method ($\lambda_1 = 0, \lambda_2 = 1$), or the fully implicit method ($\lambda_1 = 1, \lambda_2 = 0$) (e.g., Dahlquist and Björck, 1974). The zonal momentum equation is solved first. Here the unknown is \vec{V}^{n+1} , where this refers to the zonal velocity. \vec{F} is known, since the east-west pressure gradient has already been determined from the time variation of the exospheric temperature which was obtained from the measurements. The meridional momentum equation cannot be solved for immediately since there are two unknowns-- \vec{V}^{n+1} , where this refers to the meridional velocity v , and the north-south pressure gradient contained in the vector \vec{F} . This difficulty can be handled by appeal to Eq. 3.8, which gives the horizontal part of the neutral wind parallel to the magnetic field (mostly the meridional component)

in terms of the measured vertical ion drift, the calculated diffusion velocity, and the electric field-induced drifts. Since the diffusion velocity calculation is most certain around the electron density peak, this equation is evaluated at 300 km. The electric field-induced drifts are usually taken to be zero as explained in Section 3.4. The consequences of this assumption will be examined later in Chapter 7. It then follows that v^{n+1} at 300 km can be determined from the value of V_{Hn} at the time $n+1$ and the height of 300 km, and from the value of $u^{n+1}(300 \text{ km})$ just determined from the solution of the zonal momentum equation.

Since only one altitude is known, use is made of the explicit form ($\lambda_1 = 0, \lambda_2 = 1$) of solving the finite difference equation in order to determine the north-south gradient at 300 km. Since the form of the equations adopted to describe the temperature and density (Eqs. 5.2 and 5.3) determine their height variation, a value of the pressure gradient at a single height is sufficient to specify a north-south "effective" exospheric temperature gradient. As explained in Section 5.2, the meridional pressure gradient can be expressed entirely in terms of the meridional exospheric temperature gradient and the meridional gradient of the bottom boundary number density for atomic oxygen. Since the incoherent scatter radar results do not provide any information on the north-south variation of atomic oxygen at 120 km this has been assumed to be zero. Thus an "effective" north-south exospheric temperature gradient is obtained which includes the effects of temperature and

composition variations with latitude. These two gradients cannot be separated and solved for separately, and since it was considered desirable to appeal to only incoherent scatter data for this study (in order to be able test models based chiefly on satellite data) it was decided to resort to the use of the "effective" meridional exospheric temperature gradient.

This approximation introduces a source of uncertainty into the calculations since the effect of the component of the meridional pressure gradient attributable to the variation in density on the lower boundary decreases with altitude. The consequences of this will be examined later in Chapter 7. Using the "effective" north-south exospheric temperature gradient, it is now possible to calculate the meridional pressure gradient at all altitudes, and so the meridional momentum equation can then be solved by the Crank-Nicholson finite difference scheme to derive meridional velocities at the time $n+1$.

If the derived meridional velocity at 300 km is different by more than 1 m/sec from the value estimated from Eq. 5.1, then the north-south pressure gradient at 300 km is changed by a small amount, leading to a change in the "effective" exospheric meridional temperature gradient, and consequently in the pressure gradients at all other altitudes. This procedure is repeated in an iterative fashion until the two meridional velocities are within 1 m/sec of each other. It is found that it is usually not necessary to enter this iterative process, except at the beginning of the initial value problem. It

is also the author's experience that the results will not diverge unless there are instability problems. A further discussion of stability criterion and the inclusion of the non-linear terms is contained in Chapter 7.

The horizontal velocities are found at the n and $n + 1$ times, while everything else, the pressure gradients, the input data, etc., are found at the times $n + \frac{1}{2}$. For convenience, however, we do not distinguish between the $n + \frac{1}{2}$ and $n + 1$ times. The previous paragraphs have described how u^{n+1} , v^{n+1} , and the meridional pressure gradient are found from u^n , v^n , $V_{Hn}^{n+\frac{1}{2}}$ at 300 km, and the input data. This procedure is repeated throughout a 48 hour period.

5.5 Final Velocity Calculations

After the meridional "effective" exospheric temperature gradient has been determined over a 24 hour period, it is harmonically analyzed in order to find the amplitudes d_n and phases s_n of equation 5.10. At this point, the equations of motion are again solved for a latitude 0.2° to the north of Millstone Hill in addition to repeating the solution at Millstone Hill with the smoothed temperature gradient. The procedure is the same as that described in Section 5.4, except that the step of determining the meridional pressure gradient is eliminated. The values of the meridional velocity v at the latitude $\varphi_{MH} + 0.2$ are stored and used with the value of v at the Millstone Hill latitude of φ_{MH} to calculate the meridional gradient of the

meridional velocity $\partial v / \partial y$ for the determination of w from the continuity equation. The assumptions that were made about the input parameters at the latitude of $\phi_{MH} + .2$ are described in the next section.

5.5.1 Assumptions about Latitudinal Variations

Electron and ion temperatures, the plasma diffusion velocity $V_{D//}$ and electric field-induced drifts (if present) were assumed to be the same at $42.8^{\circ}N$ and $42.6^{\circ}N$. This same assumption was made for the derived values of $\partial T_{\infty} / \partial \phi$. The latitudinal variation of T_{∞} and $\partial T_{\infty} / \partial t$ is set by the form of Eq. 5.10. The electron density variations were treated more carefully and were generally not assumed to be latitudinally constant.

The electron density generally decreases towards the poles at geomagnetic mid-latitudes. Two data sources were employed to estimate the size of the decrease. The first source was ionosonde records of f_oF2 frequencies which were plotted at Millstone Hill from ionosondes located at Ottawa ($45.4^{\circ}N, 75.7^{\circ}W$) and Millstone Hill ($42.6^{\circ}N, 71.5^{\circ}W$). The f_oF2 frequency defines the electron density peak, N_{max} and is written in Eq. 2.10. Values for f_oF2 vary between about 2 and 8MHz between night and day, and the Ottawa frequencies are usually about $\frac{1}{4}$ to $\frac{1}{2}$ MHz below the Millstone Hill frequencies. This translates into about a 1% decrease in N_{max} in 0.2° of latitude. The Ottawa f_oF2 values are not always less than the Millstone Hill values. Particularly on summer nights and winter days, the f_oF2 values are nearly the same as those at Millstone Hill, with Ottawa occasionally larger.

Similar conclusions were reached from the second data source of topside ionosphere soundings taken by the Allouette satellites. Global electron density maps from this source have been reported by many researchers (see, for example, Wu (1969)). The geomagnetic latitude of Millstone Hill is about 56° N and there is a general decrease of electron density towards the pole at this latitude which nearly disappears on some summer nights and winter days. The gradient also depends on geomagnetic activity. The average decrease appeared to be about 4% in 1° of latitude or 0.8% in 0.2° , and this constant decrease was included in the calculations at 42.8° N. A few calculations were made assuming the electron density was latitudinally constant in order to compare the solutions and see what changes occurred for reasonable latitude variations of electron density.

5.5.2 Averages

The 24-hour averages of a number of separate quantities were calculated and their diurnal variations plotted. These quantities include terms in the momentum equations, continuity equation, and the input data. The seasonal variations of some of these averages over the two-year span of data from December 1969 to December 1971 were examined in great detail. In particular a seasonal variation in the mean meridional velocity was sought since this would define the inter-hemispheric transport of light minor constituents.

In addition to determining neutral wind velocities that are consistent with the ionospheric data, temperatures, densities, and

pressure gradients observed above Millstone Hill, the foregoing model is also capable of determining velocities that match the pressure gradients contained in various neutral models when the ion drag is fixed by the density data gathered at Millstone Hill. Some cases of this type of calculation were undertaken for comparative purposes. In particular, the results using the MSIS model pressure gradients were found for every day that was analyzed. The analysis procedure is outlined in Figure 5.1b. The computer programs that were used in this study and descriptions of them are available through the Meteorology Department at MIT.

The results obtained from the analyses outlined above are presented and discussed in the next two chapters. As has been indicated, uncertainties are introduced both by inaccuracies in the radar data and by lack of knowledge concerning some of the parameters needed in the analysis (e.g. the electric fields and the variation of composition and electron density with latitude). A discussion of the affect of these uncertainties on our conclusions is undertaken in Chapter 7.

6. REPRESENTATIVE RESULTS

The procedures described in the previous chapters were followed in analyzing two years of ionospheric data collected at Millstone Hill. Some typical results are discussed in detail in this chapter and these are compared with results obtained using the atmospheric models of MSIS, OGO-6, and Jacchia 1971.

We begin by discussing a single summer day, June 23-24, 1970, and subsequently discuss a winter day January 20-21, 1971.

6.1 Representative Summer Day

June 23-24, 1970 was one of a few days that were analyzed extensively. The contours of constant electron density vs height and time measured on this day are plotted at intervals of \log_{10} in Figure 6.1. The maximum electron densities occurred in the morning around 0930 LT at 9.3×10^5 electrons/cm³ with a secondary peak about 1730 LT around 4 hours before sunset. The post-sunrise increase in electron density was not as abrupt as seen on most days.

The exospheric temperature deduced for June 23-24, 1970, and its representation by a mean and the first three harmonics is plotted in Figure 6.2. The sunrise increase in exospheric temperature is not as rapid as it usually found for summer months. On many summer days the exospheric temperature exhibits an almost square wave appearance with abrupt increases and decreases around sunrise and sunset, while on winter days, the exospheric temperature

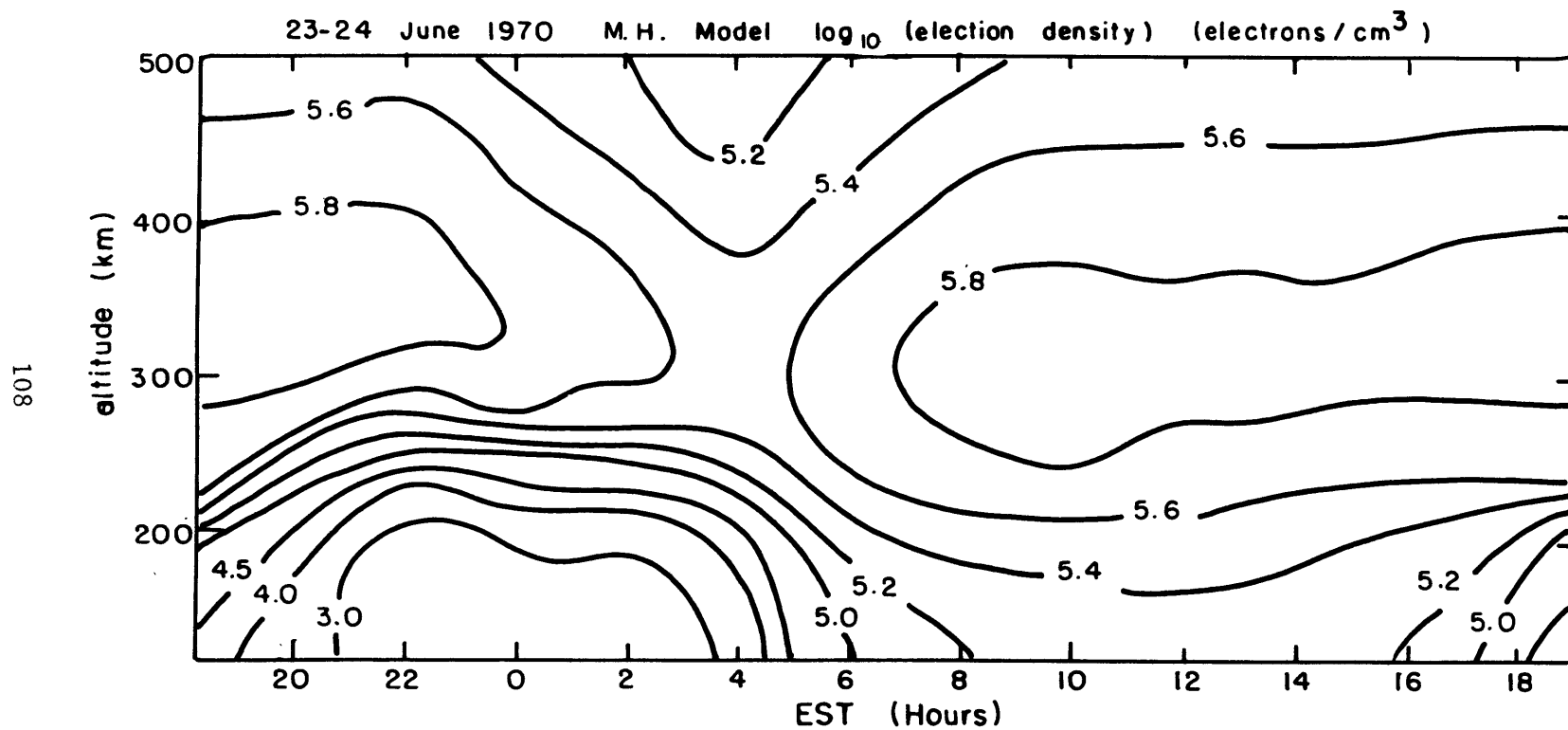


Fig. 6.1: Smoothed electron densities in intervals of \log_{10} measured above Millstone Hill on June 23-24, 1970.

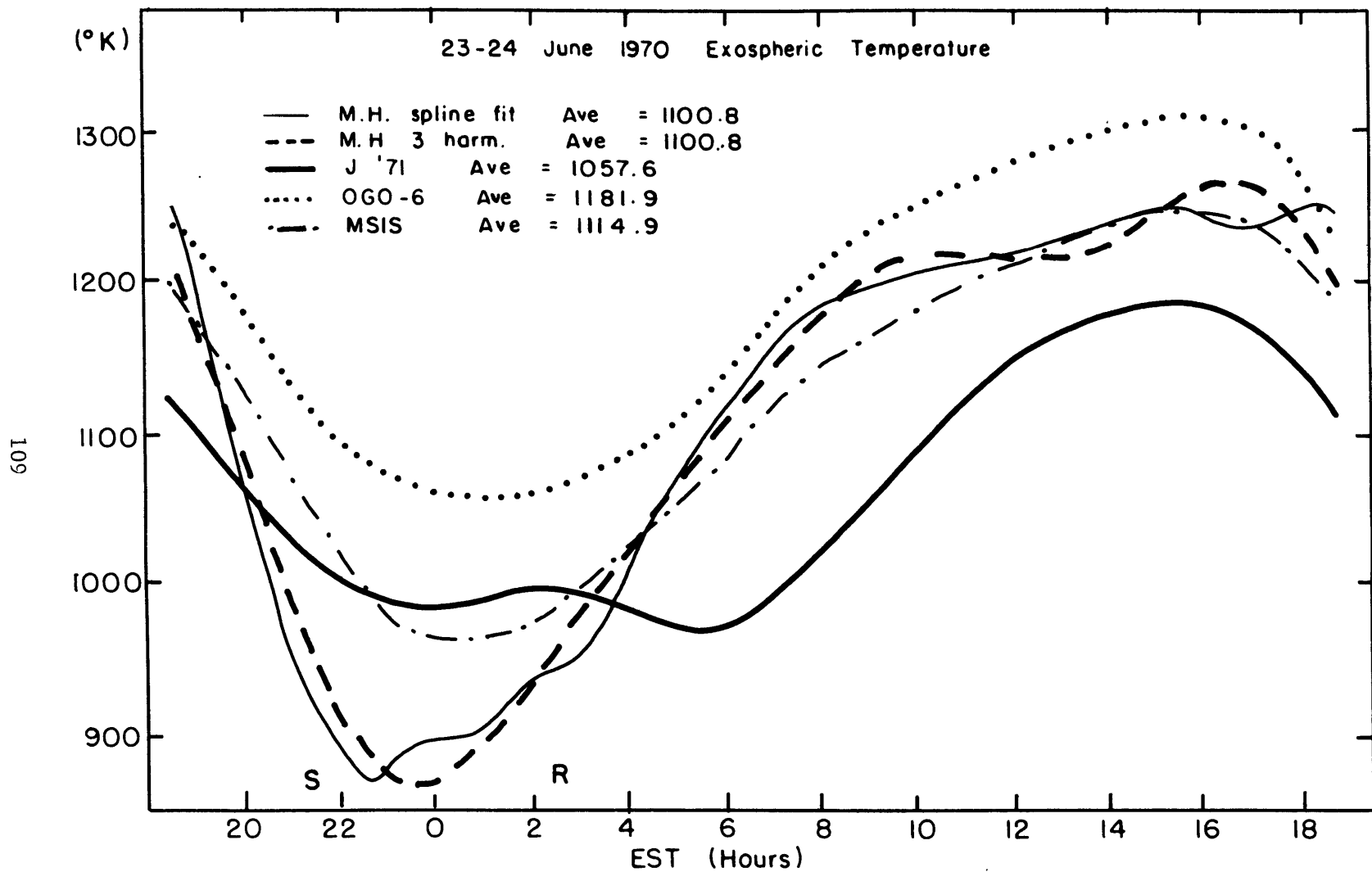


Fig. 6.2: Spline fit to the exospheric temperature above Millstone Hill for June 23-24, 1970. Also included is its representation in 3 harmonics and the exospheric temperatures deduced by the Jacchia 1971, OGO-6, and MSIS models. R and S are sunrise and sunset at 250 km.

looks more like a sine wave. Also plotted in Figure 6.2 is the exospheric temperature predicted by the Jacchia 1971, OGO-6, and MSIS models for the solar conditions found on this day. The results of these other models will be discussed later in Section 6.1.3. The average exospheric temperature above Millstone Hill on June 23-24, 1970 is 1092°K with a day-night difference of about 400°K . The neutral temperature is shown in Figure 6.3 as a function of time and height.

The diurnal variation of the zonal (time) derivative of the exospheric temperature is plotted in Figure 6.4. The Millstone Hill derivative is almost twice the derivatives of the three other models around sunset and sunrise. Since the time (zonal) derivative of the temperature largely controls the size of the zonal pressure gradient, these large zonal gradients produce large zonal winds. For the meridional momentum equation the major balance is achieved between the Coriolis and ion drag forces and the derived pressure gradient forces.

The "effective" meridional derivative of the exospheric temperature was derived by requiring that the calculated value of the horizontal neutral wind speed in the magnetic meridional plane (V_{Hn}) at 300 km be within 1 m/sec of the value deduced from the ionospheric data when the neutral number density was set by the MSIS model. The diurnal variations of the first three harmonics of the derived meridional exospheric temperature gradient are plotted in Figure 6.5. The values of V_{Hn} that were calculated at 300 km using

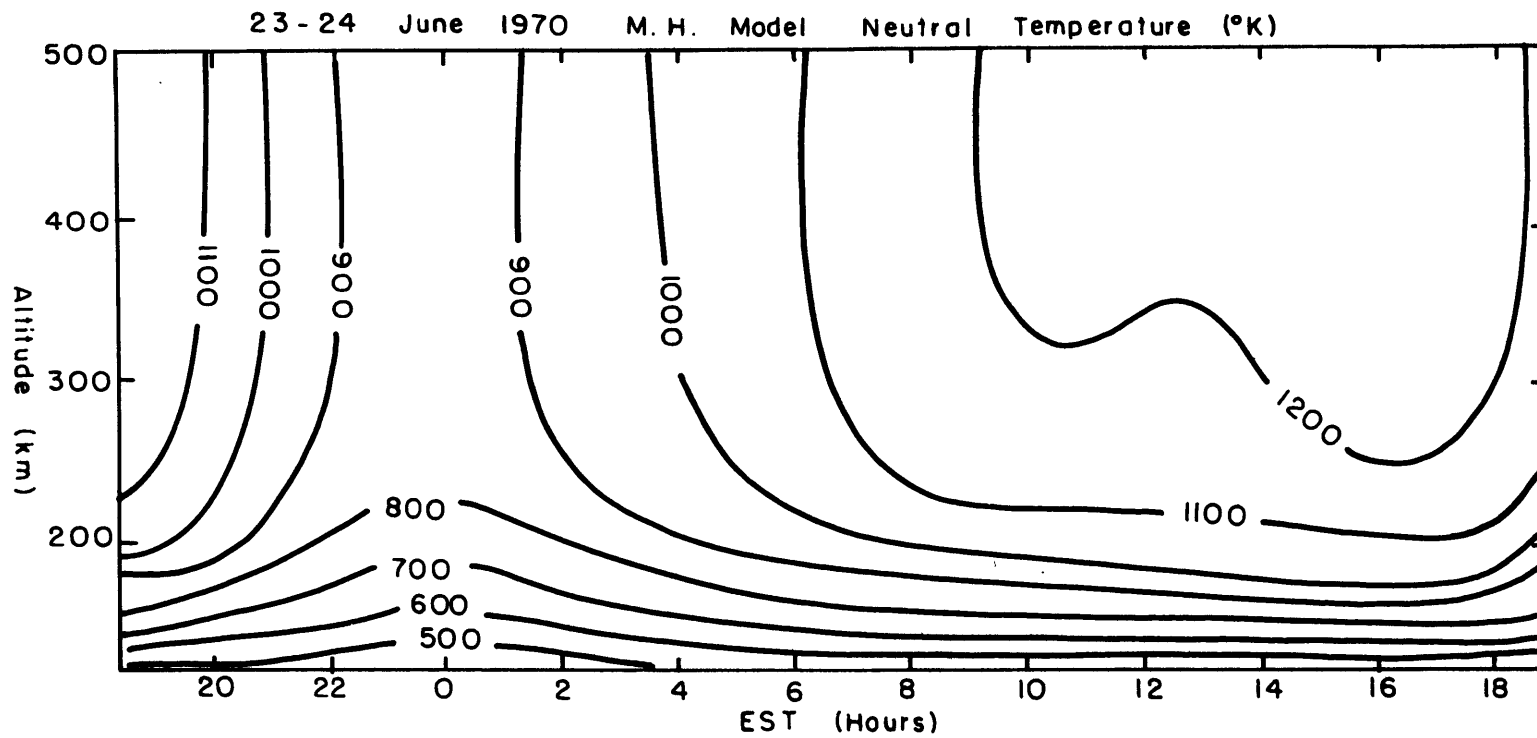


Fig. 6.3: Neutral temperature above Millstone Hill on June 23-24, 1970.

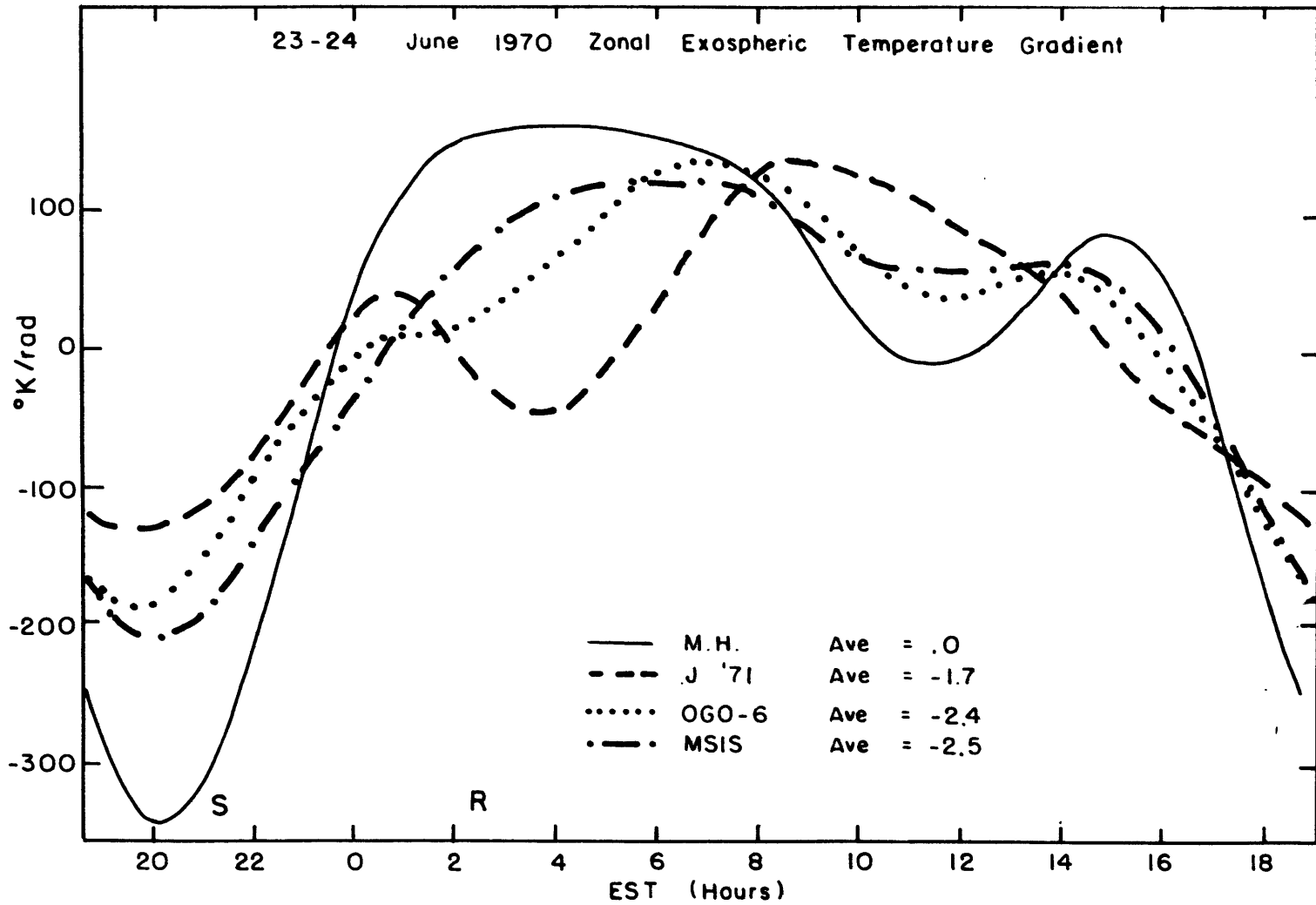


Fig. 6.4: Zonal exospheric temperature gradient above Millstone Hill on June 23-24, 1970. Also plotted are gradients from the Jacchia 1971, OGO-6, and MSIS models.

this smoothed gradient are compared in Figure 6.6 with the experimental estimates. The velocity averages 40 m/sec towards the magnetic south and ranges from 135 m/sec southward around 2300 LT to 35 m/sec northward around 1000 LT. The root mean square deviation between the observed and calculated values is 14.5 m/sec.

The north-south exospheric temperature gradient for Millstone Hill (Figure 6.5) varied over $465^{\circ}\text{K}/\text{rad}$. The average value was $12^{\circ}\text{K}/\text{rad}$, increasing temperature towards the pole, which is as expected for days exhibiting mean equatorwards winds. Decreasing polewards temperatures were deduced during the night, which is opposite to the predictions of the Jacchia, OGO-6, and MSIS atmospheric models. The large zonal winds, created in response to the large zonal pressure (temperature) gradients, introduce large Coriolis effects in the meridional equation of motion. The Coriolis force causes the meridional pressure (temperature) gradient, which is a free parameter, to mimic the diurnal variation of the zonal pressure gradient.

6.1.1 The Equations of Motion

The equations of motion were discussed in Section 4.1 and Table 4.1 listed the variations in the terms of Eq. 4.4 found for September 7-8, 1971 at several altitudes. The magnitudes of the terms were somewhat smaller for June 23-24, 1970. Figures 6.7a and b plot the diurnal variations at 300 km on June 23-24, 1970 of each of the terms in the final momentum Eq. 4.5 as well as the calculated

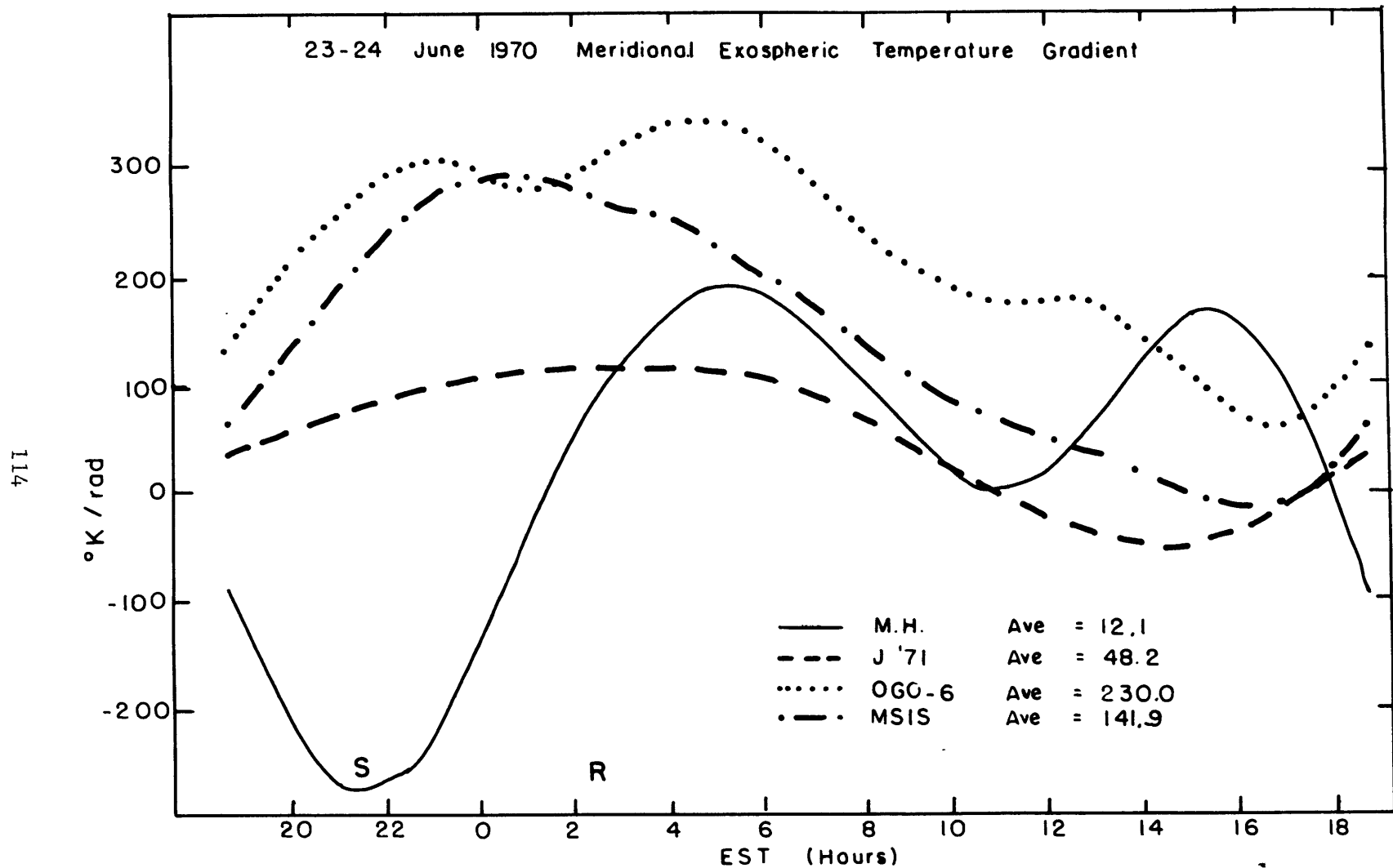


Fig. 6.5: Derived meridional exospheric temperature gradient above Millstone Hill on June 23-24, 1970. Also plotted are gradients from the Jacchia 1971, OGO-6, and MSIS models.

values of the east-west and north-south non-linear terms, $-u \partial \vec{v} / \partial x$ and $-v \partial \vec{v} / \partial y$. The terms are abbreviated in the figures as follows:

$$\begin{aligned}
 0 = & \frac{-\partial u}{\partial t} - u \frac{\partial u}{\partial x} - v \frac{\partial u}{\partial y} + \frac{u v \tan \phi}{r} - \frac{1}{\rho} \frac{\partial \rho}{\partial x} + f v \\
 & + 1/\rho (\mu \partial^2 u / \partial z^2 + \partial \mu / \partial z \partial u / \partial z) + \lambda (u_{\text{ion}} - u) \\
 = & \text{ACCEL} + \text{EWNL} + \text{NSNL} + \text{CURV} + \text{PG} + \text{COR} + \text{VISC} + \text{IDRG}
 \end{aligned}
 \tag{6.1}$$

The abbreviations are similar for the meridional momentum equation.

As described previously, the major balance, at least in the zonal momentum equation, is between the ion drag and the pressure gradient forces with the other terms contributing very little except at night when the electron density (and thus the ion drag) is reduced.

The mean circulation pattern resulting from the solution of the equations of motion is a clockwise progression of the wind vector from southwards flow at night, to westwards at dawn, to northwards during the day, to eastwards at dusk. The flow is generally from high pressures to low pressures, in contrast to the lower atmosphere where the air flows around low pressure systems. The zonal and meridional velocities for June 23-24, 1970 at 300 km are plotted in Figure 6.8 along with the calculated magnetic meridional velocity V_{Hn} . The zonal velocities varied between 380 m/sec to the east shortly after sunset to 275 m/sec to the west 2 or 3 hours after sunrise. The average was 5 m/sec westwards. The meridional velocities were not as large, varying between 25 m/sec toward the north around sunset to 110 m/sec towards the south after sunrise, with an average of 42 m/sec

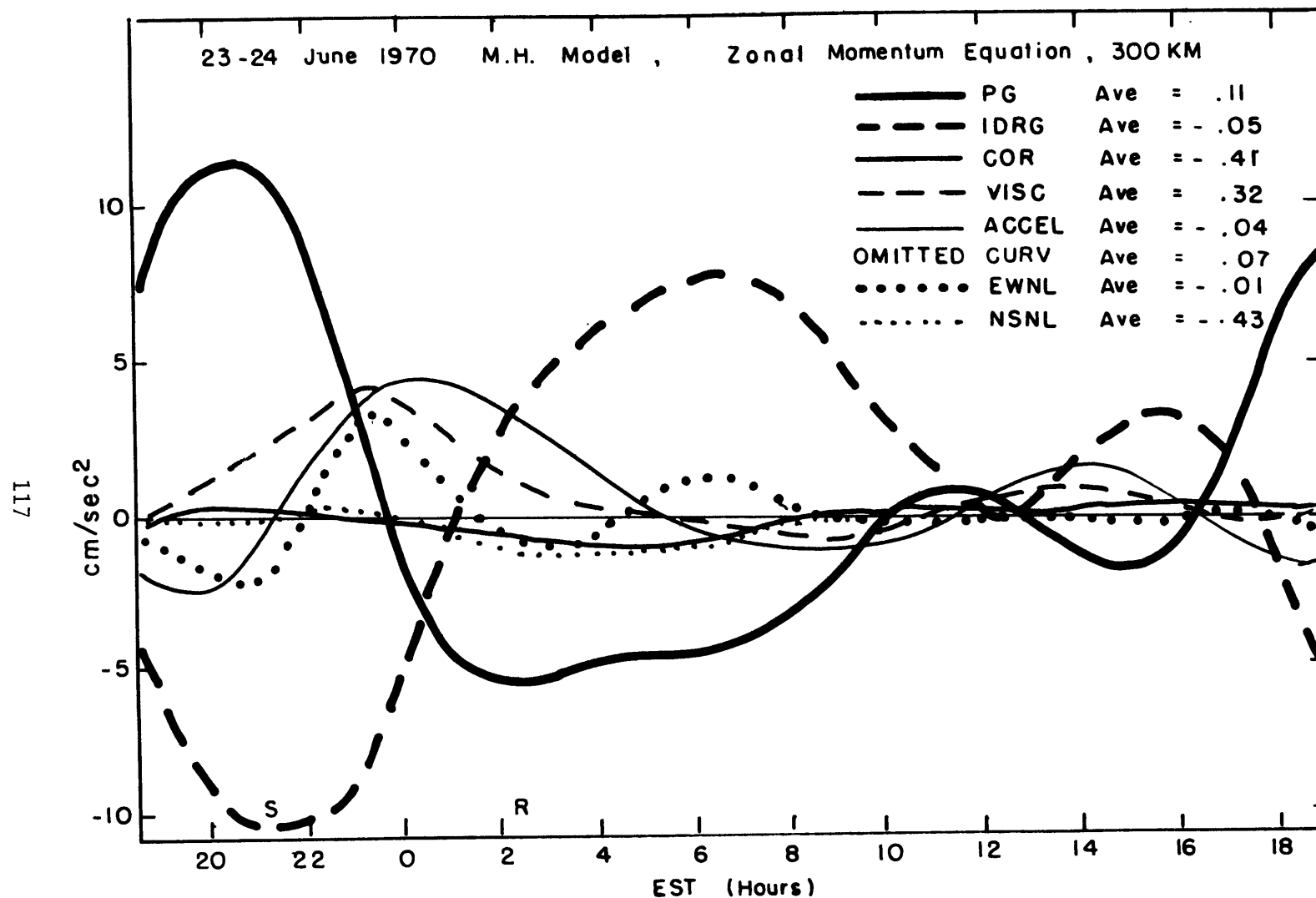


Fig. 6.7a: Variations and averages of the terms in the zonal momentum Eq. 4.5 at 300 km plus estimates of the non-linear terms for the Millstone Hill model of June 23-24, 1970. See text for explanation of abbreviations. All terms which were omitted were less than $\pm 0.6 \text{ cm/sec}^2$.

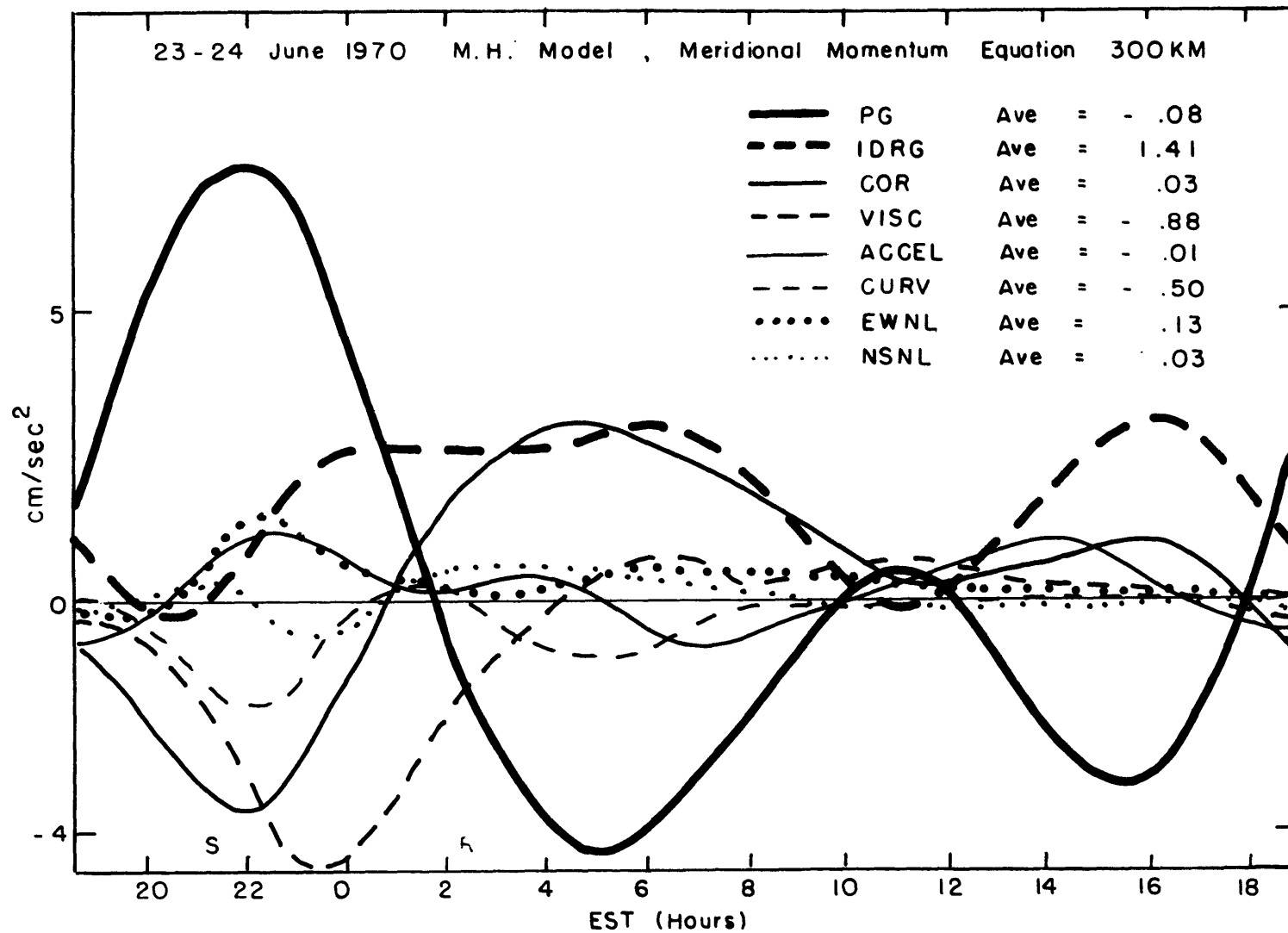


Fig. 6.7b: Same as Figure 6.7a except this is for the meridional momentum equation.

southwards. The meridional velocities are about one-third of the zonal velocities; this means that in the meridional momentum equation the ion drag term is about three times smaller than in the zonal momentum equation, while the Coriolis term is about three times larger. Thus on this particular day the Coriolis terms is about as important as the ion drag term in the meridional momentum equation. The magnitude of the meridional velocity is largely determined through fitting the experimental values of V_{Hn} at 300 km, the horizontal wind in the plane of the magnetic meridian. Figures 6.9a and b are contour plots of the zonal and meridional velocities.

6.1.2 The Continuity Equation

The terms contained in the equation for w (4.7) are discussed in detail in this section, first in a generalized manner and then specifically with regard to the summer day of June 23-24, 1970.

Vertical velocities commonly vary between ± 10 m/sec, and are usually downwards at night and generally upwards during the day. The mean vertical velocity at 300 km for June 23-24, 1970 is downwards at 1.2 m/sec, with generally downward velocities at night, maximizing around one hour after sunset at -13.3 m/sec. There are generally upwards velocities during the day maximizing about 4 hours after sunrise at 4.1 m/sec. Figure 6.10 shows the diurnal variation of the terms in Eq. 4.7 for the vertical velocity w , and lists their averages. Eq. 4.7 can be re-written as

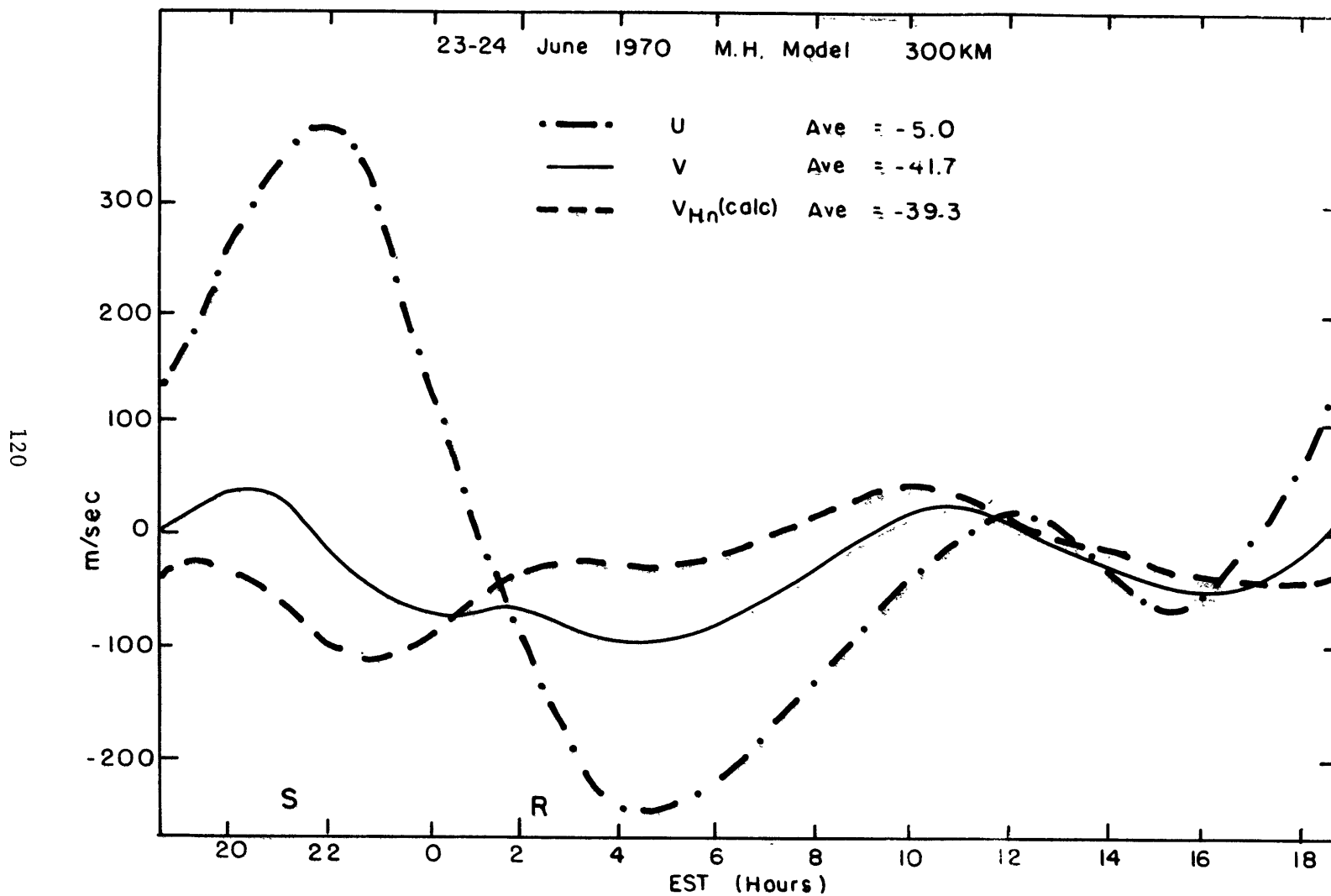


Fig. 6.8: Horizontal velocities at 300 km calculated with the Millstone Hill model on June 23-24, 1970. Positive velocities are towards the east (u), north (v), and magnetic north ($V_{Hn}(\text{calc})$).

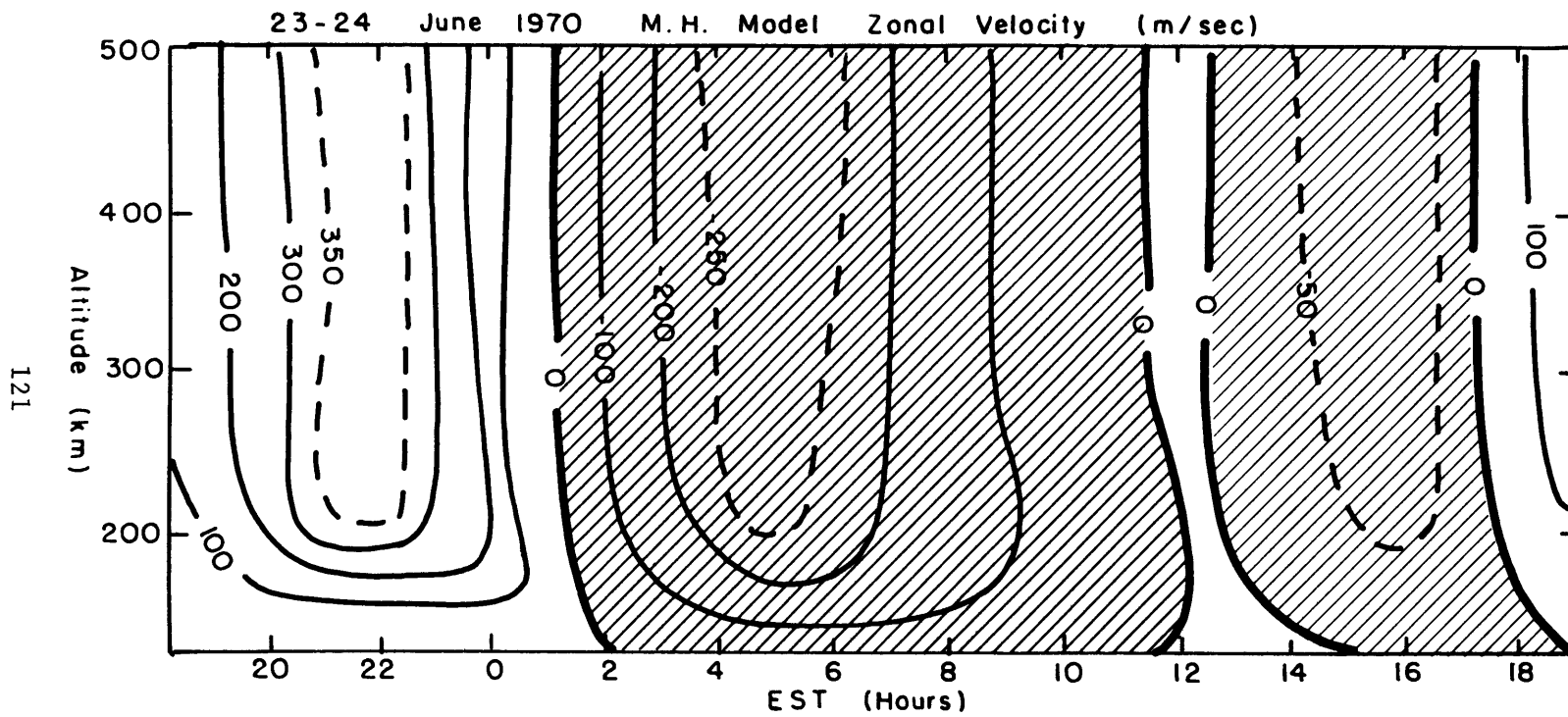


Fig. 6.9a: Zonal velocity computed with the Millstone Hill model on June 23-24, 1970. Positive velocities are toward the east.

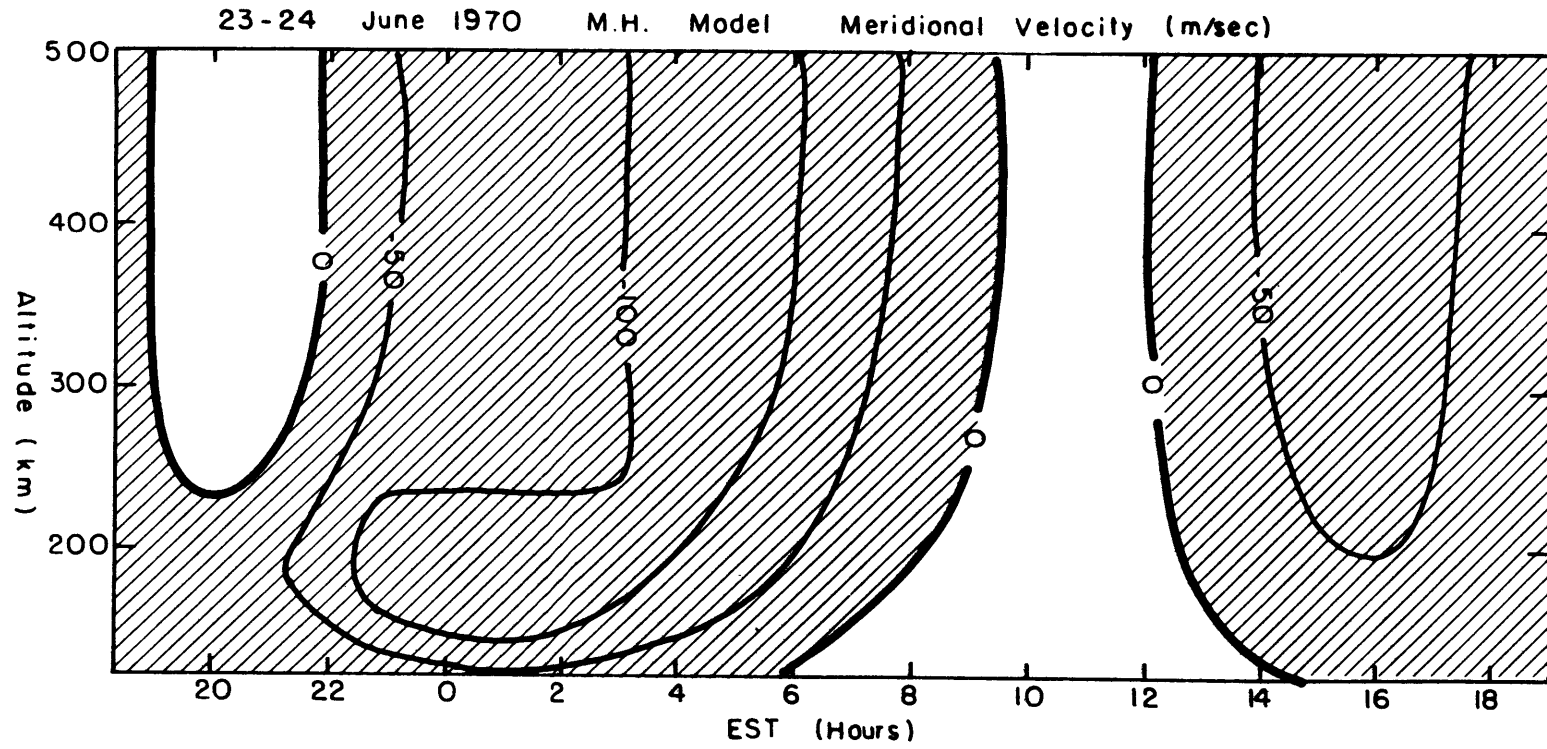


Fig. 6.9b: Meridional velocity computed using the Millstone Hill model on June 23-24, 1970. Negative values are towards the south.

$$w(z) = \frac{1}{\rho(z)} \int_z^{\infty} \left[\frac{\partial \rho}{\partial t} + \left\{ u \frac{\partial \rho}{\partial x} + v \frac{\partial \rho}{\partial y} + \rho \frac{\partial u}{\partial x} + \rho \frac{\partial v}{\partial y} \right\} - \frac{\rho v \tan \varphi}{r} \right] dz \quad (6.2)$$

This is abbreviated in Figure 6.10 as

$$w = WRHO + WDRX + WDRY + WDUX + WDVY + WTAN \quad (6.3)$$

The first term $1/\rho \int_z^{\infty} \partial \rho / \partial t \, dz$ (= WRHO) represents the rise and fall of the pressure surfaces throughout the day (see Eq. 4.8). It has the same variation as $\partial \rho / \partial x$ or $\partial T / \partial x$, with peaks around sunrise and sunset when the temperature and density are changing most rapidly. For June 23-24, 1970, this term contributes a downward velocity of 4.7 m/sec at 2000 LT, and an upward velocity of 2.4 m/sec at 0300 LT (see Fig. 6.10). Its diurnal average is near zero, which is to be expected since the temperature and density are required to begin and end at the same values over a 24 hour period.

The next four terms represent the divergence of the neutral wind. The first component $1/\rho \int_z^{\infty} u \, \partial \rho / \partial x \, dz$ (= WDRX) is also largest around sunrise and sunset where both u and $\partial \rho / \partial x$ take on their largest values. Since u is positive (eastwards) at sunset when $\partial \rho / \partial x$ is negative (decreasing), and u is negative (westwards) at sunrise when $\partial \rho / \partial x$ is positive (increasing), the average of this term is always negative. This is not surprising since a balance between ion drag and pressure gradient predicts that u is proportional to $-\partial \rho / \partial x$. The magnitude of this net downward velocity is largely dependent on the day-to-night difference in exospheric temperature

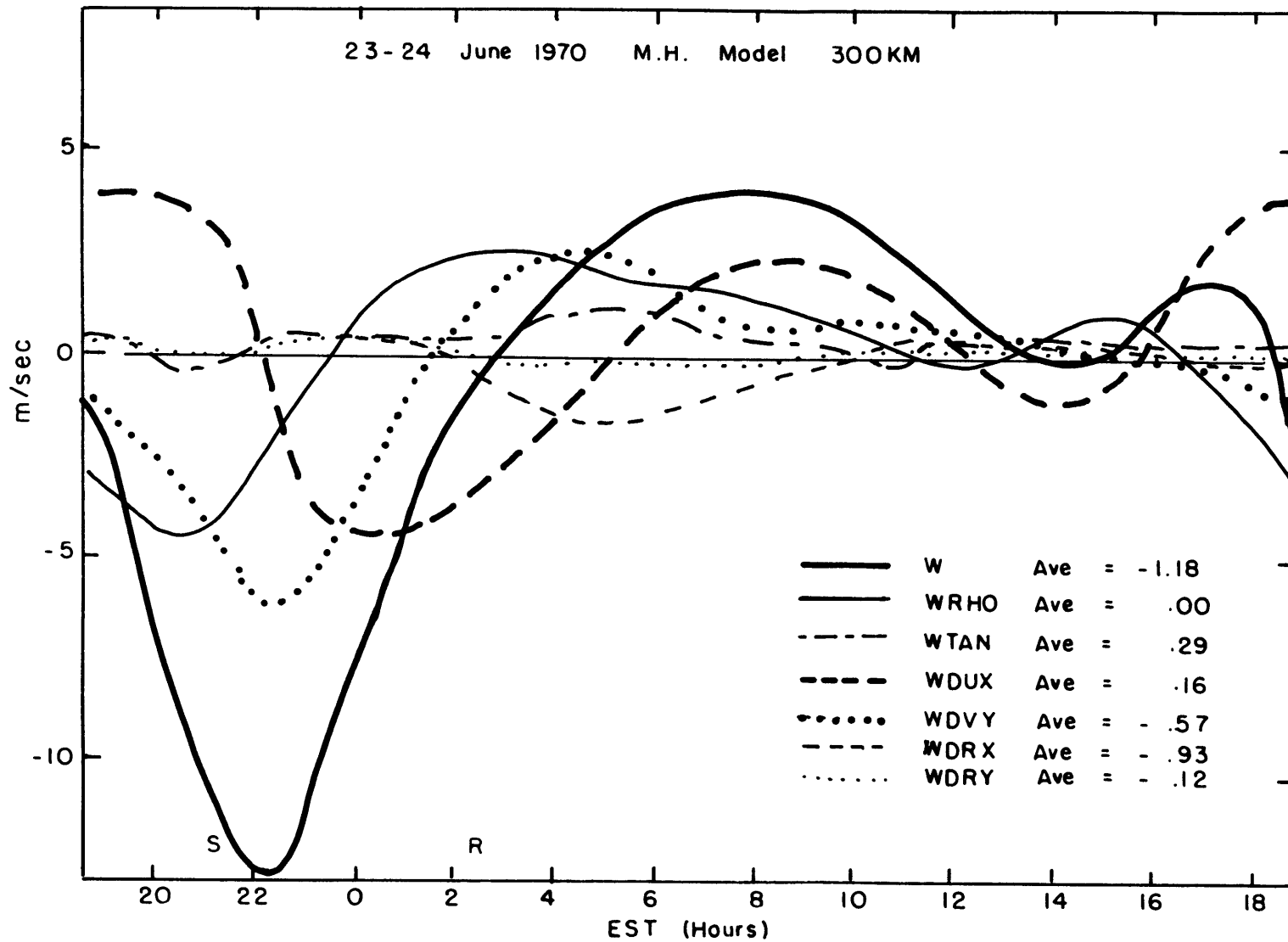


Fig. 6.10: Vertical velocity at 300 km on June 23-24, 1970 and its components. Pressure gradients were derived from the Millstone Hill model. See text for explanation of abbreviations.

and the length of the transition period. For June 23-24, 1970, this term had a diurnal average of -0.9 m/sec, and contributed downwards velocities of 4.2 m/sec at 2100 LT and 1.6 m/sec at 0500 LT (see Figure 6.10).

The next term, $1/\rho \int_z^\infty v \partial \rho / \partial y dz$ (\equiv WDRY), is very similar to the term just discussed. A balance between pressure gradient and ion drag predicts v proportional to $-\partial \rho / \partial y$. Therefore, the average value of this term should always be negative. On June 23-24, 1970, the average is -0.1 m/sec downwards. Its diurnal variation is very small (see Figure 6.10).

The third term in the divergence part for w is $1/\rho \int_z^\infty \rho \partial u / \partial x dz$ (\equiv WDUX). Now $\partial u / \partial x$ is approximately zero, but $1/\rho \int_z^\infty \rho dz$ is larger during the day than during the night. Also, $\partial u / \partial x$ is generally positive during the day since the wind basically shifts from westwards at dawn to eastwards at dusk. Therefore, the average vertical velocity contributed by this term is usually a small upward component. For June 23-24, 1970, the mean velocity contributed by this term was 0.2 m/sec upwards with a downward peak of 5.0 m/sec at 0000 LT and two upward peaks of 4.1 m/sec and 2.2 m/sec at 1800 LT and 0800 LT respectively (see Figure 6.10).

The last term in the divergence part of Eq. 6.2 for w is $1/\rho \int_z^\infty \rho \partial v / \partial y dz$ (\equiv WDVY). The latitudinal gradient of the meridional velocity v will be discussed in detail in Section 7.4 and in Appendix C, where it is shown that the variation of $\partial v / \partial y$

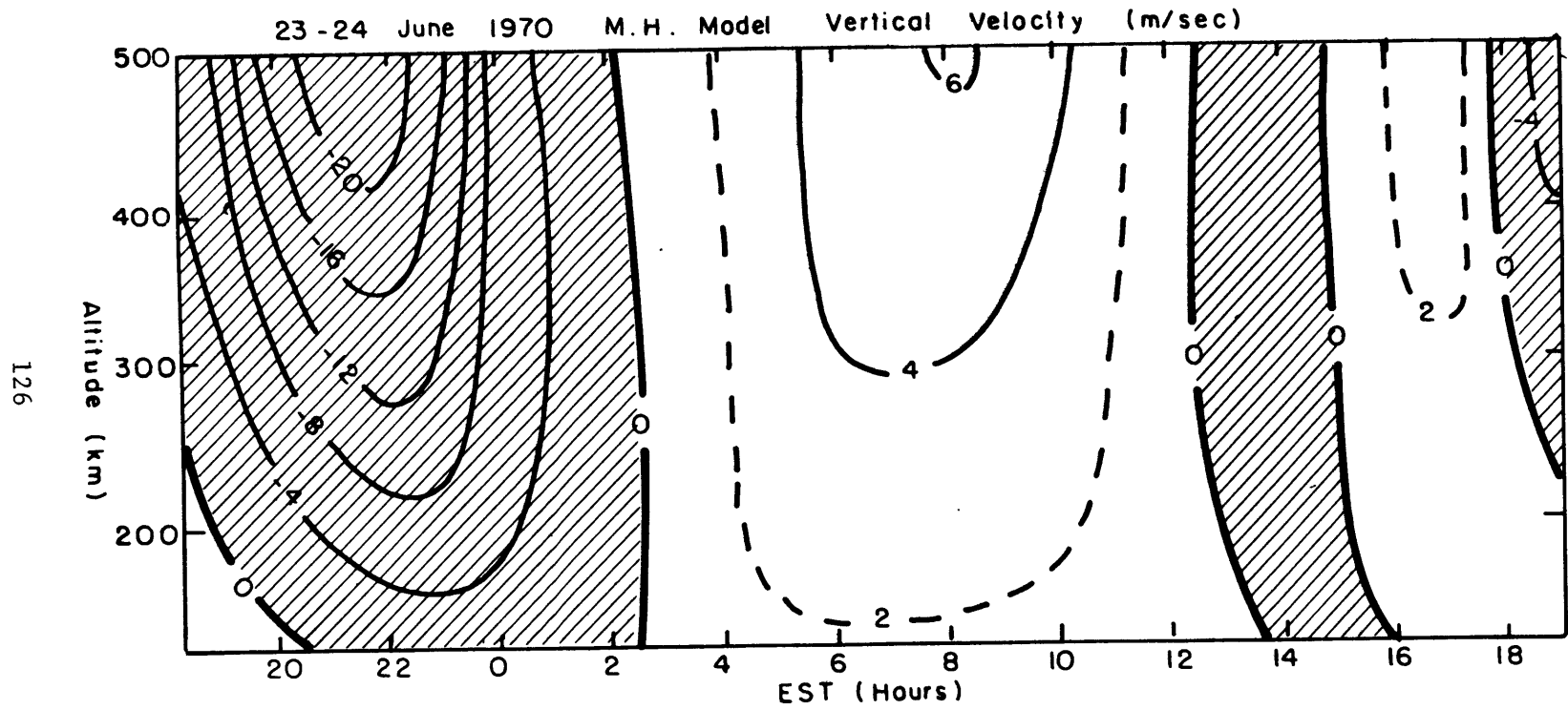


Fig. 6.11: Vertical velocity computed from the Millstone Hill model on June 23-24, 1970.

is quite different around sunrise in the Millstone Hill model than it is in the OGO-6 and MSIS atmospheric models. For the Millstone Hill model of June 23-24, 1970, WDVY had a diurnal average of -0.6 m/sec with a peak downwards velocity of 6.5 m/sec around 2200 LT and a peak upwards velocity of 2.4 m/sec around 0400 LT. (see Figure 6.10).

The final part of w , $1/\rho \int_z^\infty -\rho v \tan \phi/r dz$ ($=WTAN$), is not very large, being upwards at night and downwards during the day. However, its average is significant and is of the same sign as $-v$. For June 23-24, 1970, the average contribution to w from this term is upwards at 0.3 m/sec. The peak upwards velocity was 0.8 m/sec at 0500 LT and the peak downwards velocity was 0.2 m/sec at 2100 LT (see Figure 6.10).

Figure 6.11 is a contour plot of the vertical velocity deduced on June 23-24, 1970. The typical behavior of the vertical velocity deduced for Millstone Hill in the summer is for a downward velocity of the order of 10 m/sec to be established shortly after sunset and then an upward velocity about half that magnitude a few hours after sunrise. The rest of the day and night, the velocities are less, being about 3 m/sec upwards during the day and downwards at night. The divergence term WDVY, which is not well known in the Millstone Hill model, usually contributes substantially to the existence of the peak vertical velocities. Therefore, the diurnal variation of the vertical velocity is somewhat different when model temperatures and gradients are used.

6.1.3 Comparison with Other Models

Pressure gradients from global atmospheric models such as the MSIS, OGO-6, or Jacchia 1971 models can be used to solve the equations of motion (4.5) with the ion drag parameter λ and the diffusion velocity $V_{D//}$ (in u_{ion} and v_{ion}) determined by the ionospheric data from Millstone Hill. The steps in this type of analysis were outlined in Figure 5.1b for the case of the MSIS model pressure gradients. This section will discuss some of the results obtained using these three global atmospheric models to describe the winds on June 23-24, 1970.

The average exospheric temperatures predicted by the MSIS, OGO-6, and Jacchia 1971 atmospheric models were shown in Figure 6.2 along with the temperatures deduced from the radar data. The average temperatures are within 35°K of each other, except for the OGO-6 temperature which, at 1182°K , is about 100°K larger than the others. The day-night differences are about 200°K for the Jacchia model, 250°K for the OGO-6 model, 300°K for the MSIS model, and 400°K for the Millstone Hill case. Larger day-night differences imply that the zonal pressure gradients are larger, and hence that the zonal velocities are larger.

The zonal exospheric temperature gradients for the four models (Millstone Hill, Jacchia 1971, OGO-6, and MSIS) are shown in Figure 6.4. The gradients are smallest for the Jacchia 1971 model and are very nearly the same for the OGO-6 and MSIS models.

The gradients determined from the diurnal variation of the exospheric temperature deduced above Millstone Hill are about twice the size of those of the models around sunrise and sunset.

The diurnal variations of the meridional exospheric temperature gradients (Figure 6.5) exhibit maximum poleward increases in temperature at night for all but the Millstone Hill results. As discussed previously, the Millstone Hill diurnal variations are established by the role of the Coriolis force in determining the free parameter $\partial T_{\infty} / \partial \varphi$. The minimum poleward (or maximum equatorward) temperature increase generally occurs in the afternoon. Again, the Millstone Hill model was the exception. The diurnal range of the meridional exospheric temperature gradient is about $150^{\circ}\text{K}/\text{rad}$ for the Jacchia model, $290^{\circ}\text{K}/\text{rad}$ for the OGO-6 model, $310^{\circ}\text{K}/\text{rad}$ for the MSIS model, and $465^{\circ}\text{K}/\text{rad}$ for the Millstone Hill model.

The average meridional exospheric temperature gradients are quite different, reflecting different assumptions about the meridional density gradients, especially that for atomic oxygen. The meridional pressure gradient is directly proportional to the meridional exospheric temperature gradient in the present study. The Jacchia 1971 model has constant conditions at 90 km and varying conditions above this. The density is tied to the temperature except for semiannual variations below 200 km and variations with geomagnetic activity below 200 km. Seasonal-latitudinal variations in helium and hydrogen are also permitted, but there are none with

respect to atomic oxygen. As a result, the meridional pressure gradient is also very nearly directly proportional to the meridional exospheric temperature gradient for the Jacchia 1971 model.

The MSIS and OGO-6 models have strong seasonal variations in the atomic oxygen as well as in other constituents which are not tied to the exospheric temperature. However, averages of the fraction (g/f) (defined in Section 7.3) of the meridional exospheric temperature gradient due to the bottom boundary meridional atomic oxygen gradient ($g/f \frac{1}{n(O)} \frac{\partial n(O)}{\partial \varphi}$) were computed. This procedure is discussed further in Section 7.3. The computations of the ratio g/f from the MSIS and OGO-6 models were unreliable because of the greater complexity of the models, so the value derived for the Millstone Hill case was used to approximate "effective" meridional exospheric temperature gradients for the MSIS and OGO-6 models. The value of g/f at 300 km was deduced to be $181^\circ\text{K}/\text{rad}$ on June 23-24, 1970. The ratio of the average meridional atomic oxygen gradient at 120 km over the atomic oxygen number density was -0.545 for the MSIS model and nearly twice that -0.919 for the OGO-6 model. The resulting average "effective" meridional exospheric temperature gradients were 63 and $43^\circ\text{K}/\text{rad}$ for the OGO-6 and MSIS models. The average gradients were 48 and $12^\circ\text{K}/\text{rad}$ for the Jacchia 1971 and Millstone Hill models. Positive averages (average increase of pressure towards the pole) generally indicate that the average meridional velocity is equatorwards (southwards).

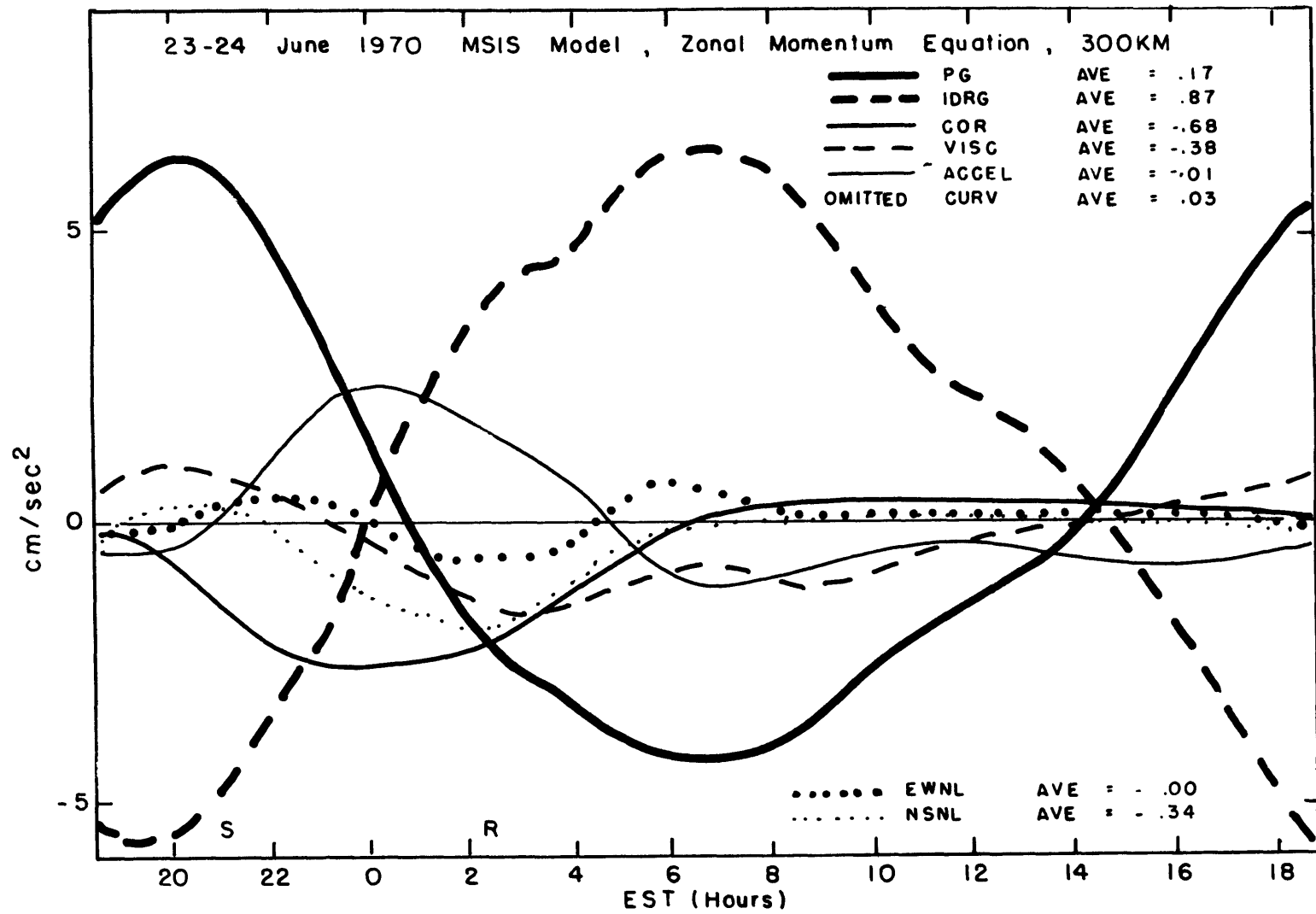


Fig. 6.12a: Same as Figure 6.7a except the pressure gradients came from the MSIS model.

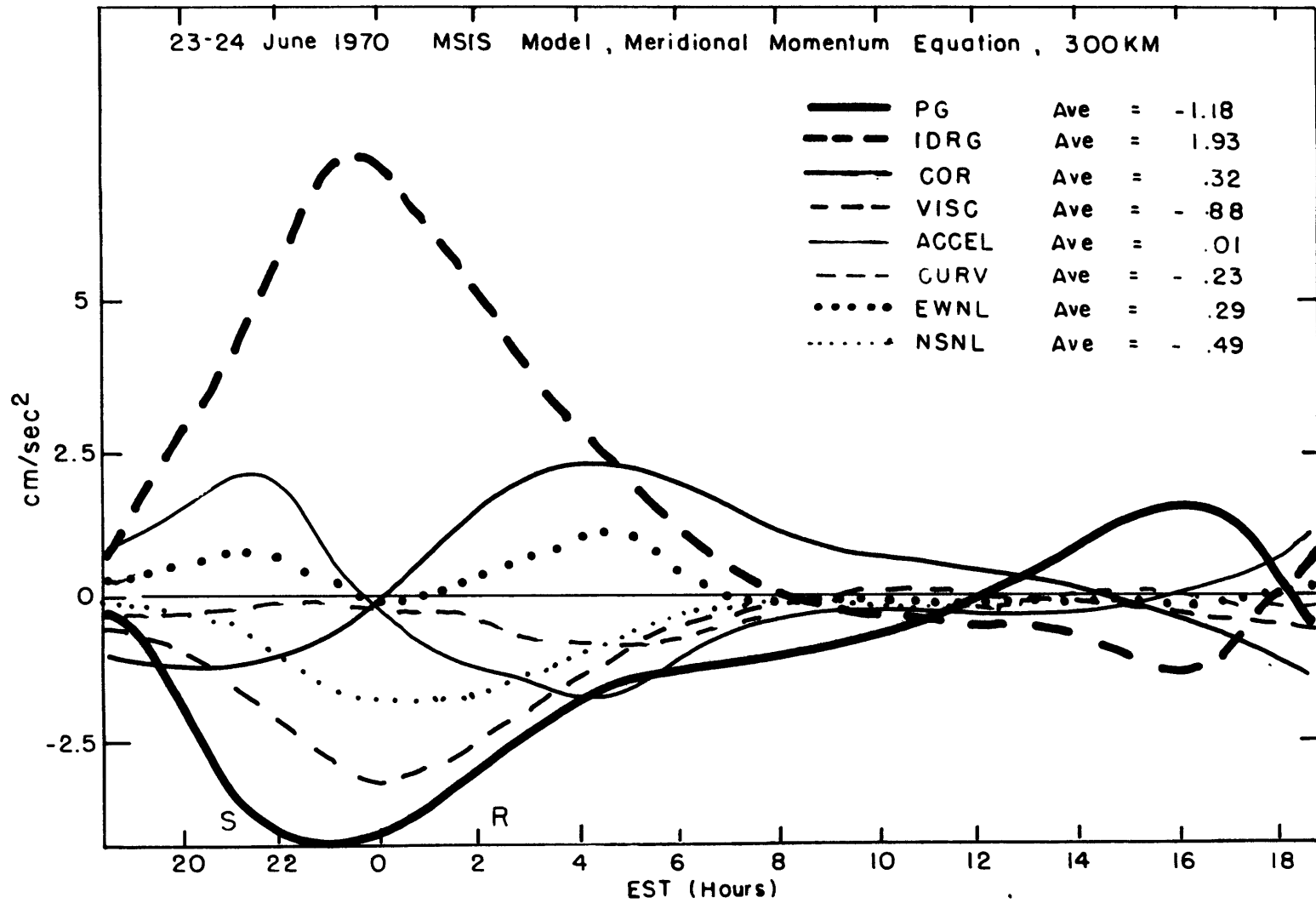


Fig. 6.12b: Same as Figure 6.7b except the pressure gradients come from the MSIS model.

Figures 6.12a and b plot the terms in the momentum equations at 300 km using the MSIS model pressure gradients. Estimates for the non-linear terms are also included. The resulting horizontal circulation at 300 km is depicted in Figure 6.12c, and the vertical velocity and its various components in 6.12d, Figures 6.13a, b, c, and d are similar plots for the case where the OGO-6 model pressure gradients were used.

As predicted, the zonal pressure gradients are slightly larger in the MSIS model than in the OGO-6 model. However, the zonal velocities are not correspondingly larger in the ion drag term because the other terms in the equation of motion add up in different ways. On the whole, the horizontal velocities derived from the two models are found to be of comparable magnitude, being within ± 250 m/sec. With respect to the radar results, this represents a reduction in the zonal velocities and an increase in the meridional velocities. The reduction in the zonal velocities follows directly from the reduction in the zonal (temporal) exospheric temperature gradients plotted in Figure 6.4. The increase in the meridional velocities results from balancing a different meridional pressure gradient (see Figure 6.5), not having a large Coriolis term, and not being constrained by radar measurements of V_{Hn} . For the models, there is an approximate balance between the pressure gradient and ion drag forces for both the zonal and meridional momentum equations. The average horizontal velocities are towards the south-west in both cases being 70 m/sec southwards and 35 m/sec

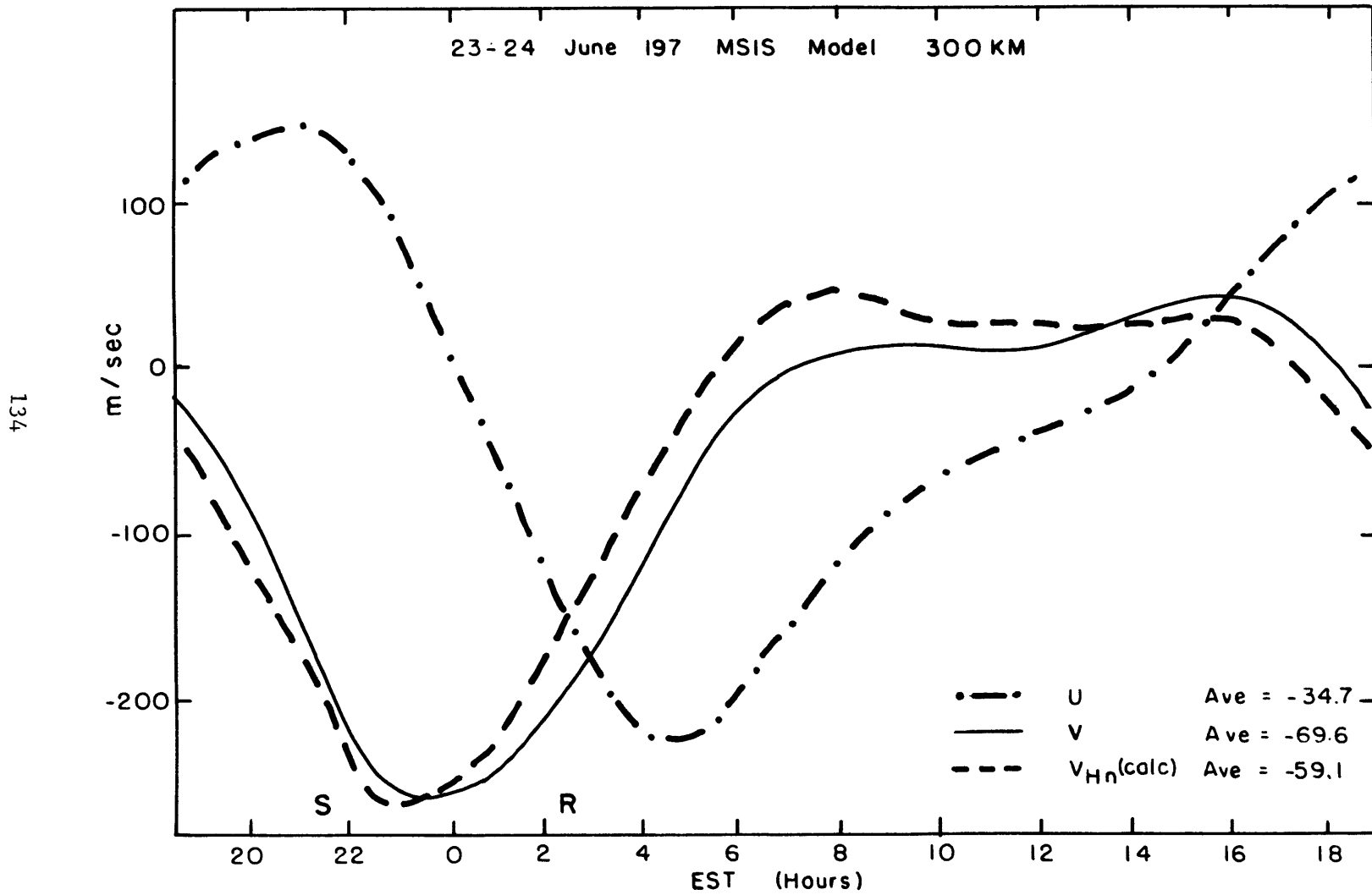


Fig. 6.12c: Horizontal velocities calculated at 300 km for June 23-24, 1970 using the MSIS model pressure gradients.

westwards for the MSIS model (Figure 6.12c) and 39 m/sec southwards and 15 m/sec westwards for the OGO-6 model (Figure 6.13c).

The estimated values of the north-south non-linear terms ($-\vec{v} \frac{\partial \vec{v}}{\partial y} = \text{NSNL}$) are almost negligible in the Millstone Hill results but are substantial in the MSIS and OGO-6 models, being up to 50% of the largest terms. The Millstone Hill results for June 23-24, 1970 are unusual in this regard. On most summer days the estimated meridional non-linear term was approximately 35% of the largest terms.

The average vertical velocities are downwards at -1.4 m/sec for the MSIS model (Figure 6.12d) and -2.1 m/sec for the OGO-6 model (Figure 6.13d). The differences arise from the differences in the divergence term containing the latitudinal gradient of the meridional velocity, $\partial v / \partial y$. In both cases, the diurnal variation contained in the models is smoother than in the Millstone Hill case, the velocities being downwards at night and upwards during the day, but with a gentler change from night to day values. The strongest downward velocities are encountered just before midnight at -6.9 m/sec for the MSIS model and -9.9 m/sec for the OGO-6 model. The largest upward velocities are about 6 hours after sunrise at 3.4 m/sec for the MSIS model and 3.0 m/sec for the OGO-6 model. Both the MSIS and OGO-6 models predict $\partial v / \partial y$ to be large and negative (stronger equatorward winds poleward of Millstone Hill) around sunrise while this term is changing from negative to positive values in the Millstone Hill case.

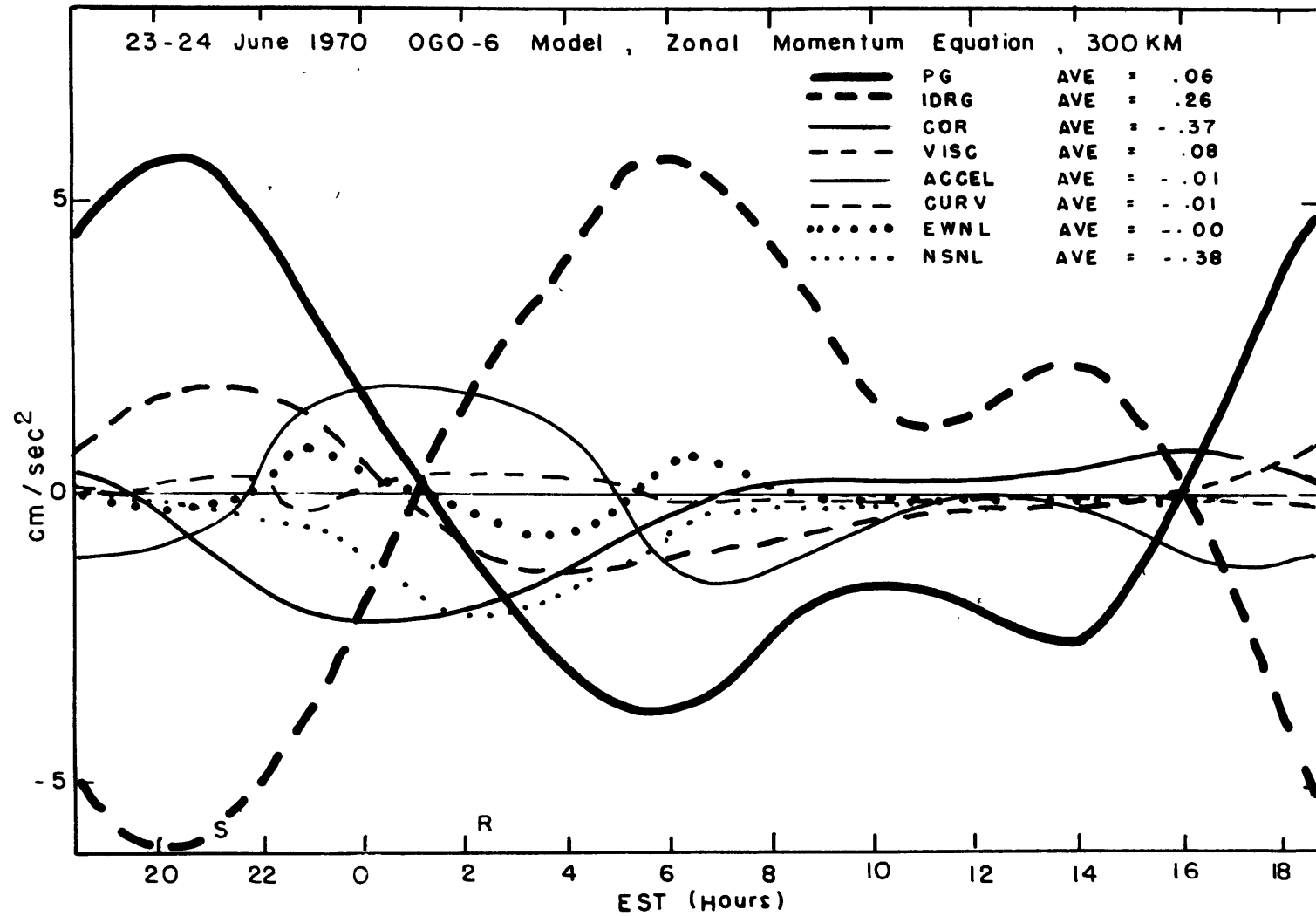


Fig. 6.13a: Same as Fig. 6.7a except the pressure gradients came from the OGO-6 model

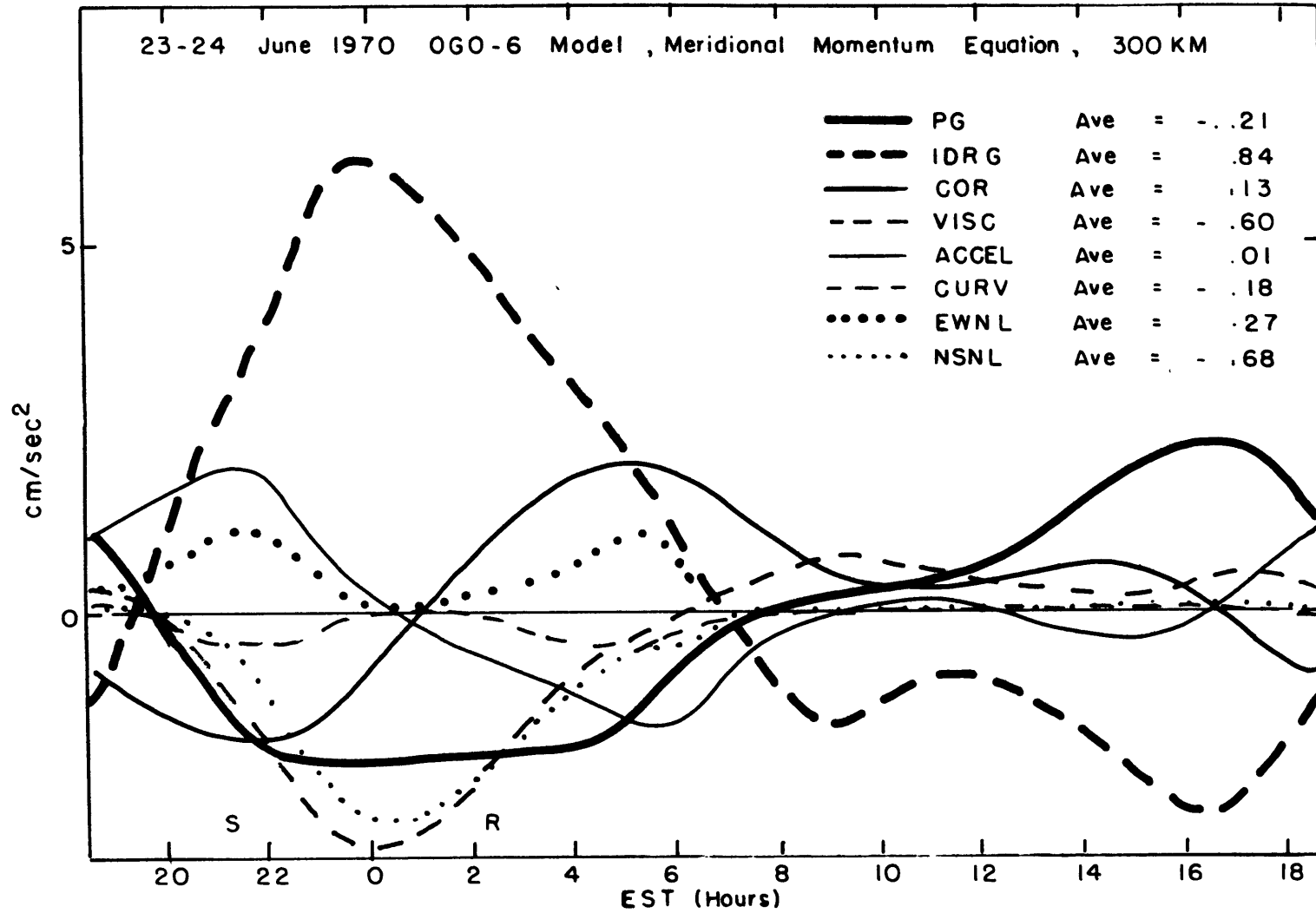


Fig. 6.13b: Same as Fig. 6.7b except the pressure gradients came from the OGO-6 model.

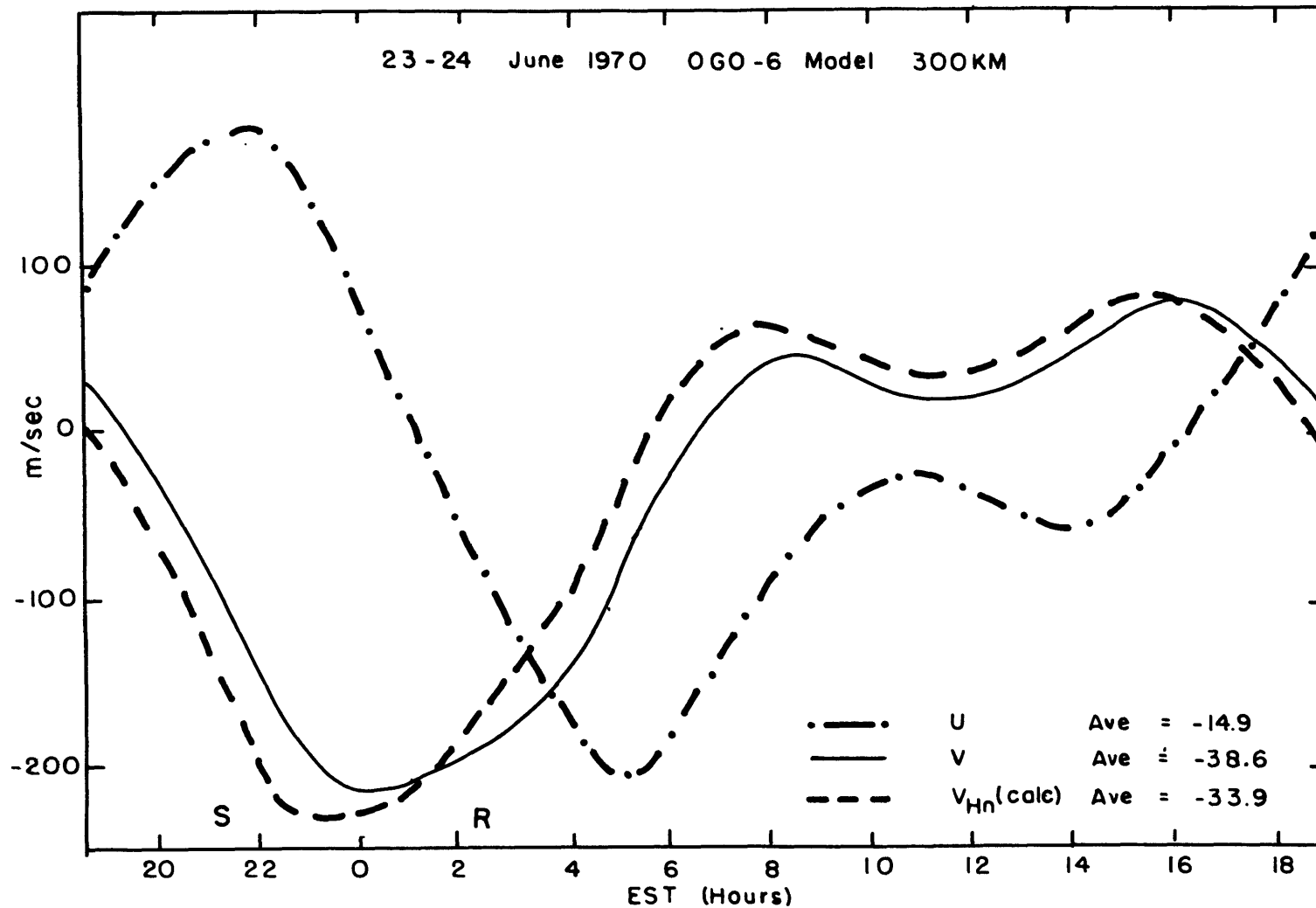


Fig. 6.13c: Horizontal velocities at 300 km on June 23-24, 1970 calculated using the OGO-6 model pressure gradients.

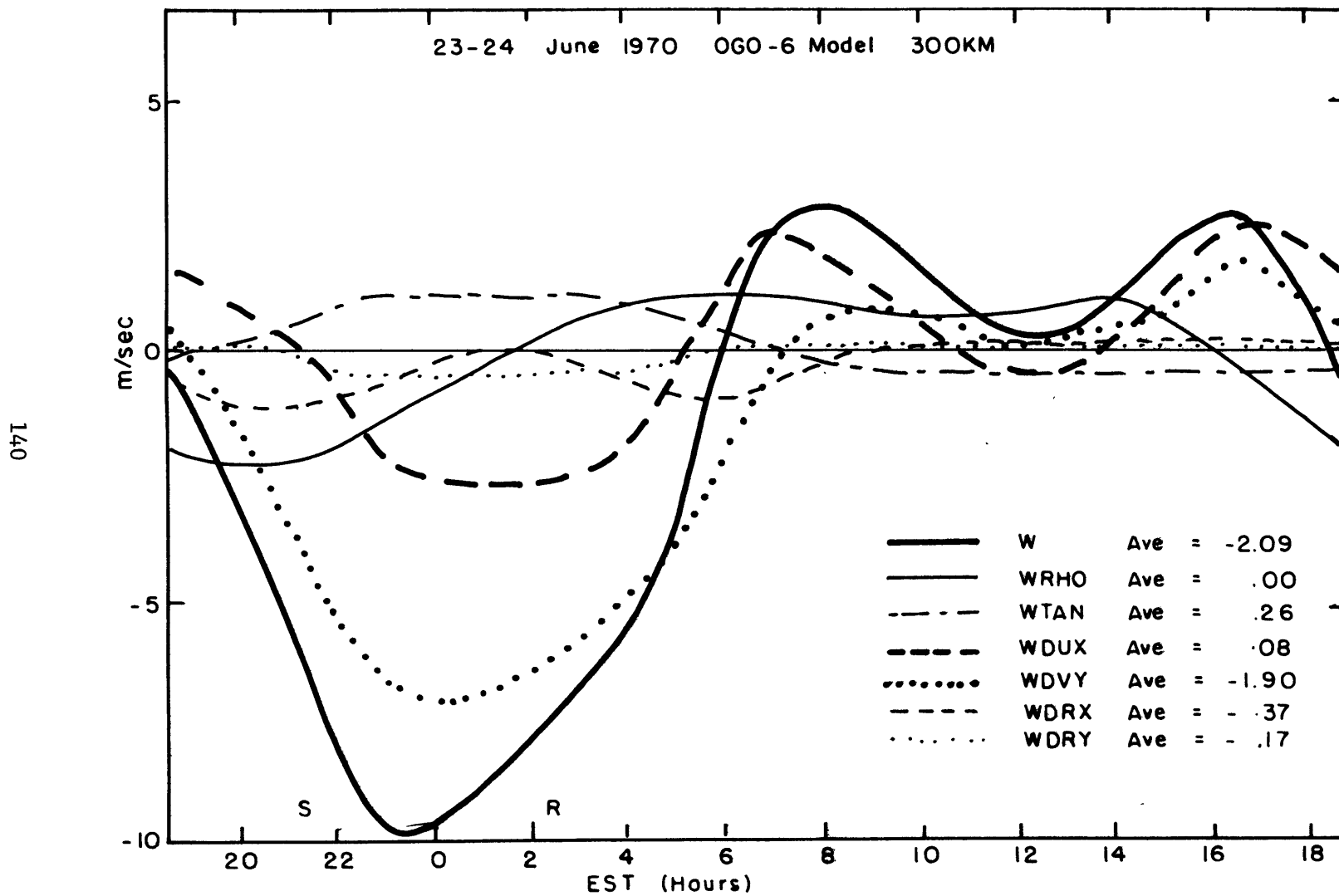


Fig. 6.13d: Same as Fig. 6.10 only the pressure gradients were from the OGO-6 model.

6.2 Representative Winter Results

The previous section dealt primarily with the results for one summer day (June 23-24, 1970), including the results for the velocity. The importance of the Coriolis term in the meridional momentum equation was demonstrated. This section will examine the results for one winter day (January 20-21, 1971) in detail and include some general remarks.

The height and time variations of electron density measured on January 20-21, 1970 are presented in Figure 6.14. The densities are larger than those measured on June 23-24, 1970 and the sudden sunrise increase in electron density is very clearly marked.

Compared to summer days most winter days exhibit a smaller day-night difference in exospheric temperature and a transition from day to night which is less abrupt. This is borne out in comparing the exospheric temperatures (Figures 6.15a and 6.2) and their zonal (time) derivatives (Figures 6.15b and 6.4) for January 20-21, 1971 and June 23-24, 1970. The day-night difference in temperature is about 290°K in January and 400°K in June. The zonal derivative at sunset was approximately two times larger on the June day than it was in January although the values were comparable around sunrise. This was because the temperature did not increase as quickly on the June day as it did on about 75% of the other summer days.

The experimental values for the magnetic meridional velocity (V_{Hn}) are more positive in the winter than they are in

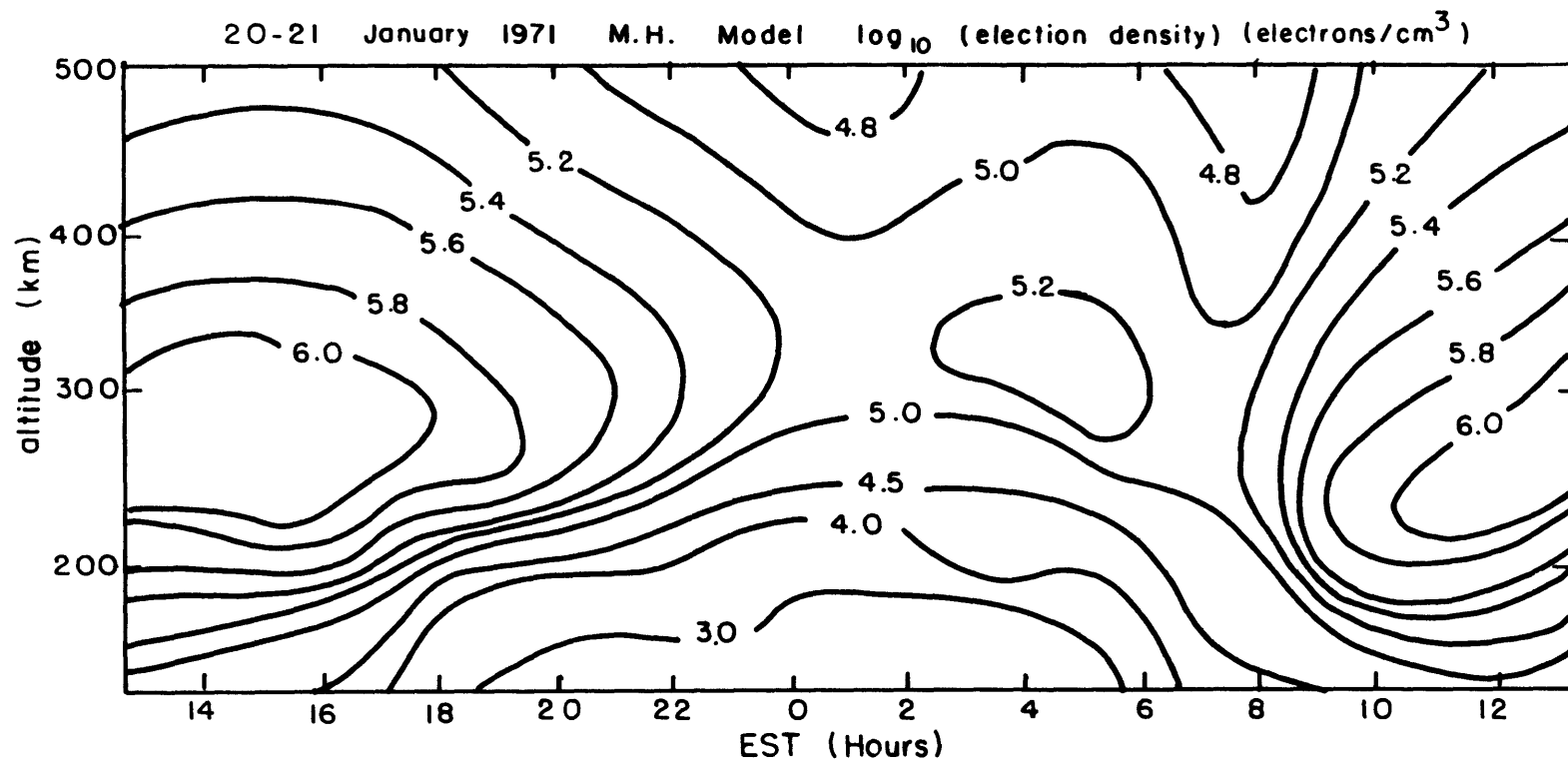


Fig. 6.14: Smoothed electron densities in intervals of \log_{10} measured over Millstone Hill on January 20-21, 1971.

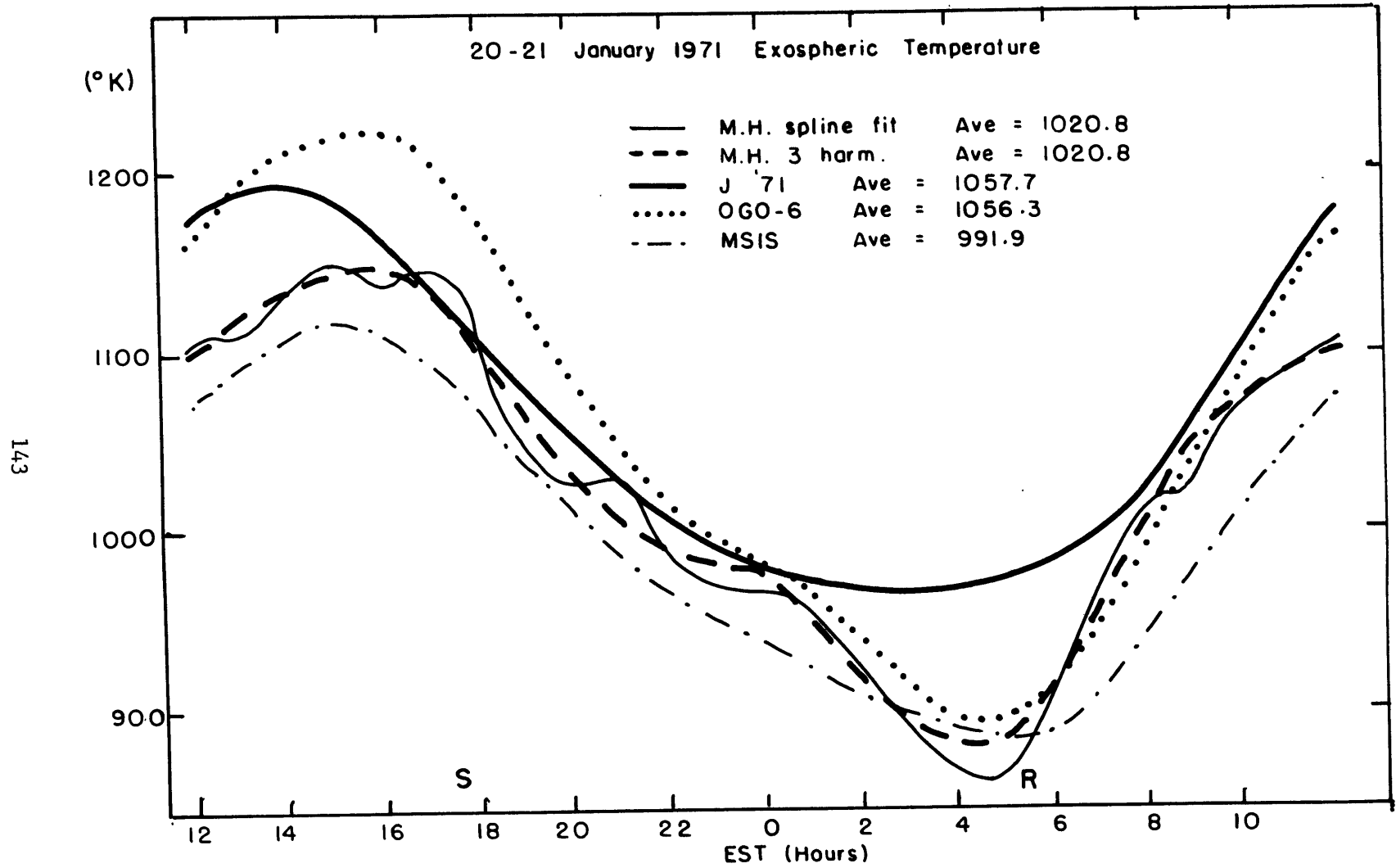


Fig. 6.15a: Same as Figure 6.2 only for January 20-21, 1971.

the summer, indicating a change from net equatorward winds to net poleward winds. Figure 6.17 is a plot of the experimental V_{Hn} at 300 km in January 20-21, 1971 and the V_{Hn} calculated using three harmonics (Figure 6.16) of the derived meridional exospheric temperature gradient. The average velocity is about 18 m/sec towards the north. (The average was 40 m/sec towards the south on June 23-24, 1970). The velocity varied from 160 m/sec southwards around 0200 LT to 110 m/sec northwards around 0700 LT, an hour or two after sunrise. The root mean square deviation between the observed and calculated values was 19 m/sec.

The corresponding meridional exospheric temperature gradient (Figure 6.16) had an average of $-123^{\circ}\text{K}/\text{rad}$, or a net decrease in temperature towards the pole. The diurnal variation in the gradient was over about $230^{\circ}\text{K}/\text{rad}$ as opposed to a variation over twice this range on the June day.

Figure 6.18a and b are plots of the terms in the equations of motion (Eq. 4.5) plus estimates of the neglected non-linear terms. The non-linear terms are not important and the major balance is between the ion drag force and the pressure gradient. Coriolis forces still affect the shape of the derived meridional exospheric temperature gradient at night but not to the extent they did on the June day (and other summer days).

The terms in the equations of motion for January 20-21, 1971 (Figures 6.18a and b) are smaller in magnitude than the terms

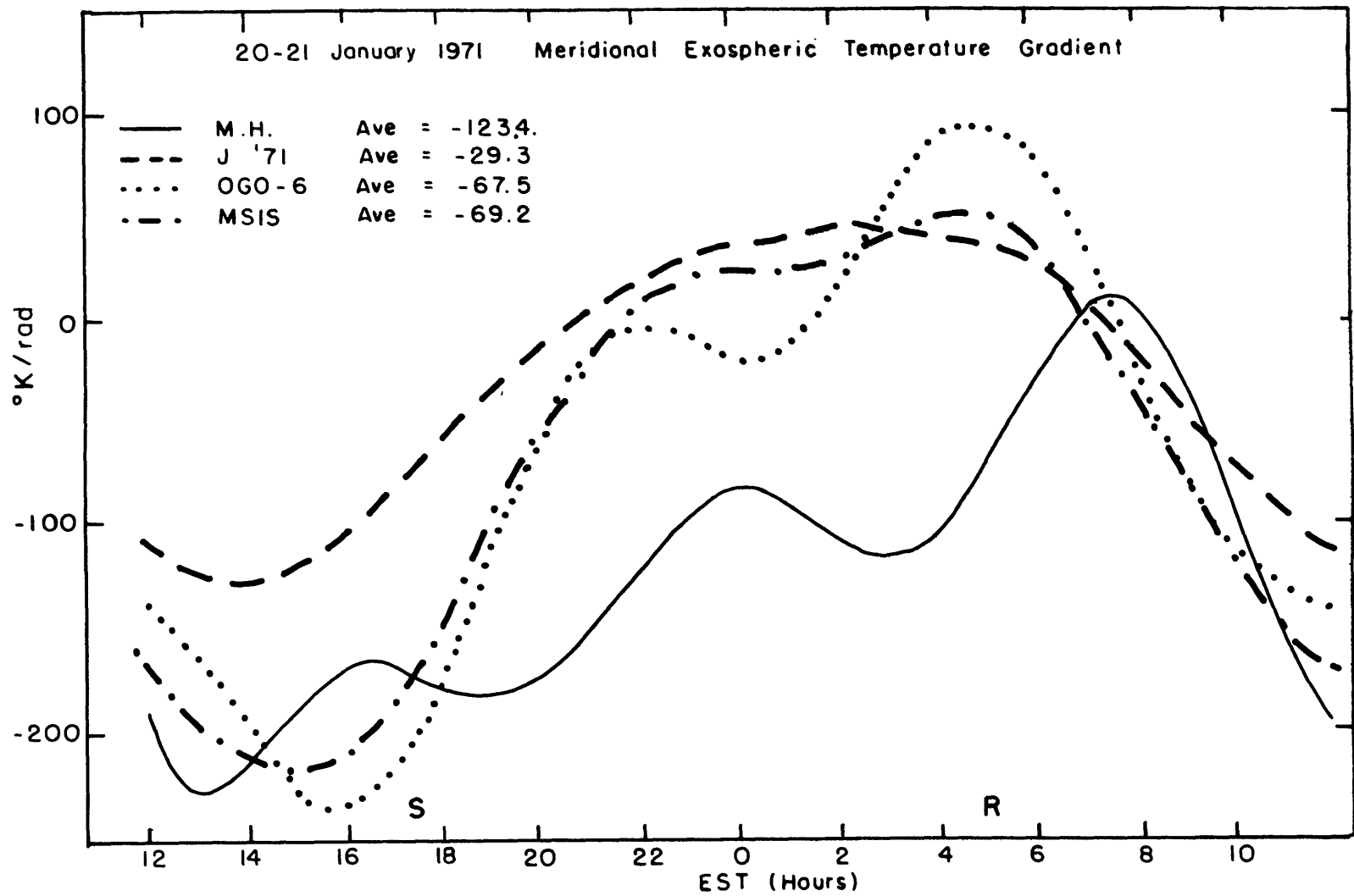


Fig. 6.16: Same as Figure 6.5 only for January 20-21, 1971.

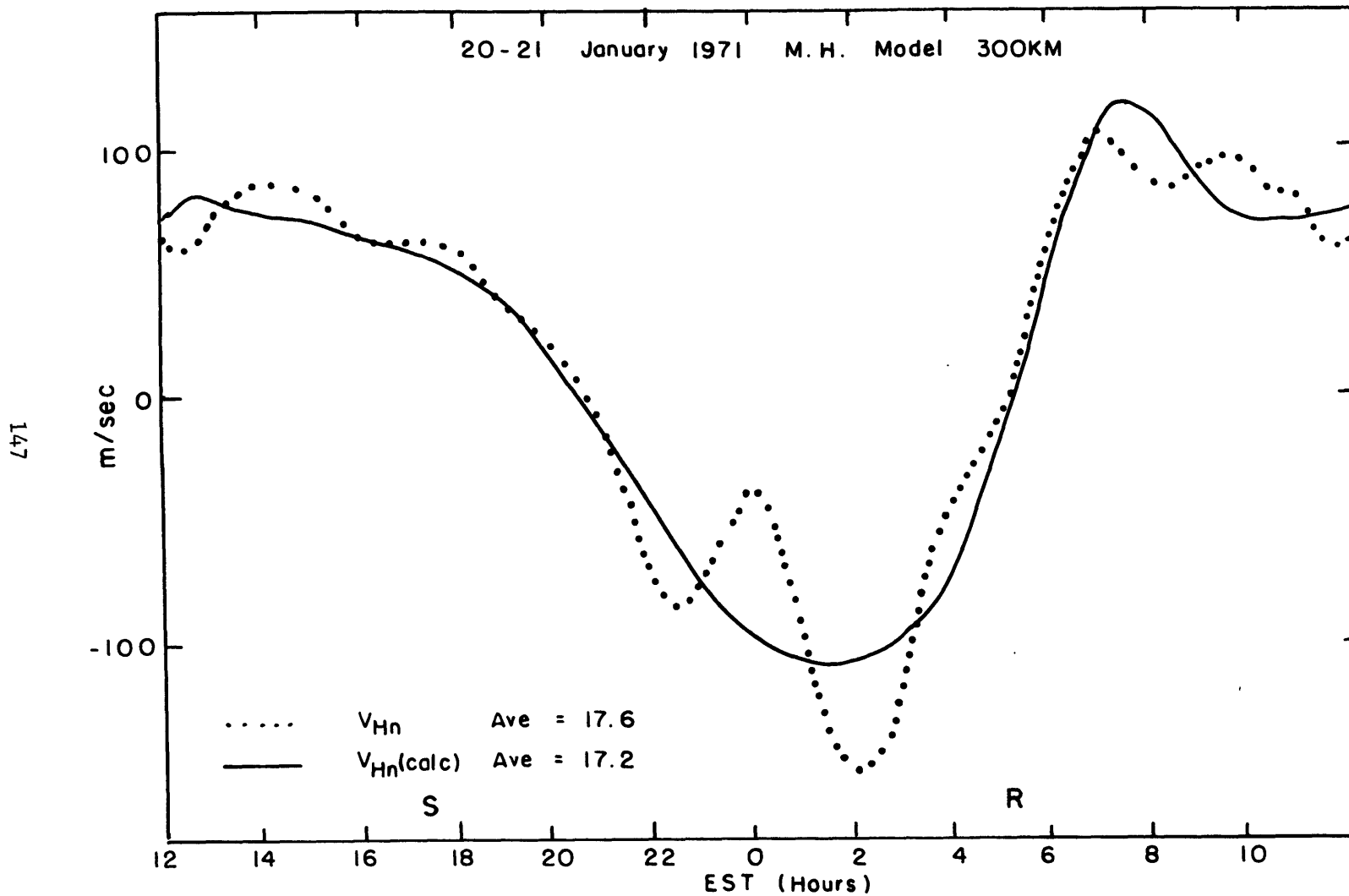


Fig. 6.17: Same as Figure 6.6 only for January 20-21, 1971.

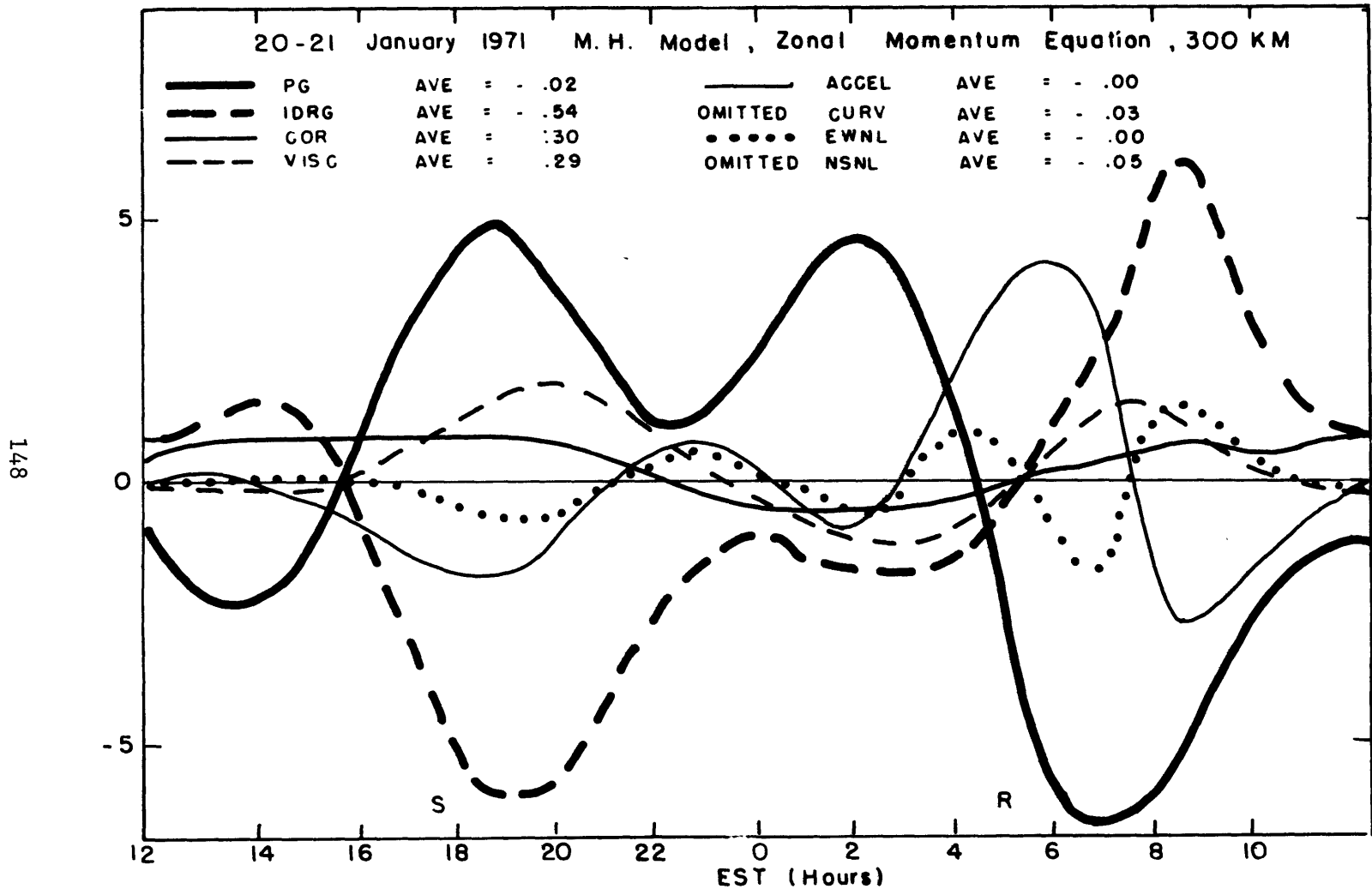


Fig. 6.18a: Same as Figure 6.7a except this is for January 20-21, 1971.

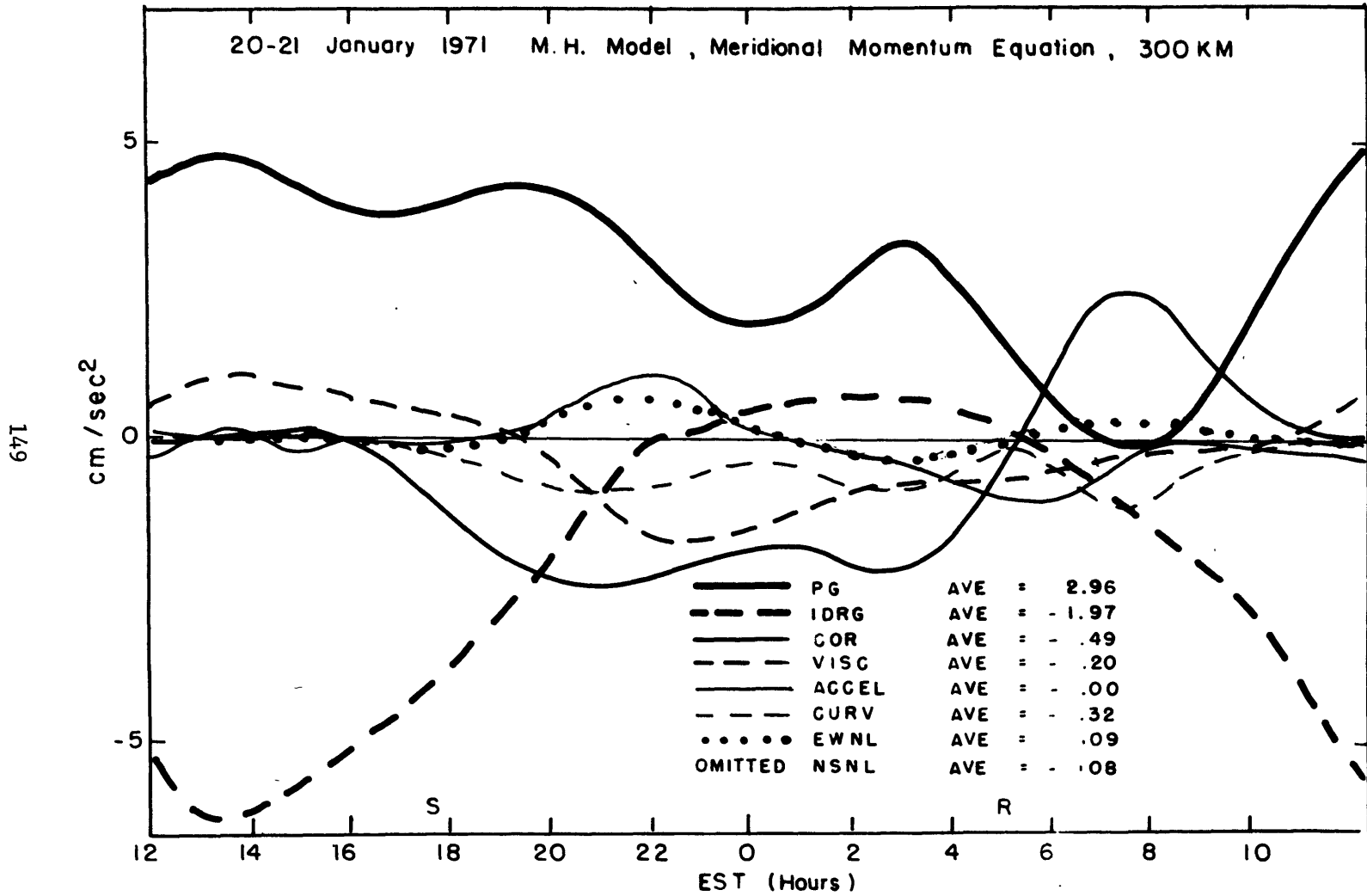


Fig. 6.18b: Same as Figure 6.7b except this is for January 20-21, 1971.

for June 23-24, 1970 (Figures 6.7a and b). There is a corresponding decrease in the size of the resulting circulation (Figures 6.19a and 6.8). The zonal wind for January at 300 km varies between 230 m/sec to the east around 2100 LT and 0300 LT and 250 m/sec towards west a couple of hours after sunrise around 0800 LT. The average zonal velocity is 50 m/sec towards the east. The mean meridional wind is 30 m/sec northwards and varies between 70 m/sec to the south at 0100 LT to 85 m/sec to the north in the afternoon and early evening.

The two periods of peak eastward winds at night contribute to creating (through the WDUX term) two periods of downward velocities during the night. For the Millstone Hill case on January 20-21, 1971, the average velocity is downwards at .8 m/sec, with peak downward velocities of 6.4 m/sec around 2200 LT and 3.8 m/sec around dawn (0500 LT). (See Figure 6.19b). The peak upwards velocity is at 7.2 m/sec about 4 hours after sunrise (~0900 LT).

6.2.1 Comparison with Other Models

Comparisons similar to those made for June 23-24, 1970 were made for January 20-21, 1971. The exospheric temperatures predicted by the MSIS, OGO-6, and Jacchia 1971 models at the latitude of Millstone Hill for the prevailing solar and geomagnetic conditions of January 20-21, 1971 are plotted in Figure 6.15a. There is a much closer correlation of observed and predicted temperatures (and hence

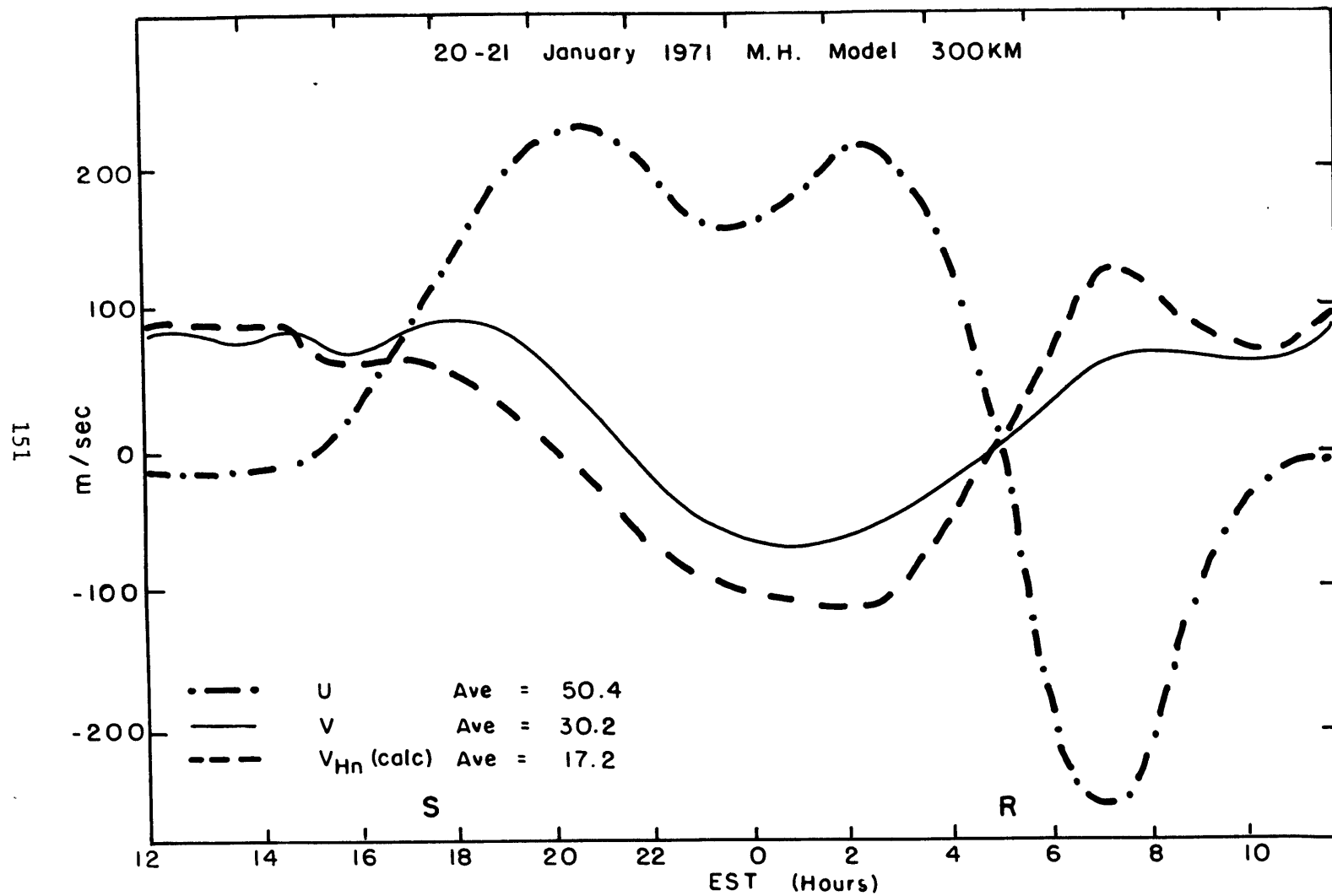


Fig. 6.19a: Horizontal velocities at 300 km calculated with the Millstone Hill model on January 20-21, 1971.

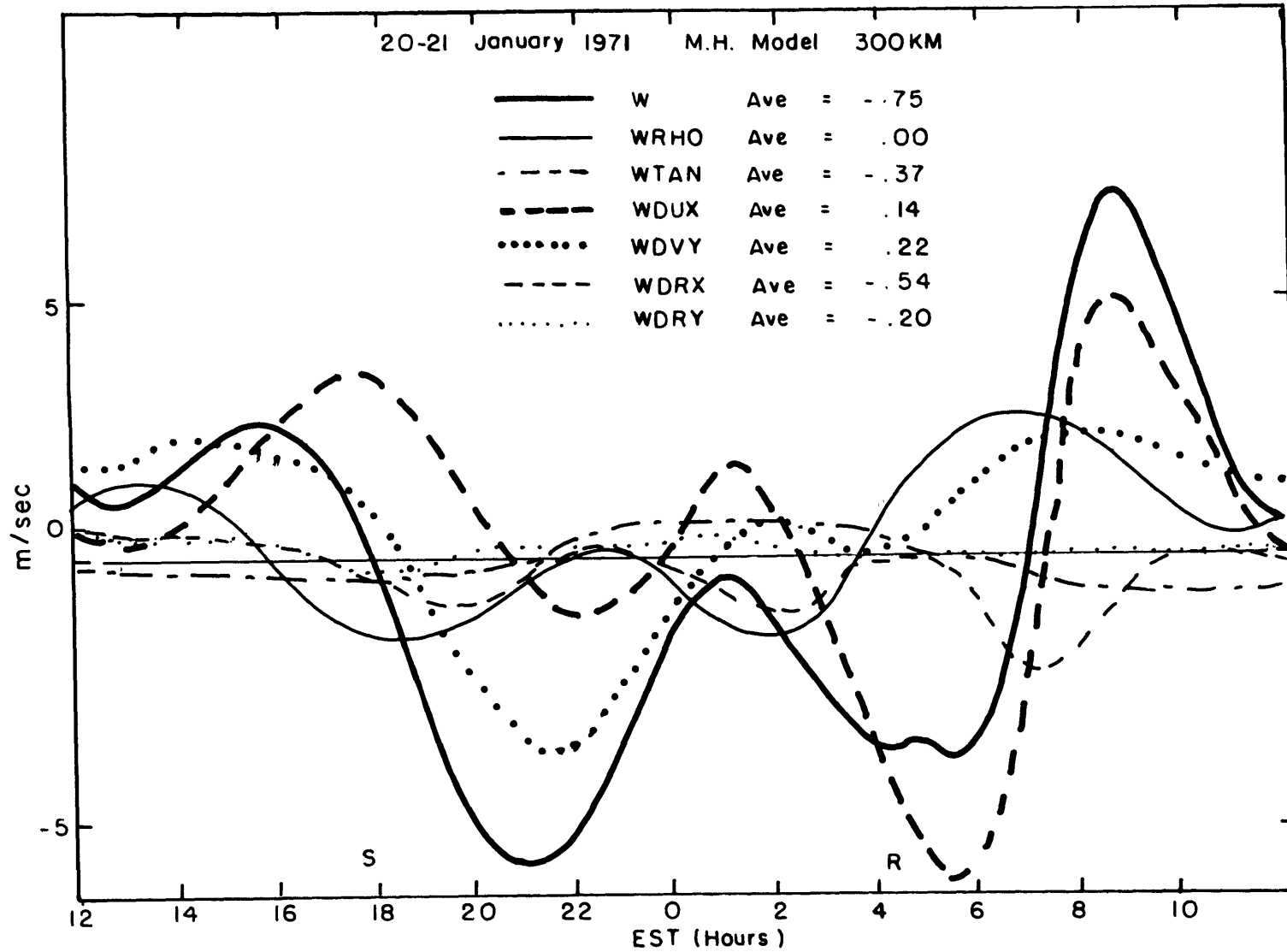


Fig. 6.19b: Same as Figure 6.10 only for January 20-21, 1971.

zonal derivatives (Figure 6.15b)) on this January day than on the June day (see Figures 6.2 and 6.4).

The meridional temperature derivatives (Figure 6.16) are also more closely correlated. The approximate average "effective" meridional temperature gradients are -116 and $-121^{\circ}\text{K}/\text{rad}$ for the OGO-6 and MSIS models. The averages for the Millstone Hill and Jacchia 1971 models are -123 and $-29^{\circ}\text{K}/\text{rad}$. The variation of the meridional temperature gradient derived for Millstone Hill still departs from the predictions of other models at night. This is due to the larger Coriolis force in the meridional equation of motion (cf. Figures 6.18b and 6.20b) and to the fact that the partial balance between the Coriolis and acceleration forces evident in the OGO-6 and MSIS models does not exist. This balance can be seen in the terms of the equations of motion on the June day (Figures 6.12a, b, 6.13a, b) and the January day (Figures 6.20a and b), and is probably a product of having a global, as opposed to a latitude strip model. Estimated non-linear terms are negligible in the winter.

The circulation at 300 km resulting from use of the MSIS pressure gradients on January 20-21, 1971 is shown in Figures 6.21a, b, and c. The circulation system is generally smaller in extent than was the case of the Millstone Hill model. Average velocities are northwards and eastwards at 39 and 56 m/sec. (For the OGO-6 model, the average velocities at 300 km are 27 m/sec north and 33 m/sec east.) A comparison of V_{Hn} at 300 km derived above Millstone Hill

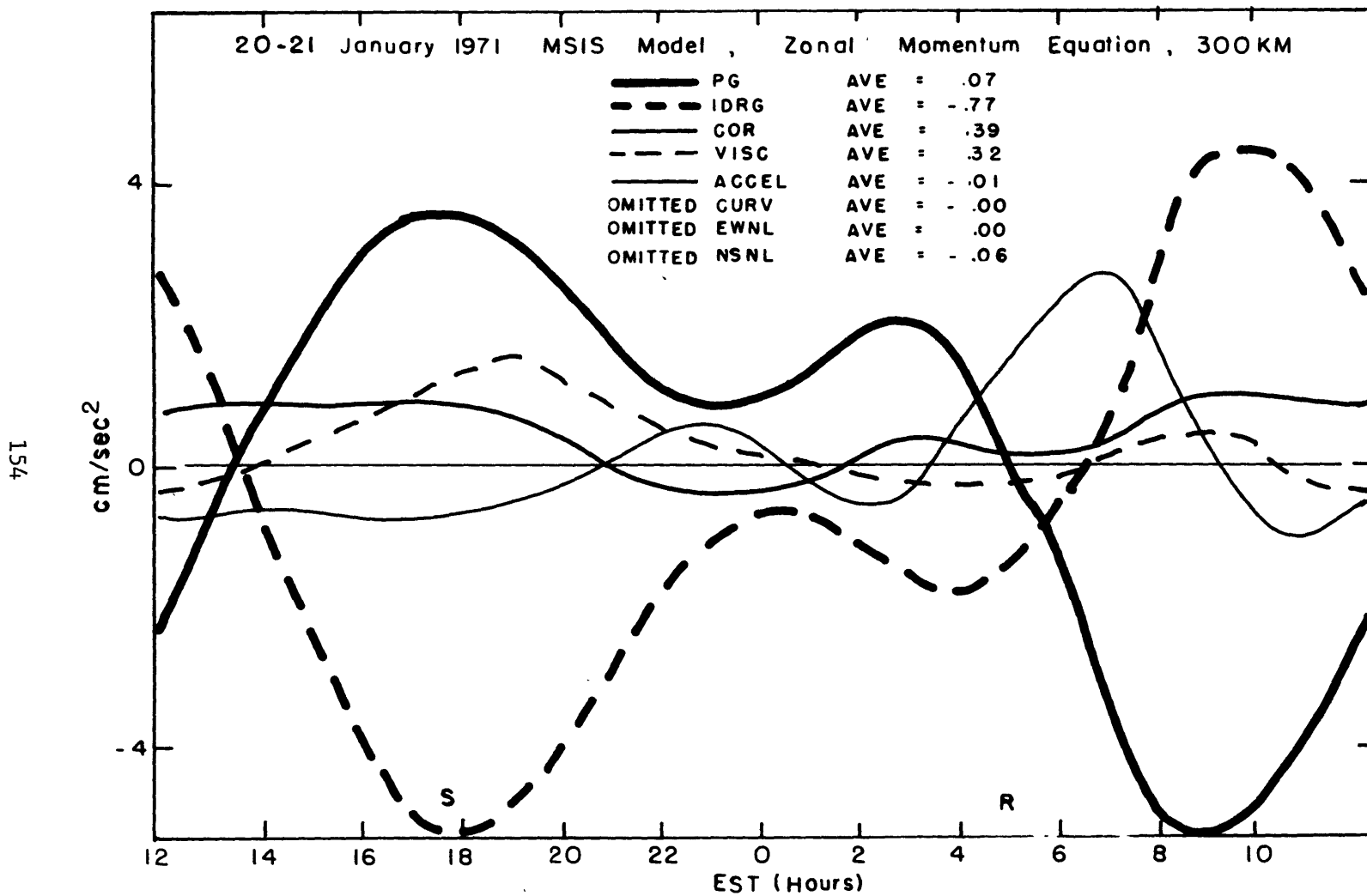


Fig. 6.20a: Same as Figure 6.7a only for January 20-21, 1971, using pressure gradients from the MSIS model.

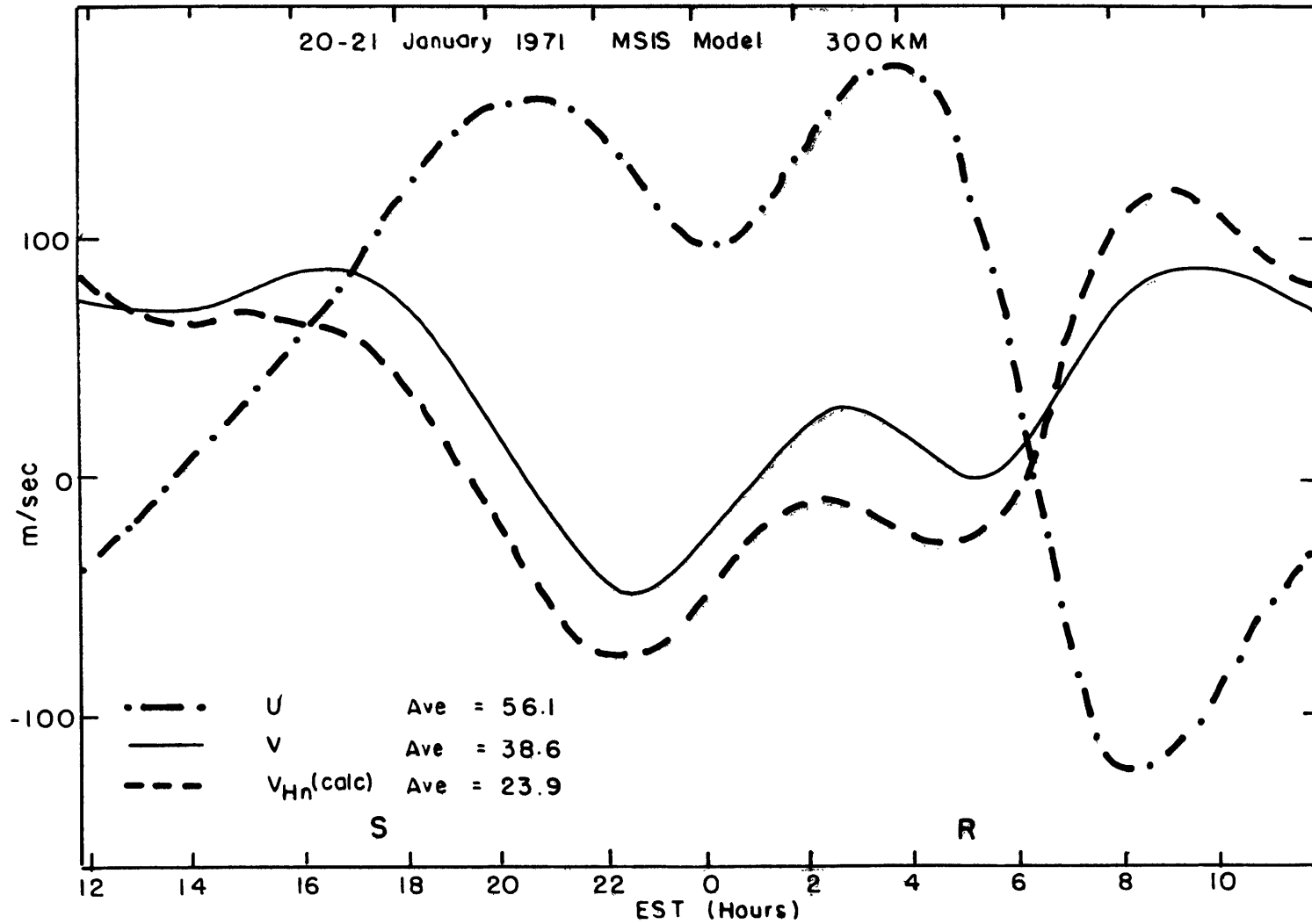


Fig. 6.21a: Horizontal velocities at 300 km calculated with MSIS model pressure gradients for January 20-21, 1971.

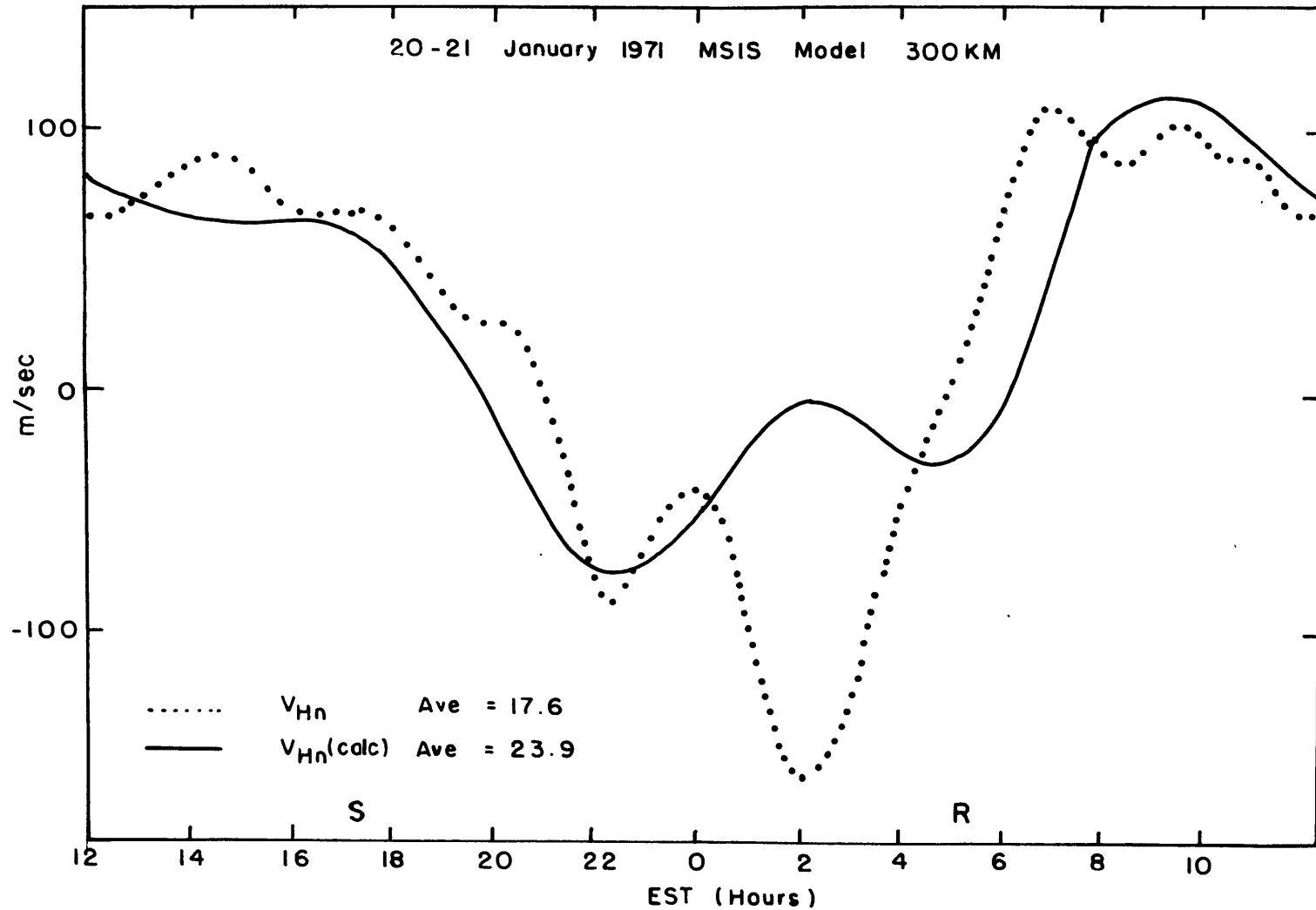


Fig. 6.21b: Experimentally derived V_{Hn} at 300 km for January 20-21, 1971 and the values found through the use of the MSIS model pressure gradients.

and predicted by the MSIS model is given in Figure 6.21b. The root mean square deviation between the two curves is 46 m/sec. The vertical velocities are downwards at night and upwards during the day with average downward velocities of 0.7 m/sec for the MSIS case (Figure 6.21c) and 1.2 m/sec for the OGO-6 case. There are two periods of downward velocity at night, arising from contributions from the two divergence terms of $WDUX$ and $WDVY$. The peak upwards velocity is about 6 hours after dawn and is largely the result of the $WDVY$ term. The major differences in the OGO-6 and MSIS models arise from differences in the term containing $\partial v / \partial y (WDVY)$. Again, both models predict this term to be large and negative around sunrise while in the Millstone Hill case it is changing sign. Aside from this, the two terms containing $u \partial \rho / \partial x$ and $\rho \partial u / \partial x$ contributed more in the Millstone Hill case because the zonal velocities were larger and had larger time gradients.

The representative diurnal circulations covered in detail in this chapter are similar in nature to the circulations found in other theoretical and experimental studies (e.g. Geisler, 1967, Kohl and King, 1967, Roble *et al.*, 1976, Amayenc, 1974, Hernandez and Roble, 1976). Detailed comparisons of average circulations will be made with other experimental studies in Chapter 8. The next chapter will outline the uncertainties in the experimental data and uncertainties resulting from the specific technique used and assumptions made.

7. UNCERTAINTIES AND CONSEQUENCES OF VARIOUS ASSUMPTIONS

7.1 Experimental Uncertainties

The zonal winds and thus part of the meridional pressure gradient depend upon the electron density and on the magnitude of the time derivative of the exospheric temperature. The uncertainty in the electron density is about 5%. The exospheric temperature is uncertain to 50°K especially at night when the signal to noise ratio of the returned echo power decreases. It is particularly difficult around sunrise to get a consensus of the value of the exospheric temperature when solving the ion heat balance equation at various altitudes. The time of the evening decrease and morning increase in temperature is uncertain to about an hour. A crude estimate of the error in the time (zonal) gradient of the pressure at sunrise and sunset can be derived by finding the error involved in a $\pm 50^{\circ}\text{K}$ change in the day-night temperature difference divided by the product of the mean exospheric temperature and the transition time between day and night ± 1 hour [see Eq. 7.4 and the definition of γ (section 5.2)].

During the summer of 1970, the difference between the minimum and maximum temperatures was about 395°K . For the summer of 1971, this figure was 355°K , and was 250°K for the winter months. Average exospheric temperatures were 1140°K , 990°K , and 1025°K for the 1970 summer, 1971 summer, and the winter months, respectively. Transition times between night and day are about 4 hours in the

summer months and 5 hours in the winter months. The deduced uncertainty in the zonal pressure gradient is approximately 28% near sunrise and sunset for summer or winter. [Sample calculation for summer of 1970: $1/\rho \partial p/\partial x (=PGX) \propto 395/1140 \cdot 4$, $\sigma_{PGX}/PGX \sim (50^2/395^2 + 25^2/1140^2 + 1^2/4^2)^{1/2} \sim .28$, $\sigma_u/u \sim (.28^2 + .05^2)^{1/2} \sim .28$] The zonal velocity in the summer near sunrise or sunset is found to be in the range ± 365 - 405 m/sec, 28% of which is about ± 105 m/sec. Winter velocities around sunrise and sunset are typically ± 230 m/sec which yields uncertainties of ± 65 m/sec.

The percent variation in the zonal pressure gradient at times removed from sunrise and sunset is approximately the same. A rough calculation assuming that there is a $\pm 25^\circ\text{K}$ error in a temperature change of 100°K and an error of ± 1 hour in the corresponding time interval of 8 hours results in a gradient variation of 28%. The net conclusion is that the zonal velocity is probably uncertain to 28% at all times.

The experimental uncertainties in the meridional velocity (v) can be deduced from the uncertainties in the magnetic meridional velocity (V_{Hn}) and the zonal velocity (u) (see Eq. 5.1). At 300 km, v can be written as

$$v = 1.03 V_{Hn} + .25 u \quad (7.1)$$

Excluding uncertainties introduced by the presence of electric fields (Section 7.2) and the proper form of the ion-neutral

collision frequency (Section 7.6), the uncertainty in V_{Hn} can be traced to estimates of neutral number densities provided by the MSIS model ($\sim \pm 10\%$ in the diffusion coefficient), experimental uncertainties in the vertical ion drift V_{iz} ($\sim \pm 5$ m/sec during the day and ± 10 m/sec at night), and experimental uncertainties in the calculation of the expected value for $V_{D//}$ ($\sim \pm 3$ m/sec). The resulting uncertainty in V_{Hn} (see Eq. 3.9) is about ± 20 m/sec during the day and ± 40 m/sec at night. The experimental uncertainty in the meridional velocity is therefore about ± 21 m/sec during the day, ± 42 m/sec at night, and ± 35 and ± 40 m/sec around sunrise and sunset for summer and winter. (Sample calculation for $u = 230$ m/sec: $\sigma_v = ((1.03*30)^2 + (.25*65)^2)^{\frac{1}{2}} = \pm 35$ m/sec).

Calculations for determining the experimental uncertainty in the vertical velocity w are carried out in a similar manner. Excluding errors introduced by assumptions about latitudinal gradients which are essential to determining $\partial v / \partial y$ (in Section 7.4), the errors in each of the terms composing w are between 30 and 40%. Roughly then, the error in w due to the experimental errors is about ± 2.5 m/sec or $\pm 4\%$.

7.2 Uncertainties Concerning Assumptions about Electric Fields

7.2.1 General Discussion

The electric field enters into the calculations in two places. The first is in the interpretation of the observed ion

drifts V_{iz} written in Eq. 3.8 and hence in the estimates of the neutral winds derived via 3.9. The electric field also alters the ion motion (Eq. 4.3) and hence the rest frame for the ions (or equivalently the ion drag term). That part of V_{Hn} attributed to electric fields can be written as

$$\begin{aligned} \Delta \vec{V}_{Hn}(E) &= [v_{nsE}(\cos I \cos 2^\circ - \sin I \cos D \sin 2^\circ) \\ &\quad + v_{ewE} \sin D \sin 2^\circ] / \cos I (\sin I \cos 2^\circ \\ &\quad + \cos I \cos D \sin 2^\circ) \simeq v_{nsE} / \sin I \end{aligned} \quad (7.2)$$

whereas the change in the horizontal ion velocity in the magnetic meridian plane can be written as

$$\begin{aligned} \Delta \vec{V}_{Hi}(E) &= u_{iE} \sin D + v_{ie} \cos D \\ &= (v_{ewE} \cos D + v_{nsE} \sin I \sin D) \sin D \\ &\quad + (v_{nsE} \sin I \cos D - v_{ewE} \sin D) \cos D \\ &= v_{nse} \sin I \end{aligned} \quad (7.3)$$

These two expressions are nearly equal since $\sin I = \sin 72^\circ = .95 \simeq 1$. Therefore, one might suppose that to a first approximation the part of the zonal neutral wind u attributable to electric fields is u_{iE} , while v_{iE} is the comparable part for the meridional neutral wind v . These initial perturbations must be altered by the effect of the Coriolis force which will serve to rotate this added wind

vector clockwise in the northern hemisphere. The wind vector must also lengthen or shorten in such a way that its projection in the plane of the magnetic meridian is approximately equal to $\Delta \vec{V}_{Hn}(E)$.

Defining δu and δv as the corrections to the first order approximations of u_{iE} and v_{iE} , Figure 7.1 illustrates the effects of the Coriolis forces and the constraint of fitting to $\Delta \vec{V}_{Hn}(E)$. Positive numbers are corrections toward the north and east. The two effects conflict in the NE and SW quadrants but combine in the NW and SE quadrants. Therefore to a second approximation, if the electric field induced ion drift in the horizontal is toward the NE or the SW, the increment to the neutral wind due to electric fields is approximately equal to the ion drift. If the ion drift is toward the NW or SE quadrants, then the change in the neutral wind will be to the right of the ion drift. The next section presents results obtained when a specific electric field model was applied.

7.2.2 Specific Example

The average electric field model for Millstone Hill of Kirchhoff and Carpenter (1975) described in Section 3.4 was used in calculations for December 8-9, 1969. In the first case, the horizontal wind in the magnetic meridian plane V_{Hn} was calculated excluding electric fields (i.e. $v_{nsE} = v_{ewE} = 0$ in Eq. 3.9). In the second case, the electric field model was used to define the motion of the ions.

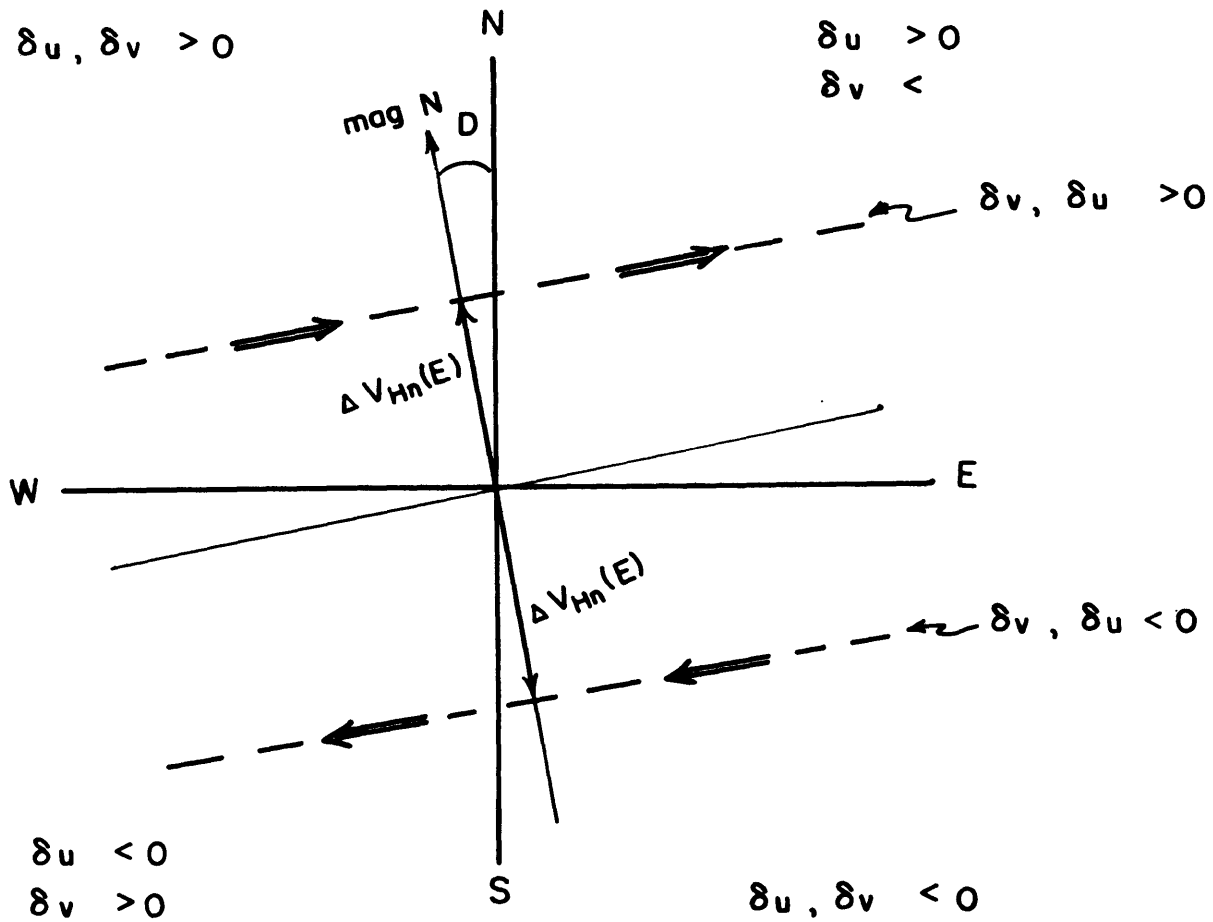


Fig. 7.1: Plot of geographic and geomagnetic coordinates illuminating the effect of Coriolis forces and the constraint of fitting to $\Delta V_{Hn}(E)$ upon the first order guess that the change in u and v due to electric fields is equal to $u_i E$ and $v_i E$.

Figure 7.2 shows the diurnal variations of u_{iE} and v_{iE} plotted against the changes in u and v brought about by including the field model. As predicted in the previous section, when the ion drift is in the NE or SW quadrants, the change in the neutral wind is usually within 5 m/sec of the ion drift. When the ion drift is in the NW quadrant, as it is for large parts of the night, the change in the neutral wind is to the right of the ion velocity, being about 10 m/sec more northwards, and up to 50 m/sec more eastwards. The change in the meridional velocity away from the first estimate is smaller than the change in the zonal velocity because the declination of the magnetic field is only 14° at Millstone Hill. The ion drift was in the SE quadrant for only about 4 hours in the afternoon, and the change in the neutral winds was approximately equal to the ion drift.

The diurnal averages of v_{iE} and u_{iE} are in the NW quadrant at 7.7 and 13.6 m/sec respectively. The diurnal averages of the change in the neutral wind v and u due to this electric field model are in the NE quadrant at 11.8 and 2.3 m/sec respectively.

The experiment was repeated for September 7-8, 1971 with strikingly similar results. It would appear that if the Kirchhoff-Carpenter average model is correct, electric fields introduce a net north-eastward velocity. However, on very quiet days, the nighttime fields are thought to be less intense than represented in the present model (Kirchhoff and Carpenter, 1976), and on other days,

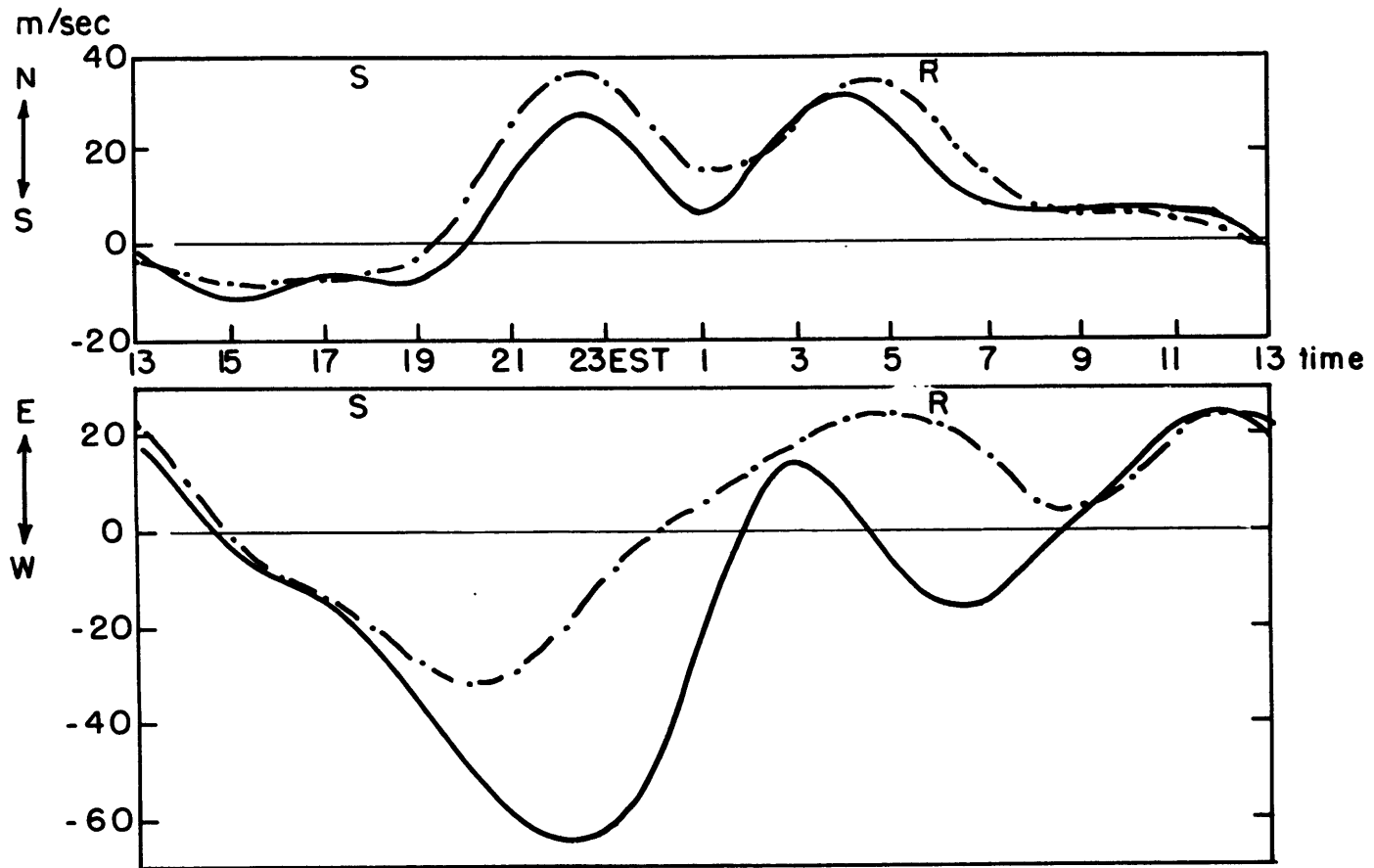


Fig. 7.2: Plot of electric field-induced ion drifts (—) from the Kirchhoff-Carpenter average model (1975) and plot of the difference between the zonal and meridional velocities with and without the field model (---) at 300 km for December 8-9, 1969 above Millstone Hill.

they may be quite variable. Therefore, for the balance of this study, the analysis undertaken ignores electric fields; this restriction must be borne in mind throughout. As regards future drift measurements, this section has shown that the change in the meridional velocity due to electric field-induced ion drifts is basically the same as the drift in the north-south direction. Therefore, if only one electric field component can be sensed, the important one to measure would be the east-west field or the north-south ion drift.

7.3 Uncertainties Introduced by the Form of the Neutral Atmospheric Model

7.3.1 General Discussion

The "effective" meridional exospheric temperature gradient was introduced in Section 5.2 and expanded upon in Section 5.4. It is directly proportional to the meridional pressure gradient at 300 km and is equal to the meridional exospheric temperature gradient if the bottom boundary atomic oxygen number density gradient is zero. As explained in Section 5.2, the Millstone Hill model assumes that σ , T_{120} , and n_j for N_2 and O_2 are constant and that their horizontal gradients are zero. The bottom boundary density for atomic oxygen $n(O)_{120}$ is constant over a day, implying the east-west gradient is zero, but varies seasonally with maximum concentrations appearing in the winter months. This variation is thought to be caused by horizontal transport of atomic oxygen from

the summer to winter hemisphere by transequatorial thermospheric winds (Mayr and Volland, 1972). Consequently, one would expect to have a positive (polewards) gradient for atomic oxygen at 120 km in the winter, and a negative gradient in the summer.

Given these assumptions, the meridional pressure gradient force can be expressed as

$$\begin{aligned} \frac{1}{\rho} \frac{\partial p}{\partial y}(z) &= \frac{kT}{\rho} \left[\sum_{j=1}^3 n_j \left\{ -\frac{\gamma_j}{T_{\infty}} \left(\ln \left(\frac{T_{120}}{T} \right) - \sigma \xi \right) \frac{\partial T_{\infty}}{\partial y} \right. \right. \\ &\quad \left. \left. - \frac{\gamma_j + \alpha_j}{T} [1 - \exp(-\sigma \xi)] \frac{\partial T_{\infty}}{\partial y} \right\} + \frac{n(0)}{n(0)_{120}} \frac{\partial n(0)_{120}}{\partial y} \right] \quad (7.4) \\ &= f(n_j, T) \frac{\partial T_{\infty}}{\partial \phi} + (kT n(0)/\rho) [(1/n(0)_{120}) \partial n(0)_{120} / \partial \phi] (d\phi/dy) \end{aligned}$$

The meridional pressure gradient is one of three unknowns solved for with three equations. It is calculated at 300 km where V_{Hn} is considered to be most accurate. However, $\partial p / \partial y$ contains two unknowns, which cannot be separated because there is no fourth equation.

Theoretically, the calculation of V_{Hn} at another altitude could be used to provide a fourth equation, but practically, the results are not sufficiently accurate to warrant this. An alternative means of handling this difficulty would be to appeal to a model (e.g., the OGO-6 or MSIS models) for the north-south bottom boundary atomic oxygen density gradient. (The Jacchia 1965 model assumes fixed conditions at 120 km, so there are no horizontal gradients in that model.) This approach is unappealing because resort is then made

to the very sources of data on which present ideas about thermospheric circulation are based and which we wish to test. Moreover, the models are themselves only approximations at low altitudes since they totally neglect important variation introduced by propagating tides (Evans, 1976). It was therefore decided to set $\partial n(0)_{120} / \partial \varphi$ to zero and find an "effective" meridional exospheric temperature gradient, $\partial T_{\infty} / \partial \varphi$, which would reproduce the meridional pressure gradient at 300 km necessary to fit V_{Hn} .

The equation for finding this "effective" gradient can be written as

$$\begin{aligned}
 \frac{1}{\rho} \frac{\partial p}{\partial y} (300 \text{ km}) &= f_{300}(n_j, T) \frac{\partial T_{\infty}}{\partial \varphi} + \frac{kT}{\rho} \frac{n(0)}{n(0)_{120}} \frac{\partial n(0)_{120}}{\partial \varphi} \frac{d\varphi}{dy} \\
 &= f_{300}(n_j, T) \frac{\partial T_{\infty}}{\partial \varphi} + g_{300}(n_j, T) r \quad (7.5) \\
 &= f_{300}(n_j, T) \frac{\partial T_{\infty}}{\partial \varphi}
 \end{aligned}$$

where r is the ratio of $[\partial n(0)_{120} / \partial \varphi] / n(0)_{120}$. The pressure gradients at other altitudes will not be the same using the "effective" gradient in place of the gradients $\partial T_{\infty} / \partial \varphi$ and $\partial n(0)_{120} / \partial \varphi$. The "effective" pressure gradient at 120 km is now zero since $f_{120}(n_j, T)$ is zero. (T goes to T_{120} , ξ goes to zero, and n_j goes to n_{j120}). At the higher altitudes where the composition is almost entirely atomic oxygen, the portion of the pressure gradient force due to the bottom boundary gradient approaches a constant value, as may be seen from Eq. 7.5. As z

increases beyond the point where the temperature is effectively isothermal and $\exp(-\sigma \xi)$ is effectively zero, the pressure gradient force will only increase approximately linearly with height in response to the $(z-120)$ term in ξ (see Eq. 7.4). It follows that the portion of the pressure gradient attributable to the bottom boundary meridional density gradient varies in altitude, being largest (100%) at 120 km and smallest at the top boundary. The net result is that if there is a non-zero bottom boundary density gradient in atomic oxygen, its effects will not be confined to the lower layers where large inaccuracies are rendered unimportant owing to the exponential increase in temperature. Instead, a decreasing percentage of the pressure gradient force above the region of exponential temperature increase will have to be offset by a change in the latitudinal temperature gradient. Specifically, if the mean meridional atomic oxygen density gradient is negative, as we suspect it to be in the summer (decreasing amount of atomic oxygen towards the summer pole), then the "effective" meridional exospheric temperature gradient required to drive the same winds will be more negative than the true gradient. Additionally, at levels below and above 300 km where the winds are matched to the observations, the "effective" pressure gradient force will be, respectively, more positive and more negative than the true pressure gradient force.

The Coriolis force term is most important at the lower altitudes, since the circulation patterns in the lower atmosphere can largely be expressed as a balance between the pressure gradient

and Coriolis forces. Unfortunately, this altitude dependence coupled to a mismatch in the pressure gradient in altitude can introduce uncertainties in the results. For example, if the "effective" meridional pressure gradient is more positive at 250 km than is really the case, then a balance between ion drag and the pressure gradient will predict a meridional velocity more negative (southwards) than it ought to be. The Coriolis term will then cause the derived zonal velocity to be more negative (westwards) than it ought to be. This more negative zonal velocity will still be evident at 300 km, where it will be compensated in the fitting of V_{Hn} by a meridional velocity that is more negative (southwards) than it should be. Figure 7.3 provides a schematic representation of these ideas.

In summary, the neglect of a negative bottom boundary gradient in atomic oxygen (in summer) results in the mean winds deduced at 300 km being more westwards and southwards than otherwise. Neglecting a positive (winter) bottom boundary density gradient will result in mean winds at 300 km being more eastwards and northwards than otherwise. Since the computed meridional mean winds tend to be more southwards in summer than they are in the winter, their seasonal difference will be more pronounced if the "effective" meridional exospheric temperature gradient is used. The magnitude of these effects will generally depend on the magnitude of the ratio $(1/n(O)_{120}) \partial n(O)_{120} / \partial \phi$. Appendix B goes over the

Figure 7.3: An illustration of the consequences of using an "effective" meridional exospheric temperature gradient

$$\frac{\partial T_{\infty e}}{\partial \varphi} = \frac{\partial T_{\infty}}{\partial \varphi} + \frac{g_{300}(n_i, T)}{f_{300}(n_j, T)} \frac{\partial n(0)_{120}}{\partial \varphi} \frac{1}{n(0)_{120}}$$

where $g/f > 0$ and decreases with increasing altitude.

Summer: minimum $n(0)_{120}$, expect $\partial n(0)_{120}/\partial \varphi < 0$

(decreasing polewards), $\partial T_{\infty}/\partial \varphi > 0$

at 250 km: $\partial n(0)_{120}/\partial \varphi < 0$

$$\implies 1/\rho(\partial p_e/\partial y) > 1/\rho(\partial p/\partial y)$$

$$\implies (v_e - v) - 1/\lambda \rho (\partial p_e/\partial y - \partial p/\partial y) < 0$$

$$\implies (u_e - u) f/\lambda (v_e - v) < 0$$

at 300 km: still have $(u_e - u) < 0$, and $V_{Hne} = V_{Hn}$

$$\implies (v_e - v) = -(\sin - 14^\circ / \cos - 14^\circ) (u_e - u) < 0$$

\implies net shift to SW

Winter: maximum $n(0)_{120}$, expect $\partial n(0)_{120}/\partial \varphi > 0$

(increasing polewards), $\partial T_{\infty}/\partial \varphi < 0$

Similar to the summer case. Change all $<$ signs to $>$ and vice versa.

Get a net shift to NE.

CONCLUSION: $\partial n(0)_{120}/\partial \varphi < 0 \implies$ net shift of winds

to SW when using $\partial T_{\infty e}/\partial \varphi$

$\partial n(0)_{120}/\partial \varphi > 0 \implies$ net shift of winds

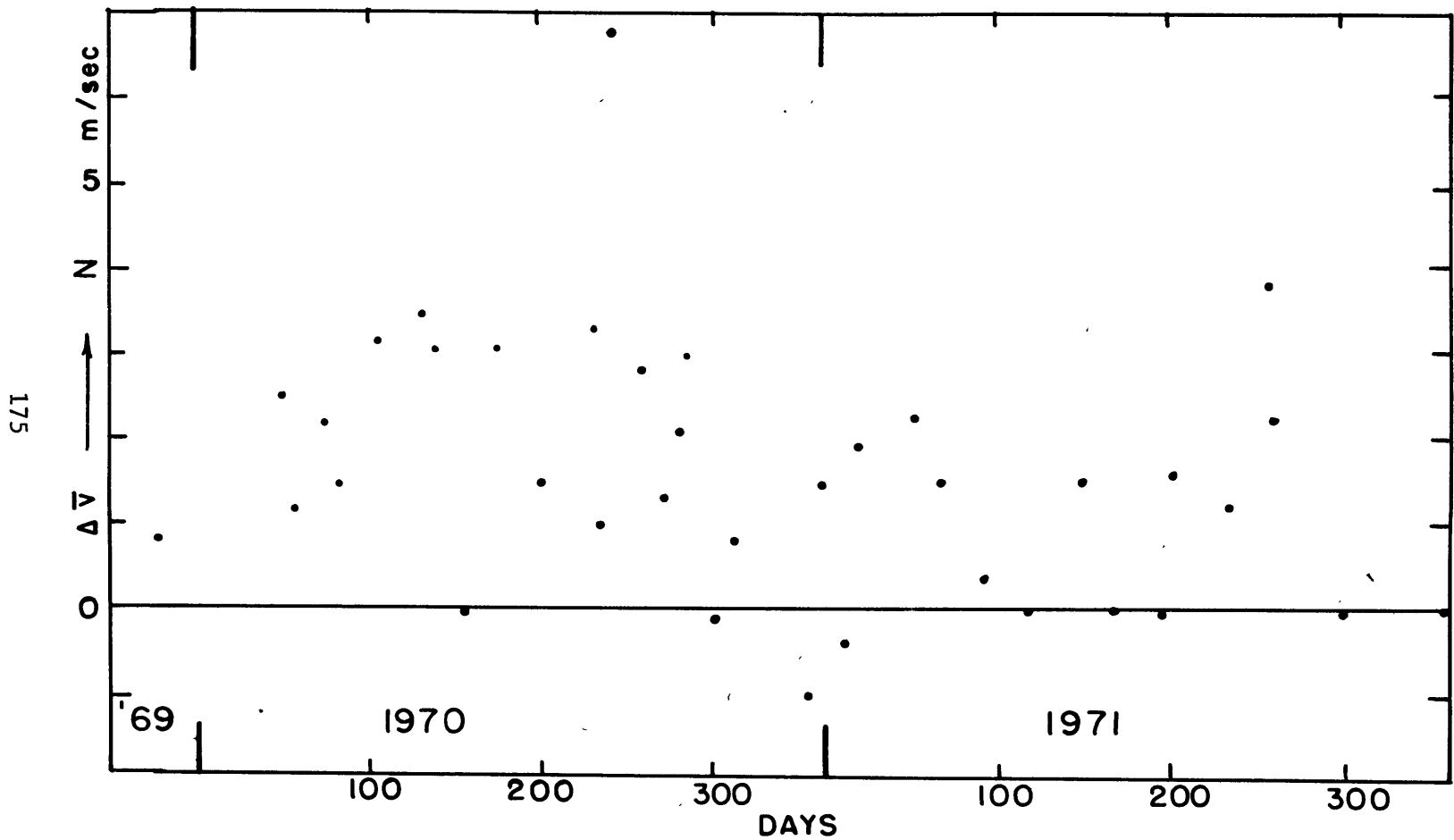
to NE when using $\partial T_{\infty e}/\partial \varphi$

specific experiments that were designed to estimate the errors that may be introduced as a consequence of using an "effective" meridional pressure gradient in the atmospheric model. The major conclusions reached were that the magnitude of the effects is larger for increasing ratios of r and/or g/f (see Eq. 7.5), and smaller for increasing absolute magnitudes of the mean meridional velocity. The change in the meridional velocity is one-fourth that in the zonal velocity because of the necessity to fit V_{Hn} at 300 km (see Eq. 7.1).

7.3.2 Corrections Made to Average Velocities

Thirty-nine days were analyzed between December 1969 and December 1971, and corrections to their mean horizontal velocities were made according to the procedures outlined in Appendix B. Figure 7.4 is a plot of the corrections to the average meridional velocity.

Most of the additions are to the north at about 1.5 m/sec, and most are less than 4 m/sec. The values remained small because either the ratio of $1/n(0)_{120} \partial n(0)_{120} / \partial \phi$ was small or the average meridional velocity was large. The corrections to the north in the winter and in the summer of 1971 are about 1 m/sec. For the summer of 1970, the corrections are about 3 m/sec. This results in an average seasonal difference of about 1 m/sec, which is approximately the scatter in the data points.



The corrections to the zonal mean velocity are just four times the size of the corrections to the mean meridional winds (see Eq. 7.1 or B.4). Therefore, the corrections are toward the east at about 8 m/sec in the summer and 4 m/sec in the winter. The seasonal difference is thus about 4 m/sec.

The corrections to the meridional velocity are only about 6% of the mean annual velocity and 1% of the seasonal variation. For the zonal velocity, the corrections are about 40% of the mean annual wind and about 5% of the annual variation. The seasonal wind variations will be discussed in more detail in Chapter 8.

7.4 Uncertainties Concerning Assumptions about Latitudinal Gradients

The calculation of the north-south non-linear term ($v \partial \vec{v} / \partial y$) or the vertical velocity via the continuity equation 4.7 requires knowledge of meridional derivations of the horizontal velocity above Millstone Hill. This implies that the velocities need to be known above at least one other latitude in order to find their meridional gradient. The general procedure which is followed is to solve the equations of motion at a latitude 0.2 degrees to the north of Millstone Hill after certain assumptions are made concerning the changes in the input data.

The assumptions made for this study were stated in section 5.5.1. Reiterating them, the electron and ion temperatures, and the plasma diffusion velocity were assumed to remain constant, as

was the derived value of $\partial T_{\infty} / \partial \phi$. The latitudinal variations of T_{∞} and $\partial T_{\infty} / \partial t$ were set by the form of Eq. 5.10, and the electron densities were assumed to decrease uniformly toward the poles at a rate of 4% in 1 degree of latitude.

Three factors were examined which could have a large effect on the magnitude of the winds at another latitude. The first factor was the effect of the changing Coriolis parameter f , which increased by 0.4% in the 0.2 degrees of latitude to the north of Millstone Hill. 0.4% of a 250 m/sec velocity is 1.0 m/sec, so it is conceivable that the changing Coriolis parameter will be an important determining factor of the size of the north-south velocity gradients.

The second factor that was studied was the effect reasonable variations in the latitudinal structure of the electron density would have on latitudinal changes in velocity. Reasonable variations were taken to be a 0.8% decrease in electron density in the 0.2 degrees to the north of Millstone Hill and a latitudinally constant electron density.

The assumption of a latitudinally constant meridional exospheric temperature gradient was examined next through the device of observing how important latitudinal changes in this gradient were in global atmospheric models such as the MSIS model. The details of the examination of these three factors for June 23-24, 1970 is in Appendix C. A comparison with the latitudinal wind differences of

the non-linear global wind system of Blum and Harris (1975) is also in Appendix C. What follows is a summary of the results.

7.4.1 Summary and Conclusions

The differences between the zonal and meridional velocities at a latitude 0.2° to the north of Millstone Hill and those at Millstone Hill are defined to be Δu and Δv , where $\Delta u \propto \partial u / \partial y$, etc. Changing the Coriolis parameter alone produced velocity differences in 0.2° of latitude of ± 1 to 2 m/sec. Typically Δu was of the same sign as v while Δv was of the opposite sign to u .

These correlations still held true when, in addition to varying the Coriolis parameters, the exospheric temperature and its diurnal gradient were allowed to vary according to Eq. 5.10. However, the magnitude of the velocity differences increased by about 50%. The inclusion of a 0.8% decrease in electron density in 0.2 degrees polewards of Millstone Hill resulted in a further increase of 20% in the magnitudes of the velocity differences. For the MSIS model the difference in velocities at the two latitudes was smaller at about ± 1 m/sec. A linear polewards decrease in the electron density increased this by 50% or more.

The diurnal variation of the changes in the east-west pressure gradient over the 0.2 degrees of latitude was very similar in the MSIS and Millstone Hill cases — perhaps fortuitously so. The MSIS model showed that changes in the meridional pressure (and hence exospheric temperature) gradient were very important over 0.2 degrees

of latitude, and that the variation around sunrise was very different from that in the Millstone Hill case. This is an indication that the assumption of a constant meridional exospheric temperature gradient is inadequate, implying that another term should be added to the form of the exospheric temperature (Eq. 5.10) to account for variations in this gradient. This inadequacy affects the north-south gradient of the meridional velocity, rendering calculations of the vertical velocity suspect. Roughly, it is expected that the vertical velocity should remain downward until after sunrise and rise to peak later in the morning, rather than rising early and maximizing upwards just after dawn. The errors introduced into the vertical velocity through uncertainty in the latitudinal structure of the electron density are about ± 2 m/sec. The errors introduced by not knowing the pressure gradients precisely at another latitude are about ± 2 m/sec, in general, with a positive bias of about 5 m/sec around sunrise and a negative bias of about 2 m/sec in the late morning hours (assuming the MSIS and OGO-6 models are reasonably accurate).

The agreement between the latitudinal differences in the meridional wind deduced from the global circulation of Blum and Harris (1975) and deduced above Millstone Hill was slight at best. This is probably a result of the fact that the velocity differences in 0.2° predicted by the Millstone Hill or MSIS models would produce physically unrealistic velocity differences of about 100 m/sec in 10 degrees of latitude if they were linearly extrapolated. The

changing latitudinal variations in the electron density, the pressure gradients, and the Coriolis parameter would have prevented such large velocity differences from occurring.

In conclusion, neither the vertical velocities nor the north-south non-linear terms can be estimated well enough to use for other purposes when radar data is the basis of a model.

7.5 Uncertainties Introduced by the Neglect of the Non-Linear Terms

To be included in the equations of motion (4.5), the non-linear terms must conform to certain stability criteria which are derived in Appendix D. Briefly, the interchange of time and longitude cause the stability criteria for the inclusion of the east-west non-linear term to be that the zonal velocity be less than about 355 m/sec. This restriction is often violated at sunrise when there are steep temperature (and pressure) gradients.

For the north-south non-linear term, the stability criteria can be met for a meridional velocity of 380 m/sec if the time step is decreased to 1 min or if the latitude step is increased to 4° . Increasing the latitude step would aggravate the already serious problems of the accuracy of assumptions about latitudinal gradients. Instead of decreasing the time step, it was decided to add one or both of the non-linear terms to the equations of motion as outside forcing functions.

The non-linear terms were computed and stored to be used in the next round of computations over 24 hours. At each step, new estimates of the non-linear terms were estimated and stored, and the fit to the experimental magnetic meridional wind V_{Hn} was adjusted. Computations of this nature involving June 23-24, 1970 and December 8-9, 1970 are reported in Appendix D. The following is a summary of the results.

Just adding the east-west non-linear term without attempting to adjust the fit to V_{Hn} , resulted in shifting the mean diurnal velocity to the north-east by about 10 m/sec for June 23-24, 1970. Adjusting the fit and continuing the iterative procedure of adding the zonal non-linear term, resulted in a net shift of the mean velocity to the south-west by about 3 m/sec.

The first inclusion of the north-south non-linear term resulted in a net shift of the mean wind to the north-west for the Millstone Hill case and toward the south-west for the MSIS model. In the attempt to adjust the fit to V_{Hn} , the Millstone Hill case diverged. The MSIS model converged in the case of a latitudinally constant electron density.

Adding both non-linear terms on December 8-9, 1969, when the north-south non-linear term was very small, resulted in convergence to a stable state where the mean velocities were less than 2 m/sec different than they were in the linear case.

7.5.1 Other Non-Linear Studies

The completely non-linear treatment of Blum and Harris (1975) has already been referred to in Section 7.4 and in Appendix C. They calculated only the average, diurnal, and semi-diurnal components of the wind, and found them to be reduced by 5 to 8% at mid-latitudes in the non-linear solution with no appreciable change in phase. Other investigators also found changes of 10% or less in the winds when non-linear terms were included.

Rüster and Dudeney (1972) described the effect of including the east-west non-linear term on the winds at the position of 45° S, 55° W. They found the effects to be significant only in the early morning hours, where there was an increase in the north-westward velocity and an earlier shift from northwards to westwards velocity. (A north-westward velocity is expected in the early morning hours for the Southern Hemisphere, and a south-westward velocity for the Northern Hemisphere.) The pressure gradients in this study were taken from the atmospheric model described by Jacchia and Slowey (1967, 1968). Calculations of the north-south non-linear term presented in Figure 5 of Rüster and Dudeney were of the order of 1 to 2 cm/sec^2 and in the direction to produce a net change in the wind towards the NW. This is similar to a change towards the SW in the Northern Hemisphere. Magnitudes of this order are found for the north-south non-linear terms of the MSIS and OGO-6 models, and for the present models in the summer months. The east-west non-

linear terms in Figure 5 of Ruster and Dudeney were only about 1 cm/sec^2 , which is about the size found for the MSIS and OGO-6 models, but which is two or three times smaller than values found in the present study.

The only completely non-linear treatment published so far is the Blum and Harris (1975) study. This is based on the Jacchia 1965 neutral atmosphere model which has a simpler latitudinal variation than later models. However, it appears that a change in latitude alone can introduce latitudinal velocity gradients of the order of 1 to 2 m/sec in 0.2° , and that reasonable latitudinal electron density differences introduce changes of the same magnitude. The latitude effect at least is present in the Blum and Harris model. It therefore seems reasonable to conclude that if the inclusion of the non-linear terms should make a 10% or less difference in the circulation pattern of the Blum and Harris study, then they should make about a 20% or less difference in the present study, allowing for exospheric temperature gradients (and thus pressure gradients) being up to two times larger than the gradients for the other models.

To summarize, the non-linear terms had to be omitted in the present study because (i) they introduced stability problems, (ii) they are not accurately known (especially the $\partial v / \partial y$ term), and (iii) it appears that they will not make a major change in the results. In particular, the average horizontal velocities should not be affected much by the inclusion of the east-west non-linear term (although the deduced meridional pressure gradient will be

affected). Adding the north-south non-linear term as well probably has little effect in winter, but may shift the average velocities to the west by as much as 40 m/sec and to the south by 10 m/sec in summer.

7.6 Effects of the Uncertainty in the Ion-Neutral Collision Frequency

As described in Section 3.2.1, the $O^+ - O$ ion-neutral collision frequency is only known within 25%. Stubbe (1968) has suggested a formulation for the collision frequency which yields values about 25% larger than those proposed by Banks (1966b), which were based on experiment and theory. Throughout this study the Banks formula has been used but an experiment was performed to determine the possible error in the event that the Stubbe approximation is more nearly correct. This was done for June 23-24, 1970, where the collision frequencies were all taken from Stubbe instead of Banks.

The first result of changing the collision frequency is a 20% reduction in the magnitude of $V_{D//}$, the diffusion velocity. The reduction is not as large as 25% because the $O^+ - N_2$ and the $O^+ - O_2$ collision frequencies remain unchanged. The average diffusion velocity decreased 21% from -30.3 to -25.1 m/sec. The reduction in $V_{D//}$ led in turn to changes in the computed values of V_{Hn} , the horizontal neutral wind parallel to the magnetic field. These changes ranged from reductions of about 35% or 40 m/sec at the

peak southwards velocity to increases of about 20% or 8 m/sec at the peak northwards velocity. The new average V_{Hn} was 16.4 m/sec ($\approx (30.3-25.1)/\cos 72^\circ = 16.8$ m/sec) more positive (northward). In addition, the ion drag coefficient in the equations of motion was increased between 15 and 22%. This did not change in the same proportion as the change in $V_{D//}$ because the neutral number densities were deduced from Millstone Hill data and not taken from the MSIS model. The new average meridional velocity was 19.7 m/sec more northwards and 11.3 m/sec more eastwards. The average meridional exospheric temperature gradient was $27^\circ\text{K}/\text{rad}$ more negative, which is in the direction to produce more northward winds. The velocities were on the whole usually smaller in magnitude by about 15%. In the early morning hours, the westward velocities were about 15% less (~ 35 m/sec) and the southward velocities about 27% less (~ 25 m/sec). The daytime northward velocities were about 35 to 40% greater (~ 10 to 15 m/sec), and the evening eastward velocities were about 3% less (~ 12 m/sec).

In summary, a 25% larger $O^+ - O$ collision frequency leads to mean diffusion velocities which are about 20% less, which in turn lead to average V_{Hn} velocities which are more positive by about 3.2 ($= 1/\cos I$) times the change in $V_{D//}$. This means the average meridional velocity is increased to the north by approximately this amount. Zonal velocities are in general small and more eastward, and meridional velocities smaller and more northwards. A 25%

decrease in the $O^+ - O$ collision frequency leads to approximately opposite effects, with velocities generally larger and more south-westwards. The magnitude of the change in the average meridional velocity is directly related to the size of the average diffusion velocity $V_{D//}$.

The average diffusion velocity is downwards throughout the year at 300 km, but approximately 15 m/sec downwards in the winter and 30 m/sec downwards in the summer. Therefore the change produced in the average meridional velocity by different collision frequencies would be twice as large in the summer as in the winter. Specifically, a 25% increase in the $O^+ - O$ collision frequency would shift the average meridional winds northward about 10 m/sec in the winter and 20 m/sec in the summer resulting in a 10 m/sec decrease in the annual variation of the winds.

As an aside, it should be noted that it was not necessary to be very careful about the precise ion composition. Assuming all ions to be O^+ did not change the results appreciably (Emery, 1975).

7.7 Total Uncertainties in the Velocities

This section will try to draw together all the uncertainties discussed in the previous sections and derive total uncertainties for daily, mean, and annual velocity variations.

7.7.1 Daily Uncertainties

The sources of uncertainty for the zonal velocity are experimental (28%), O^+ - O collision frequencies (15%), non-linear effects (15%), and electric fields (-20 m/sec at night before midnight and + 10 m/sec otherwise). The errors due to electric-fields and to the O^+ - O collision frequency are biases and will be treated separately from the more random experimental errors and errors resulting from the neglect of the non-linear terms. Random errors will be root mean squared, but biases will be added together. Thus the uncertainty in u before midnight is about ± 24 m/sec from random errors and -31 to -9 m/sec for biased errors.

In the calculation of the diffusion velocity (Eq. 3.3), the errors are about 10% from experimental sources, 10% from use of the MSIS model neutral densities, and 20% from the uncertainty in the O^+ - O collision frequency, yielding point-by-point uncertainties at 300 km of the order of $\pm 14\%$ from random errors and $\pm 20\%$ from the O^+ - O bias. The errors in the magnetic north-south wind V_{Hn} (Eq. 3.9) come from electric fields (+ 10 m/sec in the morning, +15 m/sec at night, and -10 m/sec in the afternoon), the diffusion velocity and the vertical ion drift (± 5 m/sec during the day and ± 10 m/sec at night). The resulting uncertainty is approximately ± 38 and - 10 to +42 m/sec at night and ± 20 and -14 to -6m/sec in the afternoon.

As described in Section 7.1 (Eq. 7.1), the meridional velocity v is a function of V_{Hn} and u . The uncertainty for v at night is thus ± 40 and $-18 + 40$ m/sec.

There is an uncertainty in the vertical velocity of about ± 2 m/sec from each of three sources: general experimental errors, latitudinal electron density variations, and latitudinal pressure gradient variations. Hence, the total error in w , excluding biases, is about ± 3.5 m/sec. There appear to be biasing errors as well (Section 7.4 or D.3) of about 5 m/sec upwards velocity around sunrise and 2 m/sec downwards velocity in the late morning.

7.7.2 Diurnal Average Uncertainties

The uncertainty in the daily mean of the horizontal winds will be estimated by ignoring the biasing errors of the point-by-point velocities and adding the mean biasing errors of the electric fields (2 m/sec eastwards, and 12 m/sec northwards) and the $O^+ - O$ collision frequencies (± 10 m/sec in \bar{u} and ± 10 to ± 20 m/sec in \bar{v} , the larger numbers for summer months). The electric field uncertainties assume that the Kirchhoff-Carpenter (1975) average model (Sections 3.4 and 7.2) is approximately correct. There are roughly 45 original experimental points taken throughout the 24 hour observational period which are used. Fifteen of them will be assumed to be over the sunrise or sunset period.

For the zonal velocity this procedure results in a mean uncertainty of ± 29 to ± 43 m/sec in the winter and summer months with biasing errors of -8 to +12 m/sec. (Sample calculation for summer: $\sigma^2 = [(30*24)^2 + (15*120)^2] / 45^2 \approx 43^2$). The uncertainty in the diurnal average meridional velocity is about ± 19 and -8 to + 32 m/sec for the summer months and ± 22 and + 2 to +22 m/sec for the winter months. Excluding biases, the uncertainty in the vertical velocity diurnal average is ± 0.5 m/sec.

7.7.3 Uncertainties in Seasonal Differences

This uncertainty can be estimated by removing the contribution of the $O^+ - O$ collision frequency from the biased uncertainty of the mean velocities and adding a ± 10 m/sec uncertainty from this source later (The electric field biases will cancel out.) There were about 12 summer days and 12 winter days (and 12 equinox days) in the data sample. The root mean square deviation from random errors in the mean of the 12 summer and winter days for the zonal velocity is ± 26 m/sec. It is ± 15 m/sec for the meridional velocity. The average corrections due to the form of the atmospheric model (Appendix B) will be added later.

The uncertainty in the annual average zonal velocity for 36 data points is ± 21 , -8 to + 12 m/sec. For the meridional velocity it is ± 12 m/sec plus +2 to +22 m/sec.

7.7.4 Uncertainties in the MSIS Model Velocities

The uncertainty in the velocities deduced with MSIS model pressure gradients will be derived with the assumption that this model is correct, and therefore is not a source of error. The sources of uncertainty therefore lie with the $O^+ - O$ collision frequencies (20%), and in the neglect of electric fields and the non-linear terms (10%). Thus, for example, resulting uncertainty at night for the meridional velocity is about ± 15 m/sec plus +15 to +45 m/sec. Mean daily velocities are averages of 72 points, so uncertainties in the zonal and meridional velocities are about ± 8 , -14 to +18 m/sec and ± 8 , -4 to +28 m/sec, respectively. The uncertainties in the collision frequencies and in the electric fields will cancel out in an examination of seasonal variations since their effects on winter and summer are in the same direction at about the same magnitude. So excluding these two sources of error, the uncertainty in the seasonal difference in velocities found in this study is about ± 6 m/sec for the horizontal velocities. The uncertainty in the annual averages (based on 36 days) is ± 1 m/sec plus the electric field bias of 2 m/sec to the east and 12 m/sec to the north.

8. RESULTS

Thirty-nine days between December 1969 and December 1971 were analyzed in the manner described in Chapters 2 through 5. In addition, the MSIS model pressure gradients were found for each day and used in conjunction with the Millstone Hill ionospheric data to find the resultant circulation pattern. Table 8.1 lists these 39 days, their solar conditions, and some of the results of the analysis, which will be discussed in the following sections.

8.1 Solar and Geomagnetic Conditions Encountered

The solar conditions on each day are represented by the daily 10.7 cm flux which is computed for a 24 hour period just preceding the experimental data. The 10.7 cm flux is a rough representation of the amount of solar radiation absorbed by the thermosphere for a particular day, and is positively correlated with the sunspot number. Its units are in 10^{-22} watt m^{-2} (cycle/sec) $^{-1}$. The fluxes range from 195.0 on May 18-19, 1970 to 94.4 on June 18-19, 1971. The fluxes are plotted in Figure 8.1 and show a general downward trend from 1970 to 1971 corresponding to a decrease in sunspot activity over this period.

The magnetic activity of these days is represented by the average A_p , which is computed from the K_p indices in a 24 hour period centered 6 hours before the midpoint of the experimental data. The K_p index is a 3-hour planetary index designed to measure the

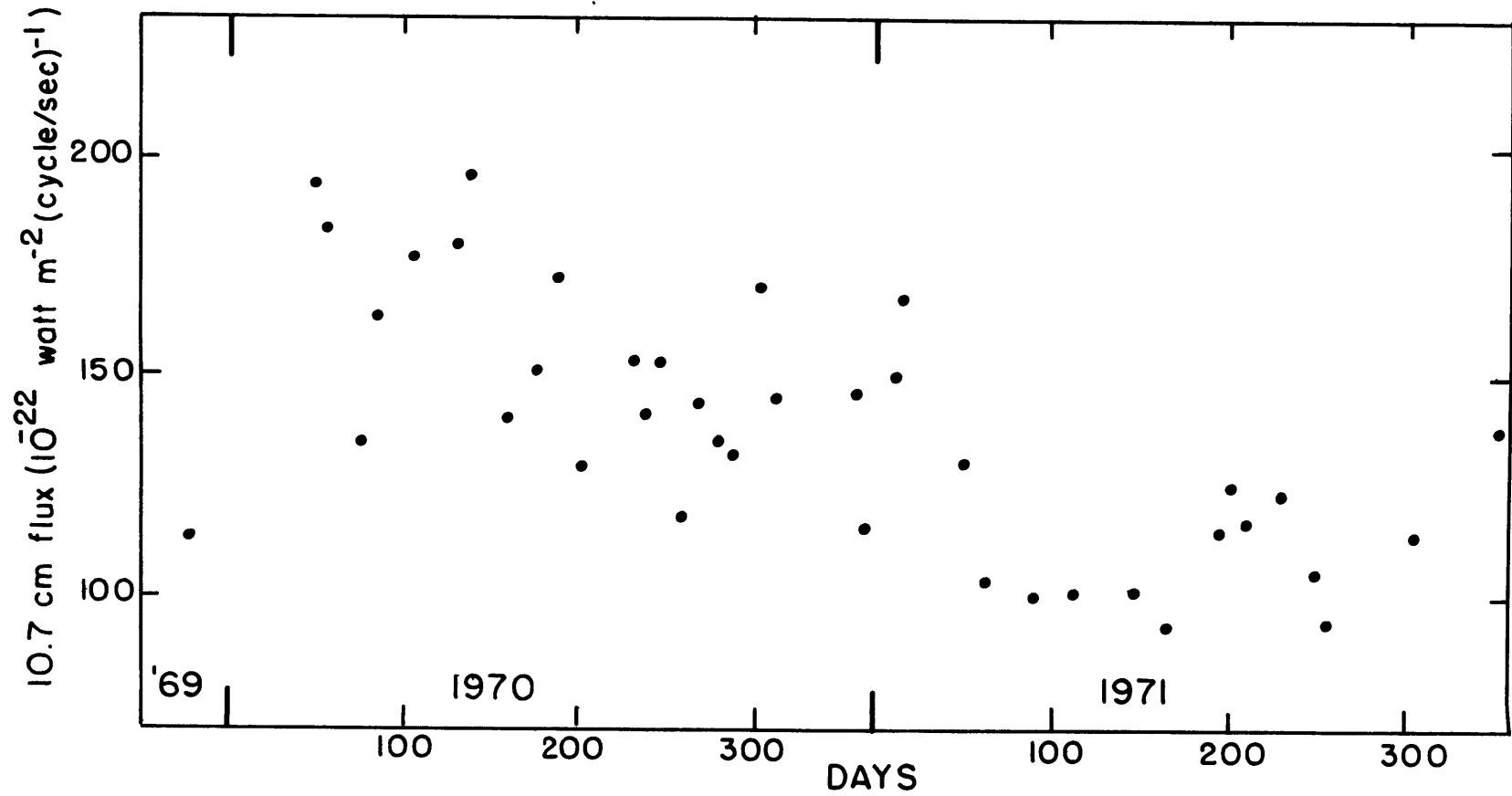


Fig. 8.1: Average daily 10.7 cm solar flux values computed 24 hours previous to each of the days analyzed.

irregular variations in magnetograms after local effects have been removed. It is intended to be a measure of geomagnetic activity at high latitudes and depends upon fluctuations in the auroral electrojets. It is deduced from 12 stations ranging in geomagnetic latitude from 80 to 63° (Lincoln, 1967). It is a good average index for most of the Northern Hemisphere (since 11 of the stations are there), but cannot pinpoint substorm activity, which may affect a local area for a few hours, especially at night. The K_p scale ranges from 0 to 9 in steps of 1/3 and is roughly a log scale of magnetic activity. The a_p index is directly related to the K_p index, but is linear and runs from 0 to 400. A_p is a 24 hour average of a_p which, like K_p , is a 3-hour index.

The activities ranged from and exceptionally quiet A_p of 2.1 on July 28-29, 1971, to a storm day of 49.2 (average $1 K_p \sim 5$) on August 17-18, 1970. The next largest average A_p was a moderate 23.6 ($K_p \sim 4$) on March 30-31, 1971. Since electric fields are assumed to be zero, the present analysis may not suffice for magnetically active days. As a result, three days were removed from the final analysis, but remain in Table 8.1 and some of the plots for the sake of interest. The three days were August 17-18, 1970, October 31-November 1, 1970, and December 22-23, 1971. The August day was mentioned previously as having the largest average A_p value. The October day was distinguished by large (75 m/sec) upward drifts of the ions for about 4 hours around midnight. This is suggestive of substorm activity, although the average A_p index was quite low at 3.4. The upward drifts were probably a result of

Table 8.1: List of days analyzed, their geomagnetic and solar conditions, and average values derived from the Millstone Hill (M.H.) and MSIS models.

Date dayno	A _p	F107*	(no./cm ³)		$\frac{1}{n(O)_{120}}$	$\frac{\partial n(O)_{120}}{\partial \phi}$	T _∞ (°K)	(m/sec)		
			M.H.: n(O) ₁₂₀	MSIS: n(O) ₁₂₀				\bar{u}	\bar{v}	\bar{w}
08-09, Dec, 1969				1.349E11	0	962.5	27.6	1.5	-.36	
342	10.2	114.3	1.056E11		-.058	919.8	60.6	35.8	-.57	
17-18, Feb, 1970				1.054E11	0	1093.5	19.5	5.0	-.33	
48	12.2	193.7	1.028E11		-.144	1070.5	25.3	11.8	-.41	
23-24, Feb, 1970				.917E11	0	1019.7	24.8	18.9	-.43	
54	6.7	183.8	1.027E11		-.092	1063.1	21.7	4.8	-.50	
17-18, Mar, 1970				.850E11	0	1105.0	-19.5	-31.5	-.66	
76	5.6	135.7	.943E11		-.202	1042.8	-2.2	-16.1	-.54	
23-24, Mar, 1970				.798E11	0	1077.7	4.7	5.6	-.43	
82	2.6	163.1	.969E11		-.097	1070.8	-1.3	-17.6	-.61	
14-15, Apr, 1970				.661E11	0	1085.8	-19.0	-28.6	-.94	
104	3.4	178.6	.862E11		-.310	1131.8	-18.4	-37.5	-.80	
12-13, May, 1970				.528E11	0	1145.3	-79.2	-53.5	-1.54	
132	13.2	179.6	.678E11		-.668	1197.9	-77.3	-84.0	-1.30	
18-19, May, 1970				.474E11	0	1201.3	-18.0	-51.5	-1.40	
138	4.9	195.0	.671E11		-.552	1191.2	-42.7	-80.6	-1.62	
10-11, Jun, 1970				.347E11	0	1126.3	-60.9	-96.9	-2.89	
161	5.6	140.4	.557E11		-.605	1125.8	-61.4	-82.6	-1.61	
23-24, Jun, 1970				.293E11	0	1100.8	-5.0	-41.7	-1.18	
174	4.3	150.1	.546E11		-.545	1114.9	-34.7	-69.6	-1.43	

*F107 = daily 10.7 cm solar flux.

Table 8.1 continued

Date	A _p	F107	M.H.: MSIS:	(no./cm ³) n(O) ₁₂₀	$\frac{1}{n(O)_{120}}$	$\frac{\partial n(O)}{\partial \phi}_{120}$	T _∞ (°K)	(m/sec)		
Dayno								\bar{u}	\bar{v}	\bar{w}
07-08, Jul, 1970				.301E11	0		1155.4	-67.6	-95.0	-1.37
188	5.5	171.3		.565E11	-.536		1129.4	-55.1	-67.2	-1.24
18-19, Jul, 1970				.329E11	0		1094.3	-17.9	-58.2	-.64
199	4.4	129.1		.573E11	-.454		1060.9	-47.5	-76.3	-1.19
17-18, Aug, 1970				.624E11	0		1275.3	-37.3	-64.2	.08
229	49.2	153.9		.684E11	-.910		1127.7	-89.5	-92.4	-1.64
24-25, Aug, 1970				.695E11	0		1144.9	-77.2	-64.5	-2.09
236	5.6	140.9		.792E11	-.295		1038.5	-55.2	-43.3	-.42
31 Aug - 01 Sep 1970				.808E11	0		1160.1	-9.3	-12.5	-.16
243	18.0	153.5		.839E11	-.438		1074.3	-40.4	-49.2	-.34
16-17, Sep 1970				.934E11	0		1041.1	-33.4	-24.2	-.74
259	7.9	118.2		.961E11	-.234		997.7	-21.0	-42.6	-.37
28-29, Sep, 1970				1.106E11	0		1081.1	28.5	28.4	-.30
271	4.4	144.6		1.097E11	-.109		1019.3	-4.6	-24.1	-.40
05-06, Oct, 1970				1.148E11	0		1035.6	16.5	3.8	-.30
278	5.7	135.0		1.127E11	-.124		1009.8	-1.9	-25.5	-.30
13-14, Oct, 1970				1.289E11	0		1076.7	10.5	7.0	.06
286	10.2	132.5		1.156E11	-.173		1015.7	3.5	-19.9	-.21
31 Oct-01 Nov, 1970				1.493E11	0		1158.9	-35.1	-69.0	-.66
303	3.4	170.2		1.268E11	.034		1022.6	23.4	9.7	-.51
08-09, Nov. 1970				1.544E11	0		1104.1	.0	.2	.13
312	5.9	145.6		1.213E11	-.041		999.6	35.4	9.6	-.42
21-22, Dec, 1970				1.357E11	0		1050.4	35.2	18.3	.10
355	4.6	147.5		1.077E11	.068		953.8	82.2	35.2	-.82
28-29, Dec, 1970				1.299E11	0		1027.7	9.4	23.6	-.40
362	16.6	117.6		.992E11	-.117		929.2	70.0	35.5	-.56

Table 8.1 continued

Date	A _p	F107	M.H.: MSIS:	(no./cm ³) n(O) ₁₂₀	$\frac{1}{n(O)_{120}} \frac{\partial n(O)_{120}}{\partial \phi}$	T _∞ (°K)	(m/sec)		
Dayno							\bar{u}	\bar{v}	\bar{w}
11-12, Jan, 1971				1.244E11	0	1012.1	37.7	34.0	-.63
11	5.5	149.3		1.007E11	.043	944.6	62.8	46.4	-.80
20-21, Jan, 1971				1.123E11	0	1020.8	50.4	30.2	-.75
20	20.2	168.5		.978E11	-.175	991.8	56.1	38.6	-.75
19-20, Feb., 1971				.914E11	0	1039.6	-3.6	-4.9	.23
50	11.3	130.7		.926E11	-.148	945.9	25.0	11.2	-.23
08-09, Mar, 1971				.762E11	0	964.8	-26.4	-40.4	.10
67	9.2	104.2		.877E11	-.208	915.7	.2	-18.6	-.23
30-31, Mar, 1971				.739E11	0	1008.2	-76.6	-76.1	-.91
89	23.6	101.2		.787E11	-.533	956.1	-38.1	-32.9	-.17
27-28, Apr, 1971				.532E11	0	1023.5	-75.9	-99.9	-.82
117	15.9	102.1		.669E11	-.608	967.5	-57.9	-66.4	-.69
27-28, May, 1971				.322E11	0	915.8	-23.8	-49.5	-.80
147	2.2	102.4		.568E11	-.373	922.4	-35.5	-44.0	-.65
18-19, Jun, 1971				.260E11	0	938.0	-66.2	-108.7	-.71
169	5.3	94.4		.502E11	-.558	935.8	-54.0	-66.1	-.79
14-16, Jul, 1971				.290E11	0	1017.9	-95.6	-127.0	-.96
195	7.6	114.7		.528E11	-.526	958.5	-65.6	-62.5	-.69
20-21, Jul, 1971				.293E11	0	992.0	-4.4	-51.5	-1.03
201	3.8	126.8		.562E11	-.399	958.4	-33.7	-47.6	-.77
28-29, Jul, 1971				.333E11	0	1057.1	-87.5	-108.2	-3.24
209	2.1	117.5		.602E11	-.215	920.6	-26.7	-27.6	-.68

Table 8.1 continued

Date dayno	A _p	F107	M.H.: MSIS:	(no./cm ³)	$\frac{1}{n(O)_{120}}$	$\frac{\partial n(O)_{120}}{\partial \phi}$	T _∞ (°K)	(m/sec)		
				n(O) ₁₂₀				\bar{u}	\bar{v}	\bar{w}
19-20, Aug, 1971				.522E11	0		983.5	2.3	-23.2	-1.03
231	2.3	123.4		.735E11	-.125		914.9	-15.5	-25.7	-.49
07-08, Sep, 1971				.764E11	0		994.0	-37.8	-29.6	-.97
250	17.5	106.7		.823E11	-.396		932.9	-38.5	-37.2	-.13
10-11, Sep, 1971				.804E11	0		992.9	-34.3	9.1	-2.14
253	4.0	95.0		.865E11	-.161		884.7	-28.0	-32.1	-.11
02-03, Nov, 1971				1.252E11	0		972.9	59.6	46.4	-.88
306	3.7	111.4		1.108E11	.002		875.2	33.8	9.4	-.19
22-23, Dec, 1971				1.289E11	0		938.3	-56.8	-139.6	-.93
356	16.1	138.6		.962E11	-.137		901.0	64.4	38.8	-.71

electric field drifts perpendicular to the magnetic field and directed northwards, but were interpreted in the present analysis as being the result of large southward neutral winds. The average A_p for the third day eliminated (December 22-23, 1971), was again not especially high being only 16.1. However, this day appears to be characterized by intense particle precipitation that caused the electron densities and temperatures to be increased above their normal values at lower altitudes. The electron temperature was seen to decrease to a slight minimum around 450 km and then increase with altitude as usual. The ion drifts were upwards for about 17 hours from 1900 LT to 1200 LT, reaching a peak of 54 m/sec around 0720 LT. Again, these were interpreted by the program as resulting from large southward winds. In this case the interpretation may be correct, since there was obviously a large amount of heat deposited at high latitudes. Since, however, none of these days could be characterized as normal quiet days, they were included here only for interest and were excluded in the final calculation of the seasonal differences.

8.2 Exospheric Temperature

The daily average exospheric temperature, $\overline{T_\infty}$, is a function of season (length of day), solar flux, and magnetic activity, and is plotted in Figure 8.2a. The dots are MSIS model averages, and the x's are deduced from the Millstone Hill data in the manner described in Section 3.1.2. On average the Millstone Hill values are about 63⁰K

larger than the MSIS model values. In part this difference may be attributed to the effect of the new B mode corrections which served to raise $\overline{T_{\infty}}$ by 50-75°K in winter and ~25°K in summer. Figure 8.2b is a plot of the mean exospheric temperatures deduced between November 1969 and March 1971 at the French incoherent scatter station at St. Santin (44.6°N), and at Millstone Hill (42.6°N). The previous values for Millstone Hill and the values for St. Santin were taken from a study by Salah et al (1976). The previous values of the temperatures at Millstone Hill were derived from unsmoothed data using the old B mode ion and electron temperature corrections and taking neutral number densities from the Jacchia 1971 model. There were also minor differences in the ion-neutral collision frequency used and in the analysis procedure, but the biggest difference between the past and the present study was the revised B mode correction procedure (Appendix A). In the comparison made by Salah et al (1976), the Millstone Hill temperatures were generally about 30°K lower than those at St. Santin and the annual variation was about ±94°K compared to a variation of ±60°K for St. Santin. The exospheric temperatures derived in the present analysis are generally in better agreement with the St. Santin values.

The seasonal variation in $\overline{T_{\infty}}$ in Figure 8.2a appears to be over 150°K for 1970, but is masked by changes in the solar flux in 1971. The effect of the magnetic activity is most striking on the one storm day, August 17-18, 1970, which had the largest average Millstone Hill value of $\overline{T_{\infty}}$ at 1275°K. This is about 75°K larger

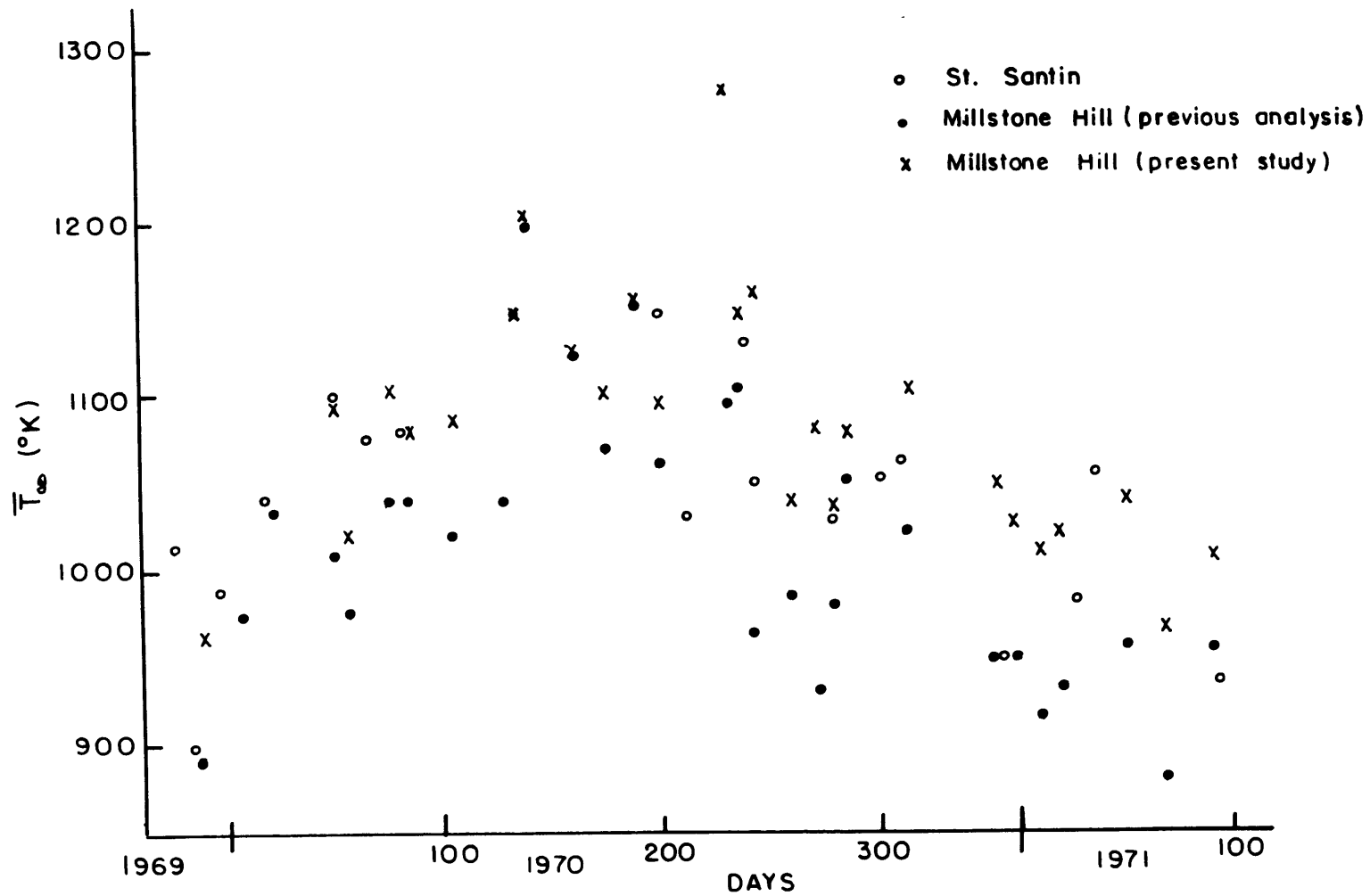


Figure 8.2b: Comparison of the diurnal average exospheric temperatures above St. Santin (44.6°N) and Millstone Hill (42.6°N). The values from St. Santin and from the previous analysis at Millstone Hill were taken from Fig. 3 of Salah *et al* (1976).

than the next largest value of $\overline{T_{\infty}}$ found for May 18-19, 1970, the day with the largest solar flux. The lowest daily average exospheric temperatures were encountered in the early summer of 1971 on two days characterized by low solar flux and low magnetic activity. The uncertainty in the average exospheric temperature for Millstone Hill is about $\pm 15^{\circ}\text{K}$.

As described in Chapter 6, the day-to-night difference in the exospheric temperature is largest in the summer and least in the winter. Differences varied between a low of 200°K in the winter to a high of 450°K in the summer. In general, the rise and fall of the temperatures was much faster in summer than in winter. This combined with the larger day-to-night difference, resulted in much larger zonal pressure gradients and thus zonal velocities.

8.3 Zonal Velocities

The zonal velocities are particularly large after dawn. On five summer days, the computed westward velocity at 300 km after dawn reached values greater than 600 m/sec. On seven other days, mostly in the summer, the zonal velocity reached values greater than 400 m/sec. These large velocities would not have been allowed in a finite difference scheme that included the zonal non-linear term in an implicit fashion. That is not to say, however, that such velocities cannot occur in the real atmosphere. They can exist, and they represent waves traveling faster than the major

diurnal wave. Sunset and sunrise are not gradual processes. Sunrise, in particular, is an abrupt event that is followed by rapid increases in electron temperatures and densities (see Figure 6.14). Its onset could thus give rise to short-lived gravity waves which travel faster than the sun. Nevertheless, the results obtained on days which have large westward velocities should be viewed with some caution.

Figure 8.3a is a plot of the average zonal velocities at 300 km deduced for all the days. A harmonic analysis of 36 of the days yielded

$$\begin{aligned} \bar{u} = & -14.4 + 43.3 \cos \left(\frac{2\pi}{365} (\text{dayno}-363) \right) \\ & + 3.0 \cos \left(\frac{4\pi}{365} (\text{dayno}-4) \right) \\ & + 7.9 \cos \left(\frac{6\pi}{365} (\text{dayno}-45) \right) \quad (\text{m/sec}) \end{aligned} \quad (8.1)$$

This fit is also plotted in Figure 8.3a. In general, the averages are eastwards in the winter at about 25 m/sec and westwards in the summer at about 50 m/sec, yielding a seasonal difference of about 75 m/sec. (The harmonic analysis predicts a difference of 87 m/sec). December 22-23, 1971 is a major exception to the above with an average velocity of 57 m/sec to the west. The average eastward velocity was as high as 60 m/sec on November 2-3, 1971, while the average westward velocity was as high as 96 m/sec on July 14-16, 1970. All ten of the days with averages larger than 40 m/sec to the west were characterized by westward velocities larger than 375 m/sec after dawn. The annual average zonal velocity is about 14 m/sec westwards.

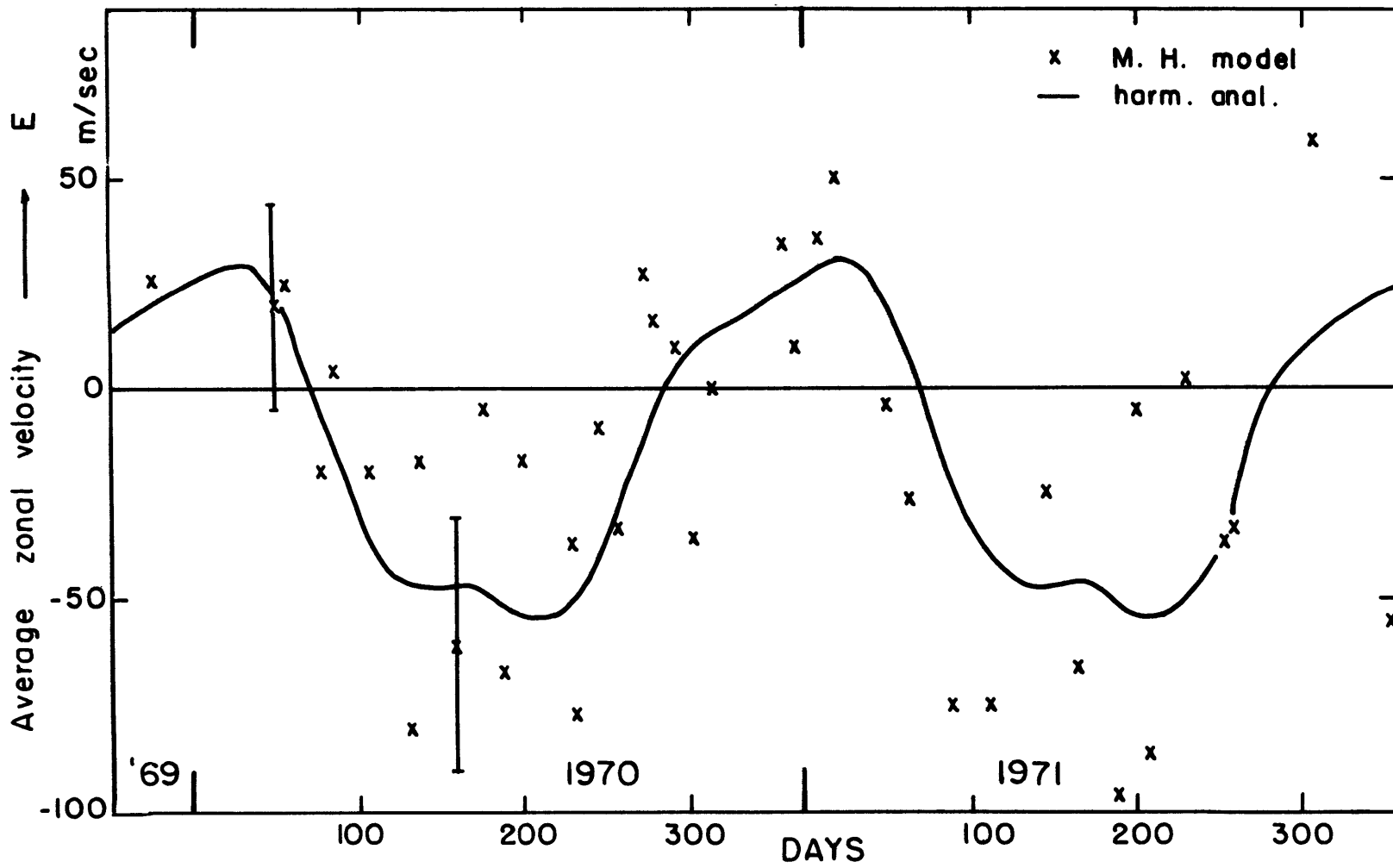


Fig. 8.3a: Average zonal velocities at 300 km calculated above Millstone Hill and a harmonic analysis of all but 3 of the data points.

Figure 8.3b is similar to Figure 8.3a, but shows the average zonal circulation resulting from pressure gradients that were determined by the MSIS model. A harmonic analysis of the velocities for 36 days

$$\begin{aligned} \bar{u} = & -3.3 + 60.4 \cos \left(\frac{2\pi}{365} (\text{dayno}-352) \right) \\ & + 13.3 \cos \left(\frac{4\pi}{365} (\text{dayno}-181) \right) \\ & + 1.8 \cos \left(\frac{6\pi}{365} (\text{dayno}-61) \right) \quad \text{m/sec} \end{aligned} \quad (8.2)$$

is also plotted. The zonal velocities deduced from the MSIS model at 300 km were less than 315 m/sec every day except for August 17-18, 1970, when they attained a westwards velocity of 370 m/sec after dawn. The average zonal velocities varied fairly smoothly from a peak eastwards velocity of 77 m/sec on May 12-13, 1970. The average westward velocity was highest on August 17-18, 1970 at 90 m/sec, but this was the storm day. The average velocities appeared to be about 10 m/sec smaller in the summer of 1971 than they were in the summer of 1970. This may be the result of decreasing pressure gradients which reflect decreasing day-to-night temperature differences resulting from the smaller solar flux. The net summer-to-winter difference is about 110 m/sec and the annual average is about 3 m/sec westwards.

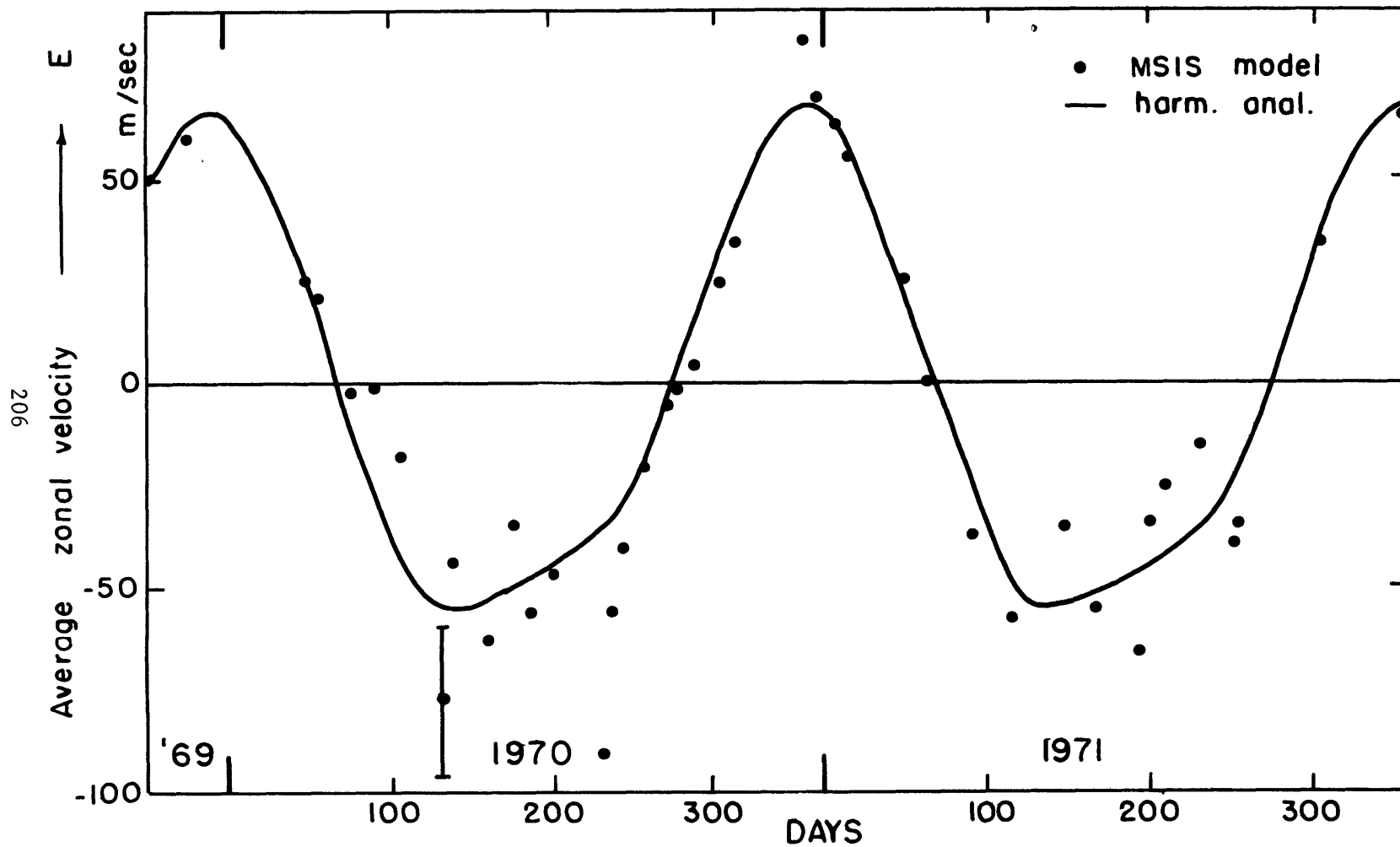


Figure 8.3b: Average zonal velocities at 300 km computed using the MSIS atmospheric model. Also plotted is the harmonic analysis of all but 3 points in the data set.

8.4 Meridional Velocities

Figures 8.4a and b are plots of the average meridional velocities at 300 km for the Millstone Hill and MSIS model cases together with their harmonic analyses. For the Millstone Hill model, the velocities are polewards (northwards) in the winter at about 20 m/sec and equatorwards (southwards) in the summer and equinox months. Both October 31-November 1, 1970 and December 22-23, 1971 have large mean southward velocities at 69 and 140 m/sec respectively, the latter being the largest of the data set. Discounting these two and the August 17-18, 1970 day, the average southward summer velocities appear to be about 65 m/sec for 1970 and 75 m/sec for 1971, yielding an average summer-to-winter velocity difference of about 90 m/sec. A harmonic analysis of the 36 days in the two year period yielded

$$\begin{aligned}\bar{v} = & -23.9 + 53.3 \cos (2\pi/365 (\text{dayno}-345)) \\ & + 9.4 \cos (4\pi/365 (\text{dayno}-87)) \\ & + 11.2 \cos (6\pi/365 (\text{dayno}-25)) \quad \text{m/sec}\end{aligned}\tag{8.3}$$

for the Millstone Hill model results.

Figure 8.5a is a plot of the maximum electron density at noon local time. The concentrations are larger in the winter than they are in the summer, the difference being about 9×10^5 electrons/cm³ or about $\pm 50\%$. Rishbeth and Setty (1961) have suggested that this is due to an increase in the ratio of atomic oxygen (the

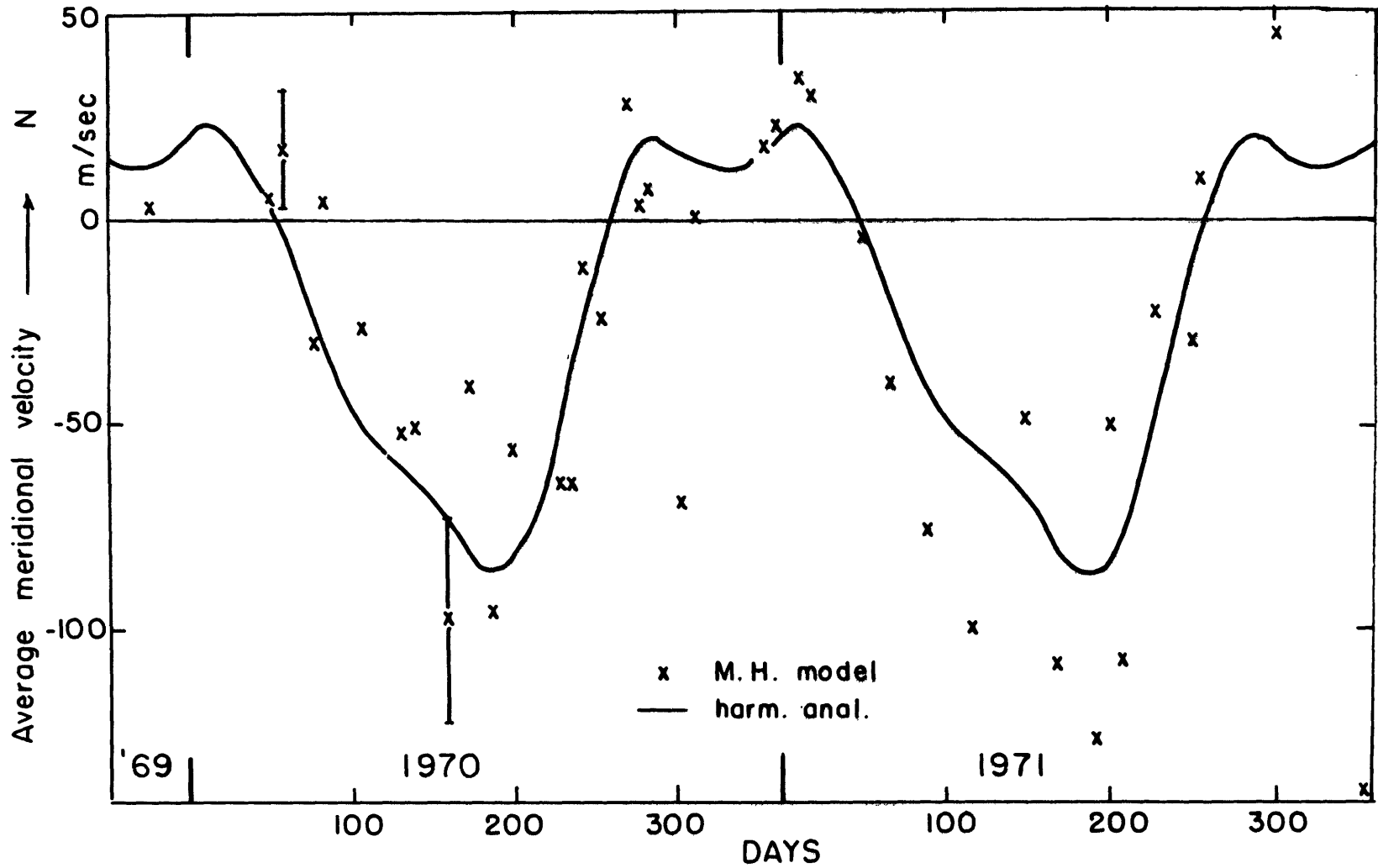


Figure 8.4a: Average meridional velocities at 300 km above Millstone Hill and a harmonic analysis of all but 3 of the 39 days plotted.

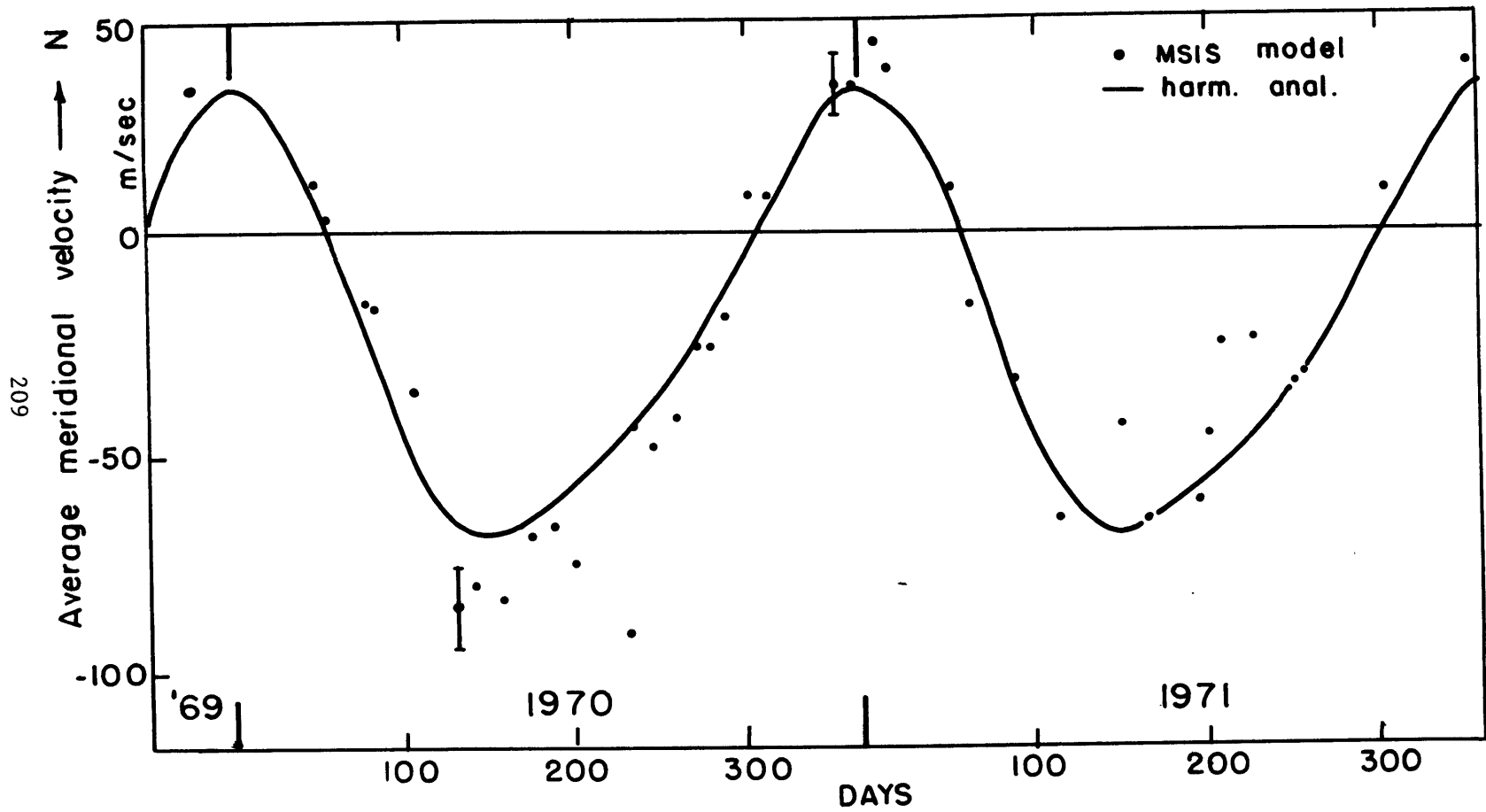


Figure 8.4b: Average meridional velocities at 300 km computed using the MSIS atmospheric model. Also plotted is a harmonic analysis of 36 of the 39 days present.

ionizable constituent) to molecular nitrogen which is responsible for loss through charge-exchange. (see Section 1.2).

Figure 8.5b is a scatter diagram of the noon maximum electron densities and the average meridional wind at 300 km. As anticipated, there is a correlation between these quantities with high electron densities associated with northward winds and low densities with southward winds.

The increase of southwards velocity from 1970 to 1971 is somewhat surprising since decreasing solar activity should lead to smaller gradients and thus smaller velocities. This expectation is borne out in the MSIS model meridional velocity averages which appear to decrease from a summer average of 75 m/sec southwards in 1970 to 50 m/sec southwards in 1971. The average velocities in the winter are northwards at about 30 to 40 m/sec, yielding a seasonal difference of about 100 m/sec. The harmonic analysis of the MSIS model velocities resulted in

$$\begin{aligned} \bar{v} = & -22.3 + 49.8 \cos (2\pi/365 (\text{dayno}-356)) \\ & + 9.6 \cos (4\pi/365 (\text{dayno}-17)) \\ & + 0.0 \cos (6\pi/365 (\text{dayno}-58)) \end{aligned} \quad (8.4)$$

The average meridional velocities deduced for Millstone Hill are simply a reflection of the average horizontal velocities in the plane of the magnetic meridian, $\overline{V_{Hn}}$. These velocities are calculated at 300 km from the vertical ion drift V_{iz} and the diffusion

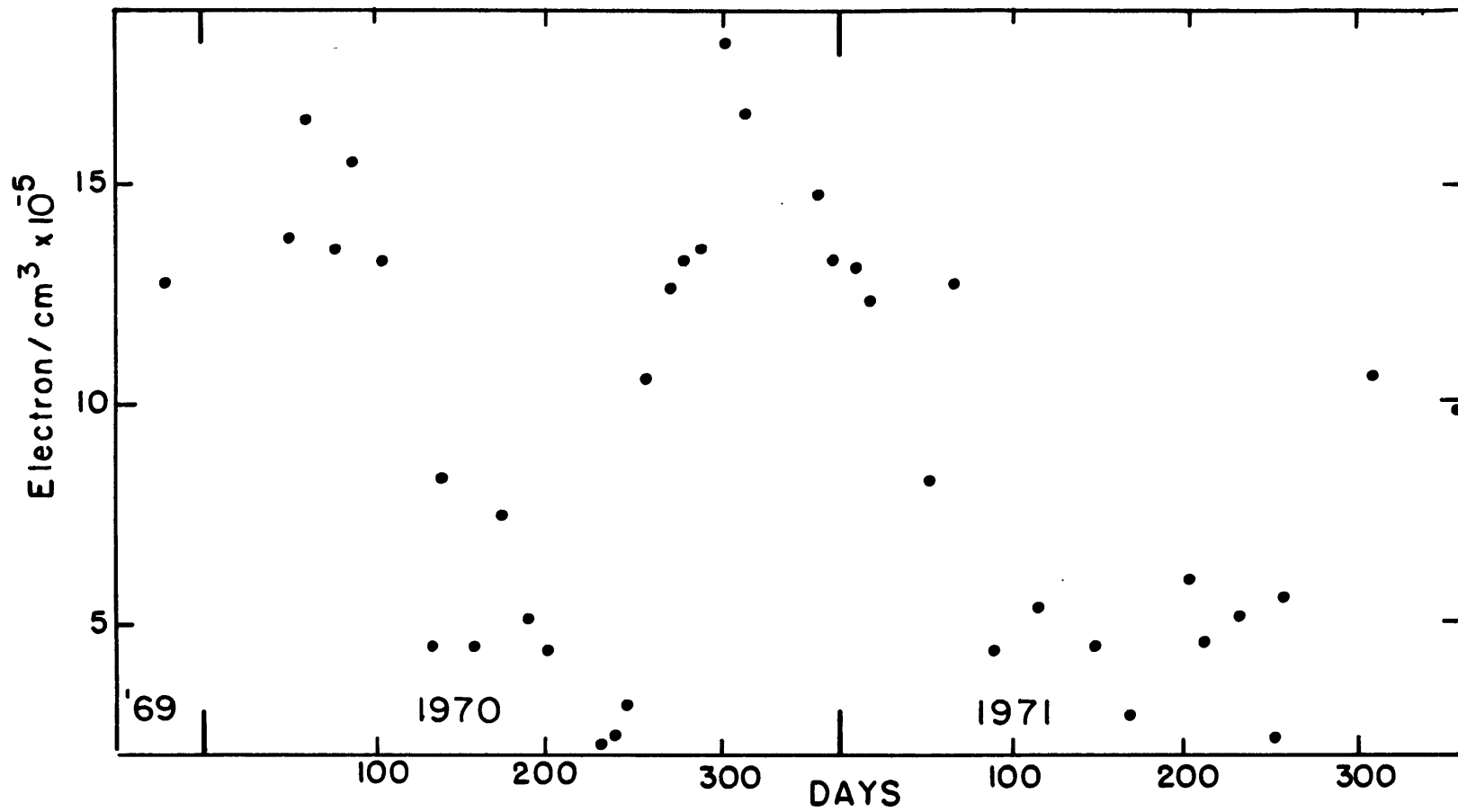


Figure 8.5a: Electron maximum concentrations at 1200 LT above Millstone Hill.

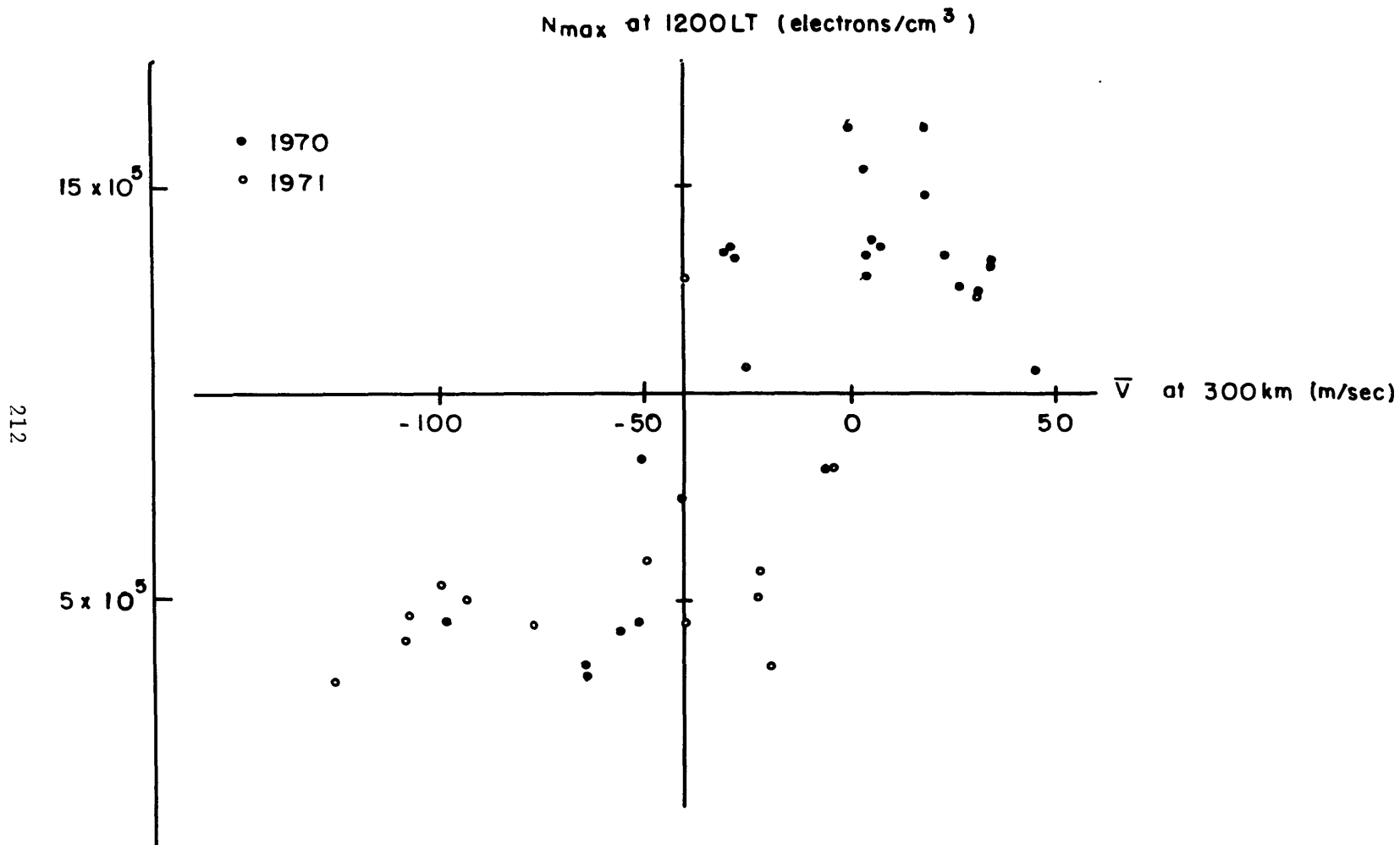


Figure 8.5b: Electron maximum concentrations at 1200 LT as a function of average meridional velocities at 300 km above Millstone Hill.

velocity $V_{D//}$, with the assumption of no electric fields. Averages for $\overline{V_{Hn}}$ at 300 km are plotted in Figure 8.6a, and averages for $\overline{V_{D//}}$ and V_{iz} in Figure 8.6b. As expected, the average meridional velocities are closely related to the average values of V_{Hn} , but are generally more southwards in the summer and northwards in the winter owing to the effect of the average westward and eastward velocities. Again, the average values of V_{Hn} appear to be larger in the summer of 1971 than in the summer of 1970. This can be explained by the averages of V_{iz} and $V_{D//}$ plotted in Figure 8.6b. The average diffusion velocities are about 32 m/sec downwards in the summer of 1970 and 28 m/sec downwards in the summer of 1971. The average vertical ion drift is generally downwards at about 17 m/sec for all but the summer of 1971 when it is downwards at about 8 m/sec. Only three days had mean upward vertical ion drifts--two of which, October 31-November 1, 1970 and December 22-23, 1971, have already been discussed and deemed anomalous. (The third day was July 28-29, 1971). The net result of a 4 m/sec decrease in $\overline{V_{D//}}$ and a 9 m/sec decrease in $\overline{V_{iz}}$ (via Eq. 3.9) is about a 15 m/sec increase in $\overline{V_{Hn}}$ from the summer of 1970 to the summer of 1971.

There is a tendency for large downward values of the diffusion velocity at 300 km to be correlated with small downward values of the vertical ion drift (see Figure 8.6b). The days when this correlation is most pronounced have large southward winds. These days are usually characterized by large positive vertical gradients in the electron density at 300 km at night. The peak

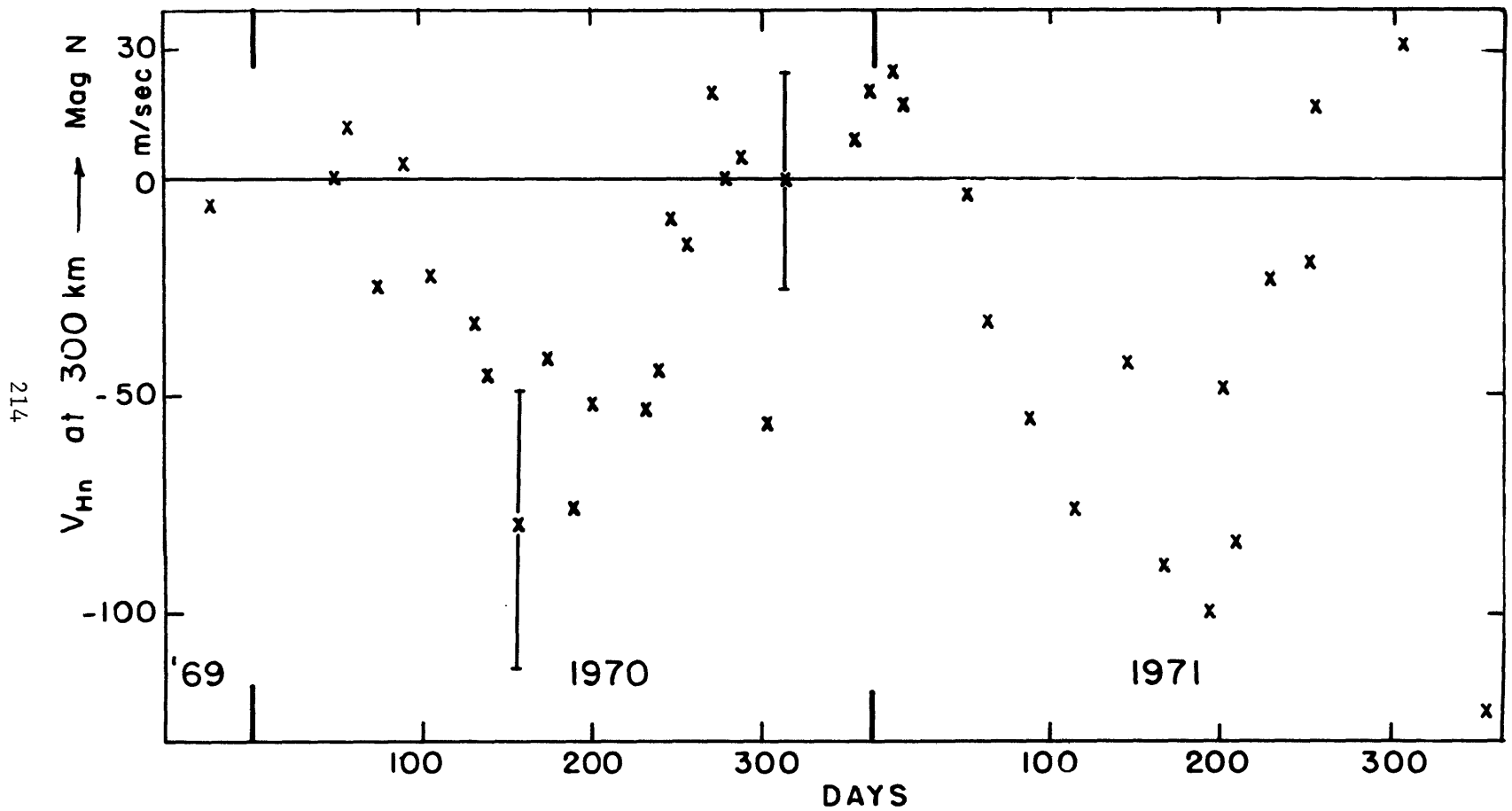


Fig. 8.6a: Plot of the average horizontal wind in the plane of the magnetic meridian, V_{Hn} , calculated at 300 km above Millstone Hill and assuming no electric fields are present.

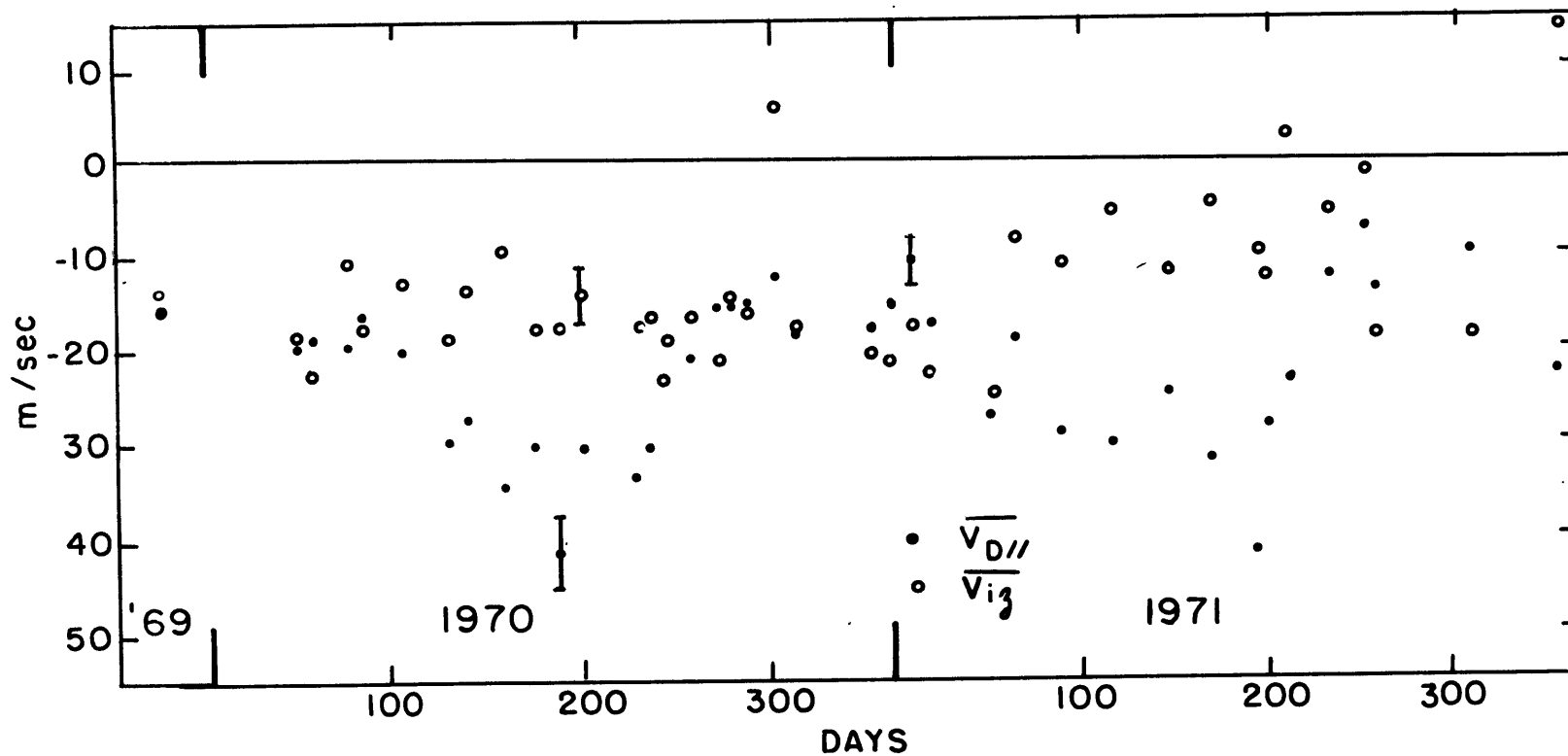


Figure 8.6.b: Plot of the average diffusion velocities parallel to the magnetic field, $\overline{V_{D//}}$, and of the average vertical ion drifts, $\overline{V_{iz}}$, above Millstone Hill.

electron density layer is above this height at night so these sharp gradients cause large downward diffusion velocities. Stated otherwise, the large positive gradients are interpreted as indicating that the ions have been blown up the field line by southward winds.

Vertical ion drifts are generally downwards except right after dawn when there is a period of upward velocities, sometimes over 100 m/sec at 850 km altitude, due to the rapid growth of the F layer at this time. These upward velocities are encountered only at higher altitudes, usually above 450 km. However, this region of upward velocities occasionally extends downward to 300 km, and this is what happened on 7 summer or equinox days in 1971. The upwards velocities peaked about 2 or 3 hours after sunrise and ranged from 3 m/sec on March 30-31, 1971 to 74 m/sec on August 19-20, 1971. One day in 1970, August 24-25, also had an upwards velocity of 1 m/sec about 2 hours after sunrise. This period of upward ion drifts at 300 km in the summer of 1971 resulted in a smaller average downwards vertical drift and thus larger southward velocities. The increased incidence of post-dawn upward drifts in 1971 can be partially accounted for by a drop in the height of the maximum electron density layer. At local noon, the peak electron densities were around 300 km for the summer of 1970 and around 275 km for the summer of 1971.

8.5 Summary of Results for the Horizontal Velocities

Defining the seasonal difference in the mean velocities to be twice the size of the annual component of the harmonic analysis, plus corrections made due to the form of the atmospheric model (section 7.3), then

$$\begin{aligned} \overline{(\bar{v}_{\text{summer}} - \bar{v}_{\text{winter}})}_{\text{M.H.}} &= -105 \pm 15, \pm 10 \text{ m/sec} \\ \overline{(\bar{u}_{\text{summer}} - \bar{u}_{\text{winter}})}_{\text{M.H.}} &= -83 \pm 26, \pm 10 \text{ m/sec} \end{aligned} \tag{8.5}$$

for the Millstone Hill model and

$$\begin{aligned} \overline{(\bar{v}_{\text{summer}} - \bar{v}_{\text{winter}})}_{\text{MSIS}} &= -100 \pm 6 \text{ m/sec} \\ \overline{(\bar{u}_{\text{summer}} - \bar{u}_{\text{winter}})}_{\text{MSIS}} &= -125 \pm 6 \text{ m/sec} \end{aligned} \tag{8.6}$$

for the MSIS model. The uncertainties were taken from Section 7.7. When there are two uncertainties, the second one represents a bias of some sort. The annual average velocities (correcting for the form of the atmosphere model again) are

$$\begin{aligned} \bar{v}_{\text{M.H. (annual)}} &= -22 \pm 12, +2 \text{ to } +22 \text{ m/sec} \\ \bar{u}_{\text{M.H. (annual)}} &= -8 \pm 21, -8 \text{ to } +12 \text{ m/sec} \end{aligned} \tag{8.7}$$

for the Millstone Hill case and

$$\bar{v}_{\text{MSIS (annual)}} = - 22 \pm 1, +12 \text{ m/sec} \quad (8.8)$$

$$\bar{u}_{\text{MSIS (annual)}} = - 3 \pm 1, + 2 \text{ m/sec}$$

for the MSIS model case. The bias uncertainties in the annual averages assume that the electric field model of Kirchhoff and Carpenter (1975) is approximately correct with average velocities of 12 m/sec toward the north and 2 m/sec toward the east.

8.6 Vertical Velocities

Figure 8.7 is a plot of the average vertical velocities deduced from the MSIS model pressure gradients and assuming a 4% decrease of electron density in 1 degree of latitude. Also plotted is the average value of one of the divergence terms contributing to the vertical velocity, $WDVY = (1/\rho) \int_z^\infty \rho \partial v / \partial y dz$, which depends heavily on the assumptions of the latitudinal gradient of electron density (see Figure C.4b). One summer and one winter day were also calculated assuming a latitudinally constant electron density and these are marked with crosses.

All of the daily average vertical velocities were downwards, the largest occurring in the summer of 1970 at 1.40 m/sec and the smallest in the equinox periods at about .25 m/sec. Winter values are about 0.75 m/sec which is similar to values for the summer of 1971. The storm day of August 17-18, 1970 had the largest average

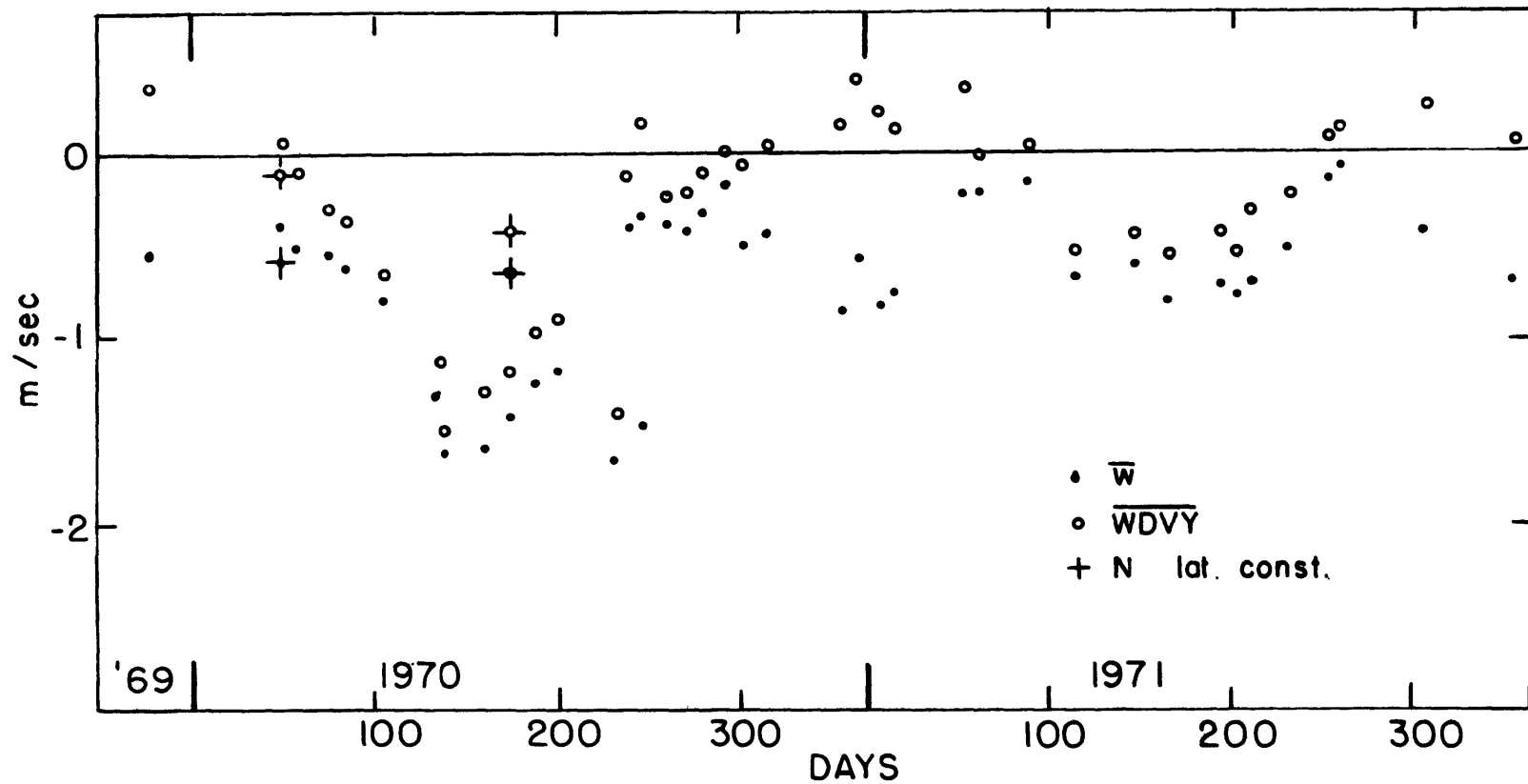


Fig. 8.7: Average vertical velocities, \bar{w} , and average $\overline{WDVY} = 1/\rho \int_0^{\infty} \rho \partial v / \partial y dz$ calculated using the MSIS atmospheric model and the ionospheric data above Millstone Hill. The electron density is assumed to decrease polewards by 4% in 1 degree of latitude except for points marked with a cross, where it is assumed to be latitudinally constant.

downward velocity at 1.64 m/sec. There appears to be a seasonal variation in \overline{WDVY} with downward values in the summer and upward or near zero ones in the winter. The combination of the other terms to the average appears to be downward at all times at approximately 0.2 m/sec in the summer and up to 0.6 m/sec in the winter. The assumption of a latitudinally constant electron density results in slightly increased average downward velocities in the winter (an increase of 0.25 m/sec) and considerably depressed velocities (a decrease of 0.75 m/sec) in the summer of 1970. Since the assumption about a linear 4% decrease in electron density towards the pole in 1 degree of latitude is least liable to be correct in the summer night, the average downward velocities may be nearer 0.65 m/sec in the summer of 1970 than their present average of about 1.40 m/sec.

Average vertical velocities were not plotted for the Millstone Hill case because they are not trusted. However, they are listed in Table 8.1 and show the same general trends as the MSIS model velocities. Here, some averages around equinox were upwards. The largest downward velocities were in the summer of 1970. The introduction of a latitudinally constant electron density halved the average velocity at this time.

8.7 Magnitudes of the Neglected Non-Linear Terms

The non-linear terms were excluded from this analysis, but were calculated approximately. The north-south non-linear term, $-v \partial v / \partial y$, usually had a negative maximum at night. At 300 km during

the winter months, this maximum was about 10% or less of other terms in the momentum equation. During equinox and summer, this term could become quite large, on one occasion it was larger than the maximum value of any other term. (This was on April 14-15, 1970). On average, the north-south non-linear term was 30 or 40% of the largest of the other terms in the summer months. This was decreased by about 10% for the MSIS model. However, a latitudinally constant electron density would reduce this percentage considerably. The size of the zonal non-linear term depended on the size of the acceleration term and on the size of the zonal velocity and could also become large, especially in the summer.

8.8 Comparison with Previous Work

Millstone Hill incoherent scatter data has been used previously to estimate neutral winds. Most recently, Roble et al (1977) examined three summer and three winter days at high sunspot number. These days were re-analyzed in the present study and a comparison of the average input data and the results of the two analyses is listed in Table 8.2. There are differences in the input data because the exospheric temperature, T_{∞} , and the calculated horizontal wind in the plane of the magnetic meridian at 300 km, V_{Hn} , were computed for the Roble, et al study with the old B mode estimates of the ion and electron temperatures, and used an incorrect version of the OGO-6 model instead of the MSIS model. The major changes are slightly increased exospheric temperatures and more northward winds

Table 8.2: Comparison of the Average Input Parameters and Results at 300 km
for Different Analyses Using Millstone Hill Data

Day	\bar{T}_{∞} (°K)		\bar{V}_{Hn} (ms ⁻¹)		\bar{u} (ms ⁻¹)		\bar{v} (ms ⁻¹)		\bar{w} (ms ⁻¹)	
	c	a	c	a	c	a	c	a	c	a
Dec. 8-9, 1969	885	962	-15.9	- 5.2	+ 1.7	+ 27.6	- 15.6	+ 1.5	- .04	-.36
Feb. 23-24, 1970	970	1020	- 9.1	+11.4	+15.2	+ 24.8	- 2.0	+ 17.9	- .30	-.43
Dec. 21-22, 1970	1035	1050	+ 8.7	+ 9.3	+17.5	+ 35.0	+ 14.6	+ 18.3	+ .10	+ .10

May 18-19, 1970	1199	1201	-50.5	-45.6	-14.1	- 18.0	- 41.6	- 51.5	- .20	-1.40
June 23-24, 1970	1101	1101	-34.3	-39.3	-13.9	- 5.0	- 40.0	- 41.7	- .06	-1.18
July 18-19, 1970	1034	1094	-50.8	-52.1	-20.5	- 17.9	- 51.9	- 58.2	+ .03	- .64

	b	a	b	a	b	a	b	a	b	a
Mar. 23-24, 1970	1000	1078	-20.1	+ 4.2	-26.1	+ 4.7	- 53.1	+ 5.6	+ .36	-.43
Sept. 28-29, 1970	1000	1081	-14.9	+20.7	-43.2	+28.5	-41.8	+28.4	+ .69	-.30

- a) present work;
- b) Roble, et al (1974);
- c) Roble, et al (1977).

in the winter which lead through Coriolis effects to more eastward winds. In addition, the Roble et al (1977) study assumed the electron density to be latitudinally constant in the calculation of the vertical velocity, w . As a result, the vertical velocities are not so strongly downwards in summer.

Table 8.2 also lists the average input data and results of two equinox days which were analyzed in the present study and also previously by Roble et al (1974). The input data for this earlier study was produced in the days before the data was smoothed and represented with a polynomial fit. Neutral densities were taken from the Jacchia 1971 model, and only atomic oxygen was considered. As mentioned previously in Section 3.2.2, the major change is a considerable decrease in the nighttime winds, leading to more northward velocities in the present analysis.

8.9 Comparison with Other Observations

Table 8.3 is a comparison of the average meridional velocities derived in the present work and derived from an analysis of drift data measured above the incoherent scatter facility at St. Santin (44.6°N , 2.3°E) and reported by Amayenc (1974). Summer is defined as being May through August, and winter is November through February. Autumn and spring are the two-month periods in-between. The French study used the atmospheric model of Jacchia, 1971 and the ion-neutral collision frequencies given by Stubbe (1968).

Table 8.3: Seasonal meridional wind variations at thermospheric heights above Millstone Hill (42.6°N, 71.5°W) and St. Santin (44.6°N, 2.3°E). Negative values are equatorwards (southwards) and westwards

	\bar{u} (ms ⁻¹)	\bar{v} (ms ⁻¹)		
	<u>a</u>	<u>a</u>	<u>b</u>	<u>c</u>
Winter	+26.1	+17.2	+10	+ 5
Spring	-35.3	-45.2	-25	-37
Summer	-46.0	-65.6	-25	-37
Autumn	-17.8	- .9	- 4	-12

- a) Millstone Hill, 1970-1971 (present study - Figures 8.3 and 8.4a)
 (Correcting for electric fields would add approximately 12 m/sec northward(positive), velocity, and 2 m/sec westwards (negative) velocity).
- b) St. Santin, 1971-1972 (Amayenc, 1974)
- c) Estimate of what (b) would have been if the ion-neutral collision frequencies were taken from Banks (1966b) instead of Stubbe (1968). (Use average of Eq.3.8, assume $v_{nsE} = 0$, $\bar{V}_{iz} = -15$ m/sec, $I = 60.8^\circ$, and $\bar{V}_{D//}$ is increased by 20%).

Harmonic Analyses:

a) $\bar{u} = -14 + 43 \cos \left(\frac{2\pi}{365} (\text{day}-363) \right) + 3 \cos \left(\frac{4\pi}{365} (\text{day} - 4) \right)$
 $\bar{v} = -24 + 53 \cos \left(\frac{2\pi}{365} (\text{day} - 345) \right) + 9 \cos \left(\frac{4\pi}{365} (\text{day} - 87) \right)$

b) $\bar{v} = -9 + 25 \cos \left(\frac{2\pi}{365} (\text{day} - 346) \right) + 10 \cos \left(\frac{4\pi}{365} (\text{day} - 87) \right)$

c) $\bar{v} \sim -19 + 30 \cos \left(\frac{2\pi}{365} (\text{day} - 346) \right) + 12 \cos \left(\frac{4\pi}{365} (\text{day} - 87) \right)$

Both analyses exhibit the same general features of a polewards wind in the winter and equatorwards winds the rest of the year, with autumn closer to winter and spring closer to summer. However, the circulation pattern above St. Santin is less intense than the one found above Millstone Hill. A harmonic analysis of the French results gives an annual mean equatorwards wind of 9 m/sec with an annual variation of ± 25 m/sec. The Millstone Hill circulation is more intense with a mean annual equatorward wind of 22 m/sec and an annual variation of ± 52 m/sec.

This difference arises partly through the use of two different sources for the ion-neutral collision frequencies. The $O^+ - O$ collision frequency given by Banks (1966) is about 25% smaller than the value given by Stubbe (1968). Assuming an average vertical ion drift of 15 m/sec downwards, and using $I = 60.8^\circ$ for St. Santin, a rough calculation of the effect of using Banks' collision frequencies instead of Stubbe's, resulted in an average annual equatorwards velocity of 19 m/sec with an annual variation of ± 30 m/sec. The results of this rough calculation are included in Table 8.3.

In addition to different collision frequencies, the data bases are different. The French data were mostly gathered during 1971 and 1972, which were periods of moderate solar activity. The lower 10.7 cm solar flux gives rise to smaller pressure gradients associated with the solar energy input, and thus might be expected

to produce a weaker circulation pattern. The geomagnetic latitude of St. Santin is about 45°N , while it is about 57°N at Millstone Hill, and this may also contribute to differences in the seasonal variation as can be seen from the discussion in Chapter 9.

The next chapter will discuss the results in the light of some of the circulation and transport theories about the neutral thermosphere.

9. DISCUSSION AND CONCLUSIONS

Keating and Prioꝛ(1968) first showed the existence of large amounts of helium in the winter thermosphere and put forward two possible explanations for its presence. Their first suggestion was the possibility of a drop of 5 to 10 km in the level of the turbopause in the winter hemisphere. The turbopause, located around 105 km, marks the height above which diffusive separation of the molecules occurs in the atmosphere according to their molecular weights. Any change in its height will alter the relative abundances of all species at greater heights. Helium concentrations decrease in altitude by 50% every 5 km around 110 km if it is well mixed (Banks and Kockarts, 1973). A drop of 5 or 10 km in the turbopause height will thus increase helium concentrations at higher levels by a factor of nearly 2 or 4 since the scale height of helium is much larger than the scale height of the major constituents.

Their second suggestion was a seasonal variation of helium below the turbopause, brought about by the diffusive transport of lighter species from the summer to the winter pole. This last hypothesis was examined theoretically by Mayr and Volland (1972) with respect to the winter atomic oxygen excess discovered using the OGO-6 ion mass spectrometer. In this chapter we review Mayr and Volland's work and the efforts of subsequent authors to achieve a theoretical understanding of the horizontal transport in the thermosphere.

9.1 A Self-Consistent Model of the Effects of Non-Diffusive Equilibrium

For a binary mixture the general diffusion equation giving the relative diffusion velocity $\vec{v} = \vec{v}_1 - \vec{v}_2$ of gas 1 with respect to gas 2, can be written as (Banks and Kockarts, 1973)

$$\vec{v} = - D_{12} \left[\frac{n^2}{n_1 n_2} \nabla \frac{n_1}{n} + \frac{m_2 - m_1}{m} \nabla (\ln p) + \alpha_T \nabla (\ln T) - \frac{m_1 m_2}{m k T} (\vec{F}_1 - \vec{F}_2) \right] \quad (9.1)$$

where n_1 and n_2 are respectively the concentration of particles 1 and 2, $n = n_1 + n_2$ is the total concentration of the binary mixture, T is the neutral gas temperature, $p = p_1 + p_2$ is the total pressure, m_1 and m_2 are the masses of particles 1 and 2, m is the mean molecular mass, \vec{F}_1 and \vec{F}_2 are accelerations of particles 1 and 2 due to external forces, D_{12} is the molecular diffusion coefficient of gas 1 in gas 2, and α_T is the thermal diffusion factor. \vec{F}_1 and \vec{F}_2 generally cancel out for neutral particles in a gravitational field but are important for charged particles in the presence of electric and magnetic fields. According to Eq. 9.1, a light gas can diffuse up its concentration gradient but down the pressure gradient in the altitude regions where it is a minor gas. It is proposed that this occurs with helium and atomic oxygen so their concentrations are elevated in the winter hemisphere at thermospheric heights. This proposal was examined by Mayr and Volland (1972).

Mayr and Volland created a three-dimensional, two-component (N_2 and O) model to examine the annual and semiannual variations in the thermosphere, where the energy and diffusive mass transport associated with the global circulation are considered in a self-consistent form. They assumed that electron densities were latitudinally constant and that the only energy source for annual variations came from the sun. The model employed an expansion in spherical harmonics. Perturbations from a basic state were found for temperature, atomic oxygen and molecular nitrogen number densities, total gas density, and the horizontal and vertical velocities u , v and w .

The derived annual circulation pattern at 300 km was upwards over the summer pole at about .5 m/sec, and downwards over the winter pole. The meridional velocity was about 22 m/sec towards the winter pole at the equator and the zonal velocities maximized at $\pm 45^\circ$ latitude being eastward in the winter and westward in the summer hemisphere at about 4.5 m/sec. Temperatures, N_2 densities and total densities maximized at the summer pole while atomic oxygen maximized at the winter pole below 440 km and at the summer pole above this height.

Table 9.1 lists the annual variations in $n^{(0)}_{120}$, T_∞ , \bar{u}_{300} , \bar{v}_{300} and \bar{w}_{300} derived from this study (Mayr and Volland, 1972) for the latitude of Millstone Hill ($42.6^\circ N$). The semiannual variations were smaller and are not discussed. The variations derived from the present work are also listed for comparison. The variations in the

Table 9.1: Annual Variations (\pm or $\bar{\pm}$) above Millstone Hill (42.6°N)
 Taken from the Present Work and Other Studies. The Top
 Signs Refer to Winter and the Bottom to Summer.

	Mayr and Volland	Present study (including correcting for the atmospheric model)	
	<u>(1972)</u>	<u>M.H.Model</u>	<u>MSIS Model</u>
$n(O)_{120}$ (no./cm ³ *10 ⁻¹⁰)	7.5 \pm 2.0	8.4 \pm 4.8	8.7 \pm 2.5
T_{∞} (°K)	1050 $\bar{\pm}$ 92	\sim $\bar{\pm}$ 75 (for 1970)	\sim $\bar{\pm}$ 100
$u_{300 \text{ km}}$ (ms ⁻¹)	0 \pm 4.5	-9 \pm 41	-3 \pm 60
$v_{300 \text{ km}}$ (ms ⁻¹)	0 \pm 15.5	-22 \pm 53	-22 \pm 50
$w_{300 \text{ km}}$ (ms ⁻¹)	0 $\bar{\pm}$.34	\sim -.87 $\bar{\pm}$.54 (for 1970)	\sim -.75 \pm .5
Dickinson <u>et al</u> (1977)			
	<u>Solar Heating</u> <u>(Fig. 9.2)</u>	<u>Solar plus sym.high</u> <u>lat.source(Fig.9.3)</u>	<u>Solar plus asym.high</u> <u>lat.source (Fig.9.4)</u>
$n(O)_{120}$ (no./cm ³ *10 ⁻¹⁰)	from OGO-6 model	from OGO-6 model	from OGO-6 model
T_{∞} (°K)	$\bar{\pm}$ 23	$\bar{\pm}$ 24	$\bar{\pm}$ 50
$u_{300 \text{ km}}$ (ms ⁻¹)	\sim 0 \sim \pm 10	\sim 2 \sim \pm 27	\sim 0 \sim \pm 42
$v_{300 \text{ km}}$ (ms ⁻¹)	3 \pm 32	-17 \pm 27	-35 \pm 65
$w_{300 \text{ km}}$ (ms ⁻¹)	-.03 $\bar{\pm}$.38	-.74 $\bar{\pm}$.32	-1.0 $\bar{\pm}$.2

bottom boundary (120 km) atomic oxygen are about 20% throughout the year, which is approximately the percent variation found for the MSIS and OGO-6 models. The variation in the Millstone Hill model is about twice that amount because the variation in O/N_2 was larger than that in the models (see Figure 3.8). The exospheric temperature for the Mayr and Volland study is about $\pm 92^\circ\text{K}$, which may be compared with the value of $\pm 75^\circ\text{K}$ found by Salah *et al.*, (1976) for the latitude of Millstone Hill and St. Santin. The zonal velocity variation derived by Mayr and Volland (1972) is about 10 times smaller than the variation found in the present study and the annual mean is zero instead of westwards.

In the model of Mayr and Volland, the diffusive transport of atomic oxygen from the summer to the winter pole is accomplished with a summer-to-winter meridional velocity variation of ± 15 m/sec at the latitude of Millstone Hill. This is approximately 30% of the variation that was found in the present work. Therefore, if Mayr and Volland have included all the important energy sources, it appears that the horizontal velocities measured are sufficiently large to account for the seasonal variations of neutral composition. A remaining problem entails explaining why the velocity difference is so much larger in the present work than it is in the Mayr and Volland study, and why there is a net equatorward flow.

9.2 Theoretical Models Based on Heating Rates

Dickinson et al (1975) have explored the circulation pattern that should be established by solar EUV heating alone. These calculations employed number densities for the various atmospheric species adopted from models and did not attempt to solve for diffusive transport at the lighter species in a self-consistent manner. At equinox they find that air should rise at the equator and be transported via the thermosphere toward the poles where it must sink. There must be a return flow (albeit accompanied by much lower mean winds) at altitudes below 120 km. Recognizing that the incoherent scatter results as well as studies utilizing empirical model atmospheres predict instead a net equatorwards flow they examined whether the input of additional heat at high latitudes could reverse the mean meridional wind.

It has been known for some time that the high latitude phenomena associated with the interaction of the solar wind with the earth can have a profound effect on the thermosphere over the entire globe. Heat is deposited in the auroral regions from Joule heating by ionospheric currents driven by magnetospheric convection and by auroral particle precipitation. The heating is quite variable and it has been very difficult to obtain a global estimate of its magnitude and distribution. Recently, Ching and Chiu (1973) and Roble and Matsushita (1975) have estimated the global distribution of Joule heating based on magnetometer data.

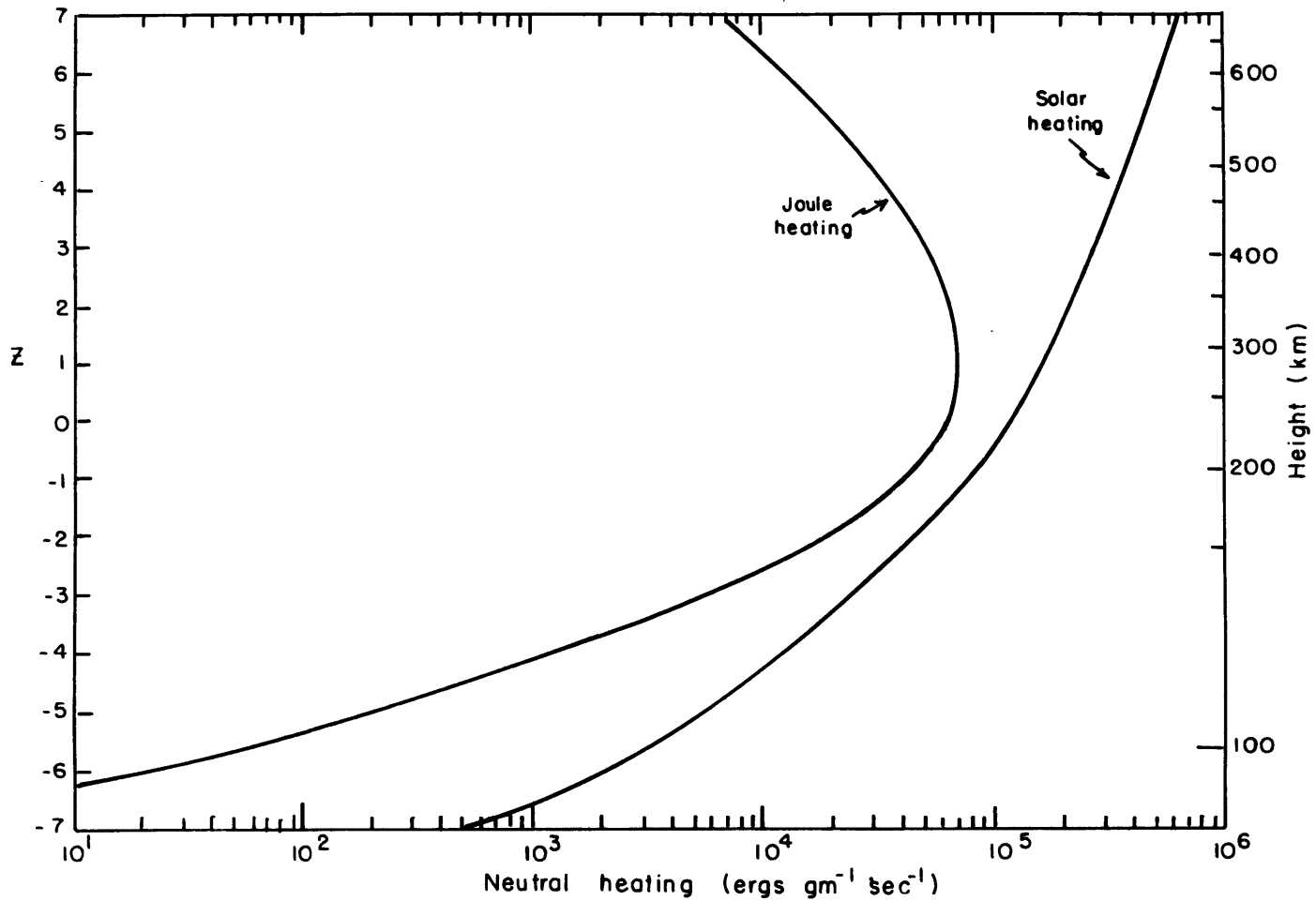


Fig. 9.1: The calculated global mean neutral gas heating rate for solar heating and for the assumed Joule heating due to ionospheric currents (taken from Dickinson et al, 1975).

Dickinson et al (1975) took the distribution of the high latitude heat source found by Roble and Matsushita (1975) and had to multiply it by a factor of 20 before they could obtain agreement between their calculated mean meridional winds and those deduced from Millstone Hill and St. Santin incoherent scatter data. The equator to pole temperature variation was similar to that contained in the OGO-6 model at equinox. The Joule heating rates found by Roble and Matsushita did not include effects due to short period fluctuations or heating in the electrojet currents. Heating by particle precipitation was also omitted. Accordingly, some upward scaling to estimate the total high latitude heat source seemed justified. The increase of a factor of 20 resulted in a height-integrated value of the global mean Joule heating rate above 120 km of $0.22 \text{ ergs cm}^{-2} \text{ sec}^{-1}$. The global mean solar heating rate above 120 km was $0.72 \text{ ergs cm}^{-2} \text{ sec}^{-1}$ for the high sunspot cycle conditions they considered. The altitude variation of the solar EUV and high latitude heating rates are shown in Figure 9.1.

9.2.1 Solstice Model Results Including a High Latitude Heat Source

In a subsequent analysis for solstice conditions, Dickinson et al (1977) again found the circulation pattern expected from including only the solar heat source. The calculated contours of the perturbation zonal (diurnal) mean temperature and winds that result are shown in Figure 9.2. Figure 9.3 shows the perturbations resulting from the inclusion of a symmetric high latitude heat source of the same magnitude as was used for the equinox case.

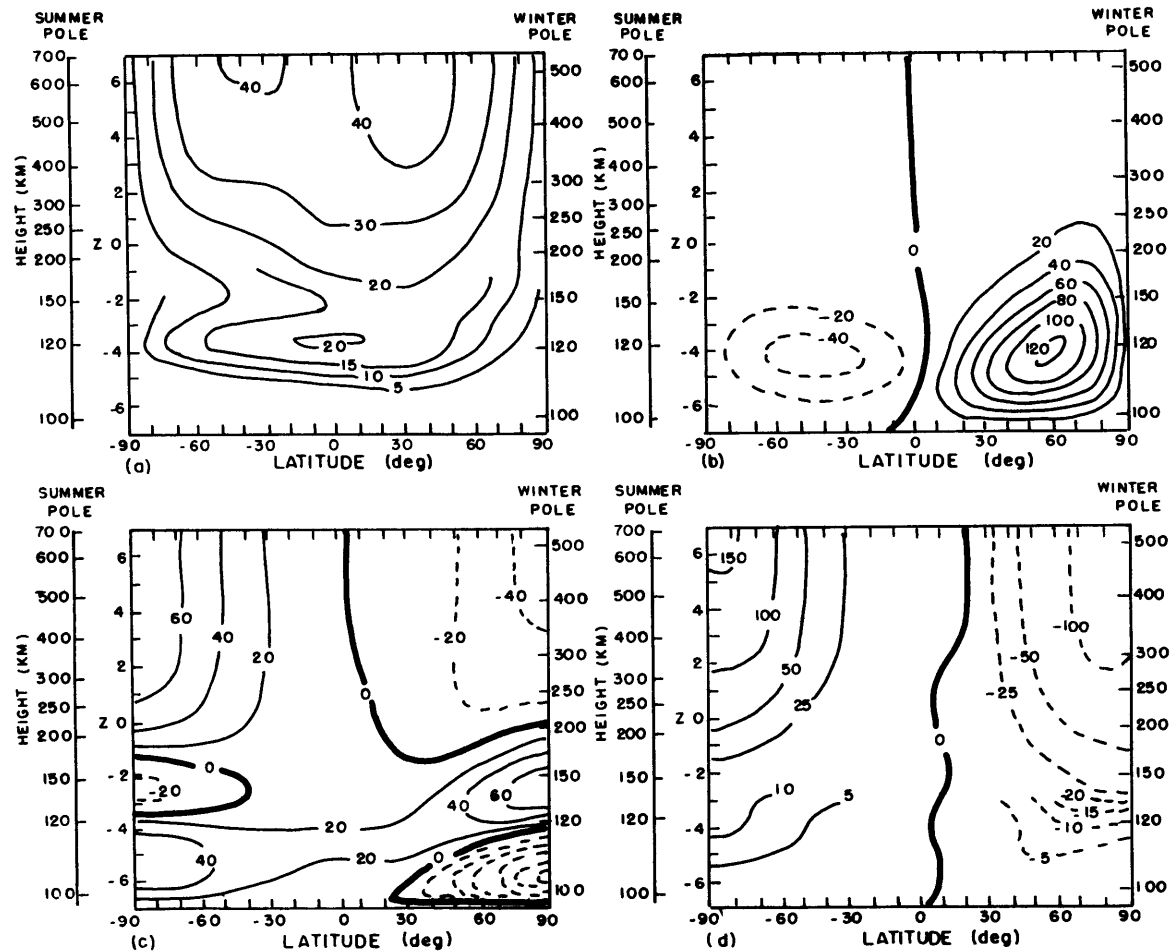


Fig. 9.2: The calculated contours of the perturbation diurnal and zonal mean temperature and winds due to forcing by solar heating alone: (a) meridional winds (ms^{-1}), (b) zonal winds (ms^{-1}), (c) temperature ($^{\circ}\text{K}$), and (d) vertical velocity (cms^{-1}). (Taken from Dickinson *et al.*, 1977).

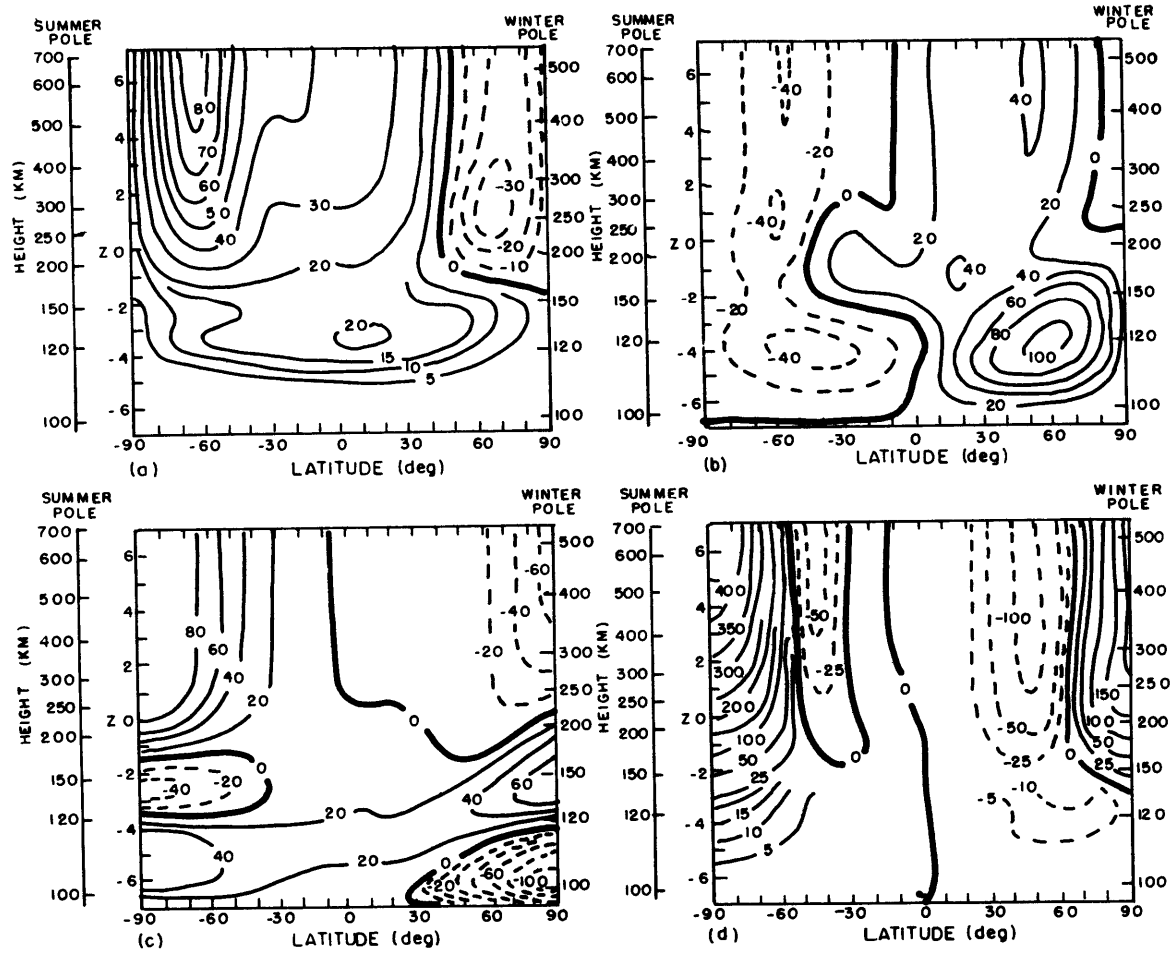


Fig.9.3: Same as Fig. 9.2 with the addition of the OGO-6 inferred momentum source and a symmetrical high latitude heat source.

Studies of the K indices of geomagnetic activity (which are similar to the K_p indices) reveal a semiannual variation with maximum activities during equinox. There is also a smaller summer hemisphere maximum (Wulf, 1971). Therefore, another case was calculated by Dickinson et al (1977) with an asymmetrical high latitude heat source in which the heating in the summer hemisphere is two and one-half times greater than in the winter hemisphere. The magnitude of the high latitude heating was again adjusted until agreement was reached between calculated and observed temperature and velocity variations. The global mean energy input above 120 km due to the high latitude heat source was $0.38 \text{ ergs cm}^{-2} \text{ sec}^{-1}$. The perturbation values are contoured in Figure 9.4

The average annual variations of the temperature and velocities estimated for the latitude of Millstone Hill from Figures 9.2 through 9.4 are listed in Table 9.1. In general, the complexity and magnitude of the winds are increased by the inclusion of high latitude heat sources. There is a net equatorwards flow in the model in mid-latitudes, which doubles in size from the symmetrical heat source case to the asymmetrical case. The results obtained using the asymmetrical high latitude heat source seem to give best agreement with the Millstone results but could be improved if the model heat source in the summer hemisphere is reduced.

The mass stream flow functions of the thermospheric circulation are shown in Figure 9.5 for the few cases studied by Dickinson et al. (The second case involved the addition of the zonal

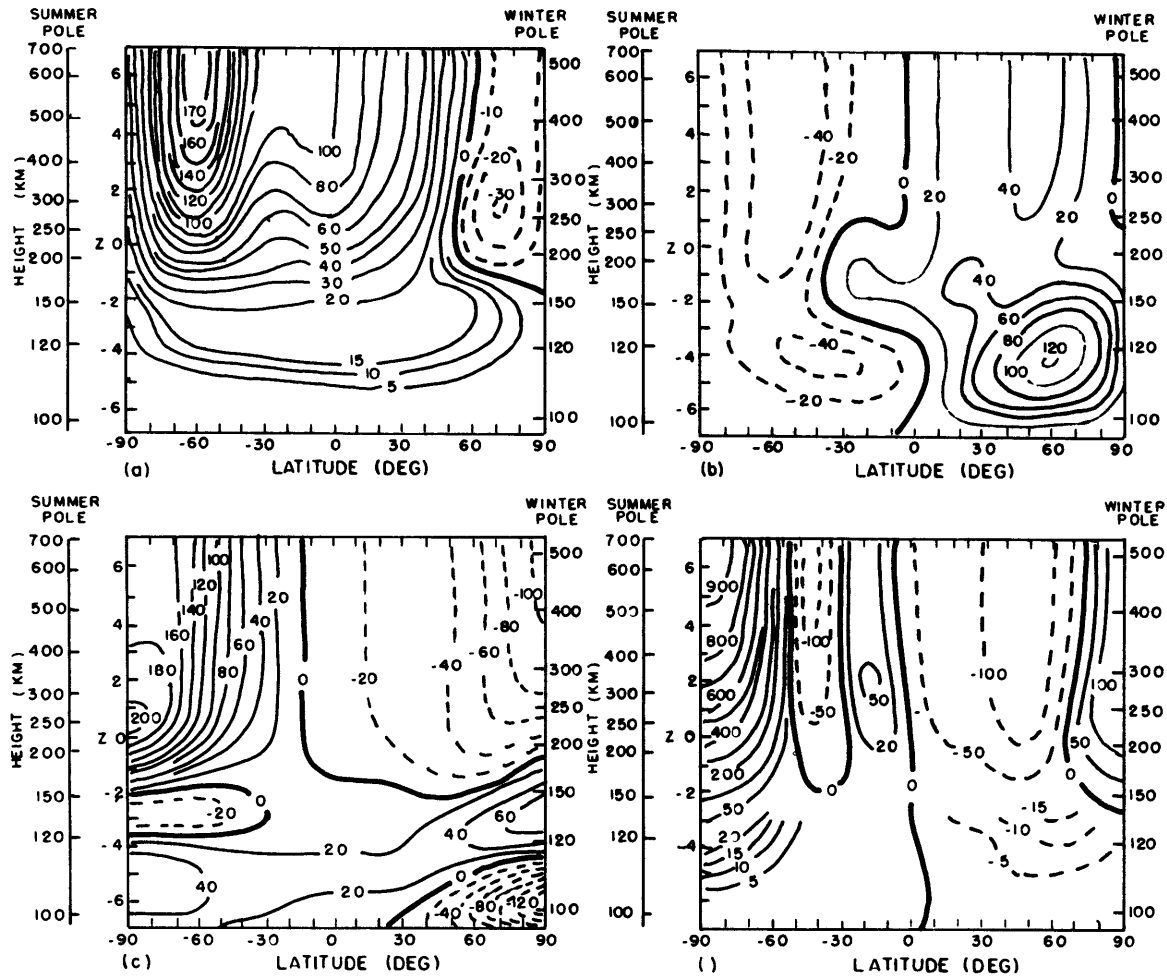


Fig. 9.4: Same as Figure 9.3 with the high latitude heating in the summer hemisphere two and one half times greater than the winter hemisphere.

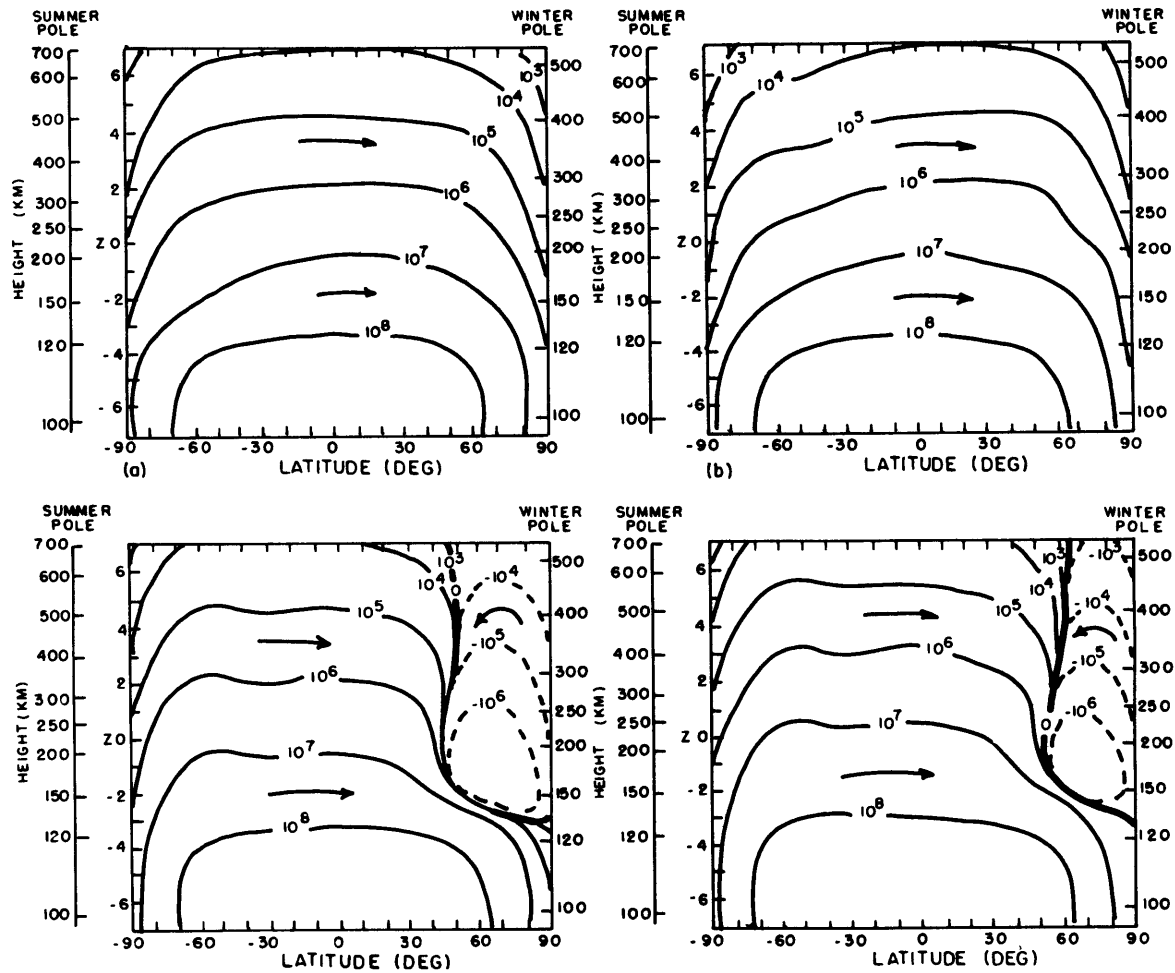


Fig. 9.5: The calculated contours of mass flow stream function (g.s.^{-1}) for (a) solar heating alone, (b) solar heating plus the OGO-6 inferred momentum source, (c) solar heating plus the OGO-6 inferred momentum source plus the symmetrical high latitude heating source, and (d) solar heating plus the OGO-6 momentum source and the asymmetrical high latitude heat source (taken from Dickinson *et al.*, 1977).

and meridional momentum sources inferred from the OGO-6 model and is not discussed here.) The high latitude heat sources introduce a reverse polar circulation cell in the winter hemisphere above 150 km. The transition region between this cell and the direct global Hadley circulation cell is near 50° latitude. The strength of the reverse cell and the latitude of transition will vary depending upon the magnitude of the winter high latitude heat source in relation to the solar heat source. In the summer hemisphere, there is a dip in the mass flow stream functions around 40° latitude which marks the region of downward velocities. The existence of downward velocities in all seasons encountered in the present study is therefore not inconsistent with the model circulation results. Moreover, the vertical velocity derived by Dickinson et al for the equinox case is about .5 m/sec downwards at 300 km over the latitude of Millstone Hill. This is smaller than the winter or summer downward velocities derived for the asymmetrical high latitude heat source case, and so the presence of a minimum vertical velocity at equinox as plotted in Figure 8.7 may be correct. However, the downward velocity found in the summer of 1970 could be too large if the proposed polewards decrease in electron density is too large.

9.3 Discussion of the Present Results

As mentioned in the previous section, high latitude heating is capable of producing the net equatorward flow which is observed above Millstone Hill. In addition, it can create average vertical velocities that are downward throughout the year over Millstone Hill.

The magnitude of the annual variation of the zonal velocity is also greatly enhanced — in keeping with the Millstone Hill results.

Higher magnetic activity should be accompanied by an increase in the high latitude heat source that results in a larger equatorward velocity at the latitude of Millstone Hill. Figure 9.6 is a scatter diagram of the average A_p values for the 36 days analyzed versus the difference in the mean velocity for each day from the value predicted by the harmonic analysis of the entire data set. There was no significant difference between winter and summer. For activities less than 5, the harmonic analysis is usually more southward than the data. The reverse holds for activities greater than 5 and less than about 10. The situation for the higher activity is somewhat scattered, possibly reflecting a response to electric fields which have been ignored in the present study.

In Figures 8.3a and 8.4a, the circulation is increased about 15% between the summer of 1970 and the summer of 1971. In the results of the MSIS model (Figures 8.3b and 8.4b), there appears to be a decrease in the circulation of about 15% between these two periods. This occurred largely because the pressure gradients decreased in the MSIS model but not in the Millstone Hill model. Table 9.2 lists some of the characteristic parameters found in the summers of 1970 and 1971. (Summer was defined as being between April 20 and September 2). The electron density at 300 km decreased by about 30% over this period, accompanying a similar decrease in the solar flux.

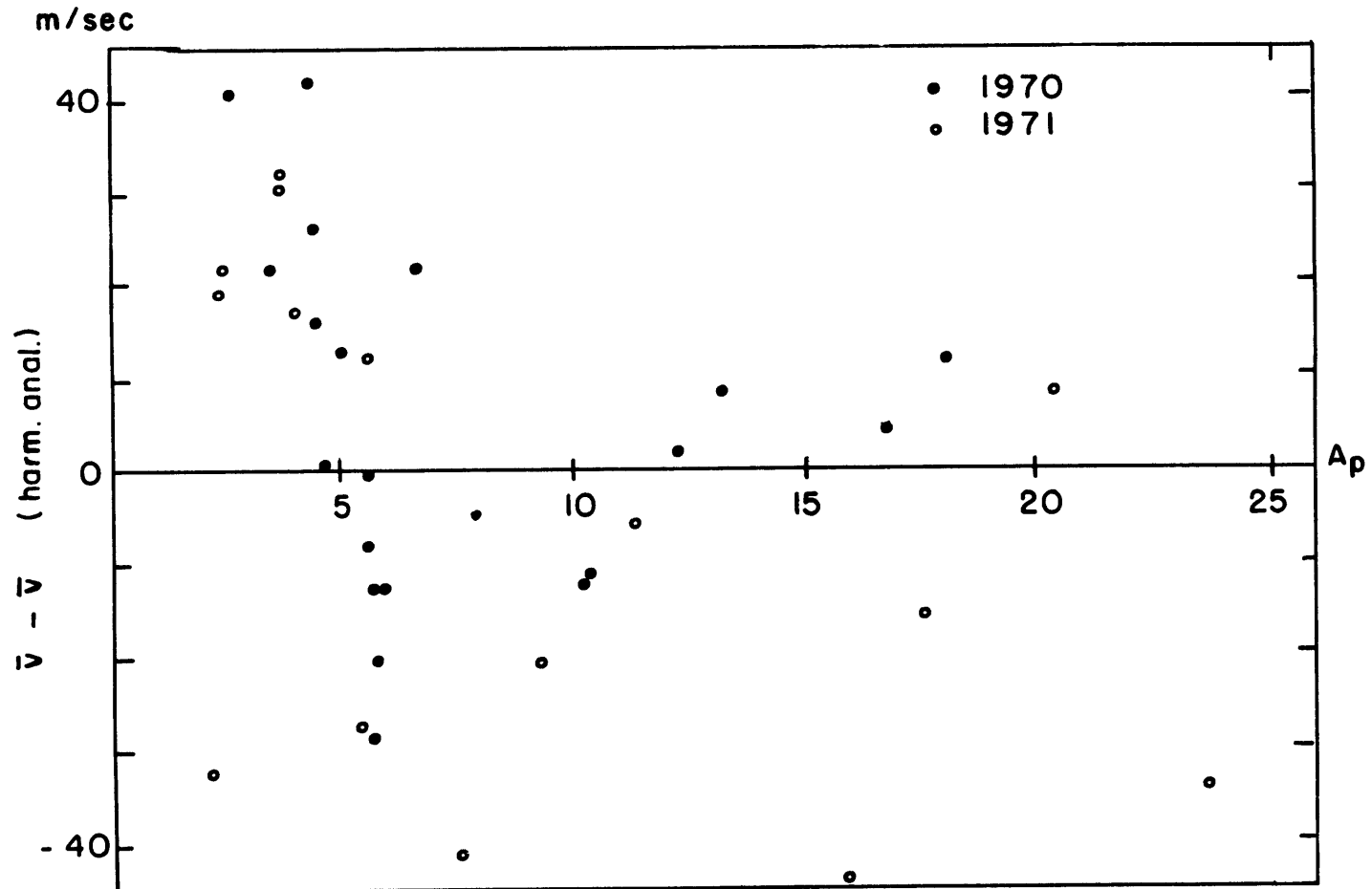


Fig. 9.6: Plot of the difference between the average daily meridional velocity and the harmonic analysis of the entire data set versus magnetic activity. Negative values are a stronger equatorwards flow than average.

In the Millstone Hill case, the mean exospheric temperature decreased by 13% and the difference between the minimum and maximum temperatures decreased by 10% from summer to summer. Since the maximum zonal pressure gradient is roughly proportional to the day-night temperature difference divided by the exospheric temperature (see Eq. 7.4 and the definition for γ_j in section 5.2), this ratio was computed in Table 9.2. This ratio rose 4% between the summer of 1970 and the summer of 1971 for the Millstone Hill case, indicating that the zonal pressure gradients increased slightly. The number density decreases with temperature at a faster than linear rate. It decreased about 32% between 1970 and 1971 while the average exospheric temperature decreased 13%. Considering a balance between the pressure gradient and the ion drag

$$\frac{.70}{.68} \frac{\bar{u}_{1971}}{\bar{u}_{1970}} \approx 1.04 \quad (9.2)$$

where all quantities are in the ratio of the 1971 value to the 1970 value ($N_{1971}/N_{1970} = .70$, $\rho_{1971}/\rho_{1970} = .68$, etc.), this equation predicts that the mean zonal velocities should be of the same magnitude in 1970 and 1971.

Applying similar reasoning to the MSIS model, one concludes that the mean zonal velocity in the summer of 1971 should be 25% less than the mean velocity in 1970. This arises because in the model, the maximum exospheric temperatures decreased faster than the minimum or mean temperatures. These arguments would predict the winds in 1971 to be more eastward than those observed. Despite this, they do seem

Table 9.2 Some Characteristic Parameters of the Summers of 1970 and 1971

Summer		M. H. MODEL			MSIS MODEL		
		1970	1971	1971/1970	1970	1971	1971/1970
\bar{T}_{∞}	($^{\circ}\text{K}$)	1141	990	.87	1117	940	.84
$T_{\infty \text{ min}}$	($^{\circ}\text{K}$)	903	800	.89	974	833	.86
$T_{\infty \text{ max}}$	($^{\circ}\text{K}$)	1298	1156	.89	1258	1045	.83
244 ($T_{\infty \text{ max}} - T_{\infty \text{ min}}$)	($^{\circ}\text{K}$)	394	356	.90	284	212	.75
	$(T_{\infty \text{ max}} - T_{\infty \text{ min}}) / \bar{T}_{\infty}$.346	.359	1.04	.254	.226	.89
	$n(\text{O} + \text{N}_2 + \text{O}_2)_{300 \text{ km}}$ (no./cm ³)	~.40E9	~.27E9	.68	~.83E9	~.49E9	.59
	\bar{u} (m/sec)	-42	-50	1.19	-48	-41	.85

able to explain why the MSIS model mean zonal velocities decreased between the summers of 1970 and 1971 while the Millstone Hill mean velocities did not. Similar effects apply to the meridional winds, but they are not reproduced here.

Magnetic activity varies with the sunspot cycle but usually lags sunspot numbers by about a year in the decreasing part of the cycle (Lincoln, 1967). This is consistent with the finding that the magnetic activity was not greatly different from 1970 to 1971 while the solar flux decreased by 30% in this same period. Therefore, one might expect the high latitude heat source to have been more important in relation to the solar heat source in 1971 than in 1970.

The high latitude heat source will produce equatorward winds at the latitude of Millstone Hill. If its effects have been underestimated in global models such as the MSIS model, then in a year where it is of larger relative importance such as in 1971, the velocities seen above Millstone Hill will be more equatorwards than those produced by the MSIS model. This does not explain why the mean meridional winds increased in magnitude between the summers of 1970 and 1971 in the Millstone Hill case, but suggests that this could occur if the relative increase in importance of the high latitude heat source were large enough.

Similarly, if the effect of the high latitude heat source on temperature has been neglected, then this neglect will probably show up most strongly during the day when the solar heat

source has its largest effect. (Daytime temperatures decrease more than nighttime temperatures between summer and winter and between sunspot maximum and minimum). Thus the increased relative importance of the high latitude heat source in 1971 can explain the observed relative increase in the equatorward winds and the maximum temperatures in the Millstone Hill case in comparison with the MSIS model case.

9.4 Average Zonal Velocities

Satellite drag studies of the upper atmosphere (King-Hele (1972a), King-Hele and Walker (1973)), suggest an average zonal velocity at 30° N and S at 300 km to be between 20 and 100 m/sec eastward (superrotation). The rotation rate can be extremely variable, exhibiting periods of mean westward winds over a couple of months as well as mean eastward winds. Analysis of the orbit of one satellite at 150 km, (King-Hele, 1972b) could be interpreted in two alternate patterns: 1) If variations with latitude are important, there are more eastward winds in the equatorial region, or 2) If the winds depend mainly on local time, then they exhibit an 8 hour periodicity with eastward peaks of about 200 m/sec at 0700, 1500, and 2300 LT. Analysis of another satellite orbit at 220 km (Walker, 1974), found that the periods of mean westward motion were correlated with periods of higher A_p values.

Radar studies of east-west ion drifts near the magnetic equator (Woodman, 1972), suggest an average neutral zonal velocity

of about 50 m/sec eastward. These radar results and the satellite drag studies essentially apply to conditions at low latitudes. Among the mechanisms suggested for superrotation are polarization electric fields at night, and southward electric fields associated with negative bays during substorm activity (Rishbeth, 1972a). If the former is true, then the superrotation would be expected to be greatest at low latitudes. If the latter, then the effect should be greatest at high latitudes.

Theories involving polarization fields require that charge can be separated at night in the F region by the eastward winds that are present. In this case the ion drag will cease to be important at night. Usually F region polarization fields cannot exist because they are immediately mapped down magnetic field lines into the E region where currents can flow and short circuit them. However, the E layer conductivity is reduced by about a factor of 30 at night and the magnetic field lines are nearly north-south in low latitudes, making it easier for polarization fields to exist. The polarization fields that are established will cause the plasma to drift in the direction of the neutral wind, and will continue to grow until this has been achieved. This reduces the frictional effect of the ion drag and allows greater wind speeds to develop across the dark hemisphere. The result is superrotation.

Magnetic substorms are associated with negative bays or decreases in the north-south magnetic field. The negative bays are produced by westward currents associated with equatorwards electric fields. The electric fields move the ions toward the east and this

motion is imparted to the neutrals through ion drag and could also result in superrotation. However, the correlation between subrotation (mean westward winds) and periods of higher magnetic activity found by Walker (1974), suggest that the negative bays associated with substorms are not a major mechanism for producing superrotation. Instead, the equatorward winds associated with the heat input of magnetic storms appear to be deflected to the west by the Coriolis force and cause subrotation.

No evidence for superrotation has been found in the present experimental study nor in the theoretical studies cited. However, the mechanisms proposed by Rishbeth have not been incorporated in the theoretical studies or in the global atmospheric models. Average zonal velocities were found to be either near zero or westwards at 5 or 10 m/sec. Of course it also is possible that the Millstone results are insensitive to these effects, so that superrotation cannot be entirely ruled out based on the present incoherent scatter and mass spectrometer measurements and/or the models derived from them.

9.5 Summary and Conclusions

In this work, an attempt was made to deduce the quiet-time thermospheric circulation pattern above the Millstone Hill (42.6°N) incoherent scatter radar facility for the years of 1970 and 1971 using measured values of ionospheric drifts, temperatures and densities. Appeal to other data sources was kept to a minimum in order to see if

the conclusions reached would support results derived from atmospheric models based on in-situ sampling. The ionospheric radar data were used to provide values of the exospheric temperature, T_{∞} , and hence the east-west pressure variation. The radar data for the altitude variation of temperature and the vertical ion drift together with neutral number densities from the MSIS atmosphere model provided the neutral horizontal wind at 300 km in the plane of the magnetic meridian, V_{Hn} . This depended upon the north-south pressure gradients and the ion drag (which was known). These could then be used (along with the ion drag data) to establish the free parameters of a two-dimensional model of the thermosphere above Millstone Hill. In this model, T_{∞} was described by 3 harmonics. Assumptions were then made about the latitudinal variation of electron density and the north-south gradient of the exospheric temperature and these permitted the calculation of the vertical velocity and north-south non-linear term.

The linear horizontal momentum equations were solved simultaneously with the equation describing u and v in terms of V_{Hn} . The 3 unknowns were u , v , and $\partial T_{\infty} / \partial \phi$. A solution was obtained by switching back and forth between a Crank-Nicholson numerical analysis scheme and an explicit scheme. V_{Hn} was fitted to within 1 m/sec. The derived diurnal variation of $\partial T_{\infty} / \partial \phi$ was then analyzed for the first 3 harmonics. Using this harmonic analysis, the equations of motion were re-solved.

The circulation pattern derived from this numerical analysis of observational data was much the same as that found in other studies. The winds were eastwards at dusk, westwards at dawn, polewards during the day, and equatorwards at night. Zonal velocities (~ 300 m/sec) were larger than deduced in some studies owing to the large diurnal gradients of the exospheric temperature. This was particularly true for the summer months. Daytime (northward) winds were of the order of 50 to 100 m/sec while nighttime (southward) winds were usually between 100 and 300 m/sec depending on the season. Mean meridional velocities at 300 km were equatorwards during equinox and summer, and polewards during the winter. The annual average velocity was equatorwards at about 20 m/sec. If the average electric field model of Kirchhoff and Carpenter (1975) were applied to all the observations, this value would be reduced to 10 m/sec. The average seasonal variation of the meridional wind was found to be of the order ± 50 m/sec. The average annual zonal wind at 300 km is about 10 m/sec westwards with an annual variation of about ± 40 m/sec. The vertical velocities were generally downwards, with largest values in the summer of 1970.

An analysis of the possible errors introduced by the experimental inaccuracy, the assumptions made in the analysis technique and all other sources of error was carried out. It was found that reasonable assumptions about the latitudinal electron density gradient could make large differences in the vertical velocities deduced during the summer months. In addition, the assumption that the gradient of

$\partial T_{\infty} / \partial \phi$ was latitudinally constant was found to be suspect. It was concluded that these two assumptions rendered the vertical velocity calculation unreliable. The total uncertainty in the mean horizontal velocity is 50% or less, and the uncertainty in the seasonal variation is between 15-30%.

The mean annual meridional velocities, and the large seasonal variations in it support the results presented by Dickinson et al, (1977) indicating the importance of a high latitude heat source. The two-year span of data started during high sunspot numbers and ended at moderate sunspot activity. The lower solar fluxes resulted in lower average temperatures, but the mean winds were not diminished and even appeared more southwards in 1971. In addition, the maximum temperatures did not decrease as quickly over the two-year data span as they did in the MSIS model. The increased importance of the high latitude heat source at times of lower solar flux was suggested as a possible explanation for these phenomena. For magnetic activities less than 10, a higher activity was usually associated with stronger southward winds. Relationships for activities greater than 10 were mixed. Inclusion of a high latitude heat source in calculations of global circulation appears capable of producing downward velocities through the year, such as were found for all but a few winter and equinox days in the Millstone Hill model.

Winds were also calculated using the pressure gradients incorporated in the MSIS model together with the data from Millstone Hill to establish the ion drag. These calculations yielded much the

same results except that the strength of the horizontal circulation pattern decreased slightly with decreasing solar activity. If the circulation pattern really remained approximately the same over the two year interval studied here this would imply that the MSIS model does not properly represent the changing balance between the high latitude and solar heat sources at all phases of the sunspot cycle.

The seasonal variation in the mean meridional wind of ± 52 m/sec at 300 km above Millstone Hill is about three times the difference needed to explain the diffusive transport of atomic oxygen from the summer to the winter pole, according to a simple two species model that assumes only an annual solar heat source. (Mayr and Volland, 1972). Diffusive transport calculations that also include the effects of a high latitude heat source have yet to be made. However, studies by Straus et al (1975) and Dickinson et al (1975, 1977) of the meridional winds expected as a result of combining solar and high latitude heat sources and the observed seasonal variations in the atmospheric constituents, yield results for the seasonal variations which are comparable to these obtained here.

9.6 Suggestions for Future Work

One of the major problems that came up in the present study in the calculation of the vertical velocity and the north-south non-linear term, was the specification of the latitudinal variations of electron densities and meridional pressure gradients. Latitudinal gradients of the electron density peak can be approximated from the

ionogram records of f_oF_2 frequencies taken at stations located at Millstone Hill (42.6°N, 71.5°W) and Ottawa (45.4°N, 75.5°W). If the latitudinal electron density gradient at the peak is a good estimate of the latitudinal gradients at other levels, the specification of the meridional electron density gradient above Millstone Hill would be accomplished. Specifying the latitudinal gradient of the meridional pressure gradient is more difficult, and recourse to atmospheric models such as MSIS may have to be made.

If the latitudinal variations of electron density and the meridional pressure gradient can be correctly approximated, then it is probably worthwhile to try to include the north-south non-linear term in the calculations. Either the time step would have to be shortened or the latitude step lengthened from what it is now, in order to satisfy the stability criterion. (Since stability criteria for including the zonal non-linear term are much harder to meet, this term can only be included later in an approximate fashion as an outside forcing function).

The data base should be extended to cover more of the solar cycle. A longer and larger data base is desirable to confirm ideas about the variation of the strength of the circulation pattern with respect to levels of solar and geomagnetic activity. At the same time the results should be examined to see if there is an equatorwards expansion of the cell controlled by the high latitude heat source in the winter hemisphere during magnetic storms.

Interpretation of the incoherent scatter data gathered on magnetically active days must take careful account of electric fields, which are liable to be large. Magnetometer records from nearby geomagnetic stations could be useful in this regard if there is no other data source available. In addition, the present thermospheric model should be altered so that non-diurnal temperature and circulation changes could be allowed. The restriction of beginning and ending a 24-hour period with the same ionospheric conditions will have to be dropped, and temperature (and hence density) derivatives can no longer be specified in terms of diurnal harmonics. Spline functions may be used instead.

Aside from these extensions of the present work, there is an obvious need for a theoretical calculation of the diffusive transport of lighter species from the summer to the winter pole which includes the high latitude heat source as well as the solar heat source as forcing functions for annual variations.

REFERENCES

- Amayenc, P., 1974: Tidal oscillations of the meridional neutral wind at mid-latitudes. Radio Sci., 9, 281-294.
- Amayenc, P., D. Alcayde, and G. Kockarts, 1975: Solar extreme ultraviolet heating and dynamical processes in the mid-latitude thermosphere. J. Geophys. Res. 80, 2887-2891.
- Banks, P., 1966a: Collision frequencies and energy transfer: Electrons. Planet. Space Sci., 14, 1085-1103.
- _____, 1966b: Collision frequencies and energy transfer: Ions. Planet. Space Sci., 14, 1105-1122.
- _____, 1969: The thermal structure of the ionosphere. Proc. IEEE, 57, 258-281.
- Banks, P.M. and G. Kockarts, 1973: Aeronomy, Part A and Part B. Academic Press, New York, 430 and 355 pp.
- Bates, D. R., 1959: Some problems concerning the terrestrial atmosphere above about the 100 km level. Proc. Roy. Soc. London, A, 253, 451-462.
- Bauer, P., P. Waldteufel, and D. Alcayde, 1970: Diurnal variations of the atomic oxygen density and temperature determined from incoherent scatter measurements in the ionospheric F region. J. Geophys. Res. 75, 4825-4832.
- Behnke, R.A. and T. Hagfors, 1974: Evidence for the existence of nighttime F-region polarization fields at Arecibo. Radio Sci., 9, 211-216.
- Behnke, R. A. and R.M. Harper, 1973: Vector measurements of F-region ion transport at Arecibo, J. Geophys. Res., 78, 8222-8234.
- Blanc, M., P. Amayenc, P., Bauer, and C. Taieb, 1977: Electric field induced drifts from the French incoherent scatter facility. J. Geophys. Res., 82, 87-97.
- Blum, P. W. and I. Harris, 1975: Full non-linear treatment of the global thermospheric wind system, Pt. 1, Mathematical method and analysis of forces, and Pt. 2, Results and comparison with observations. J. Atmos. Terr. Phys., 37, 193-212 and 213-235.

- Bowles, K. L., 1958: Observations of vertical incidence scatter from the ionosphere at 41 Mc/sec. Phys. Rev. Lett., 1, 454-455.
- Brinton, H. C., M. W. Pharo, III, H. G. Mayr, and H. A. Taylor, Jr., 1969a: Implications for ionospheric chemistry and dynamics of a direct measurement of ion composition in the F2 region J. Geophys. Res., 74, 2941-2951.
- Brinton, H. C., R. A. Pickett, and H. A. Taylor, Jr., 1969b: Diurnal and seasonal variation of atmospheric ion composition; Correlation with solar zenith angle. J. Geophys. Res. 74, 4064-4073.
- Carpenter, D. L. and N. T. Seely, 1976: Cross-L plasma drifts in the outer plasmasphere: Quiet time patterns and some Substorm effects. J. Geophys. Res. 81, 2728-2736.
- Carpenter, L. A. and V. W. F. H. Kirchhoff, 1974: Daytime three-dimensional drifts at Millstone Hill Observatory. Radio Sci., 9, 217-222.
- Ching, B. K. and Y. T. Chiu, 1973: Global distribution of thermospheric heat sources: EUV absorption and Joule dissipation. Planet. Space Sci., 21, 1633-1646.
- Cox, L. P. and J. V. Evans, 1970: Seasonal variation of the O/N₂ ratio in the F₁ region. J. Geophys. Res., 75, 6271-6286.
- Dalgarno, A., 1964: Ambipolar diffusion in the F-region. J. Atmos. Terr. Phys., 26, 939.
- Dahlquist, G. and A. Björck, 1974: Numerical Methods. Translated by N. Anderson, Prentice-Hall, Inc., Englewood Cliffs, N.J., 537 pp.
- Dickinson, R. E. and J. E. Geisler, 1968: Vertical motion field in the middle thermosphere from satellite drag densities. Mon. Wea. Rev., 96, 606-616.
- Dickinson, R. E., E. C. Ridley, and R. G. Roble, 1975: Meridional circulation in the thermosphere, I. Equinox conditions. J. Atmos. Sci., 32, 1737-1754.
- _____, 1977: Meridional circulation in the thermosphere, II, Solstice conditions. J. Atmos. Sci., 34, 178-192.
- Emery, B. A., 1975: A Radar Study of the Thermosphere, S.M. thesis in the Dept. of Meteorology, M.I.T., Cambridge, Mass., February, 1975.

- Evans, J. V., 1967: Electron temperature and ion composition in the F₁ region. J. Geophys. Res. 72, 3343-3355.
- _____, 1969: Theory and practice of ionosphere study in Thomson scatter radar. Proc. IEEE, 57, 496-530.
- _____, 1972: Measurements of horizontal drifts in the E and F regions at Millstone Hill. J. Geophys. Res., 77, 2341-2352.
- _____, 1976: Dynamics of the ionosphere and upper atmosphere. Paper presented at the AGU International Symposium on Solar-Terrestrial Physics, Boulder, Colorado (June, 1976).
- Evans, J.V. and L. P. Cox, 1970: Seasonal variation of the F₁ - region ion composition. J. Geophys. Res., 75, 159-164.
- Evans, J. V. and T. Hagfors (eds), 1968: Radar Astronomy, Chapter 2. McGraw-Hill, New York.
- Evans, J.V. and J. M. Holt, 1976: Millstone Hill Thomson Scatter Results for 1970. Technical Report No. 522, Lincoln Laboratory.
- Evans, J.V., R. F. Julian, W. A. Reid, 1970: Incoherent Scatter Measurements of F-Region Densities, Temperature, and Vertical Velocity at Millstone Hill. Technical Report No. 477, Lincoln Laboratory.
- Fejer, J., 1960: Scattering of radiowaves by an ionized gas in thermal equilibrium. J. Geophys. Res., 65, 2635-2636.
- Geisler, J. E., 1967: A numerical study of the wind system in the middle thermosphere. J. Atmos. Terr. Phys., 29, 1469-1482.
- Gordon, W. E., 1958: Incoherent scattering of radio waves by free electrons with applications to space exploration by radar. Proc. IRE, 46, 1824-1829.
- Harris, I. and W. Priester, 1962: Time-dependent structure of the upper atmosphere. J. Atmos. Sci., 19, 286-301.
- Hedin, A. E., H. G. Mayr, C. A. Reber, N. W. Spencer and G. R. Carignan, 1974: Empirical model of global thermospheric temperature and composition based on data from the OGO-6 quadrupole mass spectrometer. J. Geophys. Res., 79, 215-225.
- Hedin, A.E., J. E. Salah, J. V. Evans, C. A. Reber, G. P. Newton, N. W. Spencer, D. C. Kayser, P. Bauer, L. Cogger, and J. P. McClure, 1977: A global thermospheric model based on mass spectrometer and incoherent scatter data: MSIS Part I---N₂ density and temperature. J. Geophys. Res., in press.

- Hernandez, G. and R. G. Roble, 1976: Direct measurement of night-time thermospheric winds and temperatures 1. Seasonal variations during geomagnetic quiet periods. J. Geophys. Res., 81, 2065-2074.
- Holmes, J. C., C. Y. Johnson, and J. M. Young, 1965: Ionospheric Chemistry. Space Res. V, 756-766.
- Jacchia, L. G., 1965: Static diffusion models of the upper atmosphere with empirical temperature profiles. Smithsonian Contrib. Astrophys., 8, 257 pp.
- _____, 1971: Revised static models of the thermosphere and exosphere with empirical temperature profiles. Spec. Rep. 332, Smithson. Astrophys. Observ., Cambridge, Mass., 113 pp.
- Jacchia, L. G. and J. Slowey, 1967: The shape and location of the diurnal bulge in the upper atmosphere. Space Research VII, North-Holland Pub. Co., Amsterdam, 1077-1090.
- Jacchia, L. G. and J. W. Slowey, 1968: Diurnal and seasonal latitudinal variations in the upper atmosphere. Planet. Space Sci., 16, 509-524.
- Johnson, C. Y., 1969: Ion and neutral composition of the ionosphere, in Annals of the IQSY, Volume 5, M.I.T. Press, Cambridge, Mass., 197-213.
- Keating, G. M. and E. J. Prior, 1968: The winter helium bulge. Space Res. VIII, 982-992.
- King-Hele, D. G., 1972a: Measurements of upper atmosphere rotation speed from satellite orbit changes. Space Res. XII, 847-855.
- _____, 1972b: Analysis of the orbit of Cosmos 316 (1969-108A). Proc. R. Soc. Lond. A, 330, 467-494.
- King-Hele, D. G. and D. M. C. Walker, 1973: Analysis of the orbit of 1965-11D (Cosmos 54 rocket). Planet. Space Sci., 21, 1081-1108.
- Kirchhoff, V. W. J. H. and L. A. Carpenter, 1975: Dominance of the diurnal mode of horizontal drift velocities at F region heights. J. Atmos. Terr. Phys. 37, 419-428.
- _____, 1976: The day-to-day variability in ionospheric electric fields and currents. J. Geophys. Res., 81, 2737-2742.

- Kockarts, G. and M. Nicolet, 1963: L'Hélium et l'hydrogène atomique au cours d'un minimum d'activité solaire. Annal. Geophys., 19, 370-385.
- Kohl, H. and J. W. King, 1967: Atmospheric winds between 100 and 700 km and their effects on the ionosphere. J. Atmos. Terr. Phys., 29, 1045-1062.
- Lincoln, J. V., 1967: Geomagnetic indices, in Physics of Geomagnetic Phenomena, edited by S. Matsushita and W. H. Campbell. Academic Press Inc., New York, 67-100.
- Mason, E. A., 1970: Estimated ion mobilities for some air constituents. Planet. Space Sci., 18, 137-144.
- Mayr, H. G., A. E. Hedin, C. A. Reber, and G. R. Carignan, 1974: Global characteristics in the diurnal variations of the thermospheric temperature and composition. J. Geophys. Res. 79, 619-628.
- Mayr, H. G. and H. Volland, 1972: Theoretical model for the latitude dependence of the thermospheric annual and semiannual variations. J. Geophys. Res., 77, 6774-6790.
- _____, 1973: A two-component model of the diurnal variations in the thermospheric composition. J. Atmos. Terr. Phys., 35, 669-680.
- Moorcroft, D. R., 1963: On the power scattered from density fluctuations in a plasma. J. Geophys. Res. 68, 4870-4872.
- Nisbet, J. S., 1970: On the construction and use of the Penn State MK I ionospheric model. Ionospheric Research Scientific Report No. 355.
- Reber, C. A., A. E. Hedin, and S. Chandra, 1973: Equatorial phenomena in neutral thermospheric composition. J. Atmos. Terr. Phys., 35, 1223-1228.
- Richmond, A. D., 1976: Electric field in the ionosphere and plasmasphere on quiet days. J. Geophys. Res. 81, 1447-1450.
- Richmond, A. D. and S. Matsushita, 1975: Thermospheric response to a magnetic substorm. J. Geophys. Res., 80, 2839-2850.
- Rishbeth, H., 1967: The effect of winds on the ionospheric F2-peak. J. Atmos. Terr. Phys., 29, 225-238.
- _____, 1972a: Superrotation of the upper atmosphere. Revs. Geophys. Space Phys., 10, 799-819.
- _____, 1972b: Thermospheric winds and the F-region: A review. J. Atmos. Terr. Phys., 34, 1-47.

- Rishbeth, H. and O. K. Garriott, 1969: Introduction to Ionospheric Physics. Academic Press, New York and London, 331 pp.
- Rishbeth, H. and C. S. G. K. Setty, 1961: The F-layer at sunrise. J. Atmos. Terr. Phys., 20, 263-276.
- Roble, R. G., and R. E. Dickinson, 1973: Is there enough solar extreme ultraviolet radiation to maintain the global mean thermospheric temperature? J. Geophys. Res., 78, 249-257.
- Roble, R. G. B. A., Emery, J. E. Salah, and P. B. Hays, 1974: Diurnal variation of the neutral thermospheric winds determined from incoherent scatter radar data. J. Geophys. Res. 79, 2868-2876.
- Roble, R. G. and S. Matsushita, 1975: An estimate of the global scale Joule heating rates in the thermosphere due to time mean currents. Radio Sci., 10, 389-399.
- Roble, R. G., J. E. Salah, and B. A. Emery, 1977: The seasonal variation of the diurnal thermospheric winds over Millstone Hill during solar cycle maximum. J. Atmos. Terr. Phys., in press.
- Rüster, R. and J. R. Dudeney, 1972: The importance of the non-linear term in the equation of motion of the neutral atmosphere. J. Atmos. Terr. Phys., 34, 1075-1083.
- Salah, J. E., 1972: A Study of the Midlatitude Thermosphere by Incoherent Scatter Radar, Ph.D. thesis in the Depart. of Meteorology, MIT, August 1972.
- _____, 1974: Daily oscillations of the mid-latitude thermosphere studied by incoherent scatter at Millstone Hill, J. Atmos. Terr. Phys., 36, 1899-1909.
- Salah, J. E. and J. V. Evans, 1973: Measurements of thermospheric temperatures by incoherent scatter radar. Space Res. XIII, 267-286.
- Salah, J. E., J. V. Evans, D. Alcayde, and P. Bauer, 1976: Comparison of exospheric temperatures at Millstone Hill and St. Santin. Ann. Geophys., 32, 257-266.
- Salah, J. E. and J. M. Holt, 1974: Midlatitude thermospheric winds from incoherent scatter radar and theory. Radio Sci., 9, 301-313.
- Salah, J. E., R. H. Wand, and J. V. Evans, 1975: Tidal effects in the E region from incoherent scatter radar observations. Radio Sci., 10, 347-355.

- Schunk, R. W. and J. C. G. Walker, 1970: Thermal diffusion in the F2-region of the ionosphere. Planet, Space Sci., 18, 535-557.
- Stein, J. A. and J. C. G. Walker, 1965: Models of the upper atmosphere for a wide range of boundary conditions. J. Atmos. Sci., 22, 11-17.
- Straus, J. M., S. P. Creekmore, R. M. Harris and B. K. Ching, 1975: Effects of heating at high latitudes on global thermospheric dynamics. J. Atmos. Terr. Phys., 37, 1545-1554.
- Stubbe, P., 1968: Frictional forces and collision frequencies between moving ion and neutral gases. J. Atmos. Terr. Phys. 30, 1965-1985.
- Taylor, G. N., 1974: Meridional F2-region plasma drifts at Malvern. J. Atmos. Terr. Phys. 36, 267-286.
- Taylor, H. A. and H. C. Brinton, 1961: Atmospheric ion composition measured above Wallops Island, Virginia. J. Geophys. Res., 66, 2587-2588.
- Walker, J. C. G., 1965: Analytical representation of upper atmosphere densities based on Jacchia's static diffusion models. J. Atmos. Sci., 22, 462-463.
- Walker, D. M. C., 1974: Analysis of the orbit of 1970-65D, Cosmos 359 rocket. Planet, Space Sci., 22, 391-402.
- Warren, E. S., 1963: Some preliminary results of sounding the top side of the ionosphere by radio pulses from a satellite. Nature, 197, 636-639.
- Woodman, R. F., 1970: Vertical drift velocities and east-west electric fields at the magnetic equator. J. Geophys. Res., 75, 6249-6259.
- _____, 1972: East-west ionospheric drifts at the magnetic equator. Space Res. XII, 969-974.
- Wu, Mao-Fou, 1969. Topside ionosphere electron density concentration: Observation and theory. MIT, Dept. of Met., Planet, Circ. Project, Report No. 23, MIT-2241-54, Cambridge, Mass., 201 pp.
- Wulf, O. R., 1971: Winter-summer difference in geomagnetic activity. J. Geophys. Res., 76, 1837-1840.

APPENDIX A

CORRECTION OF B MODE TEMPERATURES

In 1971, J. E. Salah (1972) examined the results for four days in 1969-1970 and compared the B and C mode temperature estimates obtained at a mutual delay time of 3.5 msec (nominal height of 525 km). From this data set he derived an empirical correction for the B mode, assuming the C mode results were correct. He found that the ion temperature discrepancy was a function primarily of the temperature ratio T_e/T_i , with differences in T_i of up to 200°K at low values of T_e/T_i (Figure A.1). In addition, the value of the B mode estimates of T_e/T_i were too high whenever the ratio approached unity (Figure A.2). Subsequently, an attempt was made to remove these discrepancies by making corrections to the values of T_i and T_e/T_i derived using the B mode for delay times of 2.0 and 2.5 msec (300 and 375 km nominal heights) whenever the temperature ratios obtained with the B and C modes at 525 km differed by more than 0.1, or if the ion temperatures differed by more than 100°K.

These empirical corrections removed the worst features of the discrepancies, but introduced step changes in the ion temperature values (of as much as 200°K) during the nighttime. This in turn caused the exospheric temperature derived from these data to also exhibit point-to-point fluctuations at some times, and these served to enhance the amplitude of the highest frequency Fourier component (6 to 8 hour) fitted to the results.

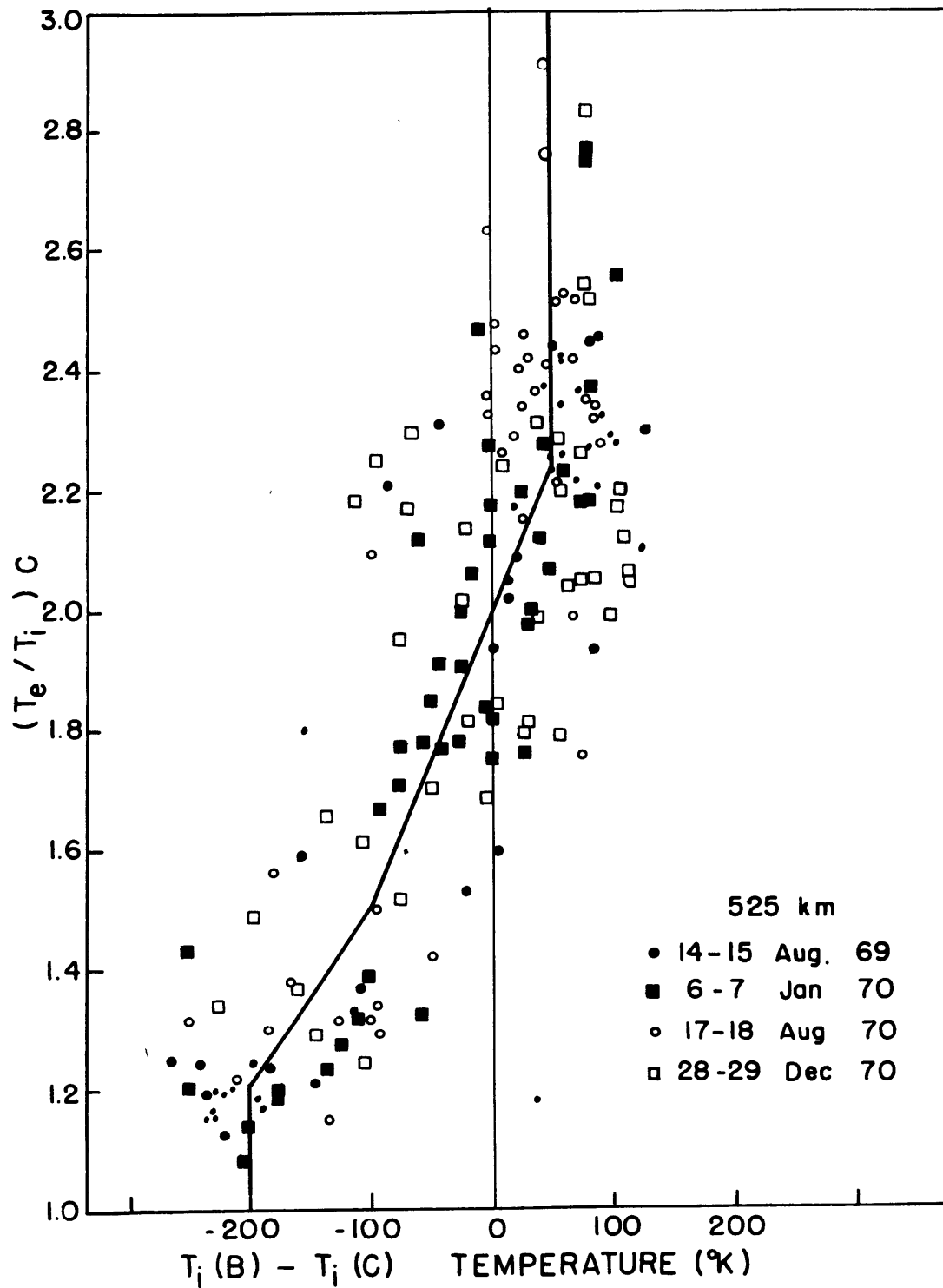


Fig. A.1: Deviation between single short and long pulse ion temperature (from Fig. A.2 of Salah, 1972).

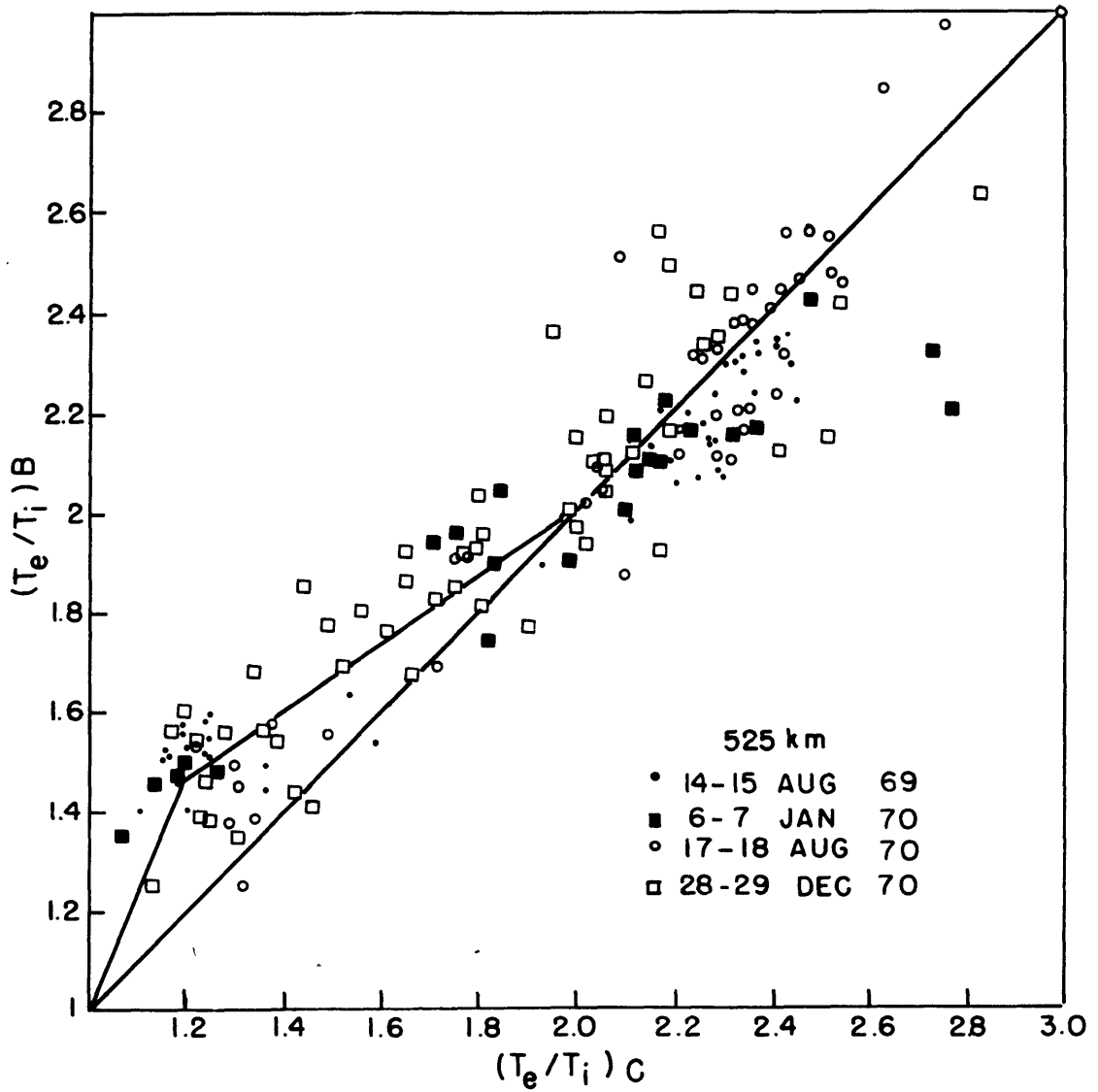


Fig. A.2: T_e/T_i derived from short and long single pulses.
 (From Fig. A.1 of Salah, 1972).

To remedy this defect a new correction procedure was devised by the author using 63 days of data spanning the three year period of 1970 through 1972. Values for the temperature obtained from spectra measured at three delays along the radar time-base in each of the two modes were examined. These were delay times of 3.0, 3.5, and 4.0 msec, corresponding to the nominal heights of 450, 525, and 600 km. (Measurements made at the 4.5 msec delay time with the B mode were considered to be too unreliable to be used).

By employing three delays it was possible to remove any altitude dependent features of the comparison. Because of the different height resolutions provided by the two modes, a proper comparison of their results requires knowledge of their equivalent or effective center heights. The "nominal" height is the center of the scattering volume defined by the delay between the transmission of the pulse and sampling the echoes. The "equivalent" height or "true" height is that height which contributes most to the scattered power. Two factors determine the equivalent height viz: i) a triangular weighting of the scattering volume centered on the nominal height imposed by the use of pulses and matched receiver filters and ii) the actual returned power vs altitude (given by eq. 2.8). Below the electron density peak the increase in N with altitude tends to cause the equivalent height to be greater than the nominal height, while the $1/h^2$ variation (eq. 2.8) tends to cause the equivalent height to be lower. The nominal

and true heights are thus not very different. Above the peak, these two effects operate in the same direction to produce an equivalent height that is always lower than the nominal height. Table A.1 shows the range of equivalent heights found for the B and C modes for delays of 3.0, 3.5 and 4.0 msec. The true heights for the C mode are lower than the corresponding ones for the B mode because of its longer pulse length.

Table A.1: Variations in the True Heights for Various Delay Times in the B & C Modes

mode	Delay time msec (nominal height km)		
	3.0 (450)	3.5 (525)	4.0 (600)
B	437-441 km	512-517 km	586-593 km
C	398-428 km	479-488 km	551-568 km

Besides adjusting the results for differences in their effective center heights, it was also necessary to remove the correction to the electron temperature that had been applied to compensate for the effect on the signal spectrum of the changing Debye length (Evans, 1969). This correction was (Evans et al, (1970))

$$T_e = T'_e / (1 - 1.62 T'_e / N) \quad (A.1)$$

where T_e and T'_e are the corrected and uncorrected electron temperatures, and N is the electron density given in units of electrons/cm³. Since it was desired to compare the interpretations of the spectra gathered at the same altitudes by the two modes it was considered necessary to remove this latter correction to the results.

A straight line interpolation of the T_e and T_i values at the three true heights corresponding to the three delays examined was used to find T_e and T_i at true heights of 450 and 525 km. The individual values were next sorted into groups of B mode ion temperatures (TIB) versus B mode temperature ratios T_e/T_i (TRB) in intervals of spanning 100°K in TIB over the range 600-1700°K and intervals of 0.2 in TRB from 0.9 to 3.1. Next all the points in each box were averaged.

The corresponding C mode temperatures and temperature ratios were then averaged to give the true values for each box. The averages were originally kept separately for the two heights (450 and 525 km), but were later combined into one to obtain a more extensive data base. Provided all height-dependent features of the data are removed, the corrections found with the data at 450 km should be the same as those found with data at 525 km. The averaged values of TIC were plotted for each TIB box versus TRB (Figure A.3). Then the TRC values for each TRB box were plotted against TIB (Figure A.4).

To obtain a smoothly varying correction for TIB and TRB, appropriate boundary conditions were then placed around the edges of these matrices and quartric surfaces were fitted to the points for TIC and TRC of the form

$$\text{TIC (or TRC)} = \sum_{i=1}^5 (a_{1i} + a_{2i} \text{TIB} + a_{3i} \text{TIB}^2 + a_{4i} \text{TIB}^3 + a_{5i} \text{TIB}^4) \text{TRB}^{(i-1)} \quad (\text{A.2})$$

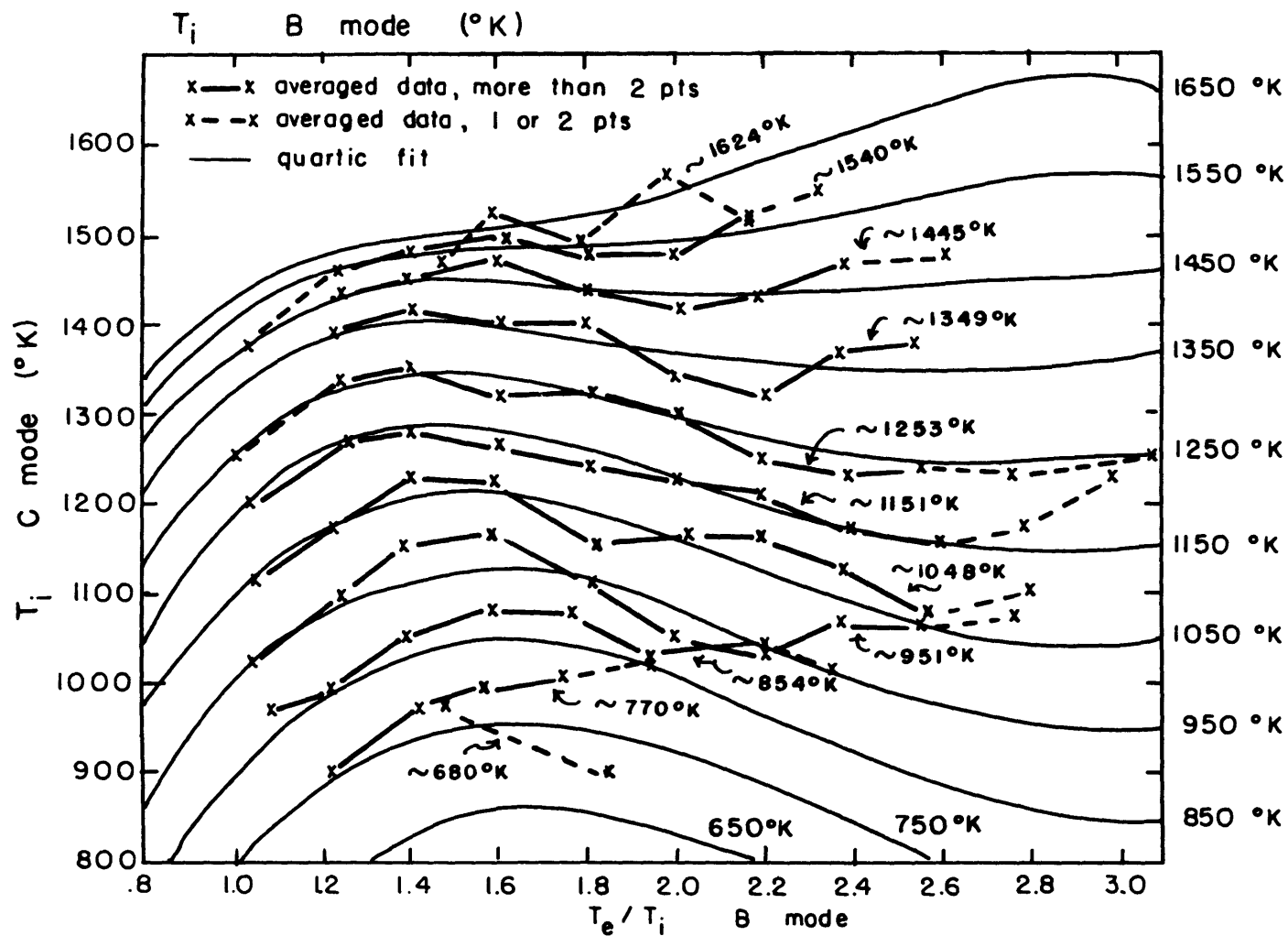


Fig. A.3: Averaged B mode ion temperature data and the quartic fit.

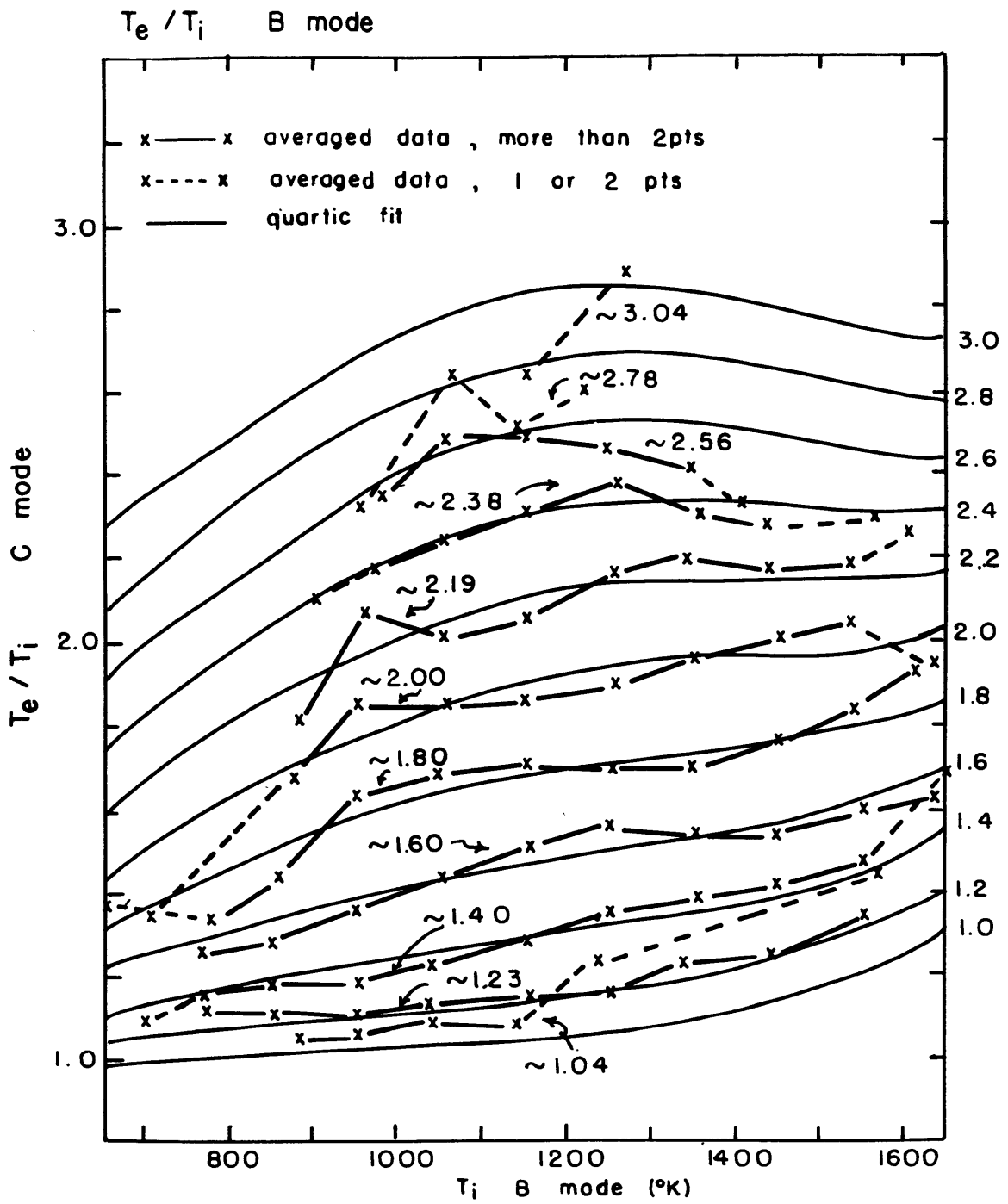


Fig. A.4: Averaged data of the ratio of T_e/T_i in the B mode data and the quartic fit.

There were 86 non-zero interior boxes and 48 exterior ones. The boundary points and most of the interior points of the matrix were given an equal weight of 50 in the fitting procedure. Exceptions were interior boxes containing only one or two data points; these were weighted one or two respectively. The interior boxes with the lowest B mode temperature ratios were weighted 200 if they contained more than two data points. The coefficients that were derived by this procedure are listed in Table A.2. Figures A.3 and A.4 show the resulting fits plotted against the averaged data.

Basically the results of this analysis are the same as those found by Salah, except that a strong dependence on T_i was found as well as the dependence on T_e/T_i . For B mode temperatures of about 1450°K , little correction to T_i is made. For temperatures above this, the correction to TIB for B mode temperature ratios less than about 2.6 is negative and is approximately -130°K for $\text{TIB} = 1650^{\circ}\text{K}$ and $\text{TRB} = 1.6$. For B mode temperatures less than 1450°K the correction to TIB is positive and approaches 200°K for $\text{TIB} = 950^{\circ}\text{K}$ and $\text{TRB} = 1.6$. For B mode temperature ratios above about 1.2, the largest corrections to TRB are at the lowest ion temperatures, the correction to $\text{TRB} = 2.0$ at $\text{TIB} = 750^{\circ}\text{K}$ being about -0.4 . For $\text{TIB} = 1150^{\circ}\text{K}$ the correction is only about -0.1 . The new corrections were applied to all the B mode data.

A deviation from the 3 year average was found for each day and each height. Although there was a great deal of scatter, the

Table A.2: Quartic Coefficients for the Fits to T_i and T_e/T_i C Mode Used in Eq.A.2

T_i C Mode:

i	a_{1i}	a_{2i}	a_{3i}	a_{4i}	a_{5i}
1	-.796867E 01	-.367180E 01	.482273E-02	-.196736E-05	.243638E-09
2	.173999E 01	.622118E 01	-.382242E-02	.652307E-06	.457058E-10
3	.106960E 00	-.205804E 01	-.500643E-03	.939378E-06	-.264987E-09
4	-.324305E 00	.146370E 00	.551828E-03	-.318412E-06	.766356E-10
5	.206308E 01	.605626E-03	-.384643E-04	-.223650E-08	.565875E-13

T_e/T_i C Mode:

i	a_{1i}	a_{2i}	a_{3i}	a_{4i}	a_{5i}
1	-.464355E 00	.786786E-02	-.953145E-05	.537837E-08	-.111904E-11
2	.149215E 01	-.110487E-01	.111261E-04	-.617450E-08	.145316E-11
3	.130935E 00	.350796E-02	-.690789E-06	-.226501E-09	.255717E-13
4	-.257652E 00	-.611208E-03	.144244E-07	.106388E-09	-.408892E-13
5	.644512E-01	.271592E-04	-.354883E-07	.273383E-10	-.156774E-14

mean of the differences in T_i at 450 km were about 30°K less than the mean of the differences in the 525 km data, and the mean of the differences in T_e/T_i were about 0.05 more at 450 km than at 525 km. It was further found that the mean differences in T_i for the year 1970 (a high sunspot number year), were about 15°K more than the mean differences for the years 1971 and 1972, although there did not appear to be any change in the differences in T_e/T_i over the three year period.

Table A.3 lists these deviations from the average. Ideally, there should not be a dependence on altitude, but delay-dependent instrumental errors could exist. These might be introduced, for

Table A.3

Deviations of Corrections to T_i and T_e/T_i of the B Mode from the Average Values. The Average Values were formed from 3 years of data, 1970-1972, and 2 altitudes, 450 and 525 km

	Deviations for T_i		Deviations for T_e/T_i	
	450km	525 km	450 km	525 km
1970	-0°K	$+24^\circ\text{K}$.030	-.021
1971-1972	-22°K	$+10^\circ\text{K}$.032	-.019
1970-1972	-12°K	$+16^\circ\text{K}$.031	-.020

example, by the ringing of the filters following the reapplication of the signals after the transmitter pulse. No variation from year to year is anticipated, but it is possible that the maintenance of the equipment varied in some fashion. However, these

differences amount to only 15% of the largest correction, and were ignored.

The quartic fits provide a smooth variation of the corrections to the B mode temperatures, as is desired, and being based on a much larger data set, should be more reliable than those employed previously. The temperatures used to create the polynomial fits found by the INSCON computer program were corrected B mode temperatures for nominal heights less than or equal to 375 km, and C mode temperatures for nominal heights equal to or greater than 600 km. For delay times corresponding to nominal heights inbetween these limits, a linear combination of the C mode and corrected B mode temperatures was used.

APPENDIX B

ESTIMATING THE EFFECT OF NEGLECTING A BOTTOM BOUNDARY MERIDIONAL GRADIENT IN ATOMIC OXYGEN

To explore the influence of the lower boundary conditions on composition, two kinds of experiments were performed. In both cases, the linear equations of motion were solved. In the first case, the ratio, r , defined to be $(1/n(0)_{120}) \partial n(0)_{120} / \partial \varphi$ was fixed and held constant throughout the day. In the second case, the values for $\partial n(0)_{120} / \partial \varphi$ were taken from the OGO-6 model which has diurnal variations of about 35% from the mean values. The OGO-6 model was used since its assumptions about conditions at 120 km most closely approximates the assumptions made in the present study. The MSIS and the 1971 Jacchia models are more complicated than the OGO-6 model, while the Jacchia 1965 model is simpler. Diurnal averages of the ratio r calculated with the OGO-6 model for an average 10.7 cm solar flux of 150, varied from a minimum at -0.87 in June (decreasing $n(0)$ towards the pole) to a broad maximum at 0.58 in early December. These were larger than the diurnal averages calculated with the MSIS model which varied from a low of -0.54 in May to a high of 0.09 in January. These ratios decreased by about 8% in both models for an average 10.7 cm solar flux of 100. The gradients contained in the MSIS model may be more reliable than those of the OGO-6 model because it was based on a larger

body of data including measurements at 150 km altitude. However, neither model includes effects caused by propagating tides.

Five days were examined in total, two days in winter and three days in summer. Their daily 10.7 cm solar flux values ranged from a low of 107 to a high of 195. Table B.1 lists the days and some of their characteristics. An "a" beside the date means the OGO-6 model atomic oxygen meridional gradients at 120 km were used. All the deviations from the basic state of $r = 0$ are normalized to ratios of $r = -1$ or deviations of the meridional temperature gradient of $100^{\circ}\text{K}/\text{rad}$. The normalization procedure assumed the changes were linear.

For one day (December 8-9, 1969) the ratio r was varied from -1.0 to 1.0 in steps of 0.2, and V_{Hn} was fit at 300 km. Figures B.1a-e show the deviations of the average zonal velocities, meridional velocities, vertical velocities, meridional exospheric temperature gradients, and meridional pressure gradient forces from their values when $r = 0$. In Section 7.3.1 we predicted a shift of winds to the SW if r were positive and a shift to the NE if r were negative. This is precisely what is observed. For $r = -1$, the net shift in the average horizontal velocity is 49 m/sec towards the east (Figure B.1a), and 12 m/sec towards the north (Figure B.1b). The change in the required meridional exospheric temperature gradient is $230^{\circ}\text{K}/\text{rad}$ (Figure B.1d), while the change in the pressure gradient is $-0.55 \text{ cm}/\text{sec}^2$ (Figure B.1e). The change in the vertical velocity

Table B.1

Table of the effects of having a non-zero bottom boundary meridional gradient in atomic oxygen. F10.7 is the 10.7 cm solar flux in units of 10^{-22} watt m^{-2} (cycle/sec) $^{-1}$. All velocities are m/sec, and the meridional exospheric temperature gradients are in $^{\circ}K/rad$.

Date	F10.7	$\Delta \overline{u(r=-1)}$	$\Delta \overline{\frac{\partial T}{\partial \phi}(r=-1)}$
December 8-9, 1969	114	53.0	235
December 8-9, 1969 (a)	114	71.6	233
May 18-19, 1970 (a)	195	15.2	231
June 23-24, 1970	150	7.6	177
June 23-24, 1970 (a)	150	6.0	171
January 20-21, 1971(a)	168	30.0	248
September 7-8, 1971(a)	107	32.2	166

(r = -1, Eq. B.1)	$(\Delta \overline{\frac{\partial T}{\partial \phi}} = 100^{\circ}K/rad)$	(r=0)
$\Delta \overline{\frac{\partial T}{\partial \phi}}$	$\Delta \overline{u}$	\overline{v}_{300}
253	22.6	2.3
253	30.7	2.3
242	6.6	-50.9
193	4.3	-75.8
193	3.5	-75.8
244	12.1	33.4
240	19.4	-30.5

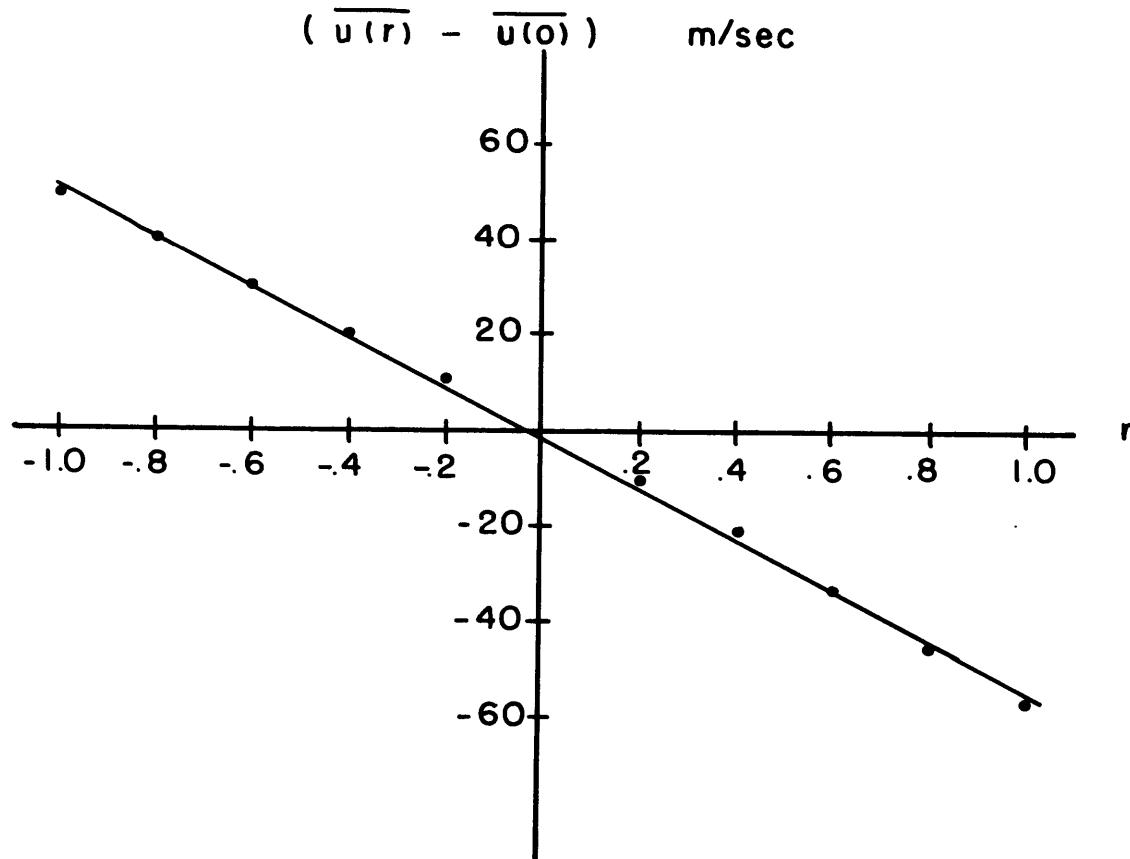


Figure B.1a: Deviations of the average zonal velocity at 300 km as a function of r for December 8-9, 1969.

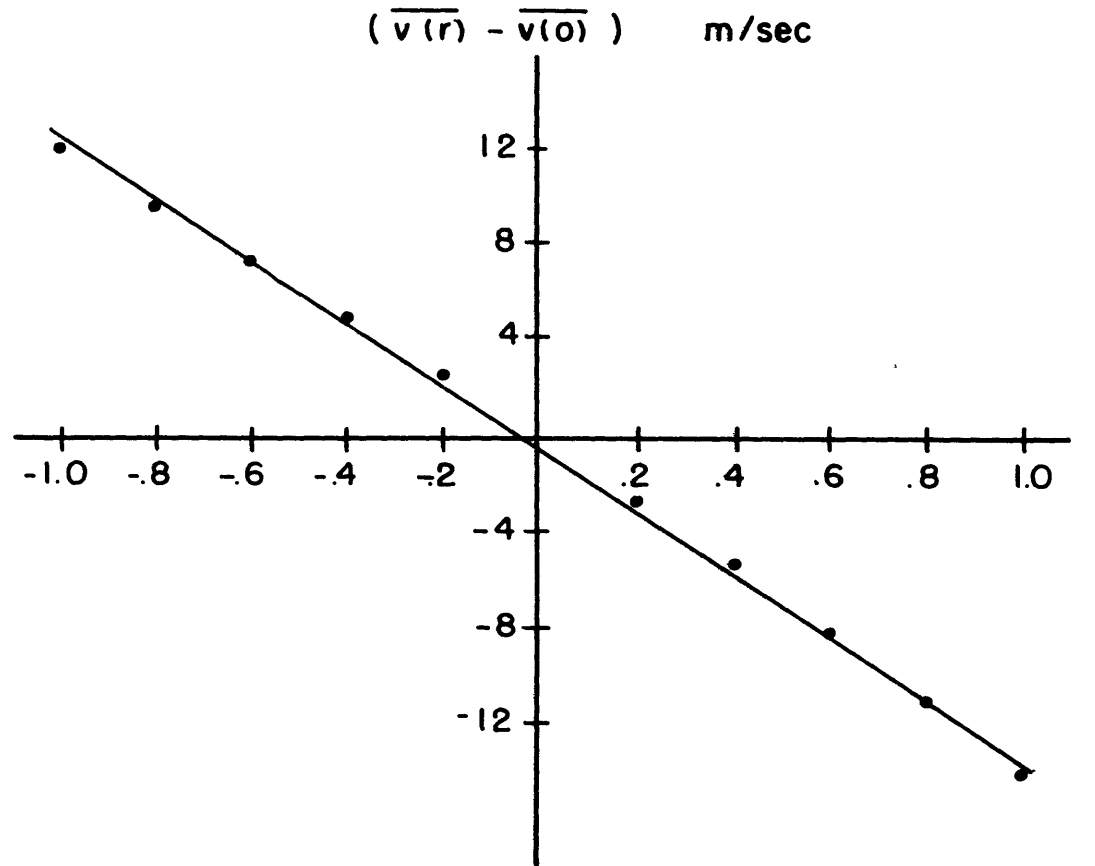


Figure B.1b: Deviations of the average meridional velocity at 300 km as a function of r for December 8-9, 1969.

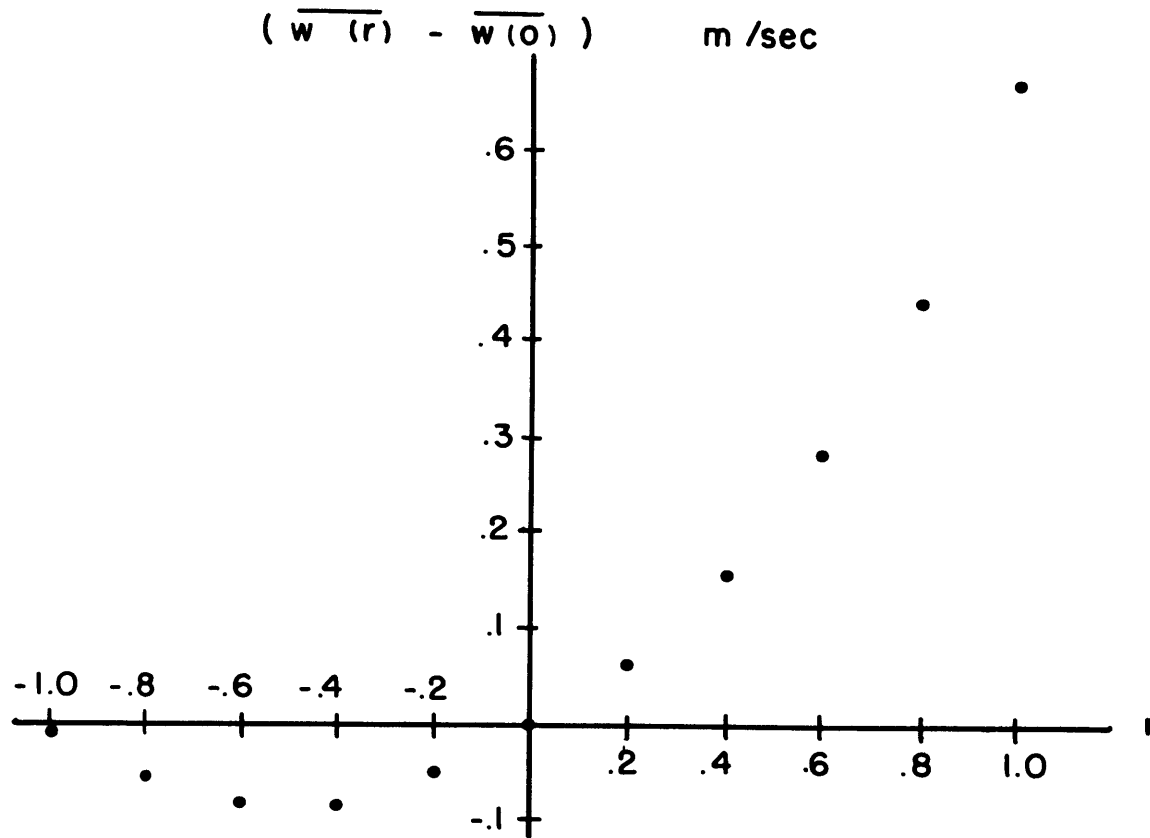


Fig. B.1c: Deviations of the average vertical velocity at 300 km as a function of r , for December 8-9, 1969 above Millstone Hill.

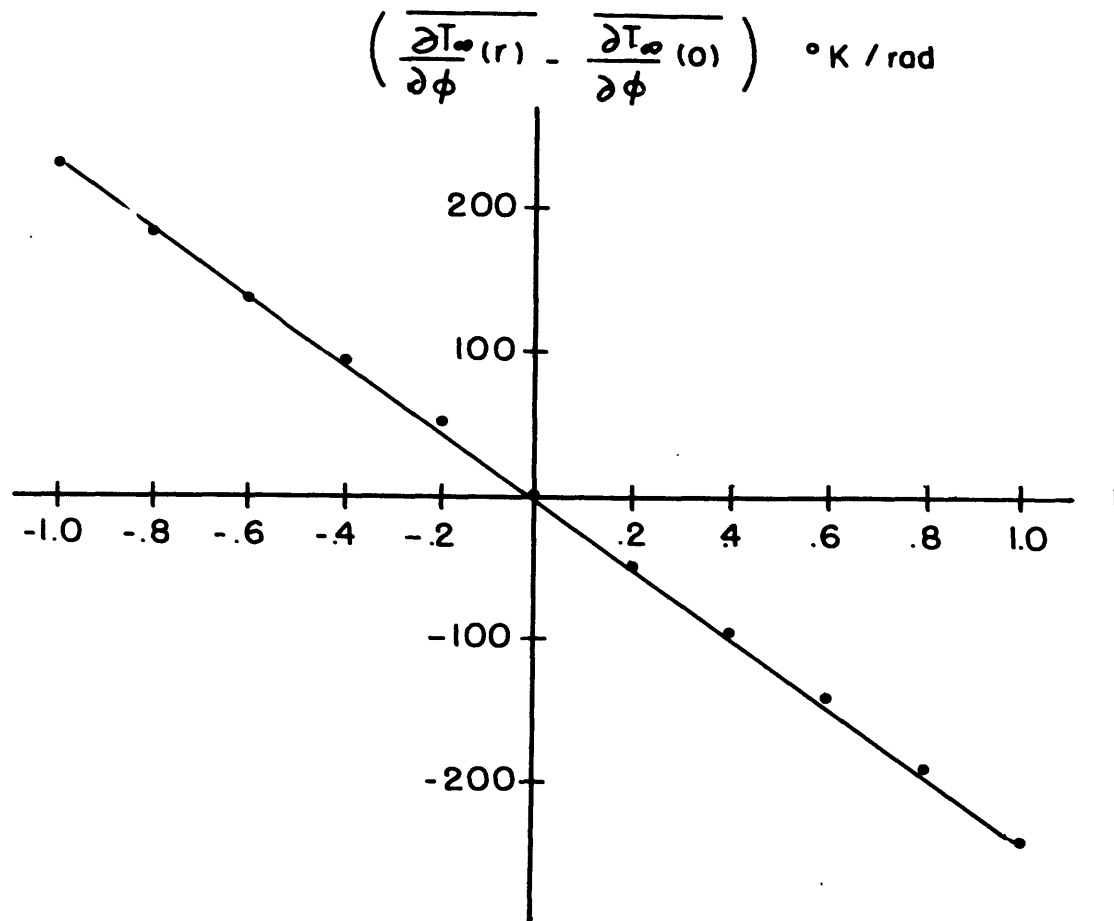


Fig. B.1d: Deviations of the average meridional exospheric temperature gradient as a function of r for December 8-9, 1969.

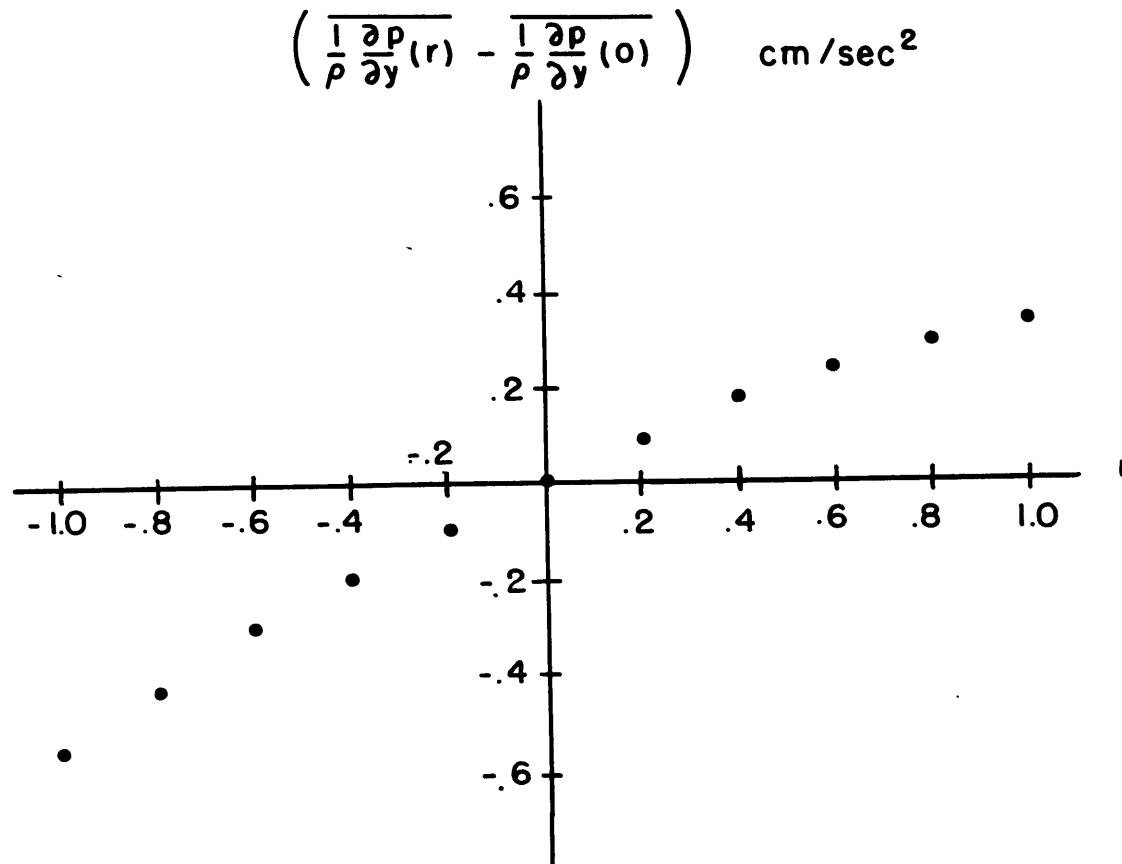


Figure B.1e: Deviations of the average meridional pressure gradient force as a function of r for December 8-9, 1969 over Millstone Hill.

at 300 km is practically negligible at -0.01 m/sec (Figure B.1c).

As can be seen in the figures, the deviations in the average zonal and meridional velocities as well as the deviations in the meridional exospheric temperature gradient are generally linear functions of r . This is not quite the case for the deviations of the meridional pressure gradient terms, $1/\rho \partial p/\partial y$, and is certainly not true for the deviations of the vertical velocity.

The changes in the mean vertical velocity with different values for r are mainly the result of changes in the term containing the gradient of the meridional velocity, $1/\rho \int_z^\infty \rho(\partial v/\partial y) dz$. Large positive values of r on this December day are associated with large poleward decreases of temperature. The large latitudinal differences cause the meridional velocity gradient to change rapidly. Meridional gradients were discussed in Section 7.4.

Since positive values of $\partial n(0)_{120}/\partial \varphi$ (increasing $n(0)$ towards the pole) are expected for winter, the net conclusion seems to be that the average vertical velocity can change considerably depending on the value of the ratio used. If the MSIS average ratios are used, there would not be much change since r would probably be at most 0.1. If the OGO-6 model average ratios were used, the change in w would be quite significant.

The non-linear behavior of the changes in the meridional pressure gradient as a function of r is a direct consequence of the almost, but not quite, linear behavior of the meridional exospheric

temperature gradient as a function of r . The difference in the changes of this latter gradient at $r = 1$ and -1 is about $8.5^\circ\text{K}/\text{rad}$, which is small compared to the average change of $230^\circ\text{K}/\text{rad}$. However, the change in the pressure gradient is the difference of two large numbers. The value of $f_{300}(n_j, T)$ in Eq. 7.5 is $0.0246 \text{ cm-rad}/^\circ\text{K-sec}^2$. Multiplying this by the $8.5^\circ\text{K}/\text{rad}$, results in a pressure gradient change over $r = \pm 1$ of 0.21 cm/sec^2 , which is what is observed in Figure B.1e ($0.35 + 0.55 = 0.20$).

A further experiment for June 23-24, 1970 was performed with similar results except the magnitudes of the changes in the velocities with respect to their values at $r = 0$ were reduced by about a factor of 10 while the magnitudes of the changes in the meridional exospheric temperature gradient were reduced by about 30% (see Table B.1). The change in the linear relationship between r and $\overline{\Delta \partial T_\infty / \partial \varphi} (= \overline{\partial T_\infty / \partial \varphi(r)} - \overline{\partial T_\infty / \partial \varphi(0)})$ arises because the factors multiplying the meridional exospheric temperature gradient and the ratio of $(1/n(0)_{120}) \partial n(0)_{120} / \partial \varphi$ in eq. 7.5 are in a different ratio to one another. This linear relationship can be written approximately as

$$\overline{\frac{\partial T_\infty}{\partial \varphi}(0)} \approx \overline{\frac{\partial T_\infty}{\partial \varphi}(r)} + \frac{\overline{g(n_j, T)}}{\overline{f(n_j, T)}} \frac{1}{n(0)_{120}} \frac{\overline{\partial n(0)_{120}}}{\partial \varphi} \quad (\text{B.1})$$

where f is the function written in Eq. 7.5 and $g = k T n(0)/\rho$. The average value of the ratio of $g(n_j, T)/f(n_j, T)$ is 253°K for the December day and 193°K for the June day. Calculations of $\overline{\Delta \partial T_\infty / \partial \varphi}$

using Eq. B.1 were within 10% of the experimental values for four of the days examined (see Table B.1). The September day yielded values that were 30% higher than those observed.

The drastic reduction in the deviations of the horizontal velocities as a function of r for the June day, results from the fact that the average meridional velocity (for $r = 0$) is 76 m/sec towards the south, whereas it is only 2 m/sec towards the north for the December day. Therefore, the average Coriolis effects on the zonal velocity are already large on the June day, and changes brought about by a non-zero r will have a small effect. Therefore, the same change in r for the December day will give rise to a much larger effect than it would for the June day.

In Table B.1, deviations of the meridional exospheric temperature gradient $\Delta \overline{\partial T_{\infty} / \partial \varphi}$ and the zonal wind $\Delta \overline{\bar{u}(r) - \bar{u}(0)}$ are listed for a ratio of -1.0. The values are based on assuming a linear relationship between $\Delta \overline{\partial T_{\infty} / \partial \varphi}$ and $\Delta \bar{u}$ and extrapolating from the experimental values. Values of $\Delta \overline{\partial T_{\infty} / \partial \varphi}$ calculated with Eq. B.1 are also tabulated. The values of $\Delta \bar{u}$ for a $\Delta \overline{\partial T_{\infty} / \partial \varphi}$ of $100^{\circ}\text{K}/\text{rad}$ are tabulated along with $\overline{v_{300}(0)}$, the average meridional wind at 300 km for the case of the ratio equal to zero. These are plotted in Figure B.2 as a function of the absolute value of \bar{v} and an approximate straight line has been fitted through the points.

In general, $\Delta \bar{u}$ can be written in terms of $\Delta \overline{\partial T_{\infty} / \partial \varphi}$ as

$$\Delta \bar{u} \cong c \Delta \overline{\partial T_{\infty} / \partial \varphi} \quad (\text{B.2})$$

$[\bar{u}(r) - \bar{u}(0)]$ m/sec for $[\overline{\partial T_{\infty} / \partial \phi}(r) - \overline{\partial T_{\infty} / \partial \phi}(0)] = 100 \text{ }^{\circ}\text{K/rad}$

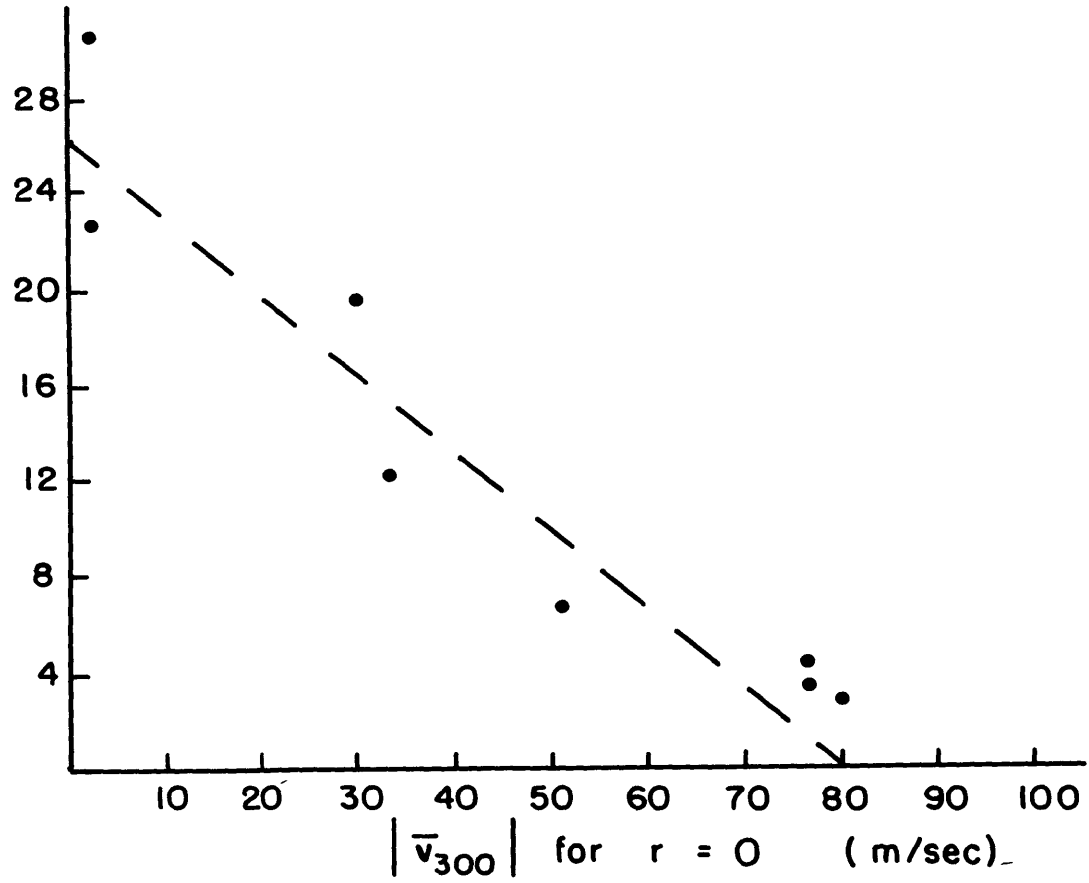


Fig. B.2: Plot of $\Delta \bar{u}$ for a $\Delta T_{\infty} / \partial \phi$ of 100°K/rad as a function of the absolute value of the average meridional velocity at 300 km for $r=0$.

where $\Delta \bar{u}$ is in m/sec, $\Delta \partial T_{\infty} / \partial \varphi$ is in $^{\circ}\text{K}/\text{rad}$ and

$$c \cong (.26 - .00325 \left| v_{300}(0) \right|) \text{ (m-rad/sec-}^{\circ}\text{K)} \quad (\text{B.3})$$

is the approximate linear relationship plotted in Figure B.2.

$v_{300}(0)$ is in m/sec.

There is also a linear relationship between $\Delta \bar{u}$ and $\Delta \bar{v}$ ($= \bar{v}(r) - \bar{v}(0)$) which is a direct result of fitting the velocities along the magnetic meridian to V_{Hn} at 300 km. The relationship can be written as

$$\Delta \bar{v} = (-\sin D \Delta \bar{u}) / \cos D = .25 \Delta \bar{u} \quad (\text{B.4})$$

where D is the declination angle at Millstone Hill (-14°).

In conclusion, if the ratio of $\overline{(1/n(0))_{120} \partial(n(0))_{120} \partial \varphi}$ is known, the effect of adding it to a basic state based on $r = 0$ can be estimated through Eqs. B.1 - 4. This has been done at the end of the analysis for each day using MSIS model values for the average ratio of r , and the results were reported in Section 7.3.2.

APPENDIX C

DETAILED EXAMINATION OF THE VARIOUS LATITUDINAL GRADIENTS

This appendix outlines the details of the examination of the magnitudes and uncertainties of the north-south velocity gradients and compares the velocity differences with those derived from the non-linear global model of Blum and Harris (1975). A summary of this appendix is contained in Section 7.4. The effects that will be examined are latitudinal variations in the Coriolis parameter, in electron densities, and in the meridional pressure gradient.

C.1 The Effect of the Changing Coriolis Parameter

The Coriolis parameter f ($= 2\Omega \sin \phi$) is a function of latitude ϕ . It was desired to see what effect this change alone had on the velocity calculation at another latitude on June 23-24, 1970. To test this out, the equations of motion were solved for with all parameters the same except for the latitude which was set 1 degree to the north of Millstone Hill. A comparison was then made between the velocities produced at this higher latitude with those calculated for the latitude of Millstone Hill.

The velocities differed by as much as 10 m/sec, which translates to a change of about 2.0 m/sec in 0.2° of latitude.

Figure C.1 is a plot of Δu and Δv between 0.2° deduced from the differences found between 1° . This assumption of a linear relationship is probably acceptable over a small variation in latitude. Δu and Δv are defined as the differences between the velocities u_2 and v_2 at the latitude of $\phi_{MH} + .2$ and the velocities u_1 and v_1 at the latitude of Millstone Hill, ϕ_{MH} (i.e. $\Delta u = u_2 - u_1$, etc.). The sign of Δu is typically the same as the sign of v while the sign of Δv is opposite to the sign of u . Assuming the major changes occur in the Coriolis and ion drag terms (since the pressure gradients remain unchanged), Δu and Δv can be written as

$$\Delta u = 1/\lambda (v \Delta f + f \Delta v) \tag{C.1}$$

$$\Delta v = - 1/\lambda (u \Delta f + f \Delta u)$$

The quantity $\Delta f/f$ is about 0.0038 for 0.2 degrees north of Millstone Hill, and its inverse is 263. The zonal velocity for this June day varied between 385 m/sec to the east and 275 m/sec to the west (see Figure 6.8). Therefore, u was often larger than $\Delta u f/\Delta f$. Since the sign of Δu is nearly the same as the sign of u (see Figures 6.8 and C.1), it is easy to see why the sign of Δv is opposite to the sign of u . Why Δu is the same sign

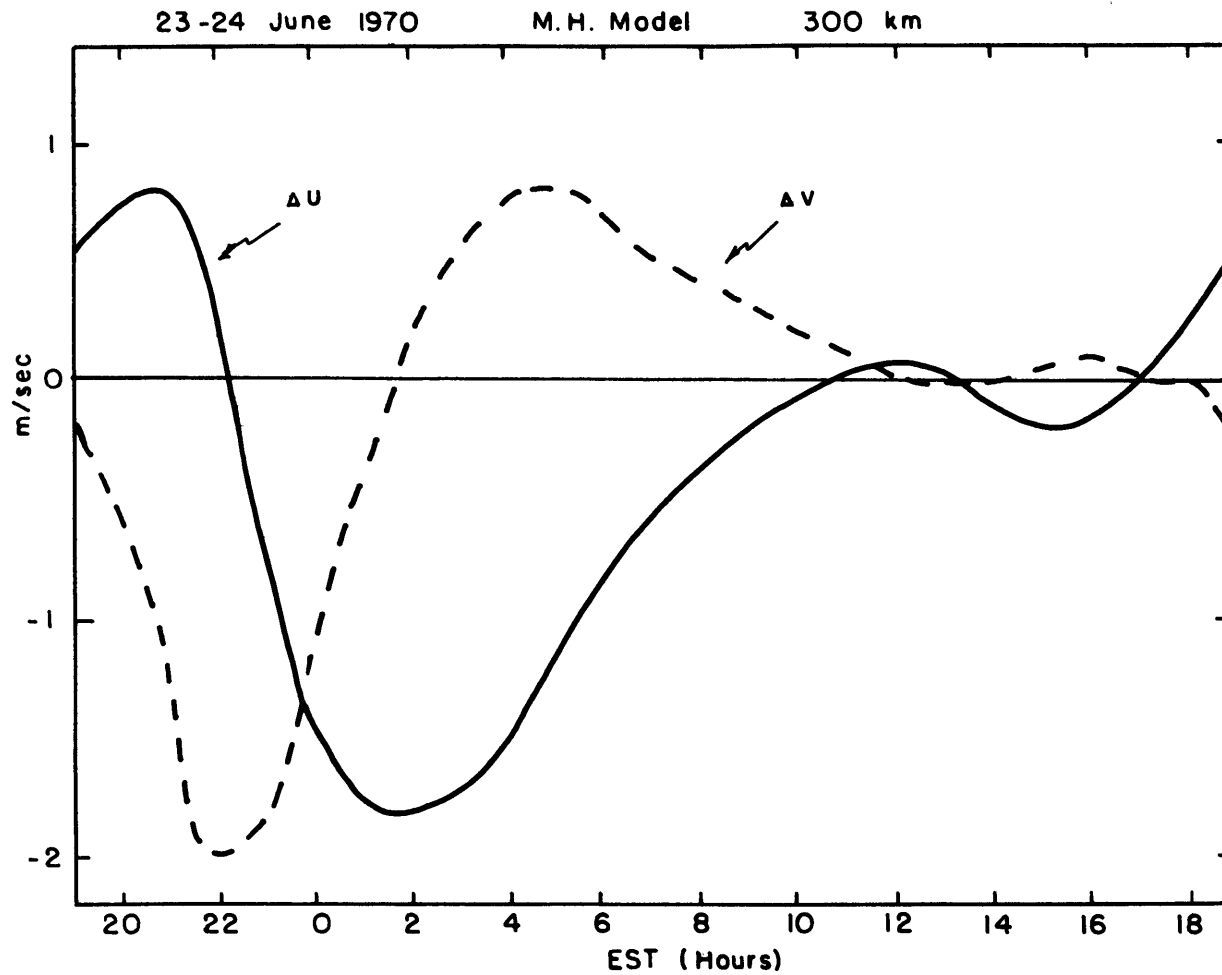


Figure C.1: Plot of Δu and Δv at 300 km in 0.2° of latitude deduced from changing the latitude by 1° at Millstone Hill on June 23-24, 1970.

as v is somewhat unclear since $\Delta v f / \Delta f$ is often larger than v and is usually the opposite sign.

The derived differences of 2 m/sec in 0.2 degrees of latitude are rather large. Linearly extrapolating, this would cause a difference of 100 m/sec in 10 degrees of latitude which is physically unrealistic. The changes in the ion drag and pressure gradients forces over several degrees of latitude would prevent such a change from occurring.

C.2 Electron Density Latitudinal Gradients

The electron density generally decreases towards the poles at geomagnetic mid-latitudes. The decrease is roughly 4% in 1 degree of latitude. However, as mentioned in Section 5.5.1, there may not be a decrease on some summer nights and some winter days. For most of the present study we assumed a uniform decrease in the electron density toward the pole, but some experiments were carried out assuming latitudinally constant electron densities to see what effect reasonable variations in the latitude structure of the electron density would have on the latitudinal changes in velocity.

Variations of the electron density in latitude only affects the ion drag coefficient $\lambda (= n_i \mu_{in} \nu_{in} / \rho)$ in the equations of motion.

λ is not greatly changed for different latitudes by different temperatures or densities since the changes in the ion-neutral collision frequency ν_{in} are largely cancelled by similar changes in the density ρ . Therefore, to a first approximation, the ion drag coefficient at a latitude 0.2° to the north of Millstone Hill is about 99.2% of its value at Millstone Hill. If there is a balance between ion drag and the pressure gradient, then the velocities at 0.2° polewards, u_2 and v_2 , and the velocities at Millstone Hill, u_1 and v_1 , can be expressed approximately as

$$\lambda_2 u_2 \approx - \frac{1}{.992 \lambda_1} \left(\frac{1}{\rho} \frac{\partial p}{\partial x} \right)_2 + \frac{1}{\lambda_2} \left(\frac{1}{\rho} \frac{\partial p}{\partial x} \right)_1 \quad (C.2)$$

$$\approx - \frac{1.008}{\lambda_1} \left(\frac{1}{\rho} \frac{\partial p}{\partial x} \right)_2 + \frac{1}{\lambda_1} \left(\frac{1}{\rho} \frac{\partial p}{\partial x} \right)_1 \quad \text{etc.}$$

Therefore, decreasing the electron density towards the pole by 0.8% in 0.2° , has the approximate effect of changing Δu by the amount $-0.008 (1/\lambda_1 1/\rho \partial p / \partial x)$ which is approximately $+0.008 u$. The same reasoning follows for changes in Δv . A 300 m/sec zonal velocity would then be expected to alter Δu by about 2.4 m/sec. This is not

what actually happens, however, because Δu and Δv also include the differences between other terms such as the viscous and acceleration terms. These terms cannot be predicted easily for another latitude so their differences can be, and often are, sufficiently large that the decreasing electron density may not be the principal change.

Figures C.2a and b show the contributions to Δu and Δv at 300 km from various terms in the equations of motion for June 23-24, 1970 assuming a uniform decrease of 0.8% in 0.2° in the electron density. The lines are labelled ΔACCEL , ΔVISC , ΔCOR , ΔCURV , ΔPGX or ΔPGY , and Δu or Δv . They are related as follows:

$$\begin{aligned}
 \Delta u \simeq & (-u_{\text{ion}} + u)_2 - (-u_{\text{ion}} + u)_1 = - (1/\rho \partial p / \partial x)_2 \lambda_2 \\
 & + (1/\rho \partial p / \partial x)_1 / \lambda_1 - (\partial u / \partial t)_2 / \lambda_2 + (\partial u / \partial t)_1 / \lambda_1 \quad (\text{C.3}) \\
 & + (uv \tan \varphi / r)_2 / \lambda_2 - (uv \tan \varphi / r)_1 / \lambda_1 + (fv)_2 / \lambda_2 - (fv)_1 / \lambda_1 \\
 & + (\mu / \rho \partial^2 u / \partial z^2 + 1 / \rho \partial \mu / \partial z \partial u / \partial z)_2 / \lambda_2 - (\mu / \rho \partial^2 u / \partial z^2 \\
 & + 1 / \rho \partial \mu / \partial z \partial u / \partial z)_1 / \lambda_1 = \Delta \text{PGX} + \Delta \text{ACCEL} + \Delta \text{CURV} + \Delta \text{COR} + \Delta \text{VISC} \\
 & \text{etc.}
 \end{aligned}$$

$V_{D//}$ and V_{iz} were assumed constant over this latitude range so $u_{\text{ion}1}$ and $u_{\text{ion}2}$ were very nearly equal. Figures C.3a and b show the same plots except here the electron density was latitudinally constant. Δu and Δv for constant electron densities are also plotted as x's in Figures C.2a and b for easy comparison.

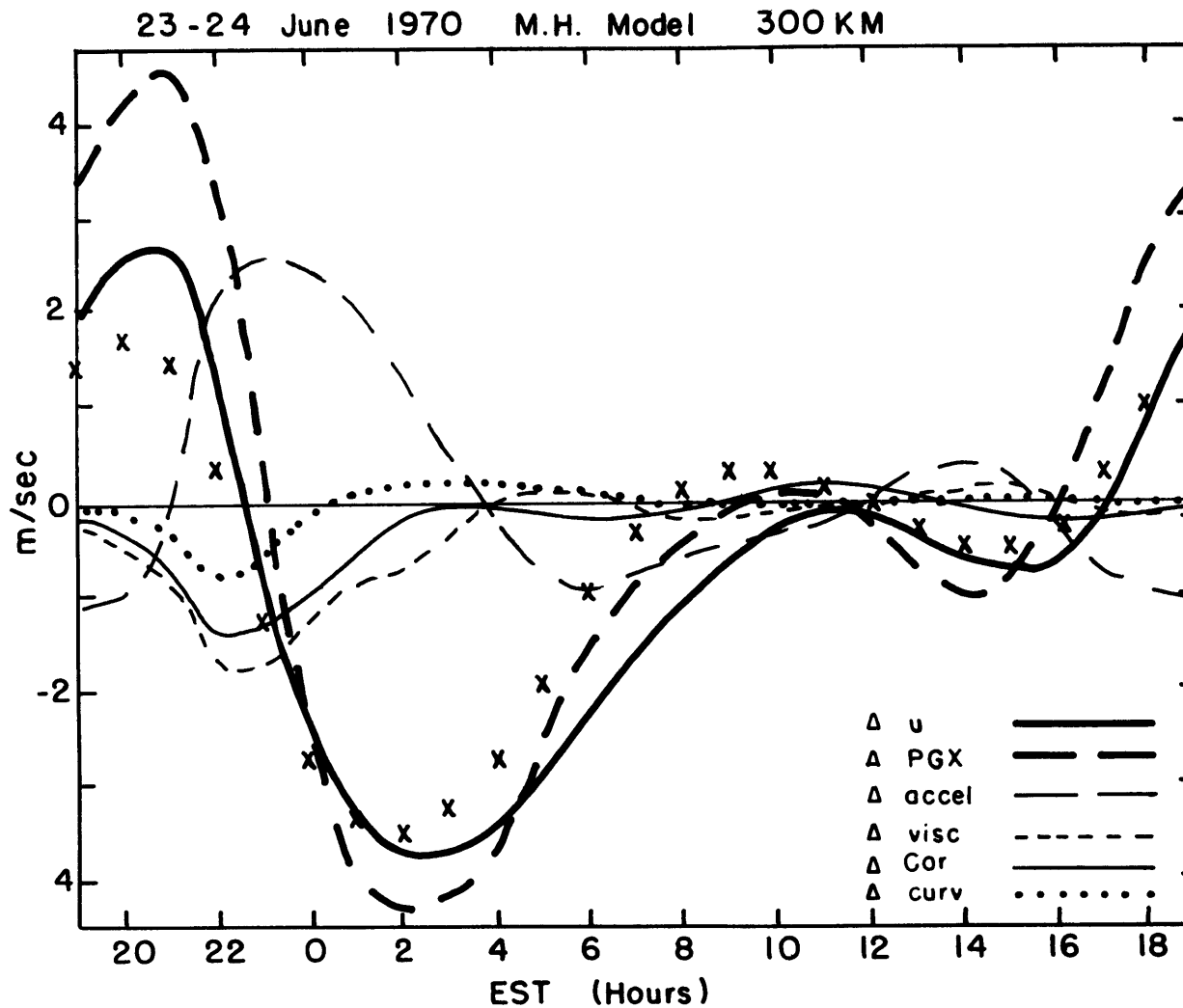


Figure C.2a: Plot of the contributors to the difference in zonal velocity Δu between $42.6^\circ N$ and $42.8^\circ N$ at 300 km for the present analysis of June 23-24, 1970. The x's are the values of Δu derived using constant electron densities (see Figure C.3a).

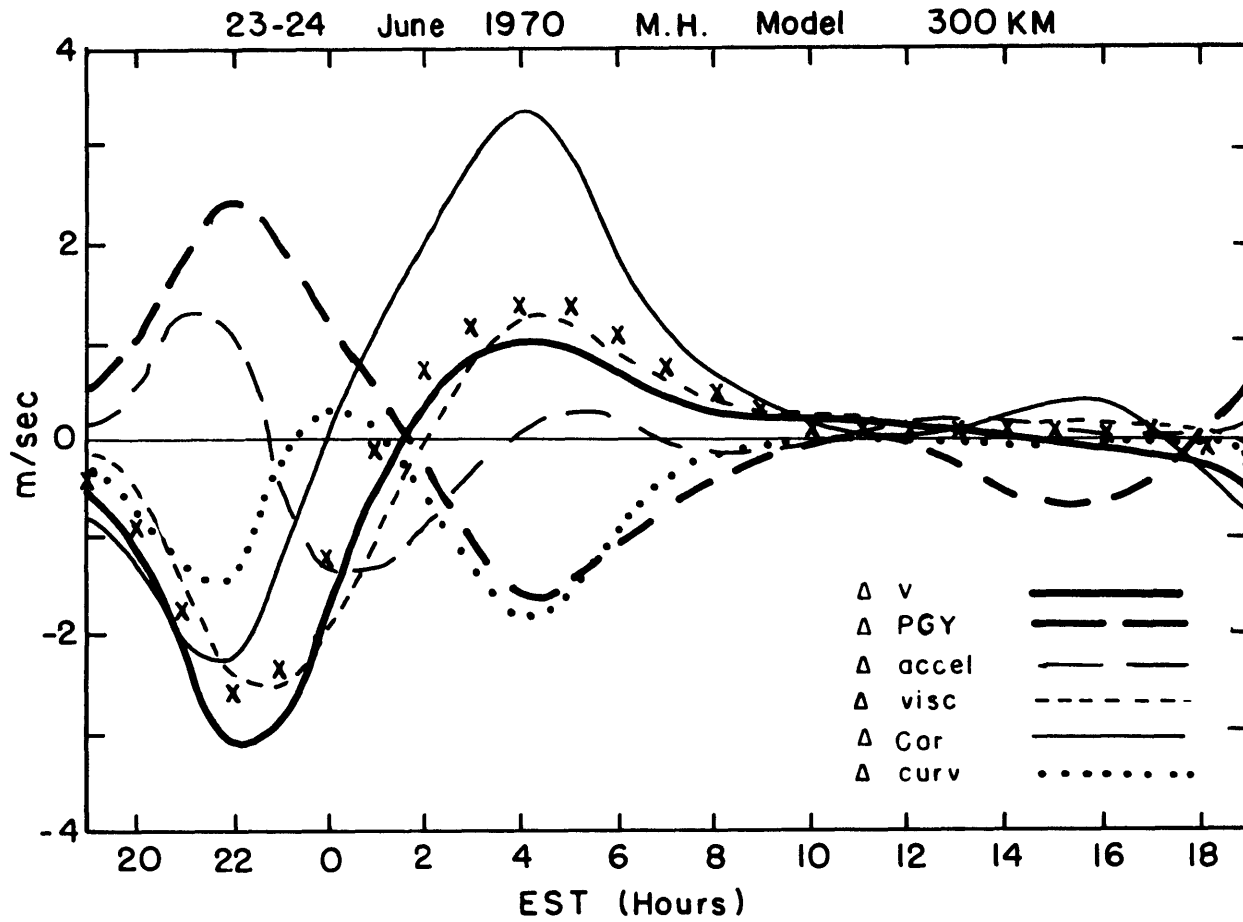


Figure C.2b: Plot of the contributors to the difference in meridional velocity Δv between $42.6^\circ N$ and $42.8^\circ N$ at 300 km for the present analysis of June 23-24, 1970. The x's are the values of Δv derived using constant electron densities (see Figure C.3b).

The diurnal variations of Δu and Δv are similar to those plotted in Figure C.1 for the case where the Coriolis parameter was changed. In the later figures, the magnitudes were somewhat larger and the specific contributors are named. In general, Δu follows ΔPGX . This follows because of the near balance of ion drag and pressure gradient and the change in latitude of $\partial T_{\infty} / \partial t$. This change is proportional to $(\phi - \phi_{MH}) \partial(\partial T_{\infty} / \partial \phi) / \partial t$. For the case of decreasing electron density, ΔPGX varies between 4.5 m/sec at 2100 LT and -4.3 m/sec at 0200 LT. Δu varies between 2.7 m/sec at 2100 LT and -3.8 m/sec at 0300 LT. Δv is more likely to follow ΔCOR . This is because of the other assumption made that $\partial T_{\infty} / \partial \phi$ remains constant over the two latitudes. The largest terms in the meridional momentum equation at 300 km are the pressure gradient, Coriolis, ion drag, and viscous forces (see Figure 6.7b). For the decreasing electron density case, ΔCOR varies between -2.3 m/sec at 2200 LT and 3.4 m/sec at 0400 LT, while Δv varies between -3.1 m/sec at 2200 LT and 1.0 m/sec at 0400 LT.

The effect of a uniform polewards decrease in electron density is to increase the magnitudes of most of the terms. This is especially striking in the case of the pressure gradients. Looking back at Figure 6.7a and 6.8 for June 23-24, 1970, there was an approximate balance between the pressure gradient and the ion drag in the zonal momentum equation. The zonal velocity at 300 km went from a peak eastwards (positive) velocity of about 380 m/sec around 2200 LT to a peak westwards (negative) velocity of about

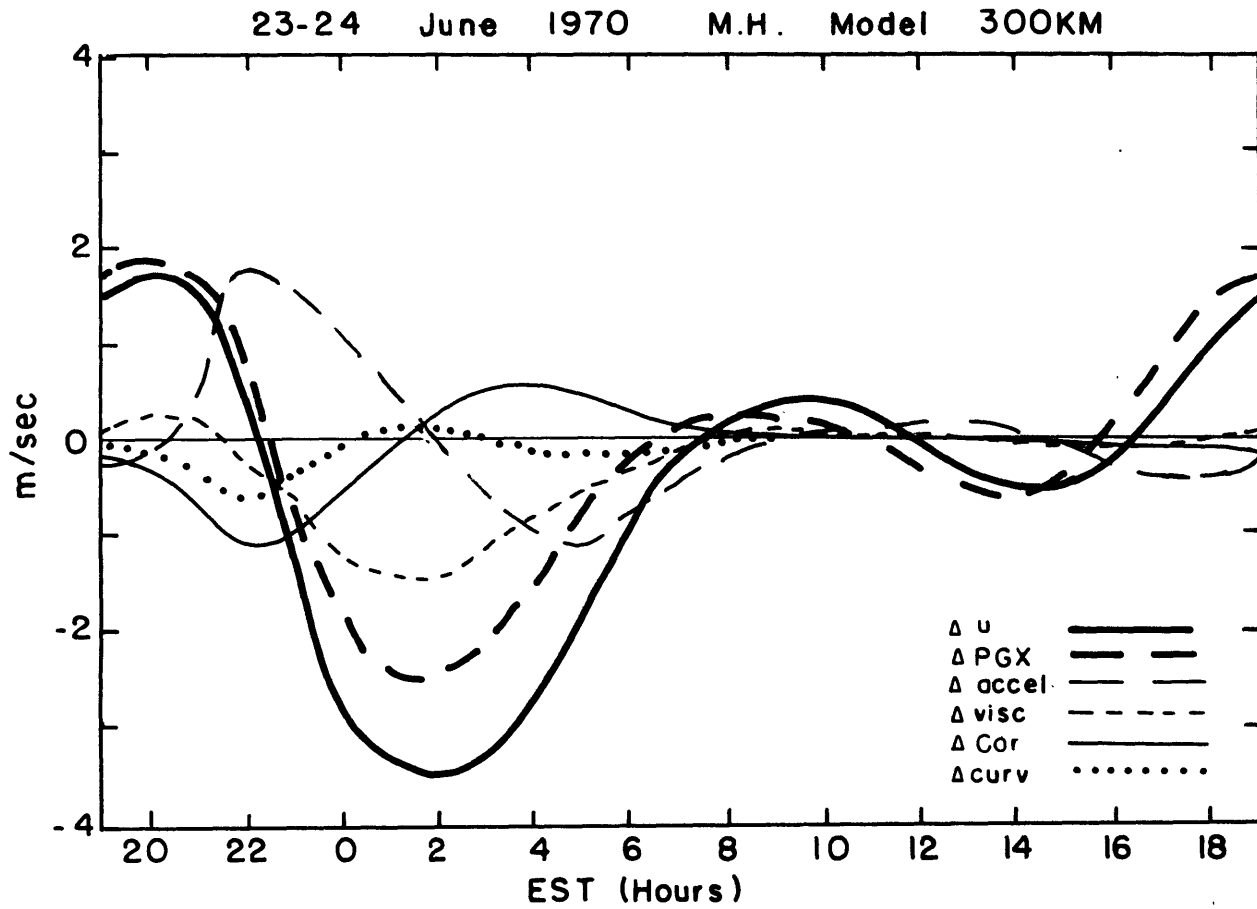


Fig. C.3a: Plot of the contributors to the difference in zonal velocity Δu between $42.6^{\circ}N$ and $42.8^{\circ}N$ at 300 km assuming constant electron densities for the present analysis of June 23-24, 1970.

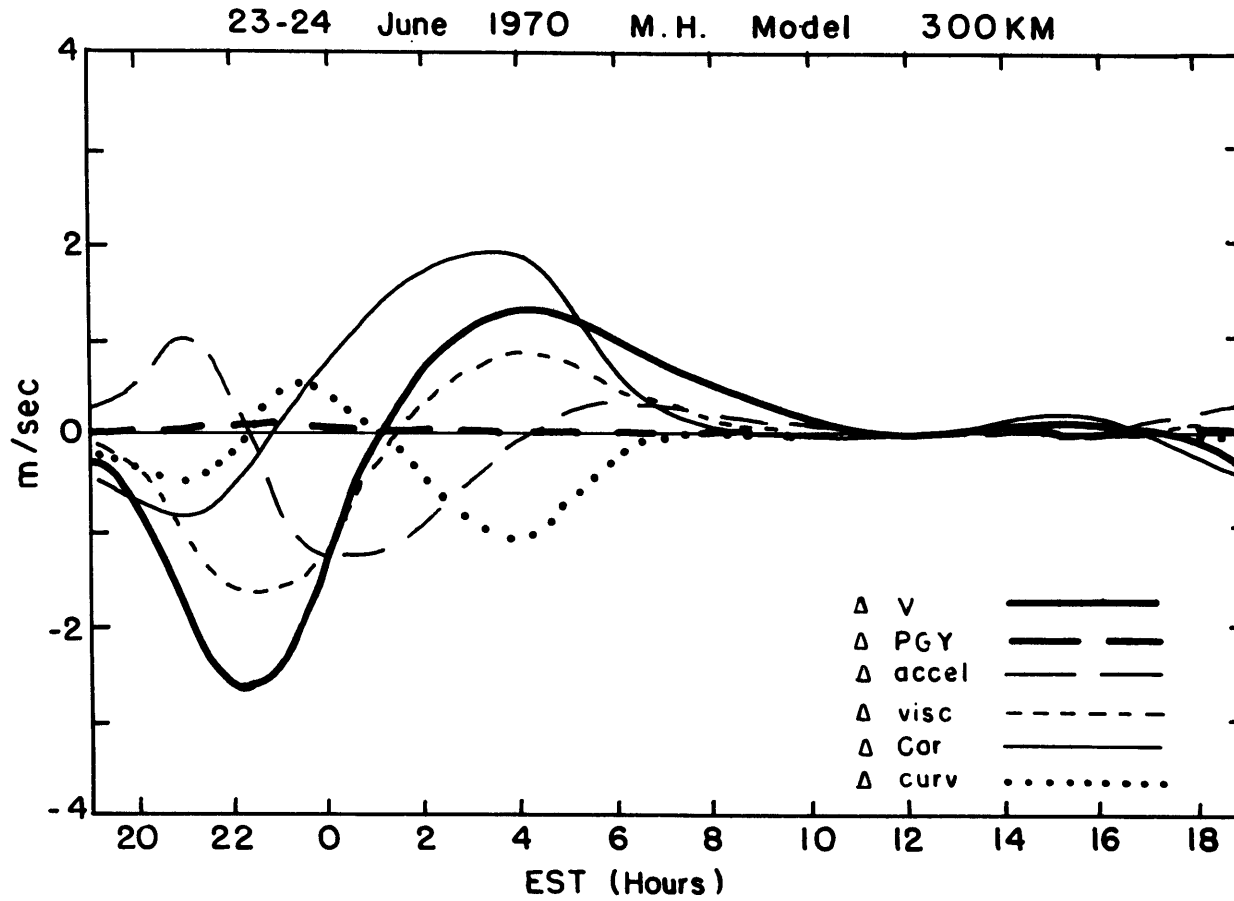


Fig. C.3b: Plot of the contributors to the difference in meridional velocity Δv between $42.6^{\circ}N$ and $42.8^{\circ}N$ at 300 km assuming constant electron densities for the present analysis of June 23-24, 1970.

250 m/sec around 0500 LT. A wind of +380 m/sec leads one to predict then ΔPGX should increase by $0.008 * 380 = 3.0$ m/sec in the case of decreasing electron density at 2200 LT. The actual increase is 2.4 m/sec since the pressure gradient is only about 78% of the ion drag term $0.78 * 3.0 = 2.3$ m/sec. There is not, however, a corresponding increase in Δu . Rather the increase is only about 1.0 m/sec since the contributions from the other terms have shifted in such a way as to ameliorate the effects of the electron density decrease. The largest changes in Δu are about 1.4 m/sec at 0700 LT. The changes in Δv are smaller, being about 0.5 m/sec around 2200 LT. ΔPGY is negligible with a constant electron density due to the assumption of constant $\frac{\partial T}{\partial \phi}$, but can be substantial (± 2 m/sec) with decreasing electron density. Its magnitude is about 0.008 $(-1/\rho \lambda_1) \partial p / \partial y$, so its sign is opposite that of $\frac{\partial T}{\partial \phi}$.

A similar experiment was carried out using the MSIS model pressure gradients for June 23-24, 1970. Figure C.4a and b show the results of this study where the x's refer to calculations performed with latitudinally constant electron density. The differences between the two electron density cases are no more than 1.3 m/sec, but this can amount to a change of over 50%. Again, a decreasing electron density produced larger values of Δu and Δv , ranging up to 2 m/sec.

A polewards decrease of electron density of 4% in 1° of latitude on June 23-24, 1970 thus increased Δu and Δv by 20 to

50%, in the Millstone Hill case and by 50% or more in the MSIS case. This is a relatively large variation in the meridional derivatives of the horizontal winds. Assuming the results on this June day are comparable to other days, the errors introduced into the latitudinal velocity gradients by not knowing the latitudinal electron density variation are of the order of ± 1 m/sec.

C.3 The Assumption of Constant $\partial T_{\infty} / \partial \phi$

This is a major assumption that will not be easy to remedy if it proves to be inadequate. One way of testing this assumption is to see whether or not the global atmospheric models of MSIS and OGO-6 predict large enough changes in the meridional pressure gradient force over 0.2° latitude to cause significant latitudinal changes in the meridional velocity. Calculations were performed with the ionospheric data collected above Millstone Hill on June 23-24, 1970 in conjunction with temperatures, densities, and pressure gradients produced by the MSIS and OGO-6 models for the given solar conditions found on that day. General comparisons of the models with the results of the present analysis were given in Chapter 6, but Figures C.4a and b show the contributions to Δu and Δv at 300 km for the MSIS model. The results of the OGO-6 model were similar.

The striking differences between these plots and the corresponding plots of C.2a and b concern ΔPGX and ΔPGY . ΔPGX of the MSIS model is two or three times smaller but has approximately the same diurnal variation and Δu still approximately follows ΔPGX .

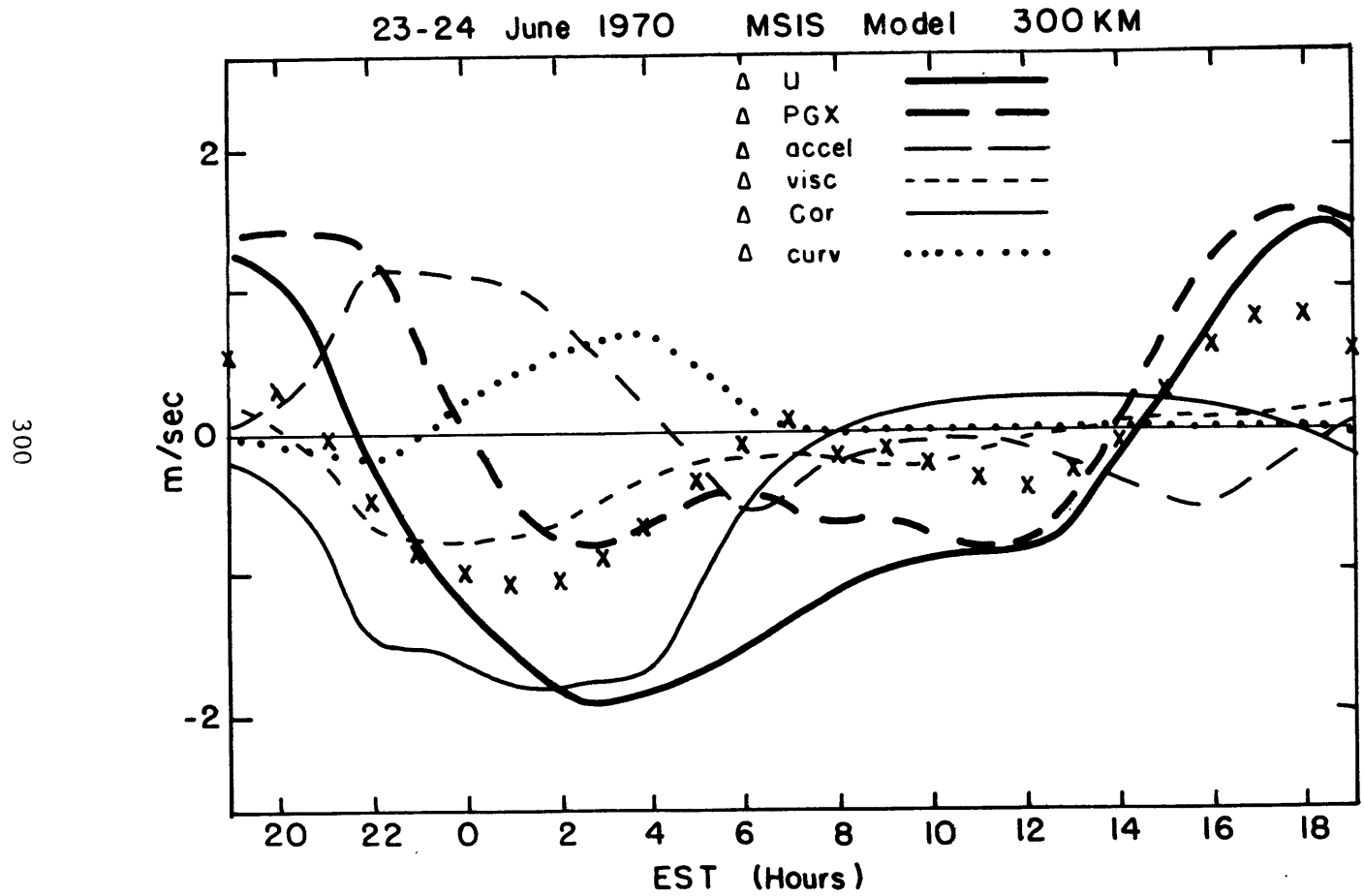


Fig. C.4a: Plot of the contributors to the difference in zonal velocity Δu between 42.6°N and 42.8°N at 300 km for the MSIS model on June 23-24, 1970. The x's are the values of Δu derived using constant electron densities.

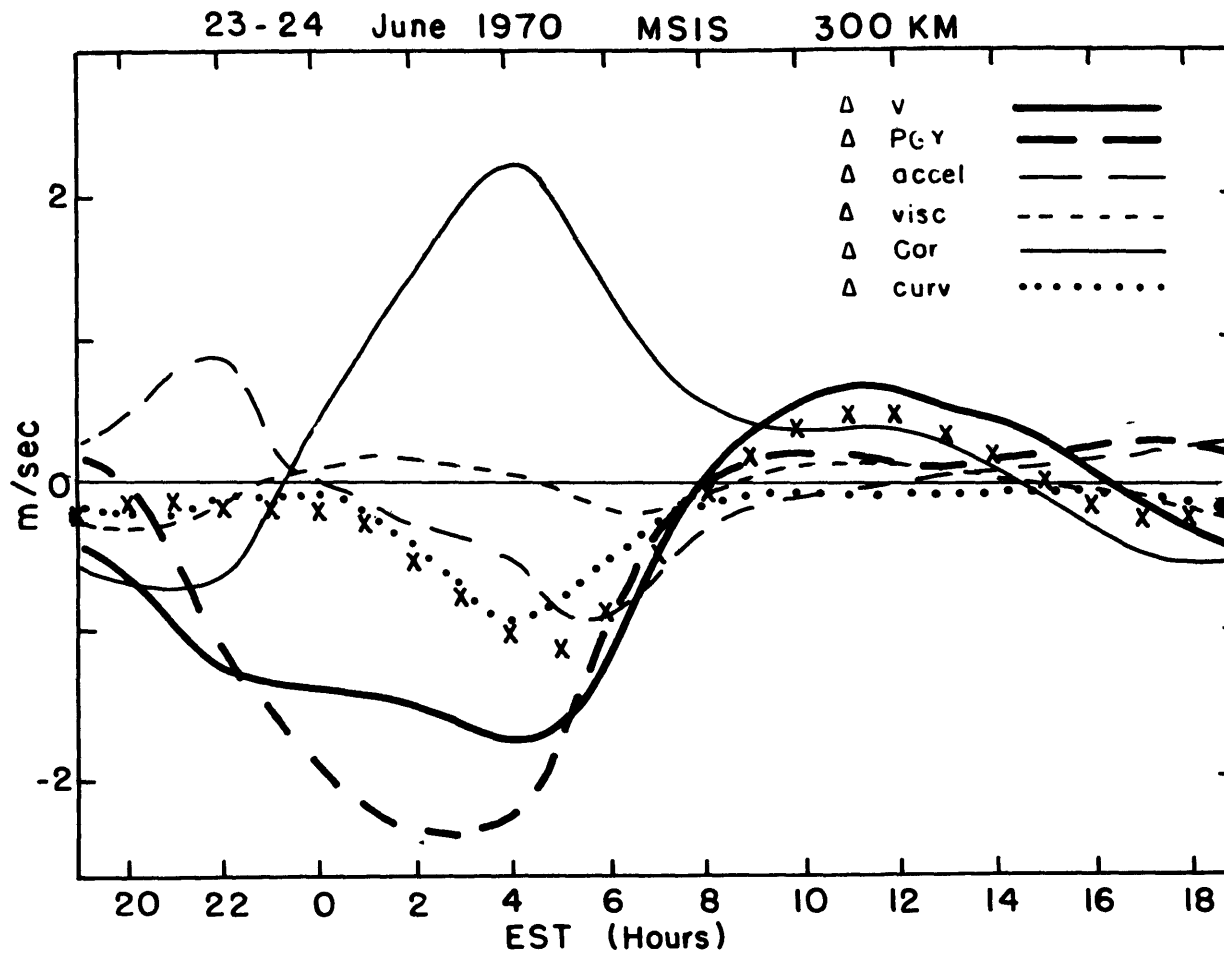


Fig. C.4b: Plot of the contributors to the difference in meridional velocity Δv between $42.6^{\circ}N$ and $42.8^{\circ}N$ at 300 km for the MSIS model on June 23-24, 1970. The x's are the values of Δv derived using constant electron densities.

The decrease in magnitude can be explained on the grounds that the pressure gradients in the MSIS model are about two times smaller than the gradients of the present study. The similar diurnal variation, though, may be only fortuitous.

The present study assumes that ΔPGX is proportional to $-\partial(1/\rho \partial p/\partial y)\partial t$. The meridional pressure gradient at 300 km is a minimum of about -7.4 cm/sec^2 around 2200 LT and a maximum of about 4.4 cm/sec^2 around 0500 LT with a later minimum around 1100 LT and maximum at 1600 LT (see Figure 6.7b). This implies that ΔPGX is negative from 2200 to 0500, and from 1100 to 1600, and positive the rest of the time. This is generally true, especially for the case of constant electron density (Figure C.3a). This reasoning will now be applied to the MSIS model case.

The meridional pressure gradient in the MSIS model has approximately the same phase as the meridional temperature gradient, despite the added influence of other terms such as the non-zero bottom boundary atomic oxygen meridional gradient. Examining the diurnal variation of the meridional pressure gradient (Figure 6.12b) one might conclude that for the MSIS model ΔPGX is negative between 1600 LT and 2300 LT and positive otherwise. Almost the complete opposite is found as can be seen in Figure C.4a, where ΔPGX is negative between 2200 and 1400 LT. For the case of constant electron density, ΔPGX was negative between 2100 LT and 0200, and between 0800 and 1400, and positive otherwise.

Both ΔPGX and ΔPGY in Figures C.4a and b have approximately the same sign as $-1/\rho \partial p/\partial x$ and $-1/\rho \partial p/\partial y$ (Figures 6.12a and b) respectively, implying that

$$\left| \frac{1}{\rho \lambda} \frac{\partial p}{\partial x, y} \right|_2 > \left| \frac{1}{\rho \lambda} \frac{\partial p}{\partial x, y} \right|_1 \quad (\text{C.4})$$

However, the decreasing electron density ($\lambda_2 < \lambda_1$) introduced some sign changes that made this relationship possible. Precisely why the diurnal variations of ΔPGX and ΔPGY are the way they are was not determined in this study.

Nevertheless, it is clear that ΔPGY contributes substantially to the determination of Δv , even with constant electron densities, so the assumption of latitudinally constant meridional exospheric temperature gradients is inadequate. At least one more term needs to be added to the expression in Eq. 5.10 to represent the latitudinal variation of $\partial T_\infty / \partial \phi$. The exospheric temperature could then be written as

$$T_\infty(\phi, t) = T_{\infty \text{MH}} + (\phi - \phi_{\text{MH}}) \left(\frac{\partial T_\infty}{\partial \phi} \right)_{\text{MH}, e} + (\phi - \phi_{\text{MH}})^2 L_e \quad (\text{C.5})$$

where MH stands for the value at Millstone Hill, e stands for "effective", and L_e is the extra term representing the latitudinal variation of $\partial T_\infty / \partial \phi$. Unfortunately, there is no way this extra term can be deduced from the available incoherent scatter data. Looking at the results of models such as the OGO-6 or MSIS models can give one an idea of what correction should be made to Δv (or

$\partial v / \partial y$), but this would defeat one of our objectives - namely, to test the models. Despite this, it appears that Δv should be more negative in the early morning hours around sunrise, and more positive in the late morning.

The implication of these experiments appears to be that it is not possible to accurately compute vertical velocities or north-south non-linear terms using only the incoherent scatter data. The experiments imply that instead of large downward velocities during the late night hours rising to a sharp upwards peak after sunrise, the velocities should remain downwards for a longer period, and rise more slowly peaking later in the day. In summary, the errors introduced by assuming a latitudinally constant meridional exospheric temperature gradient mainly affects the meridional velocity gradient, giving rise to biases of about +2 m/sec in the early morning hours and -0.5 m/sec later in the morning. These in turn introduce biases of about +5 and -2 m/sec in the velocities at these times. Correcting for these biases gives the vertical velocity a much smoother variation. The numbers given are very rough estimates and are not to be taken as reliable corrections to the results.

C.4 Comparison with Other Work

Blum and Harris (1975) have published the results of a full non-linear treatment of the global thermospheric wind system. They used the Jacchia 1965 model for temperatures, densities, and

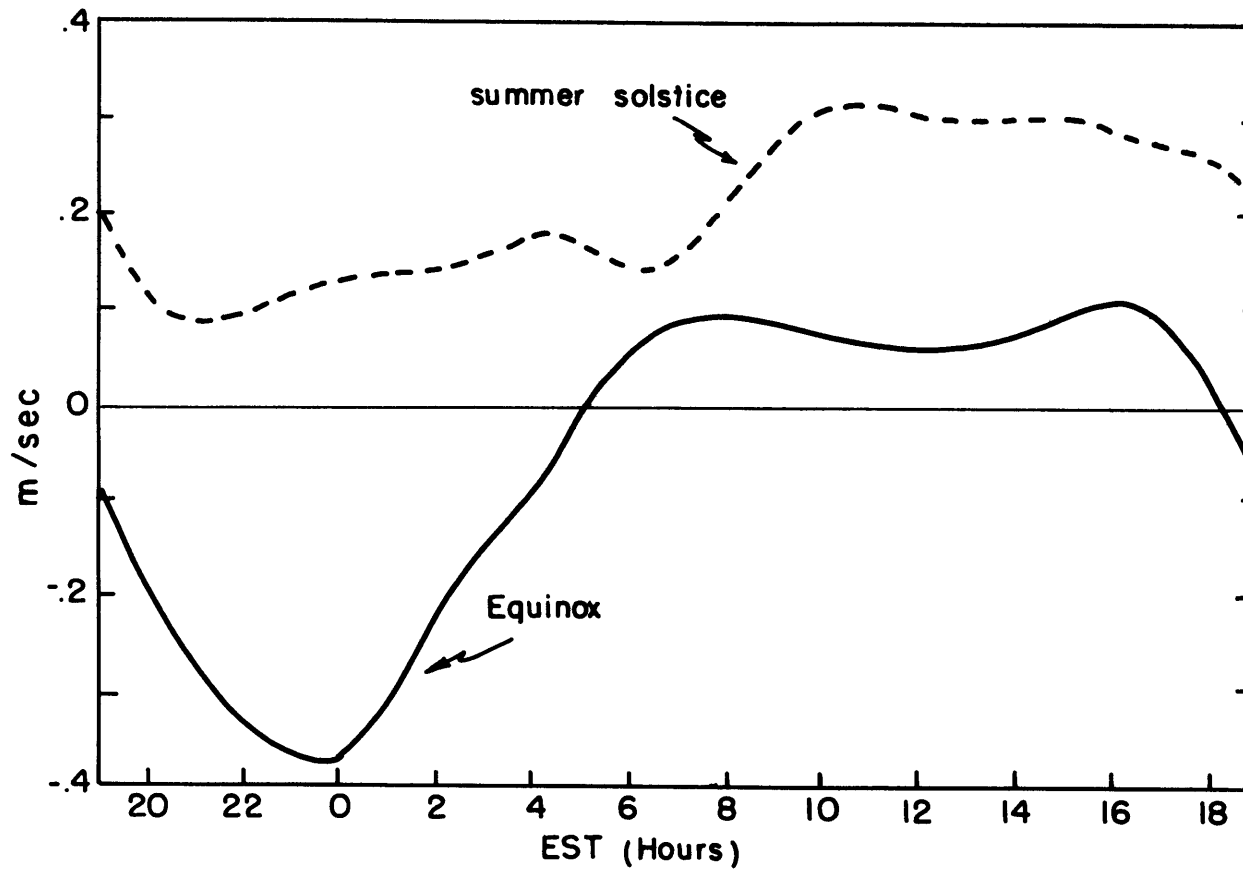


Fig. C.5: Plot of Δv at 300 km in 0.2° of latitude for mid-latitudes deduced from Figures 8 and 9 of Blum and Harris (1975).

pressure gradients, and the Penn State Ionospheric Model of Nisbet (1970) to establish the ion drag. Using such a smooth model, they could not include the higher Fourier modes. The zonal velocities in particular, showed only small meridional variation because the pressure gradients of the Jacchia model depend little on latitude. The meridional winds showed diurnal differences of up to 40 m/sec between the latitudes of 30° and 50° . This translates into a difference of 0.4 m/sec in 0.2° . Figure C.5 shows plots of Δv in 0.2° of latitude for equinox and summer solstice conditions as deduced from their Figures 8 and 9 at 30° and 50° N. Not only are the magnitudes of Δv about 10 times smaller than those found for the present study, but the variation in summer is all positive (meridional velocities more northwards at higher latitudes). The Millstone Hill calculations bear more resemblance to the equinox case. The lack of the higher Fourier modes in the Blum and Harris study and the implicit assumption that the differences is 0.2 degrees can be linearly extrapolated over 20 degrees in the Millstone Hill case are probably the reason for the differences in magnitudes. The difference in sign in the summer solstice case may be a result of different latitudinal variations in the electron density and in the pressure gradients.

APPENDIX D

NON-LINEAR TERMS: STABILITY CRITERIA AND ROLE AS OUTSIDE FORCING FUNCTIONS

D.1 Stability Criteria for Including the East-West Non-Linear Term

In Section 4.1 the assumption was made that time and longitude are interchangeable, their derivatives being related in the fashion

$$dx = (2\pi r \cos \varphi / 24 \text{ hours}) dt \quad (\text{D.1})$$

This seems a reasonable assumption, given the dominance of solar heating in the thermosphere. However, such an assumption leads to certain restrictions on the stability criteria for including the east-west non-linear term $u \partial \vec{v} / \partial x$ (or the zonal viscous term $\mu / \rho \partial^2 \vec{v} / \partial x^2$) in finite difference schemes.

A rough estimate of the conditions necessary in order that the east-west non-linear term can be included in the equations of motion 4.5, can be derived by considering only the acceleration and the east-west non-linear terms. The finite difference scheme can be written as

$$\frac{\vec{v}^{n+1} - \vec{v}^n}{\Delta t} + u_{\text{est}}^{n+\frac{1}{2}} \frac{\vec{v}^{n+1} - \vec{v}^n}{\Delta x} = 0 \quad (\text{D.2})$$

where Δt is the time step, Δx is the longitude step, and $u_{\text{est}}^{n+\frac{1}{2}} = u^n + \frac{1}{2} (u^n - u^{n-1})$ is the estimated zonal velocity at time $n + \frac{1}{2}$. This is an explicit formulation, an implicit formulation being impossible since future values of the velocity cannot be stored.

(Solving the quadratic equation $a(u^{n+1})^2 + bu^{n+1} + c = 0$ is not possible either since complex values for u^{n+1} become a problem.)

Stability for equation D.2 is achieved if

$$\left| u_{\text{est}}^{n+\frac{1}{2}} \right| \frac{\Delta t}{\Delta x} < 1 \quad (\text{D.3})$$

or if

$$\left| u_{\text{est}}^{n+\frac{1}{2}} \right| < \frac{\Delta x}{\Delta t} = \frac{2\pi r \cos \varphi}{24 \text{ hours}} = 356 \text{ m/sec} \quad (\text{D.4})$$

for 300 km above Millstone Hill. Zonal velocities of 350 m/sec are approximately associated with exospheric temperature gradients of about 50°K/hour or 300°K/6 hours. Since the day-night temperature difference is of the order of 300°K and the change-over takes place in 6 hours or less, this stability criterion is often violated at sunrise. (The decay in temperature at sunset is usually less abrupt). Such high zonal velocities are inconsistent with the idea that the earth rotates under a fixed pattern of winds driven by the sun, but data from one station can provide only temporal information, and not longitudinal information. Because of this, it was decided to remove the east-west non-linear term $u \partial \vec{v} / \partial x$ from the equations of motion 4.4, and gauge its effect after the fact by including it later as an outside forcing function. This approach is examined in Section D.3.

D.2 Stability Criteria for the Inclusion of the North-South Non-Linear Term

Section 7.4 and Appendix C described the accuracy of the latitudinal velocity gradients which are contained in the north-south non-linear term $v\partial\bar{v}/\partial y$. It was concluded that both $\partial v/\partial y$ and $\partial u/\partial y$ may be uncertain by as much as 50% of their value, while the values of $\partial v/\partial y$ also contain biases of the order of about 0.5 to 2 m/sec in 0.2° . Despite the size of these uncertainties it might be desirable to include the north-south non-linear term if this were feasible i.e., if doing so did not introduce stability problems in solving the equations. In this section we examine this question.

The stability criteria for including the north-south non-linear term is similar in form to that for including the east-west non-linear term. It is that

$$\left| v \frac{\Delta t}{\Delta y} \right| \ll 1 \quad (\text{D.5})$$

Setting $\Delta y = .2^\circ * \pi(\text{Re} + z)/180^\circ$, and $\Delta t = 20$ min, we find that the criterion is violated for meridional velocities larger than about 19 m/sec. Since Δt and Δy can be changed independently of one another, it is possible to increase the range of meridional velocities by reducing Δt to 1 min, for example. Increasing Δv to about 4° is another possibility, but this raises questions concerning the linearity of the latitudinal variations.

If the north-south non-linear term is to be directly included in the finite difference scheme, then not only must it fulfill this stability criteria, but the time stepping must be changed from a forward step to a leapfrog step, or the scheme is unstable. The acceleration and non-linear terms would then be represented by finite differences of the form

$$\begin{aligned} & \frac{\vec{v}_y^{n+1} - \vec{v}_y^{n-1}}{2\Delta t} + u_y^n \frac{\vec{v}_y^{n+1} - \vec{v}_y^{n-1}}{2\Delta x} \\ & + v_y^n \frac{\vec{v}_{y+1}^n - \vec{v}_{y-1}^n}{2\Delta y} = \dots \end{aligned} \quad (D.6)$$

where $y+1$ and $y-1$ indicate latitudes separated by $\pm \Delta y$ about a particular latitude y . The initial assumptions would be that $\vec{v} = 0$ at times $n=0$ and 1 . Boundary conditions for the meridional directions could be that $\partial^2 \vec{v} / \partial y^2 = 0$. Three latitudes would be calculated-- the latitude of Millstone Hill and the two latitudes Δy above and below it.

This more exact procedure was not utilized. Instead, the north-south non-linear term was computed at two latitudes (ϕ_{MH} and $\phi_{MH+.2}$) and $\partial \vec{v} / \partial y$ was assumed to be the same at these two latitudes and equal to $(\vec{v}_{MH+.2} - \vec{v}_{MH}) / \Delta y$. Then, as was attempted for the east-west non-linear term, these values were stored to be used later as an outside forcing function. The idea behind this approach was to compute the behavior over first 24 hours entirely linearly

and store estimates of the non-linear terms. Later, in the second computation, these stored values were used while new ones were being estimated and stored. Another fit might then be made to V_{Hn} , and the whole process repeated in an iterative fashion. It was possible to include either the north-south non-linear term, or the east-west non-linear term, or both of them.

D.3 Effects of Including the Non-Linear Terms as Outside Forcing Functions

The east-west non-linear term can be relatively large, i.e., of the same order of magnitude as the acceleration term. Due to stability problems described in Section D.1, it can only be included as an outside forcing function. If the east-west non-linear term is added later, its net effect on the mean velocities is to make them more northwards and eastwards. The evening eastwards velocity peak is delayed slightly, and remains longer. The dawn westwards peak is sharper and of shorter duration. The net result is a mean eastwards velocity increase of about 10 m/sec. There is a net northwards mean velocity of about the same magnitude which is largely the result of a net Coriolis effect to the north in the early evening hours when the eastwards velocity peak has been delayed. A north-eastward (or south-westward) wind can be partially accommodated in trying to fit V_{Hn} since the wind perpendicular to the magnetic field line will not affect the value of V_{Hn} . (This perpendicular line is rotated 14° anticlockwise from the east-west

line, so it lies in the NE and SW quadrants). Such an accommodation makes it easier for the iterative process to converge.

The iterative procedure of fitting V_{Hn} , computing and storing the east-west non-linear term, and adding this term was performed for June 23-24, 1970. The net change was a 3 m/sec increase in the mean zonal wind toward the west, a 2 m/sec increase in the mean southwards wind, a $30^{\circ}\text{K}/\text{rad}$ increase in the average exospheric temperature gradient, and an increase of $0.8 \text{ cm}/\text{sec}^2$ in the average meridional pressure gradient force. On this day, the east-west non-linear term was no more than 30% of the major terms in the equations of motion.

The north-south non-linear term is about the same order of magnitude as the east-west non-linear term in the summer, but is substantially less in the winter, because the mean meridional velocity then becomes northwards and the large southward (equatorward) velocities encountered during summer nights are reduced. Adding the north-south non-linear term tends to shift the mean winds towards the north-west. The negative values of Δu evident in the early morning hours in the plots of C.2a, C.3a and C.4a, together with the southward wind velocities prevailing at that time, give rise to increased westward velocities in the zonal momentum equation. The Coriolis term then acts on this to give a net northwards velocity, and is assisted by the positive values of Δv found at this time (see the plots of C.2b and C.3b). The net increase in the westward velocity for June 23-24, 1970 was about 30 m/sec,

resulting in a net increase in the northward velocity of about 10 m/sec. Unfortunately, a net increase in the winds toward the north-west cannot be easily accommodated when trying to fit V_{Hn} . When fits were attempted, the meridional exospheric temperature gradient increased to be consistent with a net southwards velocity needed to match the net increase in the westwards velocity. This then increased the size of $\partial u/\partial y$, which increased the net westwards velocity, and the whole process diverged. This provides indirect evidence that something is wrong with the north-south non-linear term.

To investigate this problem the process of adding the north-south non-linear term devised here was used in calculations for the winds that would be generated by the pressure gradients in the MSIS model for this day. The addition of the non-linear term added a net southward velocity of about 20 m/sec and a net westward velocity of about 40 m/sec. The value of Δv (or $\partial v/\partial y$) was negative in the early morning hours in the plot of C.4b and not positive. This gave rise to an increase in the southwards velocity instead of the northward velocity. This was encouraging, because maintaining a fit to V_{Hn} while converging did not appear to be so difficult.

An attempt was made to converge to some stable state using the MSIS model while adding the north-south non-linear term as an outside forcing function, and updating it at every iteration. It failed because the north-south non-linear term and the velocities kept growing larger and larger after every interaction, indicating some sort of instability.

Since this was a summer day and the non-linear term is largest at night when the electron density may be more nearly constant in latitude, this same procedure was repeated for the case of latitudinally constant electron densities. Here, after the first iteration, there was a net westwards velocity of 20 m/sec and a net northwards velocity of 2 m/sec. This time, the process converged to average velocities which were 22 m/sec more westwards and 0.4 m/sec more southwards.

Adding both the non-linear terms resulted in a net velocity shift to the west of 13.5 m/sec and to the north of 25 m/sec after the first iteration. Convergence was not achieved because the east-west non-linear term grew after every iteration. This happened because the instability in the east-west non-linear term was still there, but was deferred by being added as an outside forcing function.

Adding both non-linear terms as outside forcing functions was also attempted for the present analysis of December 8-9, 1969, a winter day where the north-south non-linear term was small. The whole process of fitting V_{Hn} and updating the non-linear terms to be used in the next iteration was performed. There was a partial convergence to a state where the net changes in the average velocities were 2 m/sec or less and the net change in the average meridional gradients of the exospheric temperature and the pressure were $16^{\circ}\text{K}/\text{rad}$ and $0.43 \text{ cm}/\text{sec}^2$ respectively. The non-linear terms (or more specifically the east-west non-linear terms since the north-south non-linear terms were very small) were only about 20% or less of the major terms in the equations of motion.

CURRICULUM VITAE

Barbara Ann Emery

Born: 2 December 1950, Urbana, Illinois

Education: University of Illinois, Urbana, Illinois
1968-1972
B. Sc. Physics (June 1972)

Massachusetts Institute of Technology
1972-1977
S. M. Meteorology (February 1975)
Sc. D. Meteorology (May 1977)

Honor Societies: Phi Beta Kappa, Sigma Xi

Professional Memberships: American Meteorological Society
American Geophysical Union

Research Experience: Computer Programmer
Aeronomy Laboratory
Electrical Engineering Department
University of Illinois
Urbana, Illinois
1971-1972

Fellowship in Computer Programming
National Center for Atmospheric Research
Boulder, Colorado
summer 1973

National Science Foundation Fellowship
Department of Meteorology
Massachusetts Institute of Technology
Cambridge, Massachusetts
1973-1976

Research Assistant
Department of Meteorology
Massachusetts Institute of Technology
Cambridge, Massachusetts
1976-1977

Publications:

- Emery, Barbara, 1972: Appendix I: Report on the digitization of the ionosonde output to find the calibration constant G as a function of frequency. Research in Aeronomy, April 1---September 30, 1972, Progress Report No. 72-2, Aeronomy Laboratory, Dept. of Elec. Eng., U. of Ill., Urbana.
- Emery, Barbara, 1973: The structure of neutral thermospheric winds at Millstone Hill, Massachusetts inferred from incoherent backscatter radar measurements. Summary Reports---Fellowship in Scientific Computing, Summer 1973, NCAR-TN/PROC-90, National Center for Atmos. Res., Boulder, Colorado, 33-55.
- Roble, R. G., B. A. Emery, J. E. Salah, and P. B. Hays, 1974: Diurnal variation of the neutral thermospheric winds determined from incoherent scatter radar data. J. Geophys. Res., 79, 2868-2876.
- Emery, Barbara A., 1975: A Radar Study of the Thermosphere. S. M. thesis, Dept. of Meteorology, Mass. Inst. of Tech., Cambridge, 96 pp.
- Emery, B. A., 1975: SA 47: Analysis of meridional properties of the midlatitude neutral atmosphere. Presented at the Spring meeting of the Am. Geophys. Union, Washington, D. C.
- Roble, R. G., J. E. Salah, and B. A. Emery, 1975: SM12-27: The seasonal variation of the diurnal thermospheric winds over Millstone Hill. Presented at the XVI International Union of Geodesy and Geophysics, Grenoble, France.
- Roble, R. G., J. E. Salah, and B. A. Emery, 1977: The seasonal variation of the diurnal thermospheric winds over Millstone Hill during solar cycle maximum. J. Atmos. Terr. Phys., in press.
- Emery, Barbara A., 1977: Seasonal Wind Variations in the Mid-Latitude Neutral Thermosphere. Sc. D. thesis, Dept. of Meteorology, Mass. Inst. of Tech., Cambridge.